DEPARTMENT OF COMPUTER SCIENCE (DIKU)
UNIVERSITY OF COPENHAGEN

Workshop on Breast Image Analysis

In conjunction with
the 14th International Conference on
Medical Image Computing and Computer
Assisted Intervention (MICCAI 2011)

Christine Tanner, Julia Schnabel,
Nico Karssemeijer, Mads Nielsen,
Maryellen Giger, Dawid Hawkes (Eds.)

Technical Report no. 05/2011

ISSN: 0107-8283

ISBN: 978-87-981270-9-3

Preface

Breast cancer affects many women: In the western world about 12% of women are diagnosed with breast cancer during their lifetime. Therefore, breast imaging, with applications in risk assessment, screening, diagnosis, and treatment, is an important topic. In modern breast imaging, traditional imaging modalities such as mammography and handheld ultrasound are complemented by dynamic contrast-enhanced MRI, whole breast ultrasound, and breast tomosynthesis. To make optimal use of these technologies, there is a strong need for the development of effective image analysis methods. Examples are extraction and combination of information from multimodal imaging, temporal change assessment in screening, and relating image characteristics to risk factors. Development of such methods is highly challenging due to large deformations of the breast and subtlety of the abnormalities to be detected and diagnosed.

The first Workshop on Breast Image Analysis was held on 18th of September 2011 in Toronto, Canada, in conjunction with the 14th International Conference on Medical Image Computing and Computer Assisted Intervention (MICCAI 2011). It was jointly organised by the groups at Chicago, Copenhagen, London, Nijmegen, Oxford, and Zürich, with an external scientific committee of 22 reviewers from 4 continents and 9 countries, all experts in the field. Full-length paper submissions (8 pages, LNCS style) were invited, and a total of 33 submissions from 22 international research institutions, 6 continents and 13 countries, were received. Each submitted paper was reviewed double-blinded by 3 reviewers from the Scientific Committee and the Organising Committee. Based on the reviews, a total of 23 papers were accepted and are included in these workshop proceedings. From these, 12 papers were selected for oral presentations, grouped into four themed sessions: Motion Analysis and Reconstruction; Segmentation; CAD and Quantitative Analysis; Biomechanical Modelling. The remaining 11 papers were selected for poster presentation. Authors were asked to take reviewers' comments into account for their final version. Proceedings were made available as a PDF file on the MICCAI Workshop USB stick, as well as ISBN Online proceedings.

The purpose of this first MICCAI Workshop on Breast Image Analysis was to bring together researchers in the field of breast imaging to discuss and exchange new ideas and applications, and to provide a platform for breast image analysis methodology across all imaging modalities. Substantial discussion time for posters was provided to allow for a stimulating exchange

of ideas. The invited keynote lecture by Professor Martin Yaffe, Sunnybrook Health Sciences Centre, Toronto on "Breast imaging with tomosynthesis and CT" was inspiring and very well received. A special journal issue based on topics of this workshop, as well as future Breast Image Analysis workshops, are under discussion.

On behalf of the Organising Committee, we would like to thank all members of the Scientific Review Committee, workshop presenters and contributing authors, as well as all workshop participants for making this first Workshop on Breast Image Analysis an inspiring and successful event!

Christine Tanner and Julia Schnabel

Organising Committee:

Christine Tanner	Computer Vision Laboratory, ETH Zürich, Switzerland
Julia Schnabel	Institute of Biomedical Engineering, Dept. of Engineering Science, University of Oxford, UK
Nico Karssemeijer	Dept. of Radiology, Radboud University Nijmegen Medical Centre, The Netherlands
Mads Nielsen	Dept. of Computer Science, University of Copenhagen, Denmark
Maryellen Giger	Dept. of Radiology & Committee on Medical Physics, University of Chicago, USA
David Hawkes	Centre for Medical Image Computing, University College London, UK

Scientific Committee:

Susan Astley	Medical School, University of Manchester, UK
Ulrich Bick	Dept. of Radiology, Charité, Berlin, Germany
Mike Brady	Dept. of Radiation Oncology and Biology, University of Oxford, UK
Heang-Ping Chan	Dept. of Radiology, University of Michigan, USA
Karen Drukker	Dept. of Radiology, University of Chicago, USA
Giovanni Farinella	Dept. of Mathematics and Computer Science, University of Catania, Italy
Hiroshi Fujita	Dept. of Intelligent Image Information, Gifu University, Japan
Lubomir Hadjiiski	Dept. of Radiology, University of Michigan, USA

John Hipwell	Centre for Medical Image Computing, University College London, UK
Jong Hyo Kim	College of Medicine, Seoul National University, South Korea
Despina Kontos	Dept. of Radiology, University of Pennsylvania, USA
Murray Loew	Electrical Engineering and Computer Science Dept., The George Washington University, USA
Anthony Maeder	College of Health and Science, University of Western Sydney, Australia
Robert Martí	Computer Vision and Robotics Group, University of Girona, Spain
Martyn Nash	Dept. of Engineering Science, The University of Auckland, New Zealand
Torsten Rohlfing	Stanford Research Institute (SRI) International, USA
Berkman Sahiner	Dept. of Radiology, University of Michigan, USA
Dinggang Shen	Radiology Research Labs, University of North Carolina, USA
Georgia Tourassi	Dept. of Radiology, Duke University, USA
Thorsten Twellmann	MeVis Medical Solutions AG, Bremen, Germany
Bin Zheng	Dept. of Radiology, University of Pittsburgh, USA
Reyer Zwiggelaar	Dept. of Computer Science, Aberystwyth University, UK

Workshop website:	http://www.eng.ox.ac.uk/BIA2011
Online proceedings:	http://www.diku.dk/BIA2011proceedings.pdf
	ISSN: 0107-8283
	ISBN: 978-87-981270-9-3

Table of Contents

Biomechanical Modelling

Multi-scale Analysis and Characterization

Generating Coefficients for Regularization Terms in Nonrigid Registration of Contrast-Enhanced MRI

Xi Liang[1,2], Ramamohanarao Kotagiri[1], Qing Yang[3], Marius Staring[4], and Alexander Pitman[2]

[1] National ICT Australia (NICTA)
[2] Department of Computer Science and Software Engineering, University of Melbourne
[3] Apollo Medical Imaging Technology L.t.d
[4] Department of Radiology, Leiden University Medical Center

Abstract. Nonrigid registration is a technique to recover spatial deformations between images. It can be formulated as an optimization problem to minimize the image dissimilarity. A regularization term is used to reduce undesirable deformations which are usually employed in a homogeneous or spatial-variant fashion. When spatial-variant regularization is used in nonrigid registration of dynamic contrast-enhanced magnetic resonance imaging (DCE-MRI), the local coefficients have been determined by manual segmentation of tissues of interest. We propose a framework to generate regularization coefficients for nonrigid registration in DCE-MRI, where tumor locations are to be transformed in a rigid fashion. The coefficients are obtained by applying a sigmoid function on subtraction images from a pre-registration. All parameters in the function are automatically determined using k-means clustering. The validation study compares three regularization weighting schemes in nonrigid registrations: a constant coefficient for a volume-preserving term, binary coefficients obtained by manual segmentation and a real-value coefficients using the proposed method on a rigidity term. Evaluation is performed using displacements, intensity changes and volume changes of tumors on synthetic and clinical DCE-MR breast images. As a result, the registration using spatial-variant rigidity terms performs better than using homogeneous volume-preserving terms. For the coefficient generation methods of a rigidity term, the proposed method can replace the binary coefficients requiring manual tumor segmentation.

1 Introduction

Dynamic contrast-enhanced magnetic resonance imaging (DCE-MRI) is used to differentiate between malignant and benign lesions in cancer diagnosis. A sequence of 3D MRI scans before and after the injection of a paramagnetic contrast agent is acquired to form a 4D (3D+time) DCE-MR image. The 4D imaging technique allows an analysis of the variation of the magnetic resonance (MR) signal intensity, before and after the injection of contrast enhancement. The time-intensity curve patterns can be used in the detection of tumors. However, the motion in between the image acquisitions can complicate the analysis. Image registration is used in DCE-MR image analysis to achieve alignment between images. Image registration is an optimization problem aiming to minimize the image dissimilarity. In registration of DCE-MRI, free-form deformation

ISBN: 978-87-981270-9-3

(FFD) based nonrigid registration is widely used to remove motions in between image acquisition of the pre- and post-contrast images [1]. All post-contrast images at different time steps are registered to the baseline pre-contrast image such that the same tissue is located at the same position in all images.

There are two reasons that lead to an intensity difference. One is motion occurred in between image acquisitions and the other is intensity enhancement caused by the injection of contrast agent. Therefore, minimizing the image dissimilarity during the image registration can reduce the occurred motion but also change the volume of the enhanced region [2]. This can be countered through the use of regularization.

An incompressibility constraint was proposed to preserve tumor volumes [2], which is applied on the whole breast region with the same weight for all types of tissues. The assumption is that the tissue volume does not change over a short period of time. However, most DCE-MR images require several minutes' acquisition time and the breath or body gesture changes of a patient might change the volume of soft breast tissues.

Spatial-variant rigidity constraints [3,4,5] were proposed to preserve the rigidity of tissues. When applying a rigidity term in the registration of DCE-MR images, it requires a coefficient or stiffness map on each post-contrast image to determine the penalty weight on various types of tissue. Tumors are usually assumed to be rigid while other tissue (e.g. fat) is relatively soft. Therefore a segmentation of the enhanced tumors on the post-contrast image can be used to build a binary stiffness map. Manual segmentation is usually regarded as the most accurate method but can be time consuming; and automatic enhanced tumor segmentation on subtraction images usually requires a preliminary successful registration to remove motion artifacts. Therefore, it is important to build a robust and reliable method to compute the regularization coefficients for the registration in DCE-MR images.

We propose a framework to compute the rigidity registration coefficients in application to 4D DCE-MR images. A pre-registration is performed that registers the pre-contrast image to each post-contrast image. A subtraction image is obtained, identifying corresponding tissue enhancement information. We subsequently apply a sigmoid function to map the voxel intensity in the smoothed subtraction image to form the regularization coefficients. All parameters of the sigmoid function are determined by a k-means clustering method.

In our validation study on synthetic and clinical DCE-MR breast images, we compare registration schemes with various methods to compute the coefficients of the rigidity regularization term: a constant term, a binary function that requires an explicit segmentation, and the proposed mapping method.

2 Image registration

Image registration is defined as a problem of finding a spatial transformation $\boldsymbol{T}$ relating two images of dimension d, one of which is fixed (I_F) and the other moving (I_M). In this paper, we employ intensity-based image registration, formulated as an optimization problem in which the cost function $\mathcal{C}$ is minimized with respect to the spatial transformation $\boldsymbol{T}$. The cost function defines the quality of the match, in combination with a

ISBN: 978-87-981270-9-3

regularization of the transformation. The optimization problem can be formulated as:

$$\widehat{\boldsymbol{\mu}} = \arg\min_{\boldsymbol{\mu}} \mathcal{C}_{\text{sim}}(\boldsymbol{T}_{\boldsymbol{\mu}}; I_F, I_M) + w\mathcal{C}_{\text{reg}}(\boldsymbol{T}_{\boldsymbol{\mu}}), \tag{1}$$

where the subscript $\boldsymbol{\mu}$ indicate the transformation parameters, $\mathcal{C}_{\text{sim}}$ denotes the image similarity, which is mutual information [6] in this paper, and $\mathcal{C}_{\text{reg}}$ is used to penalize nonrigid deformations as a soft constraint weighted by a scalar w. A rigidity regularization term proposed by Staring *et al.* [5] is employed in the registration package `elastix`[7]. We adopt a B-splines based transformation model [1] in this paper, called free-form deformation (FFD).

3 Method

Let $\boldsymbol{F}$ be a regularization term that can be applied on transformation $\boldsymbol{T}$ with a coefficient map function $\gamma : \mathbb{R} \rightarrow \mathbb{R}$. A general form of this term can be represented as:

$$\mathcal{C}_{\text{reg}}(\boldsymbol{T}) = \frac{\int_{x\in\Omega} \gamma(x)\boldsymbol{F}(\boldsymbol{T};x)^2}{\int_{x\in\Omega}\gamma(x)} \tag{2}$$

The coefficient mapping function γ maps each voxel in a moving image to a value that suggest the weight of the regularization term applied on it. The simplest mapping function is a constant number where all voxels x in an image are equally weighted, $\gamma(x) = \alpha$. For instance, Rohlfing [2] applied a uniformly weighed incompressibility term on all breast regions.

Another commonly used function is a binary function that requires a preliminary segmentation of various tissues. For instance by performing a tumor segmentation on the DCE-MR images, the weight on tumor tissue is 1 and non-tumor tissue is 0.

Another kind of function is to map the intensity of an image to another range when the intensity can imply the tissue types. Ruan *et al.* [4] maps a CT image into a new range where most of voxels have either value 1 (bone tissues) or 0. The assumption is the voxel intensity value that falls in a certain range in a CT image suggests the bone tissues.

In DCE-MR images, the intensity does not always link to tissue types. However, most tumors are more rigid than healthy tissue and are usually enhanced in post-contrast images. Subtraction images of pre- from post-contrast image show enhancement of tissues provided there is no motion in between. Based on the assumption that tumors get enhanced in post-contrast images, we obtain regularization coefficients by applying a sigmoid mapping function on subtraction images from a pre-registration.

Given a pre-contrast image f and post-contrast image g, f is registered to g using a rigid and then nonrigid (FFD) registration algorithm, obtaining a registered pre-contrast image f'. A subtraction image denoted as h shown in Figure 1(a) is obtained by subtracting f' from g and then smoothed by a Gaussian filter ($\sigma = 2$) shown in Figure 1(b). A non-linear mapping function, sigmoid function, is then applied on the subtraction image h, resulting in the coefficient image (Figure 1(c)).

In the pre-registration, the tumor volume in pre-contrast might have changed, but the intensity of post-contrast image will dominate the intensity in subtraction image,

ISBN: 978-87-981270-9-3

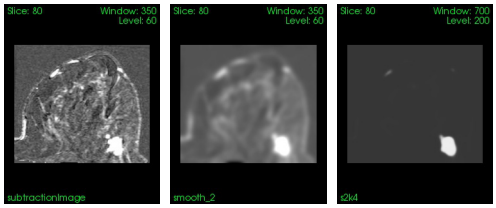

(a) Subtraction image (b) After smoothed (c) Coefficients

Fig. 1: Central slices of image volume of a subtraction image, after being smoothed and after applying sigmoid function on the subtract image.

therefore, the tumor volume change in pre-contrast image will not effect the resulting coefficient image.

Let $\boldsymbol{I}(x)$ be the intensity value at voxel x in subtraction image h, the mapping function $\gamma(x)$ transform $\boldsymbol{I}(x)$ to a new range with a center α and scale β:

$$\gamma(x) = \frac{\max - \min}{\left(1 + e^{-\left(\frac{\boldsymbol{I}(x)-\beta}{\alpha}\right)}\right)} + \min, \tag{3}$$

where $\max$ and $\min$ are maximum and minimum intensity of the image, α and β are determined by performing a k-means clustering method on the smoothed subtraction image h and partitioning it into k groups with various intensity means. The highest intensity mean value is assigned to β and the standard deviation of that cluster is assigned to α. Therefore, the only user-defined parameter is the number of clusters k. The performance of the registration is demonstrated to be insensitive to the value of k in the range of 2 to 5.

4 Validation

All DCE-MR breast images were acquired with a Siemens 1.5 MR system, where $T_R = 5.11$ms, $T_E = 2.7$ms, field of view $= 340$mm. The voxel dimensions were around $0.68 \times 0.68 \times 1$mm. The slice orientations were axial and reformatted to identity orientation for visualization convenience. The total acquisition time was 6.24 minutes, including 6 time steps in a four-dimensional DCE-MR breast image (1 before and 5 after injection of contrast agent).

4.1 Synthetic datasets

We select 3 clinical DCE-MR breast images without obvious motions to generate 3×10 synthetic images with simulated deformations. The three images show various tumor volumes ($1.5\text{cm}^3, 11.8\text{cm}^3, 22.3\text{cm}^3$) or enhancement patterns (homogeneous, heterogeneous). The subtraction images of the pre- from post-contrast images are shown in Figure 2. Two image volumes in each clinical DCE-MR breast image series are used in

ISBN: 978-87-981270-9-3

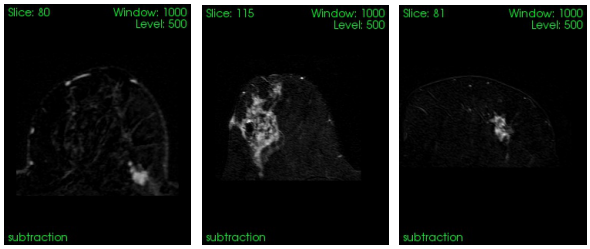

Fig. 2: Selected slices of subtraction image of pre- from post-contrast images in the three clinical image series, which are used to generate synthetic images.

building a synthetic image set: a pre- and a post-contrast image volumes at the second time point after injection of contrast agent (f_0, g_0). We manually segment the enhanced tumors s_0 from the post-contrast images, which will be used in the validation study as a ground truth of tumor volume, location and intensity.

For the deformation simulation, we randomly generate two rigid transformations ($\boldsymbol{T}_{r_1}, \boldsymbol{T}_{r_2}$), and two B-spline transformations with a grid point space of 10mm and 20mm. We later update these B-spline transformations to $\boldsymbol{T}_{b_1}, \boldsymbol{T}_{b_2}$ such that the tumors are rigidly deformed by enforcing the related control points to be zero. We subsequently compose all transformations to $\boldsymbol{T}_{\rm gt}(x) = \boldsymbol{T}_{b_1} \circ \boldsymbol{T}_{r_1} \circ \boldsymbol{T}_{b_2} \circ \boldsymbol{T}_{r_2}$, which are used to construct synthetic pre- and post-contrast images f_1, m_1 and tumor mask s_1, where $f_1 = f_0$, $g_1 = \boldsymbol{T}_{\rm gt}(g_0)$, and $s_1 = \boldsymbol{T}_{\rm gt}(s_0)$.

4.2 Evaluation method

The Target Registration Error (TRE) [8] is used to evaluate the degree of alignment between two corresponding voxels in terms of deformations:

$$\mathrm{TRE} = \sum_{x \in \Omega} ||\boldsymbol{T}_{\rm est} \circ \boldsymbol{T}_{\rm gt}(x) - x||, \tag{4}$$

where $\boldsymbol{T}_{\rm gt}$ is the simulated deformation, $\boldsymbol{T}_{\rm est}$ is the estimated transformation obtained from various registration schemes. A smaller TRE value suggests a registration can better recover the simulated motion.

We also measure the recovery of the motion in synthetic post-contrast images by measuring the intensity similarity with the corresponding original post-contrast images, using root mean squared error (RMS) and normalized correlation (NC):

$$\mathrm{RMS}(A,B) = \sqrt{\frac{1}{N}\sum_{i=1}^{N}(A_i - B_i)^2}, \qquad \mathrm{NC}(A,B) = \frac{\sum_{i=1}^{N}(A_i \cdot B_i)}{\sqrt{\sum_{i=1}^{N} A_i^2 \cdot \sum_{i=1}^{N} B_i^2}}$$

where A_i, B_i is the intensity of i-th voxel of images A and B, and N is the total number of voxels considered. Smaller RMS values and higher NC values suggest higher image similarity and hence better registration performance.

We also compute the tumor volume changes by applying the estimated transformation $\boldsymbol{T}_{\rm est}$ on the tumor mask s_1.

ISBN: 978-87-981270-9-3

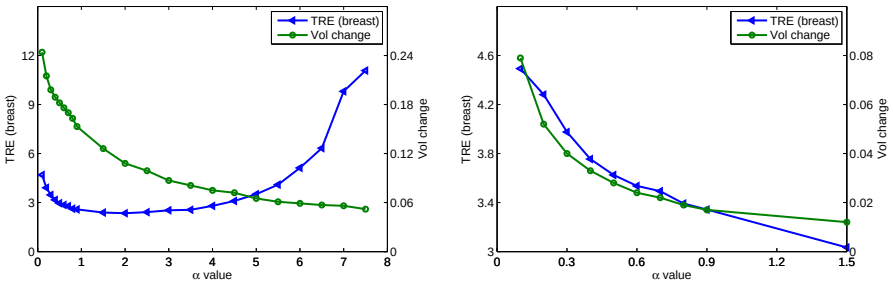

(a) VPC (b) ARC(5)

Fig. 3: TRE over the breast region is shown on left y-axis and volume change over the tumor region is on the right y-axis. (a) shows VPC registration scheme results for $\alpha \in [0.1, 7]$. The tumor volume change decreases as the weight α increase. TRE for breast region increases fast for $\alpha > 5$. (b) shows ARC(k=5) results for $\alpha \in [0.1, 1.5]$. The running time for $\alpha > 1.5$ are more than 15 minutes. Note the axes scales of (a) and (b) are different

4.3 Experiment and results

We perform registrations using three methods to compute regularization coefficients: constant number $\gamma(x) = 0$ for unconstrained FFD (denoted as UC) and $\gamma(x) = 1$ for volume-preserving constraint (VPC) [2], binary function based on manual segmentation of tumors (MRC) and our proposed automatic method (ARC(k)) for rigidity constraint [5]. We evaluate the robustness of the proposed method to the number of clusters k of range 2 to 5, used in determining the parameters of sigmoid function. Each registration scheme is tested on 30 synthetic and 5 clinical images and the performance is evaluated on the whole breast and tumor regions. Initial rigid registrations are employed in all tests. A multi-resolution scheme using 4 resolutions is employed for all nonrigid registrations, from 8, 16, 32 to 64mm. This is designed to be different from the resolution and grid space in the deformation simulation in order to reduce the evaluation bias. The breast regions are selected by performing a thresholding segmentation on cropped one-side breast images and followed by a morphology closing to remove holes. The parameter α in equation (1) is determined by finding the value that can best preserve the tumor volume while maintaining comparable or better result than unconstrained FFD scheme and the computation time is less than 15 minutes. Figure 3 shows an example of registration results on a synthetic image set using a range of α value.

Table 1 shows the registration results on synthetic images with ground-truth. Volume-preserving constrained scheme (VPC), with higher RMS and lower NC value on breast region, shows worse result than UC. However, VPC has smaller TRE than UC and the difference could come from distortion of tumors. Rigidity constrained schemes (ARC(k) for $k = 3, 4, 5$ and MRC) perform better than volume-preserving constrained (VPC) schemes in terms of smaller mean TRE and RMS, higher NC over the whole breast and tumor regions and less tumor volume loss. It demonstrates that using spatial

ISBN: 978-87-981270-9-3

	Breast regions			Tumor regions			
	TRE	RMS	NC	TRE	RMS	NC	Vol change
UC	3.42±3.11	36.20±4.56	0.90±0.01	1.09±0.79	53.11±2.15	0.79±0.03	0.20±0.11
VPC	2.40±1.36	37.30±4.50	0.89±0.02	0.33±0.19	49.32±3.36	0.82±0.03	0.04±0.02
ARC(2)	1.32±1.04	35.61±4.67	0.90±0.01	0.16±0.15	45.35±6.22	0.85±0.04	0.04±0.04
ARC(3)	1.55±0.95	34.91±3.56	0.90±0.01	0.13±0.11	45.22±5.97	0.85±0.03	0.03±0.02
ARC(4)	1.60±0.97	34.62±3.87	0.91±0.01	0.10±0.07	44.59±5.41	0.85±0.03	0.01±0.01
ARC(5)	1.60±0.71	34.75±3.94	0.91±0.01	0.10±0.07	44.72±5.07	0.85±0.02	0.01±0.01
MRC	1.50±0.86	34.40±3.87	0.91±0.01	0.10±0.06	44.76±4.88	0.85±0.02	0.01±0.01

Table 1: Evaluation result for 30 synthetic images.

variant rigidity constraint can achieve better overall and local registration performance. Within rigidity constrained registration schemes, ARC(4,5) shows similar performance on both breast and tumor regions. As k increases from 2 to 4, the registration performance improves, except for the TRE getting larger over the breast regions. The reason could be ARC(2) apply penalty on larger enhanced regions, and preserve the deformation of these enhanced regions as well in addition to enhanced tumors.

Table 2 shows registration results on 5 clinical images. Only NC is used to compute the image similarity between the registered post- to the pre-contrast images due to their different intensity levels. Note this is different from the tests on synthetic data where ground-truth is available. All registrations schemes show similar performance over breast regions in terms of NC value. ARC(2,3,4,5) and MRC preserved the volume of the tumors to an accuracy of 100%, compared to $2\% \pm 2\%$ volume change in VPC schemes. All registration schemes with constraints show significantly better than the unconstrained method (UC) of $32\% \pm 33\%$ tumor volume change. The global and local registration results obtained from clinical data are roughtly consistent with the synthetic data.

5 Discussion and conclusions

We proposed a framework to compute regularization coefficients in nonrigid registration using a sigmoid mapping method on a subtraction image obtained from a pre-registration. The evaluation results show that using a homogeneous volume-preserving constraint in nonrigid registration of DCE-MR beast images can reduce the tumor volume changes. Spatial variant rigidity constraint can further improve the volume preservation performance while showing better overall performance on the whole breast regions. The proposed method can replace the manual segmentation method to compute the rigidity term coefficients by showing comparable local and global registration performance. Note that our focus is not to create a better tumor segmentation method, but a framework that can replace the manual segmentation in computing the rigidity term coefficients.

In this framework, unconstrained FFD is used in pre-registration to remove enhancement artifact caused by motion in subtraction image, where the tumor volume in pre-

ISBN: 978-87-981270-9-3

	Breast regions	tumor regions
	NC	Vol change
UC	0.81±0.04	0.32±0.33
VPC	0.81±0.04	0.02±0.02
ARC(2)	0.81±0.04	0.00±0.00
ARC(3)	0.81±0.05	0.00±0.00
ARC(4)	0.81±0.04	0.00±0.00
ARC(5)	0.81±0.04	0.00±0.00
MRC	0.81±0.04	0.00±0.00

Table 2: Evaluation results for the 5 clinical data.

contrast image may change. Since the intensity of tumor region in subtraction image is dominated by post-contrast image, in our study we observed that the effect of volume change in pre-contrast image on the sigmoid mapping on the subtraction image is shown to be very limited. A possible future work is to evaluate the effect of pre-registration on the rigidity coefficients generation.

Acknowledgments NICTA is funded by the Australian Government as represented by the Department of Broadband, Communications and the Digital Economy and the Australian Research Council.

References

1. Rueckert, D., Sonoda, L., Hayes, C., Hill, D., Leach, M., Hawkes, D.: Nonrigid registration using free-form deformations: application tobreast MR images. IEEE Transactions on Medical Imaging **18**(8) (1999) 712–721 2, 3
2. Rohlfing, T., Maurer Jr, C., Bluemke, D., Jacobs, M.: Volume-preserving nonrigid registration of MR breast images using free-form deformation with an incompressibility constraint. IEEE Transactions on Medical Imaging **22**(6) (2003) 730–741 2, 3, 6
3. Loeckx, D., Maes, F., Vandermeulen, D., Suetens, P.: Nonrigid image registration using free-form deformations with a local rigidity constraint. MICCAI (2004) 639–646 2
4. Ruan, D., Fessler, J., Roberson, M., Balter, J., Kessler, M.: Nonrigid registration using regularization that accommodates local tissue rigidity. Proc. of SPIE **6144** (2006) 346–354 2, 3
5. Staring, M., Klein, S., Pluim, J.: A rigidity penalty term for nonrigid registration. Medical Physics **34**(11) (2007) 4098–4108 2, 3, 6
6. Mattes, D., Haynor, D., Vesselle, H., Lewellyn, T., ubank, W.: Nonrigid multimodality image registration. Proc. of SPIE **4322** (2001) 1609–1619 3
7. Klein, S., Staring, M., Murphy, K., Viergever, M., Pluim, J.: Elastix: a toolbox for intensity-based medical image registration. IEEE Transactions on Medical Imaging **29**(1) (2010) 196–205 3
8. Schnabel, J., Tanner, C., Castellano-Smith, A., Degenhard, A., Leach, M., Hose, D., Hill, D., Hawkes, D.: Validation of nonrigid image registration using finite-element methods: application to breast MR images. IEEE Transactions on Medical Imaging **22**(2) (2003) 238–247 5

Validation of breast MRI motion correction effectiveness using a quantitative indicator

Tobias Boehler* and Heinz-Otto Peitgen

Fraunhofer MEVIS, Bremen, Germany

Abstract. Motion compensation of dynamic images is essential for diagnostic magnetic resonance (MR) imaging of the breast. Indication of registration quality, especially in case of registration failure, allows a review of the affected cases. In this article, we introduce a novel, automated indicator method for quantitative assessment of breast MRI motion correction in workstation software. The indicator estimates a relative improvement and supports the detection of displacement field distortions. Effectiveness of this method was verified in a validation based on artificially deformed images and clinical cases, demonstrating its applicability.

1 Introduction

The issue of patient motion during acquisition of dynamic contrast-enhanced (DCE) breast MR images has received considerable attention. Movement between two consecutive scans adds motion artifacts to the pair-wise difference images, as anatomical structures are no longer aligned. These artifacts appear as bright structures, invalidating the analysis of contrast agent kinetics.

Lateral compression plates built into the bilateral breast coil allow a fixation of the breast, supporting the fibrotic tissue during scanning. However, these mechanical devices do not suppress motion caused by pectoral muscle contractions and breathing. Image artifacts are therefore commonly corrected by registration software during acquisition post-processing [5]. The flexibility and variability of breast tissue requires application of deformable, contrast-invariant registration methods such as the free-form deformation proposed by Rueckert et al. [10].

A validation of the accuracy of non-linear registration is challenging, as no reference deformation is available. Landmark-based correspondence estimation requires tedious annotation work and provides no dense displacement information. For breast MRI, deformations simulated from patient-specific finite-element models have been suggested as references [11]. An elasticity simulation emulates bilateral breast compressions and contraction of the pectoral muscle. Comparison of simulated and registration-estimated displacements allows an assessment of mean distances between both. Such techniques are limited to algorithm verification prior to an integration into clinical software. Once integrated, registration algorithms provide few information about the achieved quality of alignment. Apart from a visual comparison, registration performance is assessable only through computed displacements and images.

* tobias.boehler@mevis.fraunhofer.de

ISBN: 978-87-981270-9-3

An appropriate "confidence" measure must allow an identification of displacement field perturbations, support an automated execution as part of the diagnostic workflow, and provide a quantitative value of registration performance. To the best of our knowledge, no such method has been proposed. Interactive validation was suggested by Mehnert et al. [7], estimating the alignment accuracy based on closest-distances of skin surfaces and manual correspondence inspection. However, only in-plane displacements are considered, limiting its usage for the inherently three-dimensional breast deformations. Another method performs a detection of motion artifact candidates based on machine learning methods guided by user interaction [14]. Both techniques require manual input.

In this article, we introduce a novel method for the automated computation of a quality value for motion correction and discuss its validation on artificial and clinical images. The method estimates a relative improvement of image alignment and detects displacement field irregularities. It allows an on-line evaluation of registration accuracy, independent from the applied registration algorithm.

2 Methods

The subtraction of a contrast-enhanced MR image from a non-enhanced, reference image produces high intensity values in regions affected by either contrast-enhancement or motion. Contrast-induced intensity variations permit an assessment of the relative contrast-agent uptake behavior of breast tissue. Distinction between motion artifacts and contrast enhancement is difficult. However, motion artifacts are most prominent at the skin surface. In a 3-D rendering of absolute subtraction images, distinct "rim"-like artifacts appear, particularly in a maximum-intensity projection (MIP). Motion artifacts may also occur at other tissue boundaries, e.g., between glandular and adipose tissue. Pectoral muscle contraction, for example, causes a local shifting of tissues, forming wider artifacts. Consequently, an estimation of motion only at the breast surface is generally insufficient. In our approach, the following steps are performed:

1. temporal maximum-intensity projections of pair-wise difference images,
2. delineation of motion artifacts using an analysis of Hessian images,
3. entropy-based relative quantification of artifact reduction, and
4. analysis of the displacement field to detect perturbations thereof.

2.1 Temporal maximum-intensity projection

Maximum-intensity projections of the DCE image as *temporal MIPs* provide an overview of the spatio-temporal contrast enhancement distribution. Initially, voxel-wise absolute differences are computed for all non-reference images, with images reformatted to transversal orientation. Given N images, $N-1$ difference images are calculated and projected onto one single three-dimensional image volume, assigning the maximum intensity over time at each voxel (cf. Figure 1). Unlike the conventional MIP, the temporal MIP creates 3-D images of intensity changes over time. Figure 2 shows examples for temporal MIP images.

ISBN: 978-87-981270-9-3

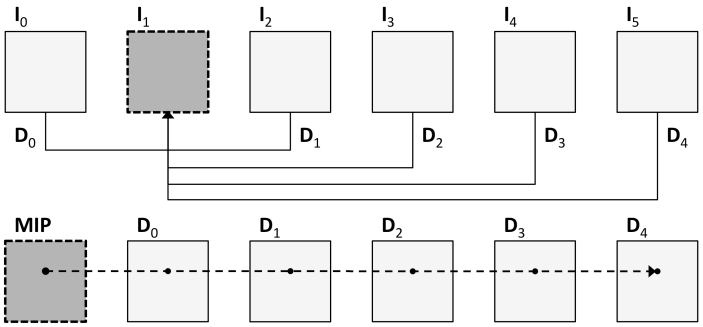

Fig. 1. Temporal MIP scheme. Initially, difference images $\mathbf{D}_k = |\mathbf{T}_j - \mathbf{T}_i|, k = 0 \ldots N-2, i = 0 \ldots N-1, i \neq j$ are computed, where j denotes the desired reference image (dark), forming the MIP image ($j = 1$, $N = 6$ in this illustration).

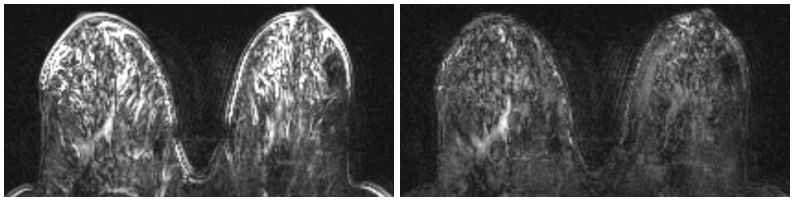

Fig. 2. Exemplary slices of temporal MIP images. Note the prominent, rim-like motion artifacts, particularly at the skin surface, before (left) and after registration (right).

2.2 Multi-scale Hessian analysis

Differentiation between contrast-enhanced and motion-affected tissue is based on an analysis of Hessian images [15]. To delineate rim-like artifacts, a vesselness measure is parameterized for a detection of sheet-like objects [3]. The method is integrated into a multi-scale analysis based on Gaussian kernels, using normal distributions around zero mean and standard deviations of 1 to 4 voxels. For all scale levels, Hessian images are computed separately. To suppress contrast-enhanced image regions, two thresholding techniques are applied. First, the cardiac region is excluded, using a dedicated breast MRI cropping technique [6]. Subsequently, automatic thresholding is applied to the masked temporal MIP of the original image [8]. The resulting segmentation mask is processed by morphological operations to account for local motion variation. The mask image is finally applied to the Hessian image on each scale level, and the four level images are accumulated through addition, as illustrated in Fig. 3.

2.3 Indicator quantification

From the two accumulated Hessian images, quantitative values for the reduction of artifacts are estimated. Under the assumption that the thresholded Hessian images contain predominantly artifact information, the change in information

ISBN: 978-87-981270-9-3

Fig. 3. Accumulated, corresponding Hessian images for the MIPs of figure 2.

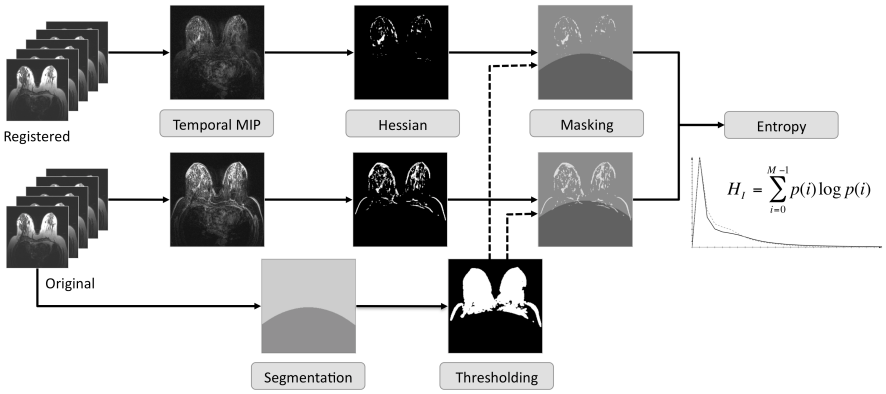

Fig. 4. Scheme of the indicator value computation (left to right): temporal MIP, coarse segmentation, Hessian analysis and thresholding, and final entropy change calculation.

content is measured. The Shannon entropy is computed from normalized image histograms, using per gray-value binning [4]. Its relative change is determined as a percentage of the pre-registration value. The scheme is illustrated in Fig. 4.

2.4 Deformation analysis

Independent from the registration method, a detection of mis-registration and flaws of the deformation is performed, as the registration method is not necessarily diffeomorphic or volume-preserving. Given the displacement field, two characteristics are computed. The amount of shrinkage or expansion, e.g., of present vessels and lesions, is measured using the Jacobian determinant, which has been introduced for volume-preserving registration [9]. Mean and extremal values are estimated over the entire image domain.

Complementary, foldings of the displacement field are detected by examination of geometric regularity, similar to the method suggested by Thirion for regularization [13]. Defined by the deformation grid, a volume mesh is generated, where each grid cell is triangulated into six tetrahedra. For each tetrahedron, the volume before and after displacement of its nodes is computed. Folding distorts the regularity of this grid, leading to an intersection of neighboring cells and sign changes of tetrahedral volumes. For such locations, the original and mapped

ISBN: 978-87-981270-9-3

Table 1. Entropy reductions in percentage of the original entropy value. Due to intensity interpolation, a complete elimination of the residual error is impossible.

Image	1	2	3	4	5	6	7	8	9	10
Red. (%)	84.57	91.85	93.16	97.27	87.77	82.56	83.27	85.15	89.69	88.24

positions are marked. Correctness of this analysis was verified on artificial and random foldings.

3 Results

Using synthetic deformations, effectiveness and reliability of the indicator were assessed. Subsequently, the method was applied to 65 clinical cases. The motion correction used explicit regularization and the local cross-correlation measure [1].

3.1 Synthetic deformations

For an initial assessment, artificial deformations were generated using a homogenous, isotropic, linear-elastic continuum model, discretized by tetrahedral finite elements [2]. We simulated lateral plate compression of the breast, as well as posterior deformations caused by pectoral muscle contraction, as proposed by other authors [11, 12]. Models for ten selected T1-weighted patient images were built and deformed. Motion correction was applied to the original dataset, which was registered to its simulation-deformed pendant. Averaged over all ten images, the mean displacement distance, estimated from voxel-wise displacement differences, was 0.11 ± 0.02mm. Results for the indicator are summarized in Table 1. All entropy improvements exceeded an reduction of 80% of their original values. On average, changes of 88.35% were achieved, with a standard deviation of 4.72% and maximum and minimum values of 97.27% and 82.56%, respectively. No deformation perturbations were detected. Improvements were confirmed by image inspection, where the indicator values were consistent with the visual impression.

Reliability. Apart from improvement measurement, the indicator has to detect invariance or degradation of the image alignment. To verify this, the displacement field was multiplied with constants, where $\times 1$ denotes the original magnitude. Seven displacement pairs $(\times 0, \times 1)$, $(\times 0.25, \times 1), \ldots$ were formed: four pairs with reduced magnitudes of $\times 0$, $\times 0.25$, $\times 0.5$ and $\times 0.75$, one pair with equal magnitude $\times 1$, and two "increased" pairs with factors $\times 1.25$ and $\times 1.5$. Deformations of factor $\times 1$ simulate invariance, factor $\times 0$ perfect matchings, and reduced and increased factors under- and mis-registration, respectively. Correspondingly, 70 deformed images were generated (cf. Fig. 5). Indicator values for these datasets are listed in Table 2. Removal of the deformation produced 99% improvement, or complete "motion" elimination. Improved alignment led to increased changes values, and to an immeasurable change of 0% for the identity $\times 1$. "Mis-alignment" caused negative changes, allowing an identification of such cases.

ISBN: 978-87-981270-9-3

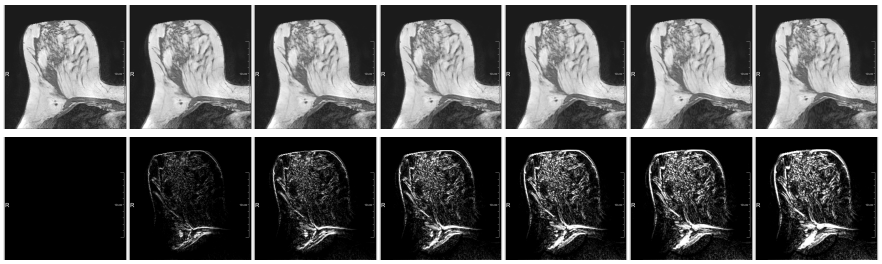

Fig. 5. Artificial deformations for the indicator assessment. Top row, left to right: corresponding transformed images. Bottom row, left to right: difference images w.r.t. the original configuration. Bright image regions indicate large intensity differences.

Table 2. Average indicator values for the 10 images with all deformation configurations applied. Note the decreasing values accompanying increasing deformation magnitudes.

	Deformation factors						
	×0	×0.25	×0.5	×0.75	×1	×1.25	×1.5
Mean	99.56	52.75	23.97	9.33	0.0	-6.7	-11.97
Std.dev.	0.13	11.51	7.41	2.96	0.0	1.6	2.71
Min.	99.33	36.71	16.2	6.36	0.0	-10.26	-18.15
Max.	99.75	76.95	40.81	15.94	0.0	-4.59	-8.49

Deformation analysis. To evaluate the folding detection, the simulated deformations were augmented with three-dimensional foldings. Similar to the initial evaluation, ten deformed images were generated and analyzed. On average, the indicator estimated $62.73\% \pm 7.67\%$ improvement, with 46.46% and 72.78% minimum and maximum reductions, respectively. Present foldings were recognized: on average $0.71\% \pm 0.14\%$ of image voxels were affected by overlaps; minimum and maximum percentages were recorded as 0.49% and 0.91%. These values reflect the small percentage of affected voxels w.r.t. the entire image. Still, any non-zero percentage is sufficient to indicate the presence of perturbations.

3.2 Patient data

An initial assessment of the indicator function on clinical data was conducted on 65 DCE MRI cases from different clinical sites and MRI vendors. The images consisted of 4 to 10 time points, with voxel resolutions ranging from $256 \times 256 \times 36$ to $700 \times 512 \times 148$ voxels. For these images, the average estimated indicator value was $8.76\% \pm 8.73\%$. The largest improvement was rated at 60.2% (for the example image of Figures 2 and 3), while the smallest was 1.24%. No negative indicator values were estimated. The indicator value exceeded 10% for 22 datasets, and 20% for three data sets. Distortions of the vector field were not present, as was

ISBN: 978-87-981270-9-3

confirmed by visual inspection of deformations and transformed images. The six cases with least improvement showed a negligible amount of motion, with indicator values ranging from 1.24% to 1.92%. With increasing values, motion artifacts become more evident, particularly in the MIP images. The six cases with highest change values range from 16.92% to 60.2%.

4 Discussion

For artificial deformations, the indicator estimated large improvements, which were confirmed through error assessment and image reviews. To rule out improvements through mis-registration, a "negative" test was conducted, over-amplifiying the deformation magnitude. For these cases, the indicator was able to distinguish between error reduction, invariance and increase. Notably, the standard deviation for the $\times 0$-deformation is almost negligible, showing that intensity interpolation has marginal influence. The negative sign accompanying "error"-increase is particularly remarkable, as it may allow automatic notification of mis-registration. Furthermore, the accuracy of the folding detector was verified in corresponding tests. The evaluation on clinical data confirmed the observations made on synthetic data: "improvement" values were positive, and no foldings or Jacobian distortions were detected. For small registration changes or minor motion artifacts, indicator values are also generally small. Contrary, the elimination of pronounced motion artifacts led to high indicator values.

5 Conclusion

A novel quantitative validation method for breast MRI motion correction accuracy was proposed, targeted at integration into clinical workstation software. Verification of its performance was carried out on artificial deformations, simulated by bio-mechanical elasticity models, as well as 65 clinical patient cases. The method successfully detected deformation distortions, in particularly foldings of the displacement field. The independency of the method from image registration algorithms allows a comparison of different registration approaches. Primarily, however, the indicator's main purpose is to support the radiologist with confidence about registration failure and, to a limited degree, success.

In summary, the conducted initial evaluation demonstrated the potential of the indicator method, although it needs to be explored more thoroughly in future work. Particularly, the breast models have to be extended by simulation of tissue contrast enhancement to further verify the robustness of the indicator. Additionally, to account for the variation of image resolutions, the usage of an adaptive number of scale levels for the Hessian analysis will be evaluated. Finally, we will investigate the applicability of assigning levels of registration "quality", e.g., user-defined quality ranges such as "improvement over 20%" or "improvement under 5%", on large and heterogenous collectives of patient cases.

ISBN: 978-87-981270-9-3

Acknowledgements

This work has been partially funded as part of the European Union's HAMAM project, 7th Framework Programme, ICT-2007.5.3, grant no. 224538. The authors would like to thank Dr. Uta Preim, University Hospital Magdeburg, and Dr. Kathy Schilling, Boca Raton Community Hospital, for the kind contribution of breast MR images.

References

1. Boehler, T., van Straaten, D., Wirtz, S., Peitgen, H.O.: A robust and extendible framework for medical image registration focused on rapid clinical application deployment. Computers in Biology and Medicine 41(6), 340–349 (2011)
2. Bro-Nielsen, M., Cotin, S.: Real-time volumetric deformable models for surgery simulation using finite elements and condensation. Comp Graph Forum 15(3), 57–66 (1996)
3. Frangi, A., Niessen, W., Vincken, K., Viergever, M.: Multiscale vessel enhancement filtering. In: Proc. MICCAI. p. 130. Springer (1998)
4. Gonzales, R., Woods, R.: Digital image processing. Prentice Hall (2002)
5. Guo, Y., et al.: Breast image registration techniques: a survey. Med Biol Eng Comp 44, 15–26 (2006)
6. Koenig, M., Kohle, S., Peitgen, H.O.: Automatic Cropping of Breast Regions for Registration in MR Mammography. In: Proc. SPIE Medical Imaging 2005. pp. 1563–1570 (2005)
7. Mehnert, A. J. H., et al.: Registration evaluation of dynamic breast MR images. In: APRS Digital Image Computing. vol. 1, pp. 21–26. Univ. of Queensland (2005)
8. Otsu, N.: A Threshold Selection Methods from Gray-Level Histograms. IEEE Trans Syst Man Cyb 9, 62–66 (1979)
9. Rohlfing, T., et al.: Volume-preserving nonrigid registration of MR breast images using free-form deformation with an incompressibility constraint. IEEE Trans Med Imag 22, 730–741 (2003)
10. Rueckert, D., et al.: Nonrigid registration using free-form deformations: application to breast mr images. IEEE Trans Med Imag 18(8), 712 –721 (1999)
11. Schnabel, J.A., et al.: Validation of nonrigid image registration using finite-element methods: application to breast MR images. IEEE Trans Med Imag 22(2), 238–247 (2003)
12. Tanner, C., et al.: A Comparison of Biomechanical Breast Models: A Case Study. In: Proc. SPIE Medical Imaging. pp. 1807–1818 (2002)
13. Thirion, J.P.: Image Matching as a Diffusion Process: An Analogy with Maxwell's Demons. Med Image Anal 2(3), 243–260 (1998)
14. Valadez, G.H., Shinigawa, Y.: Efficient features for detection of motion artifacts in breast MRI (2009), United States Patent US2009/0069669A1
15. Wang, L., Filippatos, K., Friman, O., Hahn, H.K.: Fully automated segmentation of the pectoralis muscle boundary in breast mr images. In: Proc. SPIE Medical Imaging. vol. 7963, p. 796309. SPIE Press (2011)

Matching Regions for Mammographic Views: Comparison and Compensation for Deformations

Christine Tanner[1]*, Guido van Schie[2], Nico Karssemeijer[2], and Gábor Székely[1]

[1] Computer Vision Laboratory, ETH Zürich, 8092 Zürich, Switzerland
[2] Department of Radiology, Radboud University Nijmegen Medical Centre, Nijmegen, Netherlands

Abstract. Matching features on MLO and CC mammograms has shown to improve performance of computer aided detection systems. False-positive rates can be lowered by reducing the search space during matching. Various methods have been proposed to define the search space. These do either not explicitly compensate for the breast deformation or simulate the whole process. In this study, we investigated the benefit of extending the common approaches by some basic compensations for breast deformations and compare several methods. Performance was tested on 50 pairs of mammograms with corresponding masses annotated by a radiologist. No clear advantage of straight strips or annular bands was observed for the common methods. Extensions to remove the pectoral muscle by shearing, compensating for gravity on MLO views by shearing and a volume-preserving transformation to get similar breast shapes in both views worked well when breast shapes were elliptical (mean (maximum) error of 5.3 (18.6) mm for 25 pairs). Using this strategy for elliptical breast shapes and straight strips after pectoral shearing for the rest resulted in lowest mean errors (6.7 mm) for the whole dataset.

1 Introduction

Matching mammogram masses on medial-lateral-oblique (MLO) and craniocaudal (CC) views and incorporating their joined features into a multi-view computer aided detection (CAD) systems has shown to significantly improve performance over a single-view CAD [1, 11]. The matching across views is based on extracting single-view candidates and searching for similar candidates across views. Reduction of the search space can help to lower false-positive rates while maintaining sensitivity [11]. Definition of the search space is complicated by the projective nature of the images, the different compression direction of the breast for each view and the manual positioning of the breast for imaging.

Various methods have been proposed to restrict the search region [2, 1, 7, 11]. Most common are annular bands [6, 1] and straight strips [7, 11]. Annular bands are formed by assuming that the lesion is at the same distance to the

* We acknowledge funding from the EU 7th Framework Program, HAMAM, ICT-2007.5.3 and thank the Radboud University Nijmegen Medical Centre for the images.

ISBN: 978-87-981270-9-3

nipple in both views and allowing for some deviation in the radial direction. Straight strips are created by defining a line passing through the nipple and being oriented orthogonal to the anterior-posterior (AP) direction. Preservation of the distance in AP direction to this line is then assumed. Methods vary in the way the nipple location and the anatomic orientations are defined. Annular bands needed a diameter between 48 mm and 68 mm to cover 100% of the matches [2, 6, 11] while straight strips required for the 100% coverage a width of 28 mm to 47 mm [11, 7]. Comparisons of the methods on the same datasets are rare. The straight strips outperformed the annular search region in [11] (100% coverage with a diameter of 28 mm vs. 68 mm for 200 cases). Less clear was the difference in [9], where the mean distance to the centerline of the straight strip was 7.3 mm and to the annular band center was 6.9 mm for 35 cases.

More involved methods aim to simulate the deformation process (back projection, uncompression, rotation, compression, projection) in order to determine the 3D location of matched features from both views [5, 9, 10, 8]. A 3D model deduced from two views and heuristics regarding the deformation process (e.g. no deformation in the mid-plane, uniform deformation along lines, cross-section deforms only in the plane, straight lines map to quadratic curves due to compression) were employed in [5, 9]. Search regions can then be defined with respect to the resulting epipolar curves. The mean (maximum) distance of the mass center to the epipolar curves ranged from 4.1 mm (12.4 mm) (MLO angle known, 11 cases) to 6.8 mm (27.8 mm) (MLO angle unknown, 37 cases) [5]. Mean performance was 0.5 mm better than for an annular band (6.5 mm vs. 6.9 mm) [9]. Another 3D localization method requires the acquisition of an MRI for creating a patient-specific biomechanical breast model [8], which is clearly an extra requirement outside the scope of multi-view CAD for mammography.

Few studies have compared the different search area methods and little is known what the individual steps contribute to the overall performance. Furthermore, only rather simplistic or rather involved methods have been proposed. Therefore we investigate in this study if the common methods can be improved by compensation for some of the breast deformation without simulating the whole deformation process.

2 Method

Several steps are required for defining the search region. These are described below and include segmentation of the image, definition of the breast contour, determination of the local coordinate system, approximation of breast deformations and volume preserving matching of the breast shape.

2.1 Preprocessing

Segmentation Each mammogram was segmented into breast and background region by using global thresholding. The pectoral muscle boundary in the MLO views was first detected as a straight line by a Hough transform based method [4].

ISBN: 978-87-981270-9-3

Thereafter this boundary was refined into a curve that fits the pectoral muscle boundary more precisely by means of a dynamic programming method.

Breast Contour from Convex Hull We used the convex hull method of Pu et al. [7] for extracting the relevant part of the breast contour. The method exploits that the breast generally forms the largest concave region within the background region. First the convex hull of the background was computed. Second the region with the largest convexity was extracted by comparing the contour and the convex hull outline. Finally the closing line was parallely moved by 2 mm to avoid inclusion of chest wall parts in the breast contour [7].

General Ellipse Fitting Pu et al. [7] fitted an arbitrarily oriented ellipse to the breast contour and used the result for defining the coordinate system. Briefly, the fitting is based on a general ellipse being implicitly defined by the polynomial equation $F(\mathbf{x}_j) = \mathbf{v}^T\mathbf{c}$ when satisfying constraint $c_2^2 - 4c_1c_3 < 0$, where $\mathbf{c} = [c_1\ c_2\ ...\ c_6]^T$ are the ellipse coefficients, $\mathbf{x}_j = [x_j\ y_j]$ are the coordinates of the jth points on the ellipse and $\mathbf{v}_j = [x_j^2\ x_j\ y_j\ y_j^2\ x_j\ y_j\ 1]^T$. An ellipse is fitted to a set of N points by minimizing the sum of squared differences, ie. $D = \sum_{j=1}^{N} F(\mathbf{x}_j)^2$. As recommended by Fitzgibbon et al. [3], minimization of D is achieved by solving the generalized eigenvalue system $\mathbf{A}^T\mathbf{A}\mathbf{c} = \lambda\mathbf{C}\mathbf{c}$ where $\mathbf{A} = [\mathbf{v}_1\ \mathbf{v}_2\ ...\ \mathbf{v}_N]^T$ and $\mathbf{C}$ is the matrix that expresses constraint $c_2^2 - 4c_1c_3 < 0$. This method has the advantage of always providing a unique solution which is an ellipse.

2.2 Coordinate System

The straight strip methods require the identification of the orthogonal-to-AP axis, which can be uniquely defined by its slope k and origin $\mathbf{o} = [o_x\ o_y]$. Orthogonality implies that this also uniquely determines the AP axis by using slope $-1/k$ and the same origin. Note that $\bar{x}$ and $\bar{y}$ will denote coordinates of these axes for the AP and orthogonal-to-AP direction respectively. We employed 4 methods to determine slope k and called them general ellipse (GE), convex-hull (CH), principle directions (PD) and pectoral edge (PE), see Fig. 1. For GE, the minor and major axis from the fitted general ellipse define the local coordinate system. The more vertical axis (with abs(k)>1) defined the slope of the orthogonal-to-AP axis. For CH, the closing line of the convex hull was used to determine the slope of the orthogonal-to-AP axis. For PD, a principle component analysis was performed of the positions of the breast contour points. The slope of the more vertical principle axis (abs(k)>1) was chosen for the orthogonal-to-AP axis. For PE, a line was fitted to the pectoral muscle segmentation in the MLO view. This line provided the slope of the orthogonal-to-AP axis. The AP direction for the CC view was assumed to be align with the image axis. For all methods, origin $\mathbf{o}$ was set to be at the point of the fitted general ellipse which was most anterior to the extracted line.

ISBN: 978-87-981270-9-3

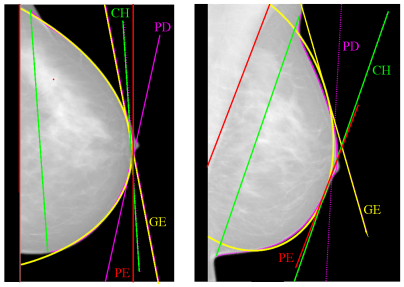

Fig. 1. Illustration of definition of coordinate system for general ellipse (GE), convex hull (CH), principle direction (PD) and pectoral edge (PE).

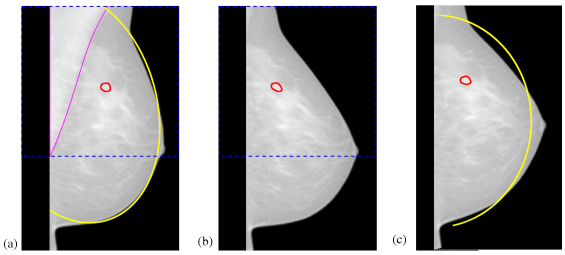

Fig. 2. Illustration of pectoral and gravity shearing. (a) original MLO image with pectoral muscle segmentation (pink contour) and superior region (blue dashed lines). (b) MLO image after local pectoral shearing in the superior region. (c) MLO image after pectoral and gravity shearing and fitted axes-oriented ellipse (yellow outline). The red contours show the mass outline.

2.3 Pectoral and Gravity Shearing

To compensate for some breast deformations, two shearing transformations were considered, namely pectoral-shearing (PS) and gravity-shearing (GS).

For PS, the MLO image was locally sheared to account for the displacement of the superior breast region by the compressed pectoral muscle [9], see Fig. 2. First, the intersection of the line fitted to the pectoral muscle segmentation with the posterior image edge was used to horizontally split the image into a superior and an inferior part. Second, the shear values was deduced from the slope of the pectoral muscle line. Finally, the superior image region was sheared while the inferior part remained unchanged. After this area-preserving transformation, the AP direction was assumed to be aligned with the image axis.

For GS, a shear transformation in inferior-to-superior direction was applied to the MLO image to counteract the deformation of the breast due to gravity before the compression, which was not compensated by the radiographer. The shear values was optimized to provide the lowest error when fitting an axes-oriented ellipse to the breast outline after the shear transformation.

ISBN: 978-87-981270-9-3

2.4 Volume Preservation

The fact that breast tissue is nearly incompressible can be exploited for further adjustment of the search region. Assuming that the breast has the shape of a half elliptical cylinder after compression, then the breast volume is given by

$$V_v = \frac{\pi}{2} a_v b_v h_v \tag{1}$$

where a_b and b_v are the radii of the in-plane ellipse and h_v is the breast thickness for view $v \in \{CC, MLO\}$. The ratio between the volumes is therefore $V_{CC}/V_{MLO} = (a_{CC}b_{CC}h_{CC})/(a_{MLO}b_{MLO}h_{MLO})$. Note that the same relationship holds for other shapes as long as the cross-sectional shape has the same function for the CC and MLO compressions, e.g. half ellipsoid.

A fact often forgotten is that the breast region captured by the CC and MLO view are likely to be of unequal volume due to differences in breast positioning. Therefore, we first aim to define equally sized breast regions. For this, we set the origin in AP direction ($o_{\bar{x}}$) to the posterior end of the breast region (e.g. on the convex hull closing line or the line fitted to the pectoral edge). Then we fitted axes-oriented ellipses to the CC and MLO view (free parameters a, b, $o_{\bar{y}}$) and calculate V_{CC} and V_{MLO} using Equ. (1), the ellipse parameters (a, b) and the recorded breast thicknesses h. For the view which provided the smaller volume, the origin $o_{\bar{x}}$ is then iteratively moved in the posterior direction until the fitted ellipse results in a similar volume as for the other view. Second, having equally sized breast regions, we transform one of the images such that the fitted in-plane ellipses have the same shape. For example the scale transformation for the MLO image would be $\hat{x}_{MLO} = a_{CC}/a_{MLO}(\bar{x}_{MLO} - o_{\bar{x}}) + o_{\bar{x}}$ and $\hat{y}_{MLO} = b_{CC}/b_{MLO}(\bar{y}_{MLO} - o_{\bar{y}}) + o_{\bar{y}}$.

2.5 Evaluation

The methods were evaluated based on corresponding masses, which were manually annotated on 50 pairs of CC and MLO mammograms by a radiologist. Mammograms with annotated masses were randomly selected from a mixed cohort of patients, resulting in 30% high-risk screening, 28% symptomatic, 20% recall, 12% control, 8% unknown, 2% screening cases. Microcalcifications were also present in 44% of the cases and 78% of the masses were malignant. On average, the annotated mass had an area of 4735±4678 mm^2. For each MLO view, the distance between the center of the annotated mass and the centerline of the search region, derived from the CC view, was calculated. Results for all cases were summarized by the mean and the maximum of the 50 distance measure. Paired t-test was employed for testing for statistical significance at the 0.05 level.

3 Results

First we compared the performance of standard search regions, see Table 1. Defining the coordinate system by the axes of the fitted ellipses resulted in very

ISBN: 978-87-981270-9-3

large errors. One reason for this poor performance is that the position of the axes is not well defined for circular shapes. Another might be an suboptimal selection of the AP-axis. Similar results of straight strips and annular bands can be observed for the coordinate systems defined by the convex-hull closing line and PCA. Annular bands provided slight lower errors when the pectoral edge was employed to define the image orientation. The maximum error, which defined the half-width to cover 100% of all masses, was as expected more variable. Results below 26.1 mm were achieved with straight strips based on the convex-hull and with annular bands based on the pectoral edge. The first extension to the common approaches, where the pectoral muscle was removed from the MLO view by shearing (PS), seemed on average to be beneficial for straight strips.

Table 2 shows the results when adding volume-preservation and shearing in SI-direction to the straight strip methods. The lowest mean error (7.5 mm) was achieved when incorporating all 3 extensions (pectoral-shear, gravity-shear, volume-preservation). However, the performance depended on how well the ellipse fitted the breast shape. Mean errors reduced to 5.3 mm for the 25 cases with the most elliptical breast shapes (maximum of mean fitting error $<$7.0 mm). Using this strategy for this subset of most elliptical shaped breasts and PS-SS for the rest resulted in the lowest mean error (6.7 mm) for the whole dataset. However, the dataset was not large enough to show statistical significance in comparison to the results from Table 1 apart for GE-SS, GE-AB and PS-AB. Mean performance degraded (range 9.9-18.0 mm) when employing annular bands for the methods in Table 2. Example results for the convex-hull and pectoral-shearing method using gravity-shearing and volume-preservation can be seen in Fig. 3. Note that the cases in column one and four belong to the subset of breasts with less elliptical shapes (mean fitting error on MLO view was 9.6 and 9.5 mm respectively).

4 Conclusion

In this study we compared the performance of several common methods to define the search region for matching masses in CC and MLO mammograms. Furthermore we extended these common methods to account for some of the breast deformations by relative simple and easy to apply transformations.

On average, the best result of 6.7 mm was achieved with a hybrid method using all three extensions (removing the pectoral muscle on the MLO view by shearing, compensating for gravity deformation on the MLO view by shearing and volume-preserving scaling to provide similar shapes) for the most elliptical breast shapes and pectoral shearing (PS-SS) for the rest.

Most common approaches provided statistically not significantly different results. Their mean performance ranged from 7.2 mm to 8.7 mm. No clear advantage of either straight strips or annular bands could be observed for the common approaches. Results were within the range of previously reported performances. The ellipse fitting method performed substantially worse than previously reported [7].

ISBN: 978-87-981270-9-3

	Straight strips (SS)	Annular bands (AB)
Ellipse (GE)	17.7 (55.0)	24.3 (65.2)
Convex-hull (CH)	8.4 (26.1)	8.3 (30.0)
PCA (PD)	8.1 (31.0)	8.6 (38.0)
Pectoral (PE)	8.7 (31.2)	7.7 (25.8)
Pectoral-shear (PS)	7.2 (31.4)	12.9 (36.3)

Table 1. Mean (maximum) error (in mm) of the straight strip and the annular band methods for 50 paired mammograms for common approaches and first extension (PS).

	VP	GS-VP	GS-VP (25 cases)	GS-VP or PS-SS
Convex-hull (CH)	11.9 (80.4)	10.8 (80.4)	8.3 (17.6)	8.4 (31.4)
PCA (PD)	10.8 (33.6)	11.2 (33.0)	10.0 (28.1)	9.2 (31.4)
Pectoral (PE)	12.8 (72.8)	11.7 (73.8)	9.2 (22.9)	9.0 (31.4)
Pectoral-shear (PS)	8.8 (35.6)	7.5 (35.7)	5.3 (18.6)	6.7 (31.4)

Table 2. Mean (maximum) error (in mm) of the straight strip methods for 50 paired mammograms employing volume-preservation (VP) and gravity-shearing (GS).

References

1. van Engeland, S., Karssemeijer, N.: Combining two mammographic projections in a computer aided mass detection method. Med. Phys. 34, 898 (2007)
2. van Engeland, S., Timp, S., Karssemeijer, N.: Finding corresponding regions of interest in mediolateral oblique and craniocaudal mammographic views. Med. Phys. 33, 3203 (2006)
3. Fitzgibbon, A., Pilu, M., Fisher, R.: Direct least square fitting of ellipses. IEEE Trans. Pattern Anal. 21(5), 476–480 (1999)
4. Karssemeijer, N.: Automated classification of parenchymal patterns in mammograms. Phys. Med. Biol. 43, 365–378 (1998)
5. Kita, Y., Highnam, R., Brady, M.: Correspondence between different view breast x rays using curved epipolar lines. Comput. Vis. Image Und. 83(1), 38–56 (2001)
6. Paquerault, S., Petrick, N., Chan, H., Sahiner, B., Helvie, M.: Improvement of computerized mass detection on mammograms: Fusion of two-view information. Med. Phys. 29, 238 (2002)
7. Pu, J., Zheng, B., Leader, J., Gur, D.: An ellipse-fitting based method for efficient registration of breast masses on two mammographic views. Med. Phys. 35, 487 (2008)
8. Rajagopal, V., Chung, J., Highnam, R., Warren, R., Nielsen, P., Nash, M.: Mapping microcalcifications between 2D mammograms and 3D MRI using a biomechanical model of the breast. Computational Biomechanics for Medicine pp. 17–28 (2010)
9. Yam, M., Brady, M., Highnam, R., Behrenbruch, C., English, R., Kita, Y.: Three-dimensional reconstruction of microcalcification clusters from two mammographic views. IEEE Trans. Med. Imaging 20(6), 479–489 (2001)
10. Yang, S., Hsu, H., Hsu, G., Chung, P., Guo, S., Lo, C., Yang, C., Lee, S., Chang, C.: 3D localization of clustered microcalcifications using cranio-caudal and mediolateral oblique views. Comput. Med. Imag. Grap. 29(7), 521–532 (2005)
11. Zheng, B., Tan, J., Ganott, M., Chough, D., Gur, D.: Matching breast masses depicted on different views:: A comparison of three methods. Acad. Radiol. 16(11), 1338–1347 (2009)

ISBN: 978-87-981270-9-3

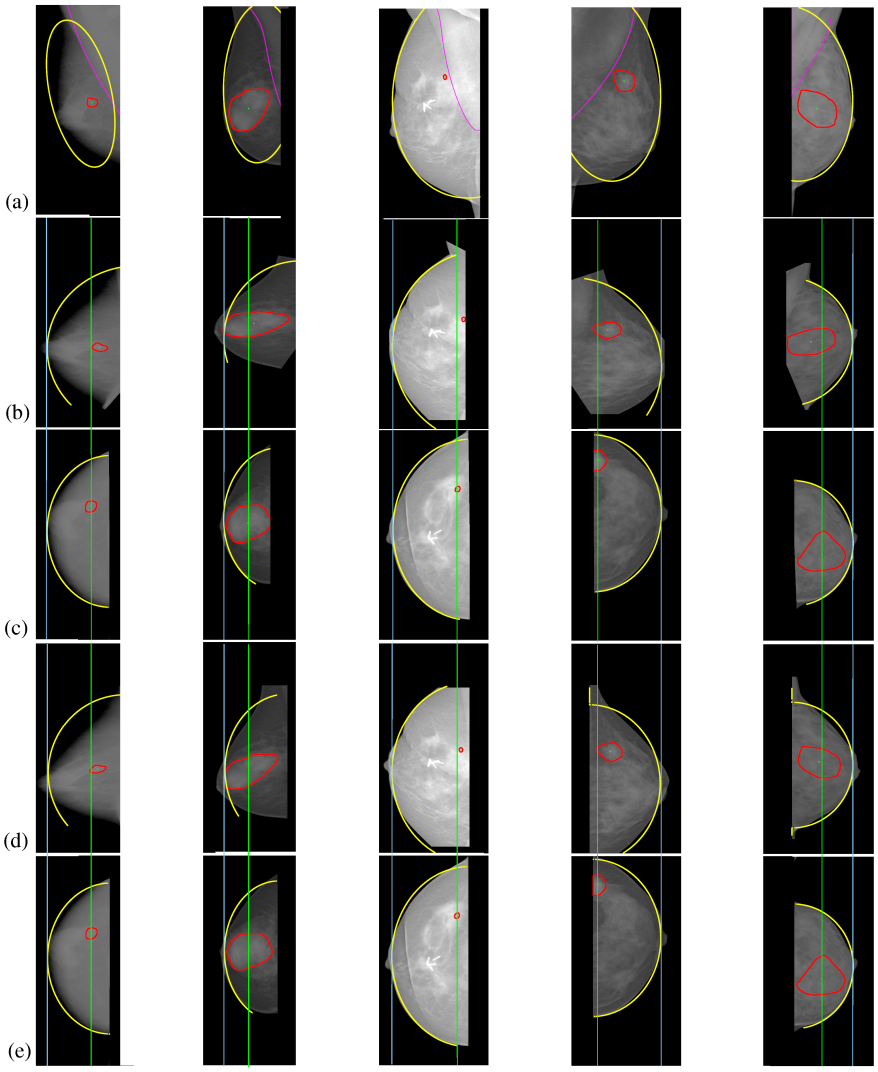

Fig. 3. Example images for 5 patients (columns) showing (a) original MLO view with pectoral muscle segmentation (pink contour); (b,c) MLO and CC results for convex-hull, gravity-shear & volume-preservation; (d,e) MLO and CC results for pectoral-shear, gravity-shear & volume-preservation. Red contour: annotated mass; green dot: center of mass; yellow contour: fitted ellipse; blue line: alignment using most anterior point; green line: (b,d) center of straight strip search area based on CC view (c,e).

ISBN: 978-87-981270-9-3

Unconstrained Simultaneous Scheme to Fully Couple Reconstruction and Registration for Digital Breast Tomosynthesis: A Feasible Study

Guang Yang[†1], John H. Hipwell[1], David J. Hawkes[1], and Simon R. Arridge[1]

Centre for Medical Image Computing, Department of Computer Science and Medical Physics, University College London (UCL), London, WC1E 6BT, UK

Abstract. Digital breast tomosynthesis (DBT) provides a pseudo-3D reconstruction which addresses the limitation of superimposition of dense fibro-glandular tissue associated with conventional mammography. Registration of temporal DBT volumes searches for the optimum deformation to transform two observed images of the same object into a common reference frame. This aligns the two images via minimising an objective function that calculates the similarity between the two datasets.

In this paper, we present a novel algorithm which combines reconstruction of a pair of temporal DBT acquisitions with their simultaneous registration. We approach this nonlinear inverse problem using a generic unconstrained optimisation scheme. To evaluate the performance of our method we use 2D and 3D software phantoms and demonstrate that this simultaneous approach has comparable results to performing these tasks sequentially or iteratively w.r.t both the reconstruction fidelity and the registration accuracy.

1 Introduction

DBT is an X-ray modality using a small number of low dose X-ray images, which are acquired over a limited angle and reconstructed into a 3D volume. Although reconstructed 3D DBT images possess a high in-plane resolution, they exhibit a lower out-of-plane resolution [1]. The premise is that this coarse depth resolution is sufficient to alleviate some of the problems of overlapping tissue structures that degrades the sensitivity and specificity of cancer detection and characterisation using conventional mammography. One significant aspect of DBT is the performance of the reconstruction algorithms, which have been extensively investigated over the last decade. Comprehensive reviews on the comparison of various approaches have been published by Dobbins III, Godfrey [2] and Zhang et al. [3]. A recent investigation by Candès, Romberg and Tao [4] into compressed sensing, indicates that it is possible to recover the original signal exactly, using a linear measurement model with incomplete data. This theoretical derivation is applicable to DBT reconstructions which are computed given incomplete forward projections. Therefore, mathematically, we can solve the DBT reconstruction

[†]Contact Email: {g.yang, s.arridge}@cs.ucl.ac.uk, {j.hipwell, d.hawkes}@ucl.ac.uk. This work has been funded by DTI Project Digital Breast Tomosynthesis TP/7/SEN/6/1/M1577G.

ISBN: 978-87-981270-9-3

problem perfectly, with a limited-angle set of projections, given judicious choice of appropriate constraints such as regularisation.

Early breast cancer detection requires the recognition of subtle pathological changes, such as those due to tumour growth, over time. These abnormal changes and deformations of the breast tissue must be distinguished from normal deformations caused by differences in breast position, compression and other imaging acquisition parameters between the two time-points. In the high throughput breast screening context [5], the additional depth information provided by DBT must be integrated into the workflow in a way that enhances performance but does not increase the workload of the clinicians involved. In this respect, image registration could play an important role in eliminating differences between the temporal DBT datasets due to patient position, allowing the observer to focus on identifying those changes which might be indicative of disease.

Previous work on DBT image registration is limited. Sinha et al. [6] describe application of a thin-plate spline registration of corresponding manually selected control points, using mutual information as the cost function. They applied this method to seven subjects' datasets which were acquired between one year and a few minutes apart and estimate the registration accuracy to be 1.8mm $\pm$1.4. Zhang and Brady [7] describe a method for feature point extraction and use the resulting landmarks to drive a polyaffine registration of a single pair of DBT datasets.

Whilst combined registration and reconstruction algorithms have been applied to other modalities (*e.g.* PET and MRI), little has been published on applying these techniques to DBT. Yang et al. [8] [9] proposed an iterative method, which *partially coupled* the two tasks by alternating between optimising image intensity and deformation parameters to obtain a reduced cost functional. Rather than registering the images after reconstruction or partially coupling them, we advocate a method which combines the two tasks simultaneously (*fully coupled*) in order to avoid the assumptions of missing data being equal to zero (implicit in algorithms such as FBP). The aim of this work is to show that reconstruction and registration are not independent, and that combining these tasks will enhance the performance of each process as a result.

2 Methods

Based on the motivation and hypothesis above, we have developed an algorithm, which outputs one unified result for the reconstruction and registration. However, the introduction of registration introduces nonlinearity of the transformation parameters making solution of the inverse problem more complex. Although the following experiments were performed using an affine transformation and sum of squared differences, as the cost function, other higher order non-rigid transformations and alternative similarity measurements can naturally be substituted into our simultaneous framework. Before presenting our simultaneous method, we first describe the *conventional method* of performing registration after both volumes have been successfully reconstructed. Then we paraphrase the *itera-*

ISBN: 978-87-981270-9-3

tive method proposed by Yang et al. [8] [9], and subsequently we propose our *simultaneous algorithm*.

2.1 Conventional Sequential Method

A 3D object, $\boldsymbol{x} \in \Re^{N_3}$, two sets of (in our case simulated) temporal data, $\boldsymbol{y_1}$, $\boldsymbol{y_2} \in \Re^{\kappa \cdot N_2}$, (acquired using limited angle DBT geometry with $\kappa = 11$ projections covering $\pm 25^{\circ}$), the parametric transformation matrix, $R_{\boldsymbol{\zeta_p}}$, and the system matrix, $A \in \Re^{\kappa \cdot N_2 \times N_3} : \Re^{N_3} \mapsto \Re^{N_2}$, can be related via

$$\boldsymbol{y_1} = A\boldsymbol{x}, \tag{1}$$

and

$$\boldsymbol{y_2} = A\boldsymbol{x^*} = AR_{\boldsymbol{\zeta_p}}\boldsymbol{x}. \tag{2}$$

A describes the forward model to mimic the X-ray attenuation, scattering or absorption properties. The reconstruction of equations 1 and 2 can be solved by minimising

$$\boldsymbol{x_1}^{\dagger} = \arg\min_{\boldsymbol{x_1}} \left(\Phi_{Rec1} = \frac{1}{2}\left\|A\boldsymbol{x_1} - \boldsymbol{y_1}\right\|_2^2 \right); \tag{3}$$

$$\boldsymbol{x_2}^{\dagger} = \arg\min_{\boldsymbol{x_2}} \left(\Phi_{Rec2} = \frac{1}{2}\left\|A\boldsymbol{x_2} - \boldsymbol{y_2}\right\|_2^2 \right). \tag{4}$$

Following reconstruction, volumes $\boldsymbol{x_1}^{\dagger}$ and $\boldsymbol{x_2}^{\dagger}$, i.e. the fixed and moving images, are registered w.r.t the registration parameters $\boldsymbol{\zeta_p}$:

$$\boldsymbol{\zeta_p}^{\dagger} = \arg\min_{\boldsymbol{\zeta_p}} \left(\Phi_{Reg} = \frac{1}{2}\left\|R_{\boldsymbol{\zeta_p}}\boldsymbol{x_2}^{\dagger} - \boldsymbol{x_1}^{\dagger}\right\|_2^2 \right). \tag{5}$$

2.2 Partially Coupled Iterative Method

According to the previous investigations of the partially coupled iterative method [8, 9], the equations 1 and 2 can be solved by alternating an incomplete optimisation, i.e. n iterations, of the reconstructed volumes $\boldsymbol{x_1}$ and $\boldsymbol{x_2}$

$$\boldsymbol{x_1}^{\ddagger} = \arg\min_{\boldsymbol{x_1}} \left(\Phi_{Rec1} = \frac{1}{2}\left\|A\boldsymbol{x_1} - \boldsymbol{y_1}\right\|_2^2 \right) \tag{6}$$

$$\boldsymbol{x_2}^{\ddagger} = \arg\min_{\boldsymbol{x_2}} \left(\Phi_{Rec2} = \frac{1}{2}\left\|A\boldsymbol{x_2} - \boldsymbol{y_2}\right\|_2^2 \right) \tag{7}$$

with registration of the current estimates $\boldsymbol{x_1}^{\ddagger}$ and $\boldsymbol{x_2}^{\ddagger}$ w.r.t the registration parameters $\boldsymbol{\zeta_p}$:

$$\boldsymbol{\zeta_p}^{\ddagger} = \arg\min_{\boldsymbol{\zeta_p}} \left(\Phi_{Reg} = \frac{1}{2}\left\|R_{\boldsymbol{\zeta_p}}\boldsymbol{x_2}^{\ddagger} - \boldsymbol{x_1}^{\ddagger}\right\|_2^2 \right). \tag{8}$$

This method is summarised in Algorithm 1. The reconstruction-registration loop repeats m times and outputs $\boldsymbol{x_1} = \boldsymbol{x_1}^{\ddagger}$, $\boldsymbol{x_2} = \boldsymbol{x_2}^{\ddagger}$ and $R_{\boldsymbol{\zeta_p}}\boldsymbol{x_2}^{\ddagger}$

ISBN: 978-87-981270-9-3

Algorithm 1: Partially Coupled Iterative Reconstruction and Registration

Input: $\boldsymbol{y_1},\ \boldsymbol{y_2}$.
Output: $\boldsymbol{x_1},\ \boldsymbol{x_2},\ R_{\boldsymbol{\zeta_p}}\boldsymbol{x_2}$.

begin
- % Initialization of $\boldsymbol{x_1}$ and $\boldsymbol{x_2}$
- ${\boldsymbol{x_1}}^{0,0} := 0$; ${\boldsymbol{x_2}}^{0,0} := 0$; ${\boldsymbol{\zeta_p}}^{0} := 0$;
- % Outer loop for the registration
- **for** $(i = 0;\ i < m;\ i++)$ **do**
  - % Inner loop for the reconstruction
  - **for** $(j = 0;\ j < n;\ j++)$ **do**
    - % $\Psi_{\boldsymbol{x}}$ is the analytical gradient of the $\boldsymbol{x}$
    - % for the CG or L-BFGS solver
    - ${\Psi_{\boldsymbol{x_1}}}^{i,j} := A^T(A{\boldsymbol{x_1}}^{i,j} - \boldsymbol{y_1})$;
    - ${\Psi_{\boldsymbol{x_2}}}^{i,j} := A^T(A{\boldsymbol{x_2}}^{i,j} - \boldsymbol{y_2})$;
    - ${\boldsymbol{x_1}}^{i,j+1} := {\boldsymbol{x_1}}^{i,j} + (A^TA)^{-1}{\Psi_{\boldsymbol{x_1}}}^{i,j}$;
    - ${\boldsymbol{x_2}}^{i,j+1} := {\boldsymbol{x_2}}^{i,j} + (A^TA)^{-1}{\Psi_{\boldsymbol{x_2}}}^{i,j}$;
  - % Run a simple hill-climbing optimisation
  - ${\boldsymbol{\zeta_p}}^{i+1} := \arg\min_{{\boldsymbol{\zeta_p}}^{i}} \frac{1}{2}\|R_{{\boldsymbol{\zeta_p}}^{i}}\boldsymbol{x_2}^{\boldsymbol{i,j+1}} - \boldsymbol{x_1}^{\boldsymbol{i,j+1}}\|_2^2$;
  - ${\boldsymbol{x_1}}^{i+1,j+1} := R_{{\boldsymbol{\zeta_p}}^{i+1}}\boldsymbol{x_2}^{\boldsymbol{i,j+1}}$;
  - ${\boldsymbol{x_2}}^{i+1,j+1} := \boldsymbol{x_2}^{\boldsymbol{i,j+1}}$;
- % Output $\boldsymbol{x_1}$, $\boldsymbol{x_2}$, and $R_{\boldsymbol{\zeta_p}}\boldsymbol{x_2}$
- $\boldsymbol{x_1} := \boldsymbol{x_1}^{\boldsymbol{i,j+1}}$;
- $\boldsymbol{x_2} := {\boldsymbol{x_2}}^{i+1,j+1}$;
- $R_{\boldsymbol{\zeta_p}}\boldsymbol{x_2} := {\boldsymbol{x_1}}^{i+1,j+1} := R_{{\boldsymbol{\zeta_p}}^{i+1}}\boldsymbol{x_2}^{\boldsymbol{i,j+1}}$.

end

2.3 Our Simultaneous Method

The ultimate goal of our simultaneous method is to obtain an enhanced reconstruction and more accurate registration of both volumes, to aid the reading process and improve the detection of malignant tissue change. Therefore, we propose a simultaneous method using an *unconstrained* reconstruction and registration framework expressed mathematically as in Algorithm 2. Firstly, the objective function is described as

$$\min_{\boldsymbol{x},\boldsymbol{\zeta_p}\in\Re^n} \Phi_{RR} = \frac{1}{2}\Big(||A\boldsymbol{x} - \boldsymbol{y_1}||^2 + ||AR_{\boldsymbol{\zeta_p}}\boldsymbol{x} - \boldsymbol{y_2}||^2\Big), \tag{9}$$

in which, $\boldsymbol{y_1}$ and $\boldsymbol{y_2}$ are the two input X-ray acquisitions, and $\boldsymbol{x}$ denotes the unknown estimated volume. We combine the two sets of reconstructions $||A\boldsymbol{x} - \boldsymbol{y_1}||^2$ and $||AR_{\boldsymbol{\zeta_p}}\boldsymbol{x} - \boldsymbol{y_2}||^2$ with an affine registration with 12 degrees of freedom $\boldsymbol{\zeta_p}, (p = 1, 2, \ldots, 12)$, which globally describes the translation, scaling, rotation and shearing in 3D, or $\boldsymbol{\zeta_p}, (p = 1, 2, \ldots, 6)$ denotes 6 degrees of freedom in 2D.

A minimiser $\boldsymbol{x}, \boldsymbol{\zeta_p} \in \Re^n$ of Φ_{RR} is characterised by the necessary condition that the partial derivative w.r.t $\boldsymbol{x}$ and $\boldsymbol{\zeta_p}$ equals 0, denoted by $\nabla\Phi_{RR} = 0$. The partial derivative w.r.t $\boldsymbol{x}$ is straightforward, and is given by

$$g_{\boldsymbol{x}} = \frac{\partial\Phi_{RR}}{\partial\boldsymbol{x}} = A^T(A\boldsymbol{x} - \boldsymbol{y_1}) + R_{\boldsymbol{\zeta_p}}^T A^T(AR_{\boldsymbol{\zeta_p}}\boldsymbol{x} - \boldsymbol{y_2}), \tag{10}$$

ISBN: 978-87-981270-9-3

in which, $\frac{\partial \Phi_{RR}}{\partial \boldsymbol{x}}$ is the gradient. Similarly the Hessian can be expressed as

$$H_{\boldsymbol{x}} = \frac{\partial \Phi_{RR}}{\partial^2 \boldsymbol{x}} = A^T A + R_{\boldsymbol{\zeta_p}}^T A^T A R_{\boldsymbol{\zeta_p}}. \tag{11}$$

To derive the partial derivative w.r.t $\boldsymbol{\zeta_p}$, we apply a small perturbation to the objective function,

$$\Phi_{RR}\Big(\boldsymbol{x}, \boldsymbol{\zeta_p} + \Delta\boldsymbol{\zeta_p}\Big) = \frac{1}{2}\Big(||A\boldsymbol{x} - \boldsymbol{y_1}||^2 + ||AR_{\boldsymbol{\zeta_p}+\Delta\boldsymbol{\zeta_p}}\boldsymbol{x} - \boldsymbol{y_2}||^2\Big) \tag{12}$$

$$\approx \frac{1}{2}\Big(||A\boldsymbol{x} - \boldsymbol{y_1}||^2 + ||AR_{\boldsymbol{\zeta_p}}\boldsymbol{x} + A\frac{\partial R_{\boldsymbol{\zeta_p}}}{\partial \boldsymbol{\zeta_p}}\boldsymbol{x}\Delta\boldsymbol{\zeta_p} - \boldsymbol{y_2}||^2\Big). \tag{13}$$

By taking the derivative w.r.t $\Delta\boldsymbol{\zeta_p}$, we obtain that

$$\Big(A\frac{\partial R_{\boldsymbol{\zeta_p}}}{\partial \boldsymbol{\zeta_p}}\boldsymbol{x}\Big)^T\Big(AR_{\boldsymbol{\zeta_p}}\boldsymbol{x} + A\frac{\partial R_{\boldsymbol{\zeta_p}}}{\partial \boldsymbol{\zeta_p}}\boldsymbol{x}\Delta\boldsymbol{\zeta_p} - \boldsymbol{y_2}\Big) = 0; \tag{14}$$

and if $g_{\boldsymbol{\zeta_p}}$ and $H_{\boldsymbol{\zeta_p}}$ denote the gradient and Hessian respectively then we have,

$$\Big(A\frac{\partial R_{\boldsymbol{\zeta_p}}}{\partial \boldsymbol{\zeta_p}}\boldsymbol{x}\Big)^T\Big(A\frac{\partial R_{\boldsymbol{\zeta_p}}}{\partial \boldsymbol{\zeta_p}}\boldsymbol{x}\Big)\Delta\boldsymbol{\zeta_p} = -\Big(A\frac{\partial R_{\boldsymbol{\zeta_p}}}{\partial \boldsymbol{\zeta_p}}\boldsymbol{x}\Big)^T\Big(AR_{\boldsymbol{\zeta_p}}\boldsymbol{x} - \boldsymbol{y_2}\Big), \tag{15}$$

and therefore,

$$\Delta\boldsymbol{\zeta_p} = -\left[\Big(A\frac{\partial R_{\boldsymbol{\zeta_p}}}{\partial \boldsymbol{\zeta_p}}\boldsymbol{x}\Big)^T\Big(A\frac{\partial R_{\boldsymbol{\zeta_p}}}{\partial \boldsymbol{\zeta_p}}\boldsymbol{x}\Big) + \lambda I\right]^{-1}\Big(A\frac{\partial R_{\boldsymbol{\zeta_p}}}{\partial \boldsymbol{\zeta_p}}\boldsymbol{x}\Big)^T\Big(AR_{\boldsymbol{\zeta_p}}\boldsymbol{x} - \boldsymbol{y_2}\Big), \tag{16}$$

in which,

$$g_{\boldsymbol{\zeta_p}} = \frac{\partial \Phi_{RR}}{\partial \boldsymbol{\zeta_p}} = \Big(A\frac{\partial R_{\boldsymbol{\zeta_p}}}{\partial \boldsymbol{\zeta_p}}\boldsymbol{x}\Big)^T\Big(AR_{\boldsymbol{\zeta_p}}\boldsymbol{x} - \boldsymbol{y_2}\Big) = \Big(AR_{\boldsymbol{\zeta_p}}^{'}\boldsymbol{x}\Big)^T\Big(AR_{\boldsymbol{\zeta_p}}\boldsymbol{x} - \boldsymbol{y_2}\Big), \tag{17}$$

and

$$H_{\boldsymbol{\zeta_p}} = \Big(A\frac{\partial R_{\boldsymbol{\zeta_p}}}{\partial \boldsymbol{\zeta_p}}\boldsymbol{x}\Big)^T\Big(A\frac{\partial R_{\boldsymbol{\zeta_p}}}{\partial \boldsymbol{\zeta_p}}\boldsymbol{x}\Big) = \Big(AR_{\boldsymbol{\zeta_p}}^{'}\boldsymbol{x}\Big)^T\Big(AR_{\boldsymbol{\zeta_p}}^{'}\boldsymbol{x}\Big). \tag{18}$$

In order to apply a generic non-linear conjugate gradient optimiser, we extract the gradients of the objective function w.r.t $\boldsymbol{x}$ and $\boldsymbol{\zeta_p}$ below

$$\nabla\Phi_{RR} = \begin{pmatrix} \frac{\partial \Phi_{RR}}{\partial \boldsymbol{x}} \\ \frac{\partial \Phi_{RR}}{\partial \boldsymbol{\zeta_p}} \end{pmatrix} = \begin{pmatrix} A^T(A\boldsymbol{x} - \boldsymbol{y_1}) + R_{\boldsymbol{\zeta_p}}^T A^T(AR_{\boldsymbol{\zeta_p}}\boldsymbol{x} - \boldsymbol{y_2}) \\ \Big(AR_{\boldsymbol{\zeta_p}}^{'}\boldsymbol{x}\Big)^T\Big(AR_{\boldsymbol{\zeta_p}}\boldsymbol{x} - \boldsymbol{y_2}\Big) \end{pmatrix}. \tag{19}$$

3 Experiments and Results

3.1 2D Shepp-Logan Phantom

For a first test, a 2D Shepp-Logan phantom is used to demonstrate the feasibility and performance of our new simultaneous approach. The fixed and moving images are of size 64^2 pixel, with a simulated affine transformation between them.

ISBN: 978-87-981270-9-3

We test with 10 different sets of deformations, which contain 6 affine parameters p_1 to p_6 as seen in Table 1, and we calculate the mean error and standard deviation between the recovered parameters and the ground truth. Fig. 1 shows the result of the test case number 5 using our simultaneous method.

Algorithm 2: Simultaneous Reconstruction and Registration

Input: $\boldsymbol{y_1}$, $\boldsymbol{y_2}$.
Output: $\boldsymbol{x}$, $\boldsymbol{\zeta_p}$.

begin
  % Initialization of $\boldsymbol{x}$ and $\boldsymbol{\zeta_p}$
  $\boldsymbol{x}^0 := 0$; $\boldsymbol{\zeta_p}^0 := 0$;

  % Simultaneous registration and reconstruction
  for $(i = 0;\ i < m;\ i++)$ **do**
    % $\Psi_{\boldsymbol{x}}$ and $\Psi_{\boldsymbol{\zeta_p}}$ are the analytical gradients
    % of the $\boldsymbol{x}$ and $\boldsymbol{\zeta_p}$ for the CG or L-BFGS solver

    $\Psi_{\boldsymbol{x}^i 1} := A^T(A\boldsymbol{x}^i - \boldsymbol{y_1})$;
    $\Psi_{\boldsymbol{x}^i 2} := R^T_{\boldsymbol{\zeta_p}} A^T(AR_{\boldsymbol{\zeta_p}}\boldsymbol{x}^i - \boldsymbol{y_2})$;
    $\Psi_{\boldsymbol{x}^i} := \Psi_{\boldsymbol{x}^i 1} + \Psi_{\boldsymbol{x}^i 2}$;

    $\Psi_{\boldsymbol{\zeta_p}^i} := (AR'_{\boldsymbol{\zeta_p}}\boldsymbol{x}^i)^T(AR_{\boldsymbol{\zeta_p}}\boldsymbol{x}^i - \boldsymbol{y_2})$;

    $\boldsymbol{x}^{i+1} := \boldsymbol{x}^i + (A^TA)^{-1}\Psi_{\boldsymbol{x}^i 1} + (A^TR^T_{\boldsymbol{\zeta_p}}R_{\boldsymbol{\zeta_p}}A)^{-1}\Psi_{\boldsymbol{x}^i 2}$;
    $\boldsymbol{\zeta_p}^{i+1} := \boldsymbol{\zeta_p}^i + (x^TA^TAx)^{-1}\Psi_{\boldsymbol{\zeta_p}^i}$;

  % Output the $\boldsymbol{x}$ and $\boldsymbol{\zeta_p}$
  $\boldsymbol{x} := \boldsymbol{x}^{i+1}$;
  $\boldsymbol{\zeta_p} := \boldsymbol{\zeta_p}^{i+1}$.
end

Table 1. Deformation parameters scenarios for 2D experiments. Column 2-4: Ground truth; Column 5: Initial guess; Column 6-8: Recovered parameters; Column 9: Mean error & standard deviation of 10 tests. Only the results of test no. 1, 5 and 8 are shown.

	G1	G5	G8	Initial	R1	R5	R8	Mean Error and S.D.
p_1	1.0677	1.1885	0.7794	1	1.0791	1.1872	0.9132	0.1287±0.1102
p_2	0.2796	0.1843	-0.4500	0	0.2482	0.1841	-0.2650	0.2157±0.2388
$p_3(t_x)$	2.0000	2.0000	3.0000	0	1.9753	1.9890	2.8537	0.1847±0.2114
p_4	-0.0480	0.1694	0.4779	0	-0.0057	0.1680	0.1068	0.3140±0.2278
p_5	0.9054	0.8179	0.6478	1	0.9031	0.8173	1.1935	0.4062±0.5178
$p_6(t_y)$	-1.0000	-4.0000	-1.0000	0	-1.0502	-3.9546	-0.8106	0.8050±1.1044

3.2 3D Toroid Phantom (Comparing outputs of the three methods)

In this second experiment we compare the performance of (a) the *sequential* reconstruction and registration, in which $n = 100$ iterations of the reconstruction of projection images, $\boldsymbol{y_1}$ and $\boldsymbol{y_2}$, are followed by a single registration of the reconstructed volumes $\boldsymbol{x_1}$ and $\boldsymbol{x_2}$ ($m = 1$); (b) the *partially coupled iterative* approach, in which $n = 10$ iterations of the reconstruction are followed by a registration and the process repeated $m = 10$ times and (c) our *simultaneous* method. A $70 \times 70 \times 70\text{mm}^3$ 3D toroid phantom image (resolution 1mm) is created for this purpose. Fig. 2 shows the comparison results using these three different methods.

ISBN: 978-87-981270-9-3

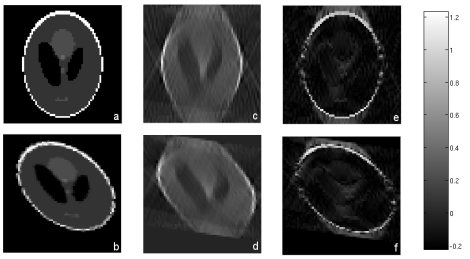

Fig. 1. *Column 1-3: The fixed image (a) and the moving image (b); the result of the simultaneous method (c), and transformation of the moving image using the recovered parameters (d); Error image (e) by subtracting (c) from (a), and error image (f) by subtracting (d) from (b).*

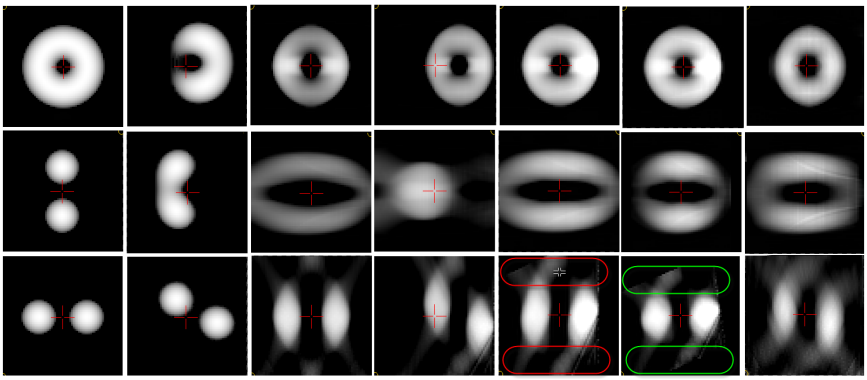

Fig. 2. *Column 1-4: Original test volume (fixed image); Its affine transformations (moving image); Reconstruction of the fixed image without registration; Reconstruction of the moving image without registration; Column 5-7: Sequential method result (transformed moving image reconstruction); Iterative method result (transformed moving image reconstruction); Our simultaneous method result (no cutting-off artefacts as shown in the colored boxes).*

4 Discussion

We have found for the first time to our knowledge that the simultaneous reconstruction and registration of DBT datasets using a generic optimisation framework is feasible. The approach jointly considers the registration and reconstruction components of the breast cancer CAD problem, and is capable of recovering both the deformation parameters, and an enhanced, reconstructed image. The performance of the new approach is demonstrated using a numerical phantom in 2D followed by a simple 3D test case. The 2D result is shown in Fig. 1, and indicates that significant reconstruction artifacts are still present. We attribute this to the fact that the unconstrained optimisation is a naïve approach, and could be improved by the addition of regularization and nonnegativity constraints.

ISBN: 978-87-981270-9-3

However, the results in Table 1 demonstrate that we have obtained reasonable recovery of the deformation parameters. These parameters are initialised using an identical transformation, in which, p_3 and p_6 are the translations t_x and t_y along each 2D direction. The mean error in t_y is relatively large because in test case no. 10 we give a large translation which translates the moving image outside of the field of view. Furthermore, the 3D test results in Fig. 2 also show that our simultaneous method is promising, and the result of our approach is compact and there is no cutting-off artefacts) when compared to the other two methods.

5 Conclusion and Perspectives

In this paper, we have presented a novel simultaneous method to fully couple reconstruction and registration for DBT, which is inspired by the motivation of detecting changes between the two sets of temporal data. SSD is employed as the registration metric, which formulates the cost criterion by the comparison between the volume estimation x and the original two sets of acquisitions y_1 and y_2. From the results on the 3D toroidal phantom images, this approach is found to reduce the misregistration artifacts with comparable reconstruction fidelity when compared to the sequential or iterative methods. There are numerous points to explore in future work. First, we would like to apply GPU acceleration for some components of our implementation, e.g. forward and backward projectors. Second, we also intend to extend the registration to incorporate non-rigid transformations. Finally, we would like to perform experiments on real DBT data, and tackle the large data size problem using multi-scale and multi-resolution techniques.

References

[1] Niklason, L.T., et al.: *Digital Tomosynthesis in Breast Imaging.* Radiology, vol. 205, 399–406 (1997)
[2] Dobbins III, J.T. and Godfrey, D.J.: *Digital X-ray Tomosynthesis: Current State of the Art and Clinical Potential.* Phys. in Med. and Bio., vol. 48, R65–R106 (2003)
[3] Zhang, Y., et al.: *A Comparative Study of Limited-angle Cone-beam Reconstruction Methods for Breast Tomosynthesis.* Medical physics, vol. 33, 3781–3795 (2006)
[4] Candès, E., Romberg, J., and Tao, T.: *Robust Uncertainty Principles: Exact Signal Reconstruction from Highly Incomplete Frequency Information.* IEEE Transactions on Information Theory, vol. 52, 489–509, (2006)
[5] Cancer Research UK: *Breast Screening in the UK: A Brief History.*
[6] Sinha, S.P., et al.: *Image Registration for Detection and Quantification of Change on Digital Tomosynthesis Mammographic Volumes.* American Journal of Roentgenology, vol. 192(2), 384–387 (2009)
[7] Zhang, W.W. and Brady, M.: *Feature Point Detection for Non-rigid Registration of Digital Breast Tomosynthesis Images.* IWDM'10, vol. 6136. LNCS, 296–303 (2010)
[8] Yang, G., et al.: *Combined Reconstruction and Registration of Digital Breast Tomosynthesis.* IWDM'10, vol. 6136. LNCS, 760–768 (2010)
[9] Yang, G., et al.: *Combined Reconstruction and Registration of Digital Breast Tomosynthesis: Sequential Method versus Iterative Method.* MIUA, 27:1–5 (2010)

ISBN: 978-87-981270-9-3

A Poisson-Laplacian framework for 3D automatic segmentation of the breast in MRI.

Cristina Gallego[1,2] and Anne L. Martel[1,2]

[1] Department of Medical Biophysics, University of Toronto, Toronto, Canada
[2] Department of Imaging Research, Sunnybrook Research Institute, Toronto, Canada

Abstract. During breast density assessment using MRI it is necessary to segment the breast in order to calculate total breast volume and exclude non-breast surrounding tissues. In this paper we describe an automatic 3D breast volume segmentation approach based on 3D local edge detection using phase congruency and Poisson surface reconstruction to extract the total breast volume in 3D. Furthermore, our breast boundary localization framework can be integrated as the starting point for a subsequent model-based segmentation by mapping model points into the initialization surface using a Laplacian framework. Our approach achieves breast-air and breast-chest wall boundary localization errors with a median of 1.36 mm and 2.68 mm respectively when tested with a breast MRI dataset from 409 women. 89.7% of the cases were correctly segmented using our approach.

1 Introduction

Breast cancer is currently the most common diagnosed cancer among women and a significant cause of death. Breast density, a representation of the amount of dense parenchyma present in the breast has been identified as a significant risk factor [1]. Although the majority of epidemiological evidence on breast density as a risk factor comes from X-ray mammography screening data, some researchers have acknowledged the advantages of studying breast density with different imaging modalities such as MRI [2]. MRI is a very versatile imaging modality that provides a 3D view of the breast for volumetric breast density assessment without the risks from exposure to ionizing radiation. As a result, ongoing epidemiological studies are looking at quantitative assessment of breast density in young women using MRI as an important biomarker influencing the later risk of breast cancer [3].

However, it is known that quantitative evaluation of breast density using MRI suffers from several limitations including inconsistent breast boundary segmentation and lack of standardized algorithms to accurately measure breast density. It is ideal to have consistent and robust computer-aided analysis tools to segment the breast and to extract the total volume of the breast in 3D. For quantitative assessment of breast density using MRI, separate images of breast water and fat can be obtained and breast water can be measured as a surrogate for fibroglandular tissue and stroma as shown in Fig. 1. Breast segmentation is further necessary to remove background noise artifacts and exclude surrounding muscle tissues in the chest wall. Robust and reliable automatic segmentation

ISBN: 978-87-981270-9-3

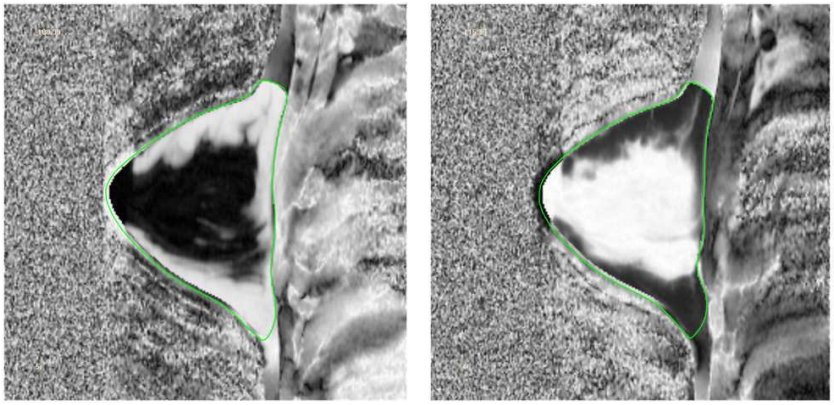

Fig. 1: Sagittal MRI slices of breast water/fat imaging. a) Fat image. b) Water image. Green contours represent the expert annotated outline of the breast region excluding surrounding chest wall and air background.

is ideal even though it is affected by a number of challenges. In breast MRI, image intensity distributions are dependent on MR protocols and acquisition parameters so that segmentation based on separation of greylevel intensities (e.g. selective thresholding) is inadequate and lacks generalization when used with different protocols. In addition, the contrast between the breast and adjacent structures such as pectoral muscles is not distinctively defined.

This work proposes a Poisson-Laplacian framework for 3D automatic segmentation of the breast in MRI. We exploit phase congruency for breast boundary edge detection as an invariant feature to intensity variations and inhomogeneities. Our approach consists on a Poisson surface reconstruction followed by a Laplacian surface mapping framework, which can be optimally applied to 3D statistical shape model (SSM) initialization. The aforementioned method is presented in two main steps: 1) Estimating an initial surface of the breast by detecting breast tissue boundaries to gain a target surface optimal for initialization, and 2) Initializing a 3D SSM model to the target surface. We demonstrate the feasibility of our approach by measuring error distances from the resulting initialization surfaces to the manually segmented volumes.

2 Materials and Methods

Sagittal breast images were acquired from a previous cross-sectional study by Boyd et al. [4]. Briefly, a modified version of the GE FSE Dixon sequence was used consisting on a 28 cm field of view, with a 256 x 128 acquisition matrix. The slice thickness was 7 mm interleaved with TE 14x8 ms, ETL 8 and TR 2500. The total imaging time for both breasts was about 13 min to obtain 45 slices covering the entire volume of both breasts.

ISBN: 978-87-981270-9-3

Each scan consists of three images of water and fat signals with phase shifts of 0, π and 2π, according to the three-point Dixon method [5]. The image corresponding to the zero degree phase shift corresponds to an image were both the fat and water signals are in phase. This in-phase image of the right breast was used for further segmentations.

Each breast was semi-automatically segmented by 3 observers (inter-reader and intra-reader agreement was more than 0.94) using an active contour approach with manual correction [4]. 2D delineated contours for each breast were stacked together in adjacent cross-sections and resampled to isotropic voxel size of 2.56 mm. Surface meshes representing the 3D volume of the breast were finally obtained and these surfaces were used as the gold-standard to measure our segmentation accuracy.

2.1 3D phase congruency edge detector

Kovesi [6] described how phase congruency can be calculated in 2D via a bank of oriented filters to obtain local phase information at a given spatial location. Computing phase congruency in 3D using a bank of filters imposes the complexity of defining a number of appropriate filter orientations and their angular spread to evenly cover the image spectrum. As an alternative, points of maximal phase congruency can be detected as points of maximal local energy [7]. In this work we estimate maximal local energy via the monogenic signal. The monogenic signal is an isotropic extension of the 1D analytic signal to higher dimensions via vector-value odd filters [8]. By convolving the 3D image with the Riesz transform, the monogenic signal is obtained. In practice, the infinite impulse response of the Riezs transform is reduced by convolving the image first with a bandpass filter such as the log-Gabor function:

$$G(w) = \exp\left[\frac{-\log\left(w/w_o\right)^2}{2\log\left(k/w_o\right)^2}\right] \tag{1}$$

where w_o is the center frequency of the filter and k/w_o is the ratio of the spread of the Gaussian describing the Log Gabor transfer function in the frequency domain to the filter center frequency. k/w_o was kept constant to achieve filters with equal bandwidths at different scales. The log-Gabor response and the log-Gabor filtered Riezs kernel responses are quadrature pair of filters that were applied to different scales and the results were summed over all scales. In contrast to the bank of oriented filters approach, there is no need for an additional summation along different orientations. The filter's center frequency at a given scale is determined by the following equation:

$$w_s = \frac{1}{\lambda_{min}(\delta)^{s-1}} \quad , \quad s = 1, 2, ..., n \tag{2}$$

here λ_{min} is the smallest wavelength of the Log-Gabor filter and δ is a scaling factor between successive scales. λ_{min} is scaled up to the total number of scales n. A noise threshold T, is applied to the computation of phase congruency. T is calculated as the mean noise response plus some multiple k of the standard deviation of the distribution at the smallest as $T = \mu + k\sigma$, $k = 2$ where μ is the mean and σ is the standard deviation of the local energy distribution.

ISBN: 978-87-981270-9-3

2.2 Estimation of initial breast boundary surface

Points of maximal phase congruency coincide with features of high edge strength and therefore can be thought as sample points from a field of edge potential. In this work, we propose to sample points of maximal phase congruency with the purpose of estimating a breast boundary isosurface using Poisson surface reconstruction [9]. The idea behind this approach is to infer the topology of an unknown surface given oriented points located on or near the surface. In order to estimate the orientation of points corresponding to maximal phase congruency we propose to sample the gradient of the image at the point locations. Kazhdan et al. [9] proposed to consider these oriented points as samples of an implicit indicator function χ whose gradient best approximates a vector field $\overrightarrow{V}$ defined by the point normals (i.e $min_{\chi}\|\nabla\chi - \overrightarrow{V}\|$). This variational problem can be transformed into a Poisson problem: finding the best solution involves computing a least-squared approximate solution of the scalar function χ whose Laplacian (divergence of the gradient) equals the divergence of the vector field $\overrightarrow{V}$:

$$\Delta\chi \equiv \nabla.\nabla\chi = \nabla.\overrightarrow{V} \tag{3}$$

The scalar function is represented in an adaptive octree and the Poisson equation is solved in successive well conditioned sparse linear systems at multiple octree depths, as in [9]. Once the scalar function is found, the surface corresponding to the breast boundary can be extracted as an iso-contour of χ using an adaptive marching cubes algorithm [10]. The reconstruction algorithm performs best with sufficient dense point samples and copes well with missing data by filling small holes.

2.3 Initializing the 3D model to the target surface

The output of the Poisson breast surface reconstruction can serve as the starting point for a subsequent model-based segmentation. We explored the feasibility of initializing the mean of a population of 3D landmarked shapes (S_{mean}) to the found breast boundary iso-surface (S_{iso}). First, we bring both surfaces into the same reference frame using a landarmk-based rigid registration that starts by aligning the centroids of the atlas and the Poisson reconstructed iso-surface. Then, mapping 3D landmarks from the mean surface to the initialization surface can be treated as a correspondence problem. In this work, we formulate this problem using a Laplacian equation:

$$\nabla^2\psi = \frac{\delta^2\psi}{\delta x^2} + \frac{\delta^2\psi}{\delta y^2} + \frac{\delta^2\psi}{\delta z^2} = 0 \tag{4}$$

with boundary conditions: $\psi = \psi_1$ on S_{mean} and $\psi = \psi_2$ on S_{iso}, where (ψ_1, ψ_2) are two different fixed potentials. The solution to the Laplace equation is a scalar field ψ that provides a transition from surface S_{mean} to S_{iso} as defined by set of nested surfaces [11]. Furthermore, given the geometric properties of the Laplace equation, by computing the normalized negative gradient of the Laplace solution:

$$\mathbf{N} = -\frac{\nabla\psi}{\| \nabla\psi \|} \tag{5}$$

ISBN: 978-87-981270-9-3

we obtain a unit vector field that defines field lines connecting both surfaces also known as streamlines. The path between two corresponding points (i.e p_1 on S_{mean} to p_2 on S_{iso}) can be found by following the streamline in a ray casting approach, starting at the mean surface in the direction of $\mathbf{N}$.

3 Results

Fig. 2 shows our phase congruency results using 3 different minimum wavelengths. We investigate the effect of different parameters on edge detection results and found that values of $\lambda_{min} = 3$, $k/w_o = 0.65$, and $\delta = 2.1$ over a total of 6 scales gave good edge localization results (see fig 2-b). The effect of decreasing λ_{min} can be appreciated

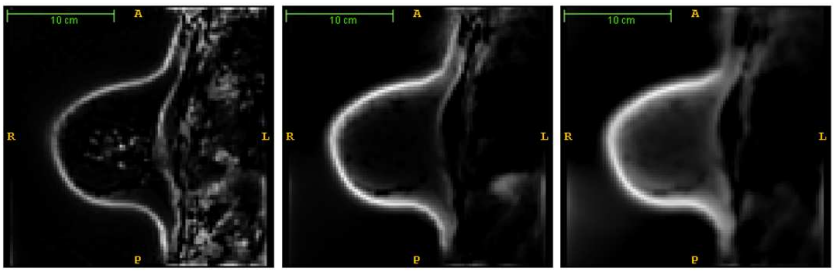

Fig. 2: Phase congruency detection examples with different filter parameters. a) $\lambda_{min} = 1$, b) $\lambda_{min} = 3$, c) $\lambda_{min} = 6$.

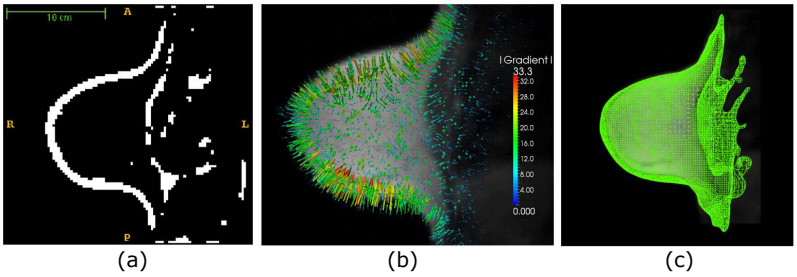

Fig. 3: Breast boundary reconstruction via Poisson framework. a) mask of maximal phase congruency points, b) Image gradient for sampling orientation of points. c) Output breast surface iso-contouring after solving Poisson system.

in fig 2-a, where the filter enhances local features at relatively higher frequencies. In contrast, increasing λ_{min} (fig 2-c) appears to blur out some features and local structure is detected at lower frequencies.

ISBN: 978-87-981270-9-3

Figure 3 shows a surface reconstruction example using an octree depth of 8, which corresponds to an octree resolution of 256^3. In some cases, spurious clusters of surface elements are captured on the chest region where edge features are also detected. These elements however not necessarily interfere with the estimation of the complete breast surface and can be removed with an additional connected-component filter. To evalu-

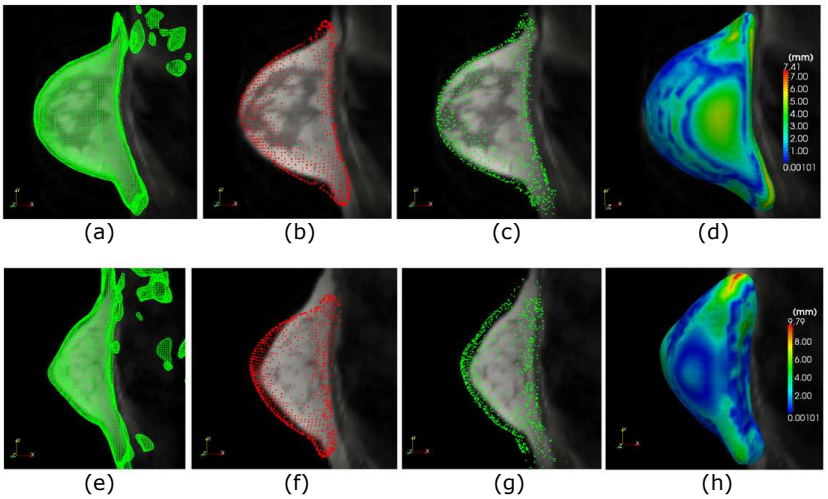

Fig. 4: Representative results of 2 breast boundary reconstructions (top and bottom): a) and e) Breast iso-surface (output of Poisson reconstruction). b) and f) Aligned mean of population showing initial position of landmark points before Laplacian mapping. c) and g) Mapping results to target surface. d) and h) Color-coded closest distances from manual annotated surfaces.

ate the feasibility of this reconstruction approach we measured target distances to the manually annotated surfaces, using a population of (n=409) landmarked shapes [12]. Distances were measured from the mean shape in the population to the breast boundary iso-surface, after finding corresponding points according to equation 6 (see fig. 4). By labelling the relative position of each individual landmark in the mean shape, we can discriminate the mapping accuracy among specific regions of the breast boundary, such as the chest-wall or the air-breast boundary regions. Figure 5 summarizes the mapping accuracy of landmark points by our algorithm as well as some standard overlap metrics of agreement and error. In addition to distance errors, we also compared total volumes between manually annotated volumes and the total volume enclosed by our segmentation boundaries according to [13]. We compared a total of 367 breast volumes, since 42 cases were excluded due to failures in the initial surface alignment (steps b) and f) in fig. 4).

For the total breast volumes measured in cm^3, the median of the absolute percent measurement error was 6.75%. Fig. 6 presents the Bland-Altman plot that compares the

ISBN: 978-87-981270-9-3

Region	Distance quartiles (mm) 0.25	0.5(median)	0.75	IQR
air-breast	0.79	1.36	2.93	2.15
chest-wall	1.12	2.68	4.82	3.70

(a)

Overlap Metrics Metric	mean ± std
Total Overlap	0.89 ± 0.05
Mean Overlap (Dice)	0.88 ± 0.04
False-negative fraction	0.11 ± 0.05
False-positive fraction	0.13 ± 0.07

(b)

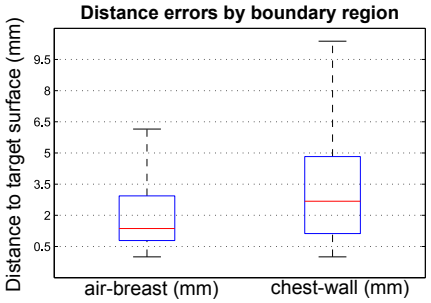

(c)

Fig. 5: a) Summary and c) Box and whisker plots of distances from manually annotated surfaces in mm discriminated by boundary region. b) Agreement and error overlap results.

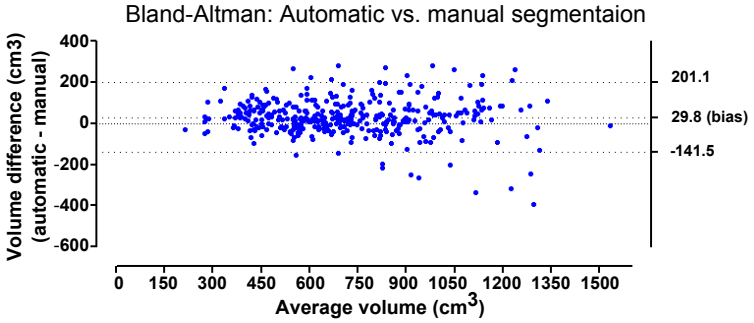

Fig. 6: Bland-Altman plot showing the difference between automatic and manual measurements of total breast volume (in cm^3) against the average of the two methods.

volumes obtained automatically with the volumes measured from the manual segmentations. The magnitude of the disagreement (in terms of bias and limits of agreement) was 29.8 cm^3 (-141.5 to 201.1) cm^3. The scatter of the values tends to increase for larger volumes. The fact that some values are more scattered on the negative side of the plot (with respect to zero difference line), indicates that in some cases the automatic segmentation tends to underestimate the true volume of large breast volumes ($<$900 cm^3). A possible fix for this is to build an volume-specific shape atlas that can account for differences between large and small breasts.

4 Conclusion

We described an automatic breast volume segmentation approach based on 3D local edge detection. Our boundary localization results demonstrate error distances from

ISBN: 978-87-981270-9-3

manual surfaces with an IQR of 2.15 mm for the air-breast boundary and 3.7 mm for the breast-chest wall boundary. This indicates that the error for localizing the breast-air boundary is within sub-resolution accuracy. Errors are relatively higher for localizing the chest-wall boundary, probably due to the low contrast between adjacent tissues to the breast in this region. However, the results obtained are encouraging for using phase congruency edge detection and Poisson surface estimation to segment the total volume of the breast. Furthermore, incorporating a manual override to our automatic segmentation framework will be a feasible approach for computing total breast volume during breast density assessment using MRI. We are currently working on adapting this work to initialize a statistical shape model (SSM) of the breast during model-based segmentation. Future work is needed to improve breast volume assessment on large breast volumes.

References

1. McCormack, V.A., Dos Santos Silva, I.: Breast density and parenchymal patterns as markers of breast cancer risk: a meta-analysis. Cancer Epidemiol Biomarkers Prev 15, 1159–1169 (2006)
2. Boyd, N.F., Martin, L.J., Bronskill, M., Yaffe, M.J., Duric, N., Minkin, S.: Breast tissue composition and susceptibility to breast cancer. Journal of the National Cancer Institute 102(16), 1224-37 (2010)
3. Boyd, N.F., Rommens, J.M., Vogt, K., Lee, V., Hopper, J.L., Yaffe, M.J., Paterson, A.D.: Mammographic breast density as an intermediate phenotype for breast cancer. Lancet Oncol 6(10), 798-808 (2005)
4. Boyd, N.F., Martin, L.J., Chavez, S., Gunasekara, A., Salleh, A., Melnichouk, O., Yaffe, M.J., Friedenreich, C., Minkin, S., Bronskill, M.: Breast-tissue composition and other risk factors for breast cancer in young women: a cross-sectional study. Lancet Oncol 10(6), 569-580 (2009)
5. Dixon, W.T.: Simple Proton Spectroscopic Imaging. Radiology 153(1), 189–194 (1984)
6. Kovesi, P.: Image features from Phase Congruency. Videre: Journal of Computer Vision Research 1(3), 1–27 (1999)
7. Morrone, M.C., Owens, R.A.: Feature detection from Local Energy. Pattern Recognition Letters 6(5), 303–313 (1987)
8. Felsberg, M., Sommer, G.: The Monogenic Signal. IEEE Transactions on Signal Processing 49(12), 3136-3144 (2001)
9. Kazhdan, M., Bolitho, M., Hoppe, H.: Poisson Surface Reconstruction In : Eurographics Symposium on Geometry Processing (2006)
10. Wilhelms, J., Van Gelder, A.: Octrees for Faster Isosurface Generation. In : ACM Transactions on Graphics 11(3), 201–227 (1992)
11. Jones, S.E., Buchbinder, B.R., Aharon, I.: Three-Dimensional Mapping of Cortical Thickness Using Laplaces Equation. In :Human brain mapping 11, 12–32 (2000)
12. Gallego, C., Martel, A.L..: Automatic model-based 3D segmentation of the breast in MRI. Proc. of SPIE Vol. 7962 796215-2 (2011)
13. Alyassin, A.M., Lancaster, J.L., Downs III, J.H.: Evaluation of new algorithms for the interactive measurement of surface area and volume. Med. Phys. 21(6), 741–752 (2007)

ISBN: 978-87-981270-9-3

Pectoral Muscle Identification in Mammograms with a Layout Consistent Markov Random Field

Yuanjie Zheng[1], Diane Nathan[1], Yan Wang[2], Brad Keller[1], Emily Conant[1], James C. Gee[1], Despina Kontos[1]

[1]University of Pennsylvania, Department of Radiology, Philadelphia PA USA
[2]University of Pennsylvania, Department of Mathematics, Philadelphia PA USA

Abstract. This paper addresses the problem of identifying the pectoral muscle in medio-lateral oblique (MLO) view digital mammograms (DM). Different from most previous work, the prior-knowledge of tissues' geometric layout (e.g. the muscle is a triangular region at the upper-posterior part of the image) in mammogram is incorporated in the segmentation process. Specifically, we pose this problem as a Markov Random Field (MRF) equipped with various constraints to encourage/enforce tissues' spatial relationships to be consistent with this prior-knowledge. Theoretical analysis and experimental results on 80 DM images show the superior accuracy and robustness of our algorithm compared with several standard previous methods.

1 Introduction

Breast cancer ranks second among cancer related mortality rates in women in the United States. It is reported that breast cancer mortality rates have declined somewhat in recent years and current thinking appears to lend more weight to mammography screening and earlier diagnosis as the primary cause [1]. Computer-Aided Diagnosis (CAD) systems in the diagnosis of breast cancer with mammography potentially provide a consistent and reproducible second opinion to radiologist. They can help to reduce the misdiagnosis caused by the large variabilities of human diagnosis.

Automatic identification of pectoral muscle is an essential step of a breast cancer CAD system with digital mammograms (DM). The pectoral muscle, being typically visible in medio-lateral oblique (MLO) view mammograms [2], appears as a triangular region of high density at the upper-posterior part of the image (as shown in Fig. 1). Due to its x-ray attenuation, it may have similar appearances to some abnormalities [3], introducing additional source of complexity in automated analysis of DM and biasing cancer detection and diagnosing procedures. Exclusion of the pectoral muscle has thus been taken as an important preprocessing procedure in many mammographic processing methods [4, 5]. Moreover, muscle identification enables the analysis of image information at muscle's edge and inside its region for identifying abnormal axillary lymph nodes [3], etc.

However, automatic identification of pectoral muscle is not a trivial for a variety of reasons. First, it suffers from the appearance similarity between pectoral

ISBN: 978-87-981270-9-3

muscle and dense tissues of the breast [3]. This similarity introduces ambiguities and renders the accurate segmentation extremely hard. Second, contour's position, shape, and intensity contrast of pectoral muscle on the MLO-view have wide variabilities [6, 4]. For example, pectoral muscle could occupy as much as half of the breast region, or as little as a few percent of it [4]. These variations are caused by the differences in individual patient variables and positioning techniques [2], specifically including variations in body habitus, length of the thorax, the presence of a pacemaker or a prominent sternum, and ability of the radiographer to relax the woman, etc. Third, although the muscle boundary is perceived to be visually continuous, there may be large variations in edge strength and obscured parts by artifacts of DM [4].

As to be detailed in Sec. 2, there is extensive work on handling the challenges in automatic identification of pectoral muscle from DM images. However, their performances are limited because they are founded either on the hypothesis that pectoral muscle boundary is a straight line or on a direct application of certain general image segmentation techniques in the image processing field to detecting a curved boundary. The assumption of straight line on muscle boundary is too simple to be always correct in practice [3]. Direct application of certain general segmentation techniques (e.g. graph-cut [5]) is not optimal because they are originally designed for a more general purpose and some unique properties (e.g. the geometric layout of breast tissues) in DM can not be combined.

In this paper, we propose a new algorithm for pectoral muscle segmentation using a Markov Random Field (MRF) model [7] equipped with various constraints on geometric relations of tissues. These constraints help to encourage/enforce the consistence between the segmentation results and the prior-knowledge on geometric layout of breast tissues in DM (as shown in Fig. 1). This geometric layout property guides the optimization in a more restricted but reasonable search space and therefore leads to higher accuracies and better robustness. Moreover, the MRF model itself brings in noise resistance and smooth segmentation boundaries. Experimental results on 40 bilateral DMs, a total of 80 images, show that our technique outperforms some state-of-the-art techniques in both accuracy and robustness.

2 Previous Work

There is extensive work [6, 5, 4, 8, 9] on pectoral muscle identification in MLO-view DM images. They can basically be classified as learning based, straight line detection based, curved line detection based, or MRF model based, respectively. Learning based methods rely on neural networks [5] or SVM [6] to decompose the DM image into several components (including pectoral muscle) or detect endpoints of muscle-breast curve. Straight line detection based approaches treat the muscle-breast boundary as a straight line and then detect it with the Hough transform or any line fitting technique. Curved line detection techniques extend the straight line of muscle-breast boundary to a curve [4]. The curve can be obtained by adjusting the straight line in its neighboring area according to image

ISBN: 978-87-981270-9-3

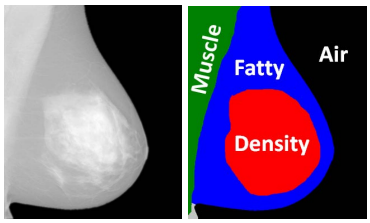

(a) DM image (b) Tissue label

Fig. 1. Breast tissues' geometric layout in DM is characterized by several facts (as shown in the right annotation image). First, pectoral muscle appears at the upper-posterior part of the DM image. Second, breast ("Fatty"+"Density") is anterior to the pectoral muscle and air is anterior to breast. Finally, pectoral muscle is characterized as a triangular region with a curved diagonal edge (muscle-breast boundary) slanted up to anterior.

gradients, using active contour models, or fitting a curve [3]. MRF model based methods [5, 8] perform image clustering while considering the consistency of neighboring pixels. Most previous methods make no use of the geometric layout (as shown in Fig. 1) and therefore their performances are limited in practice, e.g. when the density area is spatially connected to muscle (a shown in Fig. 3).

MRF model [7] based image segmentation has attracted intensive research interest for more than two decades due to its superior effectiveness and noise-resistance compared with the clustering based methods. It performs data clustering while enforcing spatial smoothness on the resulting labels. To release the computational burden, many previous works [7, 10, 11] assume the label smoothness term in the energy function to be metric or semi-metric. Recent papers [12, 13] try to relax this constraint and incorporate an arbitrary form which can be asymmetric or repulsive. This enables the incorporation of certain restrictions on geometric relations between labels. We will show that this relaxation also enables the incorporation of the pre-known tissues' geometric layout (as shown in Fig. 1) in the identification process of pectoral muscle in DM images.

3 MRF Model

MRF for 2-D image segmentation is a 2-dimensional random process defined on a finite discrete lattice. Given a 2-D DM image I with pixels denoted by set $\mathcal{P}$, MRF can be used to infer a label $l_p \in \mathcal{L}$ for each pixel $p \in \mathcal{P}$. Labels in $\mathcal{L}$ may include "pectoral muscle" ("muscle" for abbreviation), "air", "breast", "fatty", "density" (fibro-glandular tissue) [14] and others if necessary, as shown in Fig. 1(b). MRF inference amounts to minimizing the following energy function

$$E(l) = \sum_{p \in \mathcal{P}} D_p(l_p) + \sum_{(p,q) \in \mathcal{N}} V_{pq}(l_p, l_q) \tag{1}$$

where D_p is the data term measuring the disagreement between the observation of p and its assigned label l_p, $V_{p,q}$ is the smoothness term specifying the cost

ISBN: 978-87-981270-9-3

l_p \ l_q	Muscle	Fatty	Density	Air
Muscle	0	2	15	100
Fatty	500	0	5	5
Density	500	5	0	20
Air	500	500	500	0

(a) horizontal

l_p \ l_q	Muscle	Fatty	Density	Air
Muscle	0	5	20	100
Fatty	500	0	5	5
Density	500	5	0	20
Air	500	5	20	0

(b) vertical

Fig. 2. Values of f_{pq} in Eq. (2) set for enforcing/encouraging the pre-known tissues' geometric layout (as shown in Fig. 1). The left table is for a pair of horizontal neighbors while the right is for vertical.

for assigning l_p to pixel p and l_q to q, and $\mathcal{N}$ is a set of pairs of adjacent pixels. We use the standard 4-connected $\mathcal{N}$ and assume p is left to q when they are horizontally neighboring and is above q when they are vertically neighboring.

The data term D_p can be computed based on the intensity value of the original image I or certain features (e.g. texture) extracted from I. The representative intensity/feature value of each label can be specified manually or learned with certain algorithms. In our experiments, we computed D_p as the absolute difference between each pixel's intensity and the manually set representative intensity value for each label (0, 240,210, and 50 for "air", "muscle", "density", and "fatty", respectively).

The smoothness term V_{pq} encourages label's spatial consistency by penalizing neighboring pixels that are not assigned the same label. It is computed with

$$V_{pq} = w_{pq} f_{pq}(l_p, l_q). \tag{2}$$

We specify w_{pq} in Eq. (2) as being inversely proportional to image gradient with the method in [13]. That can render the boundaries of segmented regions to appear where the image bears abrupt changes. Value of f_{pq} relies only on the two labels l_p and l_q and not on the locations of the involved pixels. In many previous works [7, 10, 11], f_{pq} is required to be metric or semi-metric in order for a computational efficiency, e.g. the Potts model [10]. Recent papers [12, 13] tried to relax it to an arbitrary form, which enables the enforcement of certain geometric layout properties of the segmented objects.

4 Constraints

The pre-known geometric layout of tissues (as shown in Fig. 1) can be enforced/encouraged by setting an appropriate value for each f_{pq} in Eq. (2). For example, we know that muscle is left to breast in the left MLO-view DM image in Fig. 1. To enforce this prior-knowledge, we set $V_{p,q}$ of the horizontal neighbors $\{p, q\}$ a small value when l_p takes "muscle" while l_q taking "fatty" but a large value for the reverse. For right MLO-view DM images in which breast appears on the right side, we can just flip them left-to-right.

ISBN: 978-87-981270-9-3

Specifically, we specify the value of f_{pq} when $\{p, q\}$ are horizontal and vertical neighbors as shown in Fig. 2. With these settings, several geometric properties of the tissues' layout can be enforced/encouraged in the segmentation process. First, muscle is left to fatty, enforced by a small f_{pq} value of horizontal "muscle"-"fatty" neighbors and a very large value of horizontal "fatty"-"muscle" neighbors. Second, the muscle-breast boundary is steeply slanted up to right. This is accomplished by a smaller f_{pq} value of horizontal "muscle"-"fatty" neighbors than vertical. Third, air is right to breast, enforced by small f_{pq} values of horizontal "breast"-"air" neighbors and very large values of horizontal "air"-"breast" neighbors. Fourth, air can appear both upper and lower of breast, guaranteed by the relatively small values of vertical "air"-"breast" and "breast"-"air" neighbors. Finally, spatial label consistency inside and smoothness of boundaries between the segmented regions are encouraged by the zero f_{pq} value when $\{p, q\}$ take the same label in contrast to larger values when they take different labels.

5 Optimization

Optimization of Eq. (1) is easy to get stuck in a local minimum using many previous methods such as the well-known α-expansion optimization technique [10]. It is because the smoothness term $V_{p,q}$ in Eq. (1) is asymmetric considering the asymmetric f_{pq} as shown in Fig. 2. Fortunately, a series of new optimization techniques [12, 13] appeared recently to solve this hard task.

We employ the dynamic programming (DP) based optimization technique in [13] and tailor it to this special case of pectoral muscle identification in DM images. This technique reduces a 2D image labeling problem to a 1D optimization problem and is equivalent to finding a shortest path in a large state space. It can attain a global optimization under certain constraints.

With the DP based optimization technique [13], we try to partition a DM image (as shown in Fig. 1) into 3 regions: "muscle", "breast" and "air" corresponding to left, middle and right parts of the image, respectively. This requires the breast to appear always on the left hand side of the image.

Supposing the given image I is of size $M \times N$, we try to search simultaneously M optimal triples $\{(i_k, j_k, l_k)|k = 1, 2, \cdots, M\}$, each corresponding to one row of the image. Here, $1 \leq i_k \leq j_k \leq N$ and l_k takes a label of "fatty" or "density". For the row k of the image, we hope pixels in columns $1, 2, \cdots, i_k - 1$ are "muscle", pixels in columns $j_k + 1 \cdots, N$ are "air", and pixels in columns $i_k, \cdots, j_k$ are "fatty" or "density" specified by l_k. The resulting sequences of $(i_1, i_2, \cdots, i_N)$ and $(j_1, j_2, \cdots, j_N)$ define the muscle-breast boundary and breast-air boundary, respectively. The energy in Eq. (1) is then reformulated as

$$E(l) = \sum_{k=1}^{M} U_k(i_k, j_k, l_k) + \sum_{k=1}^{M-1} H_k(i_{k+1}, j_{k+1}, l_{k+1}, i_k, j_k, l_k) \tag{3}$$

where U_k is formed by putting together all data terms and horizontal smoothness terms (in Eq. (1)) within row k, and H_k is the summation of all vertical smoothness terms between rows k and $k + 1$.

ISBN: 978-87-981270-9-3

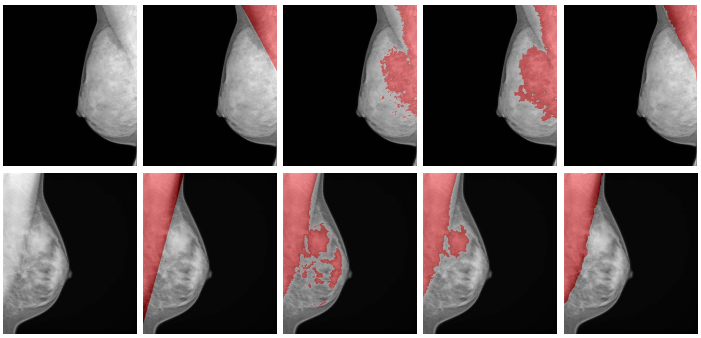

Fig. 3. Identification of the pectoral muscle is extremely difficult especially when the abnormality is spatially connected to muscle. Our method produced superior results due to the incorporation of prior-knowledge of the geometric layout (detailed in Fig. 1).

A global optimum can be obtained in $O(4M^2N)$ time for the minimization of Eq. (3) with the fast DP algorithm proposed in [13]. We omit the details of this algorithm for brevity. Interested readers are referred to the paper [13].

6 Results

Test data set is composed of 40 bilateral MLO-view post-processed digital mammograms, a total of 80 images, acquired using a standard screening protocol on a Senograph DS (GE Healthcare) full-field digital mammography system with an isotropic 100μm resolution. For each image, a trained-radiologist manually delineated the pectoral muscle with the Cumulus software (Ver. 4.0, Univ. Toronto) [14], for which the muscle-breast boundary appears as a curve composed of line segments and is treated as the ground-truth. A trained rater then adjusted the radiologist's line segments to neighboring places with a locally maximum image gradient. Although the latter can not be treated as ground-truth, manually located boundaries at places with a high image gradient have been widely used in evaluating segmentation algorithms.

With these data sets, we compared the performances of the proposed method with three previous typical methods: the Hough transform, the k-means algorithm, and the graph-cut algorithm [5]. For qualitative evaluations, we assessed each algorithm-segmented result by visually comparing with the corresponding radiologist-delineation. If they are very different (e.g. a large area of density was treated wrongly as muscle or a dominated area of muscle was missed), we assigned it as a failed case, and otherwise as a successful case, as shown in Fig. 3. Through the results, we found that the percent of successful cases is 90.0% for the proposed method, 83.7% for the Hough transform, 76.3% for the k-means algorithm, and 80.0% for the graph-cut algorithm.

ISBN: 978-87-981270-9-3

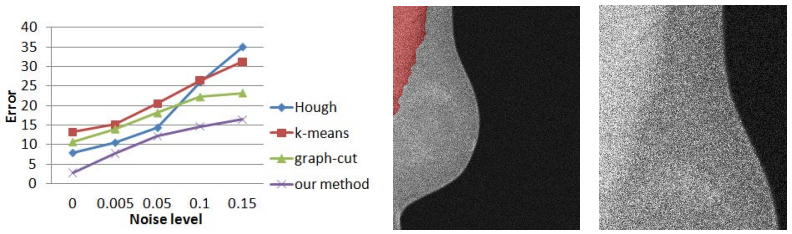

Error curves muscle segmentation local patch

Fig. 4. Error curves on our testing data sets when adding image noise in different levels. Our method can produce a good muscle-breast boundary even when the DM image bears sever noise as shown in a local patch of the image.

For quantitative evaluations, we computed the average of the shortest Euclidean distance of each pixel on the muscle-breast boundary produced by an algorithm to the corresponding manually delineated boundary. We found that the mean/std of this error measurement (in pixel) when comparing with the radiologist's manual segmentation (rater's refinement) are 4.4/3.6 (2.8/2.6) for our algorithm, 7.7/6.8 (7.9/6.9) for the Hough transformation, 14.8/12.1 (13.2/11.9) for the k-means algorithm, and 13.3/10.6 (10.7/9.3) for the graph-cut algorithm.

To evaluate the robustness to noise of our algorithm, we added in the testing images Gaussian noise (using Matlab function imnoise) with variances 0.005, 0.05, 0.1, 0.15, respectively. Error statistics measured by the average of the distance between the algorithm-segmented curve and the rater-manually-refined curve (as explained above) are shown in Fig. 4.

From the above results, we have at least three findings. First, our algorithm produced a superior accuracy and robustness than other techniques. It validates the high value of incorporating prior knowledge on the geometric layout for muscle's segmentation. Second, although the Hough transform is simple, it can outperform the k-means and graph-cut algorithm. However, it deteriorates very quickly when image bears noise. Finally, the MRF based algorithms, including the graph cut algorithm and our method, are more robust to noise.

7 Conclusion and Future Work

Different from other images, digital mammograms (DM) on the medio-lateral oblique (MLO) view have certain unique properties in the geometric layout of breast tissues. This layout is characterized by the relative spatial relations between different tissues (pectoral muscle, fatty, dense tissues and air) and the specific shape of the muscle or breast, as detailed in Fig. 1. This geometric layout is inclined to be guaranteed in the imaging process [2] and pretty uniform across different subjects.

We proposed a layout consistent MRF model to automatically identify pectoral muscle from DM images. Our method outperforms many previous techniques because the prior-knowledge of geometric layout of mammograms can

ISBN: 978-87-981270-9-3

be combined in the segmentation process. With our method, accurate muscle-breast and breast-air boundaries can be obtained, but not for the fatty-density boundary because l_k in Eq. (3) can take only one label.

Our future work would include extensions to breast images in other modalities (e.g. MRI) and to segmentations of other tissues.

ACKNOWLEDGEMENT

This work was supported in part by the American Cancer Society (Research Scholar Grant RSGHP-10-108-01-CPHPS) and the Department of Defense (Concept Award W81XWH-09-1-0355).

References

1. Mayer, M.: Treatment and outcomes for high-risk and metastatic breast cancer in california: An inquiry into disparities and research needs. Technical report, California Breast Cancer Research Program (2004)
2. Bentley, K., Poulos, A., Rickard, M.: Mammography image quality: Analysis of evaluation criteria using pectoral muscle presentation. Radiography **14** (2008) 189–194
3. Ferrari, R.J., Rangayyan, R.M., Desautels, J.E.L., Borges, R.A., Frere, A.F.: Automatic identification of the pectoral muscle in mammograms. IEEE TMI **23** (2004) 232–245
4. Kwok, S.M., Chandrasekhar, R., Attikiouzel, Y., Pickard, M.T.: Automatic pectoral muscle segmentation on mediolateral oblique view mammograms. IEEE TMI **23** (2004) 1129–1140
5. Camilus, K.S., Govindan, V.K., Sathidevi, P.S.: Computer-aided identification of the pectoral muscle in digitized mammograms. Journal of Digital Imaging **23** (2010) 562–580
6. Domingues, I., et al: Pectoral muscle detection in mammograms based on the shortest path with endpoints learnt by svms. In: 32th Annual International Conference of the IEEE EMBS. (2010)
7. Geman, S., Geman, D.: Stochastic relaxation, gibbs distributions and the bayesian restoration of images. IEEE TPAMI **6** (1984) 721–741
8. Ma, F., Bajger, M., Slavotinek, J.P., Bottema, M.J.: Two graph theory based methods for identifying the pectoral muscle in mammograms. Pattern Recognition **40** (2007) 2592–2602
9. Hong, B.W., Brady, M.: A topographic representation for mammogram segmentation. In: In MICCAI 2003. (2003) 675–695
10. Boykov, Y., Veksler, O., Zabih, R.: Fast approximate energy minimization via graph cuts. IEEE TPAMI **23** (2001) 1222–1239
11. Yedidia, J., Freeman, W.T., Weiss, Y.: Understanding belief propagation and its generalizations. In: IJCAI 2001. (2001)
12. Liu, X., Veksler, O., Samarabandu, J.: Order-preserving moves for graph-cut-based optimization. IEEE TPAMI **32** (2010) 1182–1196
13. Felzenszwalb, P.F., Veksler, O.: Tiered scene labeling with dynamic programming. In: CVPR 2010. (2010)
14. Byng, J.W., Boyd, N.F., Fishell, E., Jong, R.A., Yaffe, M.J.: The quantitative analysis of mammographic densities. Physics in Medicine and Biology **39** (1994) 1629–1638

Chest Wall Segmentation in Automated 3D Breast Ultrasound Using a Cylinder Model

Tao Tan[1], Bram Platel[2], Henkjan Huisman[1], and Nico Karssemeijer[1]

[1] Department of Radiology, Radboud University Nijmegen Medical Centre, the Netherlands
[2] Fraunhofer MEVIS, Bremen, Germany

Abstract. In this paper, we present an automatic method to segment the chest wall in automated 3D breast ultrasound (ABUS) images. We show that the visible part of the chest wall in a 3D breast ultrasound image can be accurately modeled by a cylinder. We fit the surface of our cylinder model to a set of automatically detected rib-surface points. The detection of the rib-surface points is done by a classifier using features representing local image intensity patterns and presence of rib shadows. Due to attenuation of the ultrasound signal, a clear shadow is visible behind the ribs. Evaluation of our segmentation method is done by computing the distance of manually annotated rib points to the surface of the automatically detected chest wall. In our database of 66 ABUS scans, the average mean distance of the annotated points to the segmented chest wall was 4.58 mm. By fitting the cylinder model to the manually annotated points an average distance of 1.93 mm was obtained, providing evidence that reasonable accuracy can be obtained with this model.

Keywords: chest wall segmentation, automated 3D breast ultrasound, cylinder fitting

1 Introduction

As a complementary modality to mammography, breast ultrasound has a high specificity [1] and its sensitivity can surpass that of mammography for patients with highly dense breast tissue[2]. Regular two dimensional breast ultrasound, however, suffers from operator dependence, a limited capability to visualize the entire breast and the whole procedure is time consuming.

Automated 3D breast ultrasound (ABUS) overcomes the drawbacks of 2D hand-held ultrasound (US). ABUS provides 3D ultrasound images of the breast from the skin line to the chest wall. The modality involves compression of the breast using a dedicated membrane and a wide transducer mounted in a scanning device. Fig. 1 shows a 3D breast image generated by ABUS.

For patients with dense breast tissue or for patients that are more susceptible to radiation induced breast carcinoma, ABUS might prove to be a suitable screening modality for breast lesions. However, the reading of these 3D breast ultrasound images is time consuming for radiologists. Therefore, computer-aided detection (CAD) is expected to play an important role in the future, as it has the potential to make reading more efficient and reduce reading errors.

Determining the location of the chest wall in ABUS images is necessary to remove detected CAD-candidates beyond the chest wall. Furthermore, the

ISBN: 978-87-981270-9-3

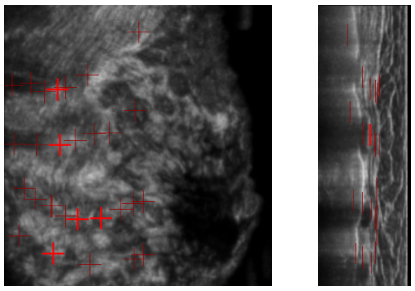

(a) (b)

Fig. 1. Manually annotated points on the surface of the ribs on coronal view(a) and sagittal view(b). The red cross are manually annotated points on rib surface, and the annotated points on the current slice are highlighted.

accurate localization of the chest wall can be of great help for inter- and intra-modal image registration algorithms[3].

In this paper we describe a novel method to accurately locate the chest wall.

2 Method

In previous related work, Huisman and Karssemeijer[4] investigated use of a deformable volume model to determine the chest wall location in ABUS images. The method was only partly validated by determining how well presence of a chest wall in a ABUS scan could be detected using a sheet detector. However, the performance of the method was limited.

In this paper we describe a new method to locate the chest wall. We use multiple features and classifiers to automatically detect points on the surface of the ribs. Subsequently a cylinder is fitted to the resulting point distribution. This cylinder models the local shape of the chest wall.

For training and validation we manually marked 20 to 30 rib surface points which are at the transition position between breast tissue and rib shadows for each scan (Fig. 1) of a series of 66 ABUS scans. All the images are generated using the automated breast ultrasound developed by U-systems, Inc. (SomoVu, Sunnyvale, CA, USA). Images were resampled to obtain 0.6 mm cubic voxels.

2.1 The chest wall as a cylinder

Our method is based on the assumption that the partial chest wall visible in an ABUS image can be modeled by the surface of a cylinder. To investigate if this conjecture is correct we fit the cylinder model to our manually annotated point sets for each of the 66 scans.

We use a non-linear optimization method [5] to fit a cylinder to the annotated points in 3D space and evaluate the validity of our assumption by observing the average distance of the annotated points to the fitted cylinder surface for each ABUS scan.

A cylinder in 3D space is fully defined by its radius R and its axis (center line). The axis in turn is defined by a point (x_c, y_c, z_c) and an orientation vector

ISBN: 978-87-981270-9-3

(v_x, v_y, v_z). To reduce the parameters of the cylinder, redundancy is removed by setting $z_c = 0$ and $v_z = 1$[6]. The normalized direction vector with length equal to 1 is denoted by (u_x, u_y, u_z).

Thus the parameter vector $\mathbf{p} = \{R, x_c, y_c, v_x, v_y\}$ fully defines the cylinder.

For any point (x, y, z) in 3D space, the closest point on the axis of the cylinder has coordinates (x_a, y_a, z_a) defined by

$$\begin{aligned} x_a &= x_c + D * u_x \\ y_a &= y_c + D * u_y \\ z_a &= z_c + D * u_z \end{aligned} \tag{1}$$

where $D = (x - x_c) * u_x + (y - y_c) * u_y + (z - z_c) * u_z$ which is the distance between the point (x_a, y_a, z_a) and (x_c, y_c, z_c) with $z_c = 0$. Therefore, given a set of annotated voxels (x_n, y_n, z_n) $(n = 1, 2, ..N)$ the averaged squared distance to the cylinder surface $ASD(\mathbf{p})$ can be computed by

$$ASD(\mathbf{p}) = \frac{1}{N} \sum_{n=1}^{n=N} (\sqrt{(x_n - x_a)^2 + (y_n - y_a)^2 + (z_n - z_a)^2} - R)^2 \tag{2}$$

where N is the number of annotated points.

We constrain the fitted cylinder by introducing a penalty term $P(\mathbf{p})$

$$P(\mathbf{p}) = w_1 * (\frac{v_x}{v_y})^2 + w_2 * (R - R_{mean})^2 \tag{3}$$

in which the first term of $P(\mathbf{p})$ ensures that the orientation of the cylinder remains close to the body axis (y is directed towards to head). The second term penalizes the deviation of the radius of the fitted cylinder from a predefined average radius R_{mean} related to local curvature of the chest wall. The parameters w_1 and w_2 define the weights for each term [1].

The total cost function $C(\mathbf{p})$ is defined by

$$C(\mathbf{p}) = ASD(\mathbf{p}) + P(\mathbf{p}) \tag{4}$$

We use Powell's optimization method [5] to find the minimum of the cost function $C(\mathbf{p})$.

The cylinder fitting method was applied to all 66 images. The average of the mean distance of the annotated points (reference standard) in each image to the fitted cylinder surface was 1.93 mm with standard deviation 0.66 mm. Given this small error we conclude that the surface of the chest wall in an ABUS scan can be approximated by the surface of a cylinder.

2.2 Chest Wall Segmentation

Our chest wall segmentation method consists of two stages: first, rib-surface points are identified and second, the previously described fitting procedure is used to fit a cylinder to these points. The extraction of rib-surface points involves two steps: the detection of rib shadows and the detection of the rib surface.

[1] In our work, we use $R_{mean} = 70mm$, which was an experimental estimate from our dataset. w_1 and w_2 were experimentally set to 100 and 25 respectively.

ISBN: 978-87-981270-9-3

Detection of Rib Shadows Due to strong attenuation of the ultrasound signal by the ribs, a shadow is cast behind them in the ABUS images (Fig. 1). The detection of these dark sheets aids us in localizing the rib-surface points. We use a set of features and a classifier to identify these rib shadows.

We apply a sheet detector to enhance the rib shadows in ABUS images. The sheet detector utilizes the eigenvalues and eigenvectors of the Hessian matrix.

We compute the elements of the Hessian matrix by convolving image $I(\mathbf{x})$ with the appropriate second order Gaussian kernel.

$$L(\mathbf{x}, \sigma) = I(\mathbf{x}) \otimes G(\mathbf{x}, \sigma) \tag{5}$$

where $G(x, \sigma)$ is the Gaussian filter and $L(x, \sigma)$ is the result of the convolution. The normalized Hessian matrix is defined as

$$H(\mathbf{x}) = \sigma^2 \begin{bmatrix} \frac{\partial L(\mathbf{x},\sigma)}{\partial x \partial x} & \frac{\partial L(\mathbf{x},\sigma)}{\partial x \partial y} & \frac{\partial L(\mathbf{x},\sigma)}{\partial x \partial z} \\ \frac{\partial L(\mathbf{x},\sigma)}{\partial y \partial x} & \frac{\partial L(\mathbf{x},\sigma)}{\partial y \partial y} & \frac{\partial L(\mathbf{x},\sigma)}{\partial y \partial z} \\ \frac{\partial L(\mathbf{x},\sigma)}{\partial z \partial x} & \frac{\partial L(\mathbf{x},\sigma)}{\partial z \partial y} & \frac{\partial L(\mathbf{x},\sigma)}{\partial z \partial z} \end{bmatrix} \tag{6}$$

where σ is normalization factor [1]. The eigenvalues of $H(\mathbf{x})$ are λ_1,λ_2 and λ_3 which correspond eigenvectors V_1, V_2, V_3 where $|\lambda_3| > |\lambda_2| > |\lambda_1|$. The dark sheet enhancement filter [7,4] is defined as:

$$DS(\lambda_1, \lambda_2, \lambda_3) = \begin{cases} \lambda_3 * e^{-(\lambda_1^2 + \lambda_2^2)} & \text{if } \lambda_3 > 0 \\ 0 & \text{if } \lambda_3 < 0 \end{cases} \tag{7}$$

The first eigenvector V_3 gives the direction of the greatest curvature. To make the operator more sensitive to sheets perpendicular to body axis or vertical direction, a weight factor F is calculated as the inner product between V_3 and body-axis vector $(0, 1, 0)$

Then, the directional dark shadow enhancement image (Fig. 2) is computed as

$$SH(\mathbf{x}) = DS(\mathbf{x}) * F \tag{8}$$

The shadow enhancement alone, however, is not specific enough. Therefore we use a number of additional features to further improve the detection of rib shadows. We use a set of features chosen to differentiate between the rather texture-less shadow region behind the ribs from the more texture rich region in front of the ribs. These features are

- image intensity (I)
- ($|Gz|$), the absolute value of the first order Gaussian derivative of the ABUS image in the depth direction (with scale 3 mm)
- the Laplacian (LP) of the ABUS image (with scale 3 mm)
- variance, skewness, and kurtosis of the image intensities within a cube of 729 mm^3 (15x15x15 voxels) centered at every voxel (VI, SI, KI)
- variance, skewness, and kurtosis of the image Laplacian values within the same cube (VL, SL, KL).

[1] σ is set to 3.6 mm which is estimated from average shadow width

ISBN: 978-87-981270-9-3

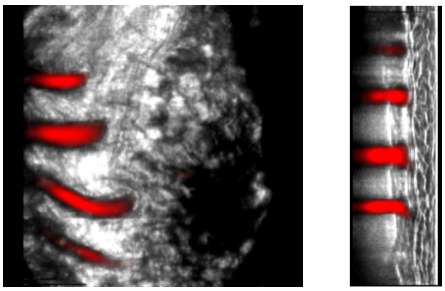

(a) (b)

Fig. 2. An ABUS image with dark shadow enhancement overlay (red). A coronal slice (a) and a sagittal slice (b) are shown.

Resulting in ten features per voxel: SH, I, Gz, LP, VI, SI, KI, VL, SL, and KL.

To compute the posterior probability that a voxel belongs to a rib shadow, we apply a two-class soft classifier using the features described above as input and using the manual annotations for training.

For the class of rib shadows we use the column of voxels below the annotated rib surface points. For the other class, we use a set of regularly spaced samples (2.4 mm in each direction) that are at least 10 mm above the chest wall (as defined by a fitted cylinder on the manually annotated rib-surface points).

We use an ensemble of five neural networks to classify this data. Each network consists of an input layer of n nodes representing the features, where n is the number of features, and a hidden layer of 8 hidden nodes and an output layer with one node. The final classifier output was computed by averaging the five network outputs. This output, $LS(\mathbf{x})$, is considered to represent the likelihood that a voxel is part of a rib shadow (Fig. 3).

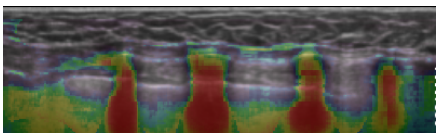

Fig. 3. A sagittal view image overlaid with the rib shadow likelihood LS. The probability ranges from blue (low) to red (high).

Detection of Rib Surface A second classifier is used to obtain the rib surface points. We use a set of features based on the ABUS image intensity and the previously described rib shadow likelihood image $LS(\mathbf{x})$. These features are

- $f1 : I(x, y, z)$ where $z = 0, 1, ..., N_z - 1$ and N_z is the number of voxels in the depth direction of the image
- $f2 : Gz_I(x, y, z)$ where $Gz_I(x, y, z)$ represents the first order Gaussian derivative in the depth direction on the original ABUS image (with scale 3 mm)

ISBN: 978-87-981270-9-3

- $f3 : Gz_{LS}(x, y, z)$ where $Gz_{LS}(x, y, z)$ represents the first order Gaussian derivative in the depth direction on the rib shadow likelihood image $LS(\mathbf{x})$ (with scale 3 mm)
- $f4 : \frac{\sum_{k>z} I(x,y,k)}{N_z - z - 1}$ which is the average intensity of voxels below the voxel
- $f5 : \frac{\sum_{k>z} LS(x,y,k)}{N_z - z - 1}$
- $f6 : \frac{\sum_{k<z} LS(x,y,k)}{z} - \frac{\sum_{k>z} LS(x,y,k)}{N_z - z - 1}$
- $f7 : z$ which the depth of a voxel.
- $f8 : dis_{np}(x, y)$ where $dis_{np}(x, y)$ is the distance of voxel (x, y, z) to the nipple in coronal view; the location of the nipple is automatically detected by using the Hough Circle Transform. This works well as the nipple in ABUS is visible as dark circle.

We use a classifier with the same settings as the classifier used in the previous step except that the classifier in this step has a input layer of 8 nodes based on the features computed above. For the class of rib-surface points we use the manually annotated points. For the non-rib voxels we we use a set of regularly spaced samples that are at least 10 mm away from the chest wall (as defined by a fitted cylinder on the manually annotated rib-surface points).

This classification yields a likelihood for each voxel $LI(x, y, z)$, representing the probability that a voxel belongs to rib surface (see Fig. 4).

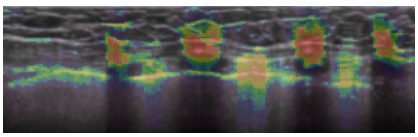

Fig. 4. An sagittal view image overlaid with the rib-surface likelihood LI. The probability ranges from blue (low) to red (high).

The rib-surface points are determined by thresholding image $LI(x, y, z)$ with threshold defined as the 98th percentile of all likelihood values in each image.

Cylinder Fitting to Detected Rib-Surface Points In this step, we fit our cylinder model to the detected rib-surface points in a similar manner as described in Sec. 2.1. However, this time we weight the contribution of each rib-surface point by its likelihood LI:

$$F(\mathbf{p}) = \frac{1}{N} \sum_{n=1}^{n=N} w(x_n, y_n, z_n)(\sqrt{(x_n - x_a)^2 + (y_n - y_a)^2 + (z_n - z_a)^2} - R)^2 \quad (9)$$

where $w(x_n, y_n, z_n)$ is defined as

$$w(x_n, y_n, z_n) = LI(x, y, z)^n \quad (10)$$

n is chosen to enhance the weight difference of rib-surface points with different likelihoods (n was experimentally set to 3).

Fig. 5 shows an example of chest wall segmentation using annotated points and detected rib-surface points respectively.

ISBN: 978-87-981270-9-3

Classifier Training We use two fold cross validation in our experiments. For each fold two classifiers are trained, one for the rib shadow detection and one for the rib surface points. These classifiers are then applied to the other fold for testing. Using this procedure bias is avoided.

3 Results

For the dataset of 66 ABUS scans, the average of the mean distance of the annotated points (reference standard) in each image to the fitted cylinder surface using detected rib-surface points was 4.58 mm with standard deviation 2.38 mm. Poor results were obtained in a few cases, as a result from too many false positives detected as rib-surface points in the second stage of classification. The worst case had a mean distance distance of 11.63 mm. Most false positives were due to posterior shadowing behind regions of dense tissue. A boxplot summarizes the result (Fig.6).

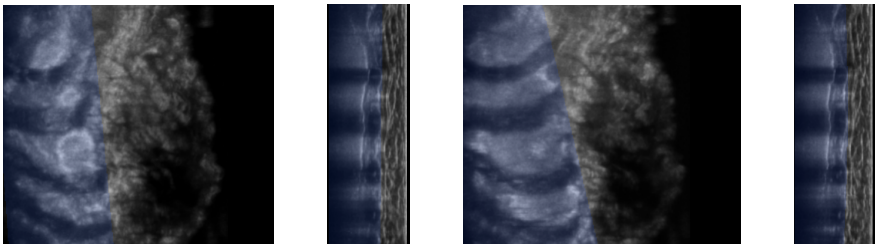

(a) (b) (c) (d)

Fig. 5. Example of chest wall segmentation. (a) and (b) show an ABUS image in coronal and sagittal view with the fitted cylinder model (blue overlay) obtained using manually annotated points. (c) and (d) show the result of the segmentation obtained by fitting the cylinder model to automatically detected rib-surface points, in coronal and sagittal view respectively.

4 Conclusion and Discussion

Our result in Section 2.1 demonstrate that the surface of the chest wall in an ABUS scan can be well approximated by the surface of a cylinder. Therefore we investigated an automated method to locate chest wall surface using this model. Using this the average of the mean distance of the annotated points to the segmented chest wall surface was 4.58 mm, which is promising for followup processing, such as computer-aided detection and inter- and intra-modal image registration. The result can also be used as a starting point for further refinement, for instance based on graph search methods [8].

Results show that the cylinder fitting suffers from false positives generated from rib surface detection. Therefore, for further improvement, false positives must be reduced by incorporating more robust features or by post-processing.

ISBN: 978-87-981270-9-3

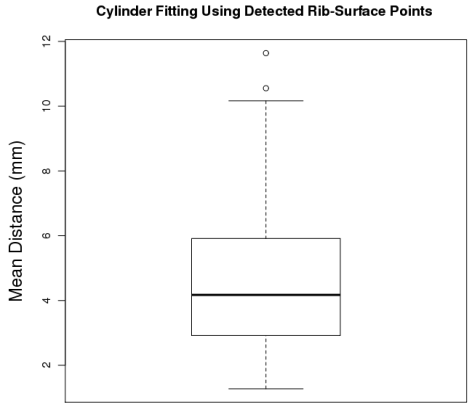

Fig. 6. Box plot of the mean distance of the annotated points (reference standard) in each image to the fitted cylinder surface using detected rib-surface points of 66 scans

References

1. N. Houssami, L. Irwig, J.M. Simpson, M. McKessar, S. Blome, and J. Noakes. Sydney breast imaging accuracy study: Comparative sensitivity and specificity of mammography and sonography in young women with symptoms. *AJR Am J Roentgenol*, 180(4):935–940, 2003.
2. W.A. Berg. Supplemental screening sonography in dense breasts. *Radiol Clin North Am*, 42(5):845–851, 2004.
3. C. Tanner, T. Carter, D. Hawkes, and G. Szkely. Cylindrical affine transformation model for image registration. *Medical Imaging of Proceedings of the SPIE 2010*, 7623:76232P–76232P–6, 2010.
4. H. Huisman and N. Karssemeijer. Chestwall segmentation in 3D breast ultrasound using a deformable volume model. *IPMI 2007*, LNCS 4584:245–256, 2007.
5. M.J.D Powell. An efficient method for finding the minimum of a function of several variables without calculating derivatives. *The Computer Journal*, 7(2):152–162, 1964.
6. http://www.nlreg.com/cylinder.htm.
7. Y. Sato, C. Westin, A. Bhalerao, S. Nakajima, N. Shiraga, S. Tamura, and R. Kikinis. Tissue classification based on 3D local intensity structures for volume rendering. *IEEE Transactions on Visualization and Computer Graphics*, 6(2):160–180, 2000.
8. M. K. Garvin, M. D. Abramoff, R. Kardon, S. R. Russell, X. Wu, and M. Sonka. Intraretinal layer segmentation of macular optical coherence tomography images using optimal 3-d graph search. *IEEE Trans Med Imaging*, 27(10):1495–1505, 2008.

ISBN: 978-87-981270-9-3

Seed selection criteria for breast lesion segmentation in Ultra-Sound images

Joan Massich[1] ⋆, Fabrice Meriaudeau[2], Elsa Pérez[3], Robert Martí[1], Arnau Oliver[1], and Joan Martí[1]

[1] Computer Vision and Robotics Group, University of Girona, Spain, jmassich@atc.udg.edu,
[2] University of Burgundy, Le2i Laboratory CNRS UMR 5158, Esplanade Erasme, 21000, Dijon, France
[3] Dept of Radiology, Hospital Josep Trueta of Girona, Spain.

Abstract. Purpose : Segmentation plays a central role in medical imaging, though is not a trivial task to perform in some screening modalities such as Ultra-Sound images. This paper addresses the role of automatic seed placement when segmenting breast lesions in B-mode Ultra-Sound images, and proposes a new algorithm to automatically locate seed regions for further region growing expansion.
Methods : In this work some state-of-the-art methodologies for seed placement are reviewed and a new method basing its region selection on assigning a probability of belonging to a lesion for every pixel depending on intensity, texture and geometrical constraints of the pixel is proposed.
Results : The proposed algorithm has been evaluated using a set of sonographic breast images with accompanying expert-provided ground truth, and successfully compared to other existing algorithms.
Conclusions : The experimental results show the performance and robustness of the method when placing seed regions in noisy environments.

Keywords: seed placement, ultra-sound, segmentation, breast cancer

1 Introduction

Breast cancer constitutes one of the leading causes of death for women in developed countries, and is most effectively treated when diagnosed at an early stage [11].

Taking this into account, Digital Mammography is still the most powerful screening tool for breast cancer [6]. However, some studies [12] have shown in a recent past that Ultra-Sound (US) images of the breast can provide useful complementary information in cases where the patients present dense glandular breast tissue, and a tumor presence can be shielded when using mammogram screening. In addition, US images is a non-expensive and non-invasive technique with no side effects, thus rendering sonography an attractive complement to

⋆ We gratefully acknowledge the help of Dr. Gururajan and Dr. Sari-Sarraf from Texas Tech University.This research was partially supported by the Spanish Government MEC grant nb. TIN2007-60553 and the University of Girona BR grant nb. 09/22

digital mammography and leading to a re-emergence of interest in image segmentation applied to ultrasound data [7] due to the segmentation's clinical value. Despite this, performing automatic segmentation in US images is a challenge because they often suffer from poor quality. US imaging tends to generate artifacts like weak edges produced by acoustic similarity between adjacent tissues, shadows presence when the signal gets completely attenuated preventing to screen any further, low contrast as a consequence of the US wave attenuation by the tissue media, or, speckle which is an unwanted collateral artifact coming from coherent interface of scatterers that appear as a granular structure superimposed on the image.

Due to segmentation's clinical value, the literature reports several techniques proposals for both guided and automatic segmentation of lesions in US images that try to overcome all the US screening inconveniences. Among those, region growing procedures that expand a seed accordingly to some criteria, have been reported to be suitable for US image segmentation [5, 4, 7]. However if seeds are not properly selected, the final segmentation results would be definitely incorrect.

This work uses an already stated framework for segmenting breast lesions in US images [5] in order to study the seed placement influence when segmenting and compare several seed selection procedures that can be plugged within such framework. This work also proposes a novel procedure combining texture and intensity features with geometric constrains. The framework has been tested with different seed selection procedures, against a data-set of sonographic images with accompanying expert-provided ground truth.

2 Seed Placement Background

Determining seed points on an US image that lead to a proper segmentation of breast lesion is not a trivial task, basically due to the noisy nature of the US images and the presence of other structures rather than lesions with similar acoustic properties (e.g. in some screening conditions, subcutaneous fat can be mistaken as a lesion). To achieve a fully automatic procedure, seeded segmentation methods require an automatic seed placement as well. The remaining of this section reviews some of those automatic procedures for selecting good seeds.

Pixel Rewarding method to select seed points (PR) Madabushi and Metaxas [4] proposed a method which rewards each pixel according to its position, intensity and texture using an assessment function. The main advantage of this pixel rewarding proposal remains in its spatially constrained seed rewarding along with the fact that the lesion's appearance is obtained by means of a learning step. On the other hand, its major disadvantage remains in choosing an appropriated neighborhood for the term representing the probability mean of the surrounding pixels when calculating the pixel reward. If the neighborhood used is too small, it might incorrectly reward a noisy region; otherwise, if the used neighborhood is too large, a proper seed can be hidden due to its neighbors' low recall.

Gradient-Based method to select seed points (GB) Drukker et al. [1] investigated the use of Radial Gradient Index (RGI) filtering technique to

ISBN: 978-87-981270-9-3

automatize Horsch et al. segmentation proposal [2] by adding automatic seed placement. Such seed placement uses the gradient as the only feature to select seeds by computing the maximum RGI [3] for all the pixels of the input image. RGI is a measure similar to Average Radial Derivative (ARD) coefficient that is used to drive the segmentation by Horsch et al. [2]. Summing up, every pixel is proposed as a potential lesion in order to determine which pixel would have the best reward, so the seed selection is deeply coupled to the segmentation procedure. Clearly, the main drawback of this seed selection is its computational cost, which was partially solved by means of subsampling techniques. However, due to the comprehensive nature of the seed determination, the method remains unadvisable for anything but offine applications.

Intensity Binarized ranked Regions method to select seed points (IBRR) Shan et al. [10] find candidate lesion regions based on intensity and rank them using the region properties; once the region is chosen, a seed point is determined within the selected region.

3 ITG: a novel seed region selection methodology

Both intensity and texture have been stated as a high specificity features when charaterizing breast lesions in US images [12]. In addition, the tendency of centering the lesions when acquiring the images by the radiologists has also been stated [4]. Figure 1 shows the proposed methodology which makes use of Intensity, Texture and Geometric constrains (ITG) and takes advantage of the mentioned statements in order to select a seed region for further region growing expansion. The proposal, combines the probability of a pixel being part of a lesion depending on its intensity, texture and position to generate a joint probability or total probability plane. Then the selection criterium selects the largest region of the connected pixels that satisfy a confidence level of being a lesion. So for selecting the best candidate regions, the probability plane gets thresholded in order to split the image with foreground and background. This thresholding has been empirically set at 0.8 as a good tradeoff between large foreground regions and low lesion belonging recall. Once determined the regions, the largest one gets selected as seed region.

Equation 1 illustrates the Joint probability calculation, where $\tau(x, y)$ indicates the total probability for a pixel (x, y) of being part of a lesion depending on its intensity i, texture t and position (x, y). Since intensity, texture and location

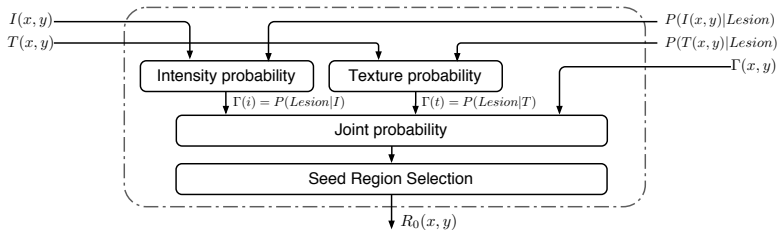

Fig. 1: Block diagram describing the seed region selection proposal.

ISBN: 978-87-981270-9-3

features can be assumed Independent and Identically Distributed (IID) [4], the total probability corresponds to the three features' probability product. The intensity probability $\Gamma(i)$ is computed from a Probability Density Function (PDF) determined during a training step necessary to compute $P(i|Lesion)$. $\Gamma(i)$ can be computed from the intensity PDF by the assumption of a Bayesian framework. $\Gamma(t)$ has the same nature as $\Gamma(i)$ and the texture PDF also needs to be determined during a training step. The seed location constrain $\Gamma(x, y)$ corresponds to a bivariate Gaussian function where the variances have been visually assessed and fixed at $\frac{1}{3}$ of the image size.

$$\tau(x, y) = \Gamma(i) \cdot \Gamma(t) \cdot \Gamma(x, y) \tag{1}$$

The texture measure used is given by equation 2 and corresponds to the difference between the pixel intensity $I(x, y)$ and the intensity mean of its N nearest neighbors (here an eight pixel neighborhood is used).

$$T(x, y) = I(x, y) - \frac{1}{N} \sum_{\delta=0}^{N-1} I_\delta(x, y) \tag{2}$$

In summary, the proposed methodology uses five inputs to automatically determine a seed region: the intensity image, the texture image, the intensity and texture PDFs, and the seed location prior; along with a fixed parameter to split the probability plane. Figure 2 illustrates all the steps involved during the course of action, where the upper row represents the procedure inputs (intensity, texture, geometrical constrains and learned PDFs), and the lower row shows the probability image for the intensity feature (e), for the texture feature (f), the total probability (g) and the final seed region selection (h). The final selected region (the largest) is depicted in magenta and the region candidates obtained when thresholding the probability plane are shown in cyan.

4 Experimental setup

The Gaussian Constraining Segmentation framework proposed by Massich et al. [5] has been used to test and evaluate the seed placement approach. Although such segmentation framework allows different user interation levels, as figure 3 depicts, only the fully automatic procedure has been used in this work. First, an initial region $R_0(x, y)$ is determined and then grown into a preliminary lesion delineation $R(x, y)$ that is used to obtain a multivariate Gaussian function describing the shape, position and orientation of the lesion ($G_{\mu\Sigma}(x, y)$). Finally the Gaussian Constraining Segmentation (GCS) procedure refines the segmentation by thresholding an intensity dependent function $\Psi(x, y)$ constrained by the multivariate Gaussian describing the lesion.

In order to evaluate the segmentations, Massich et al. [5] propose to use Simultaneous Truth and Performance Level Estimation (STAPLE) algorithm [13] to obtain the Hidden Ground Truth (HGT) from multiple expert delineations. Then use the μ-coefficient proposed as a variance of the True-Positive Ratio (TPR) or Jaccard coefficient that takes into accound the experts agreement by means of the HGT.

ISBN: 978-87-981270-9-3

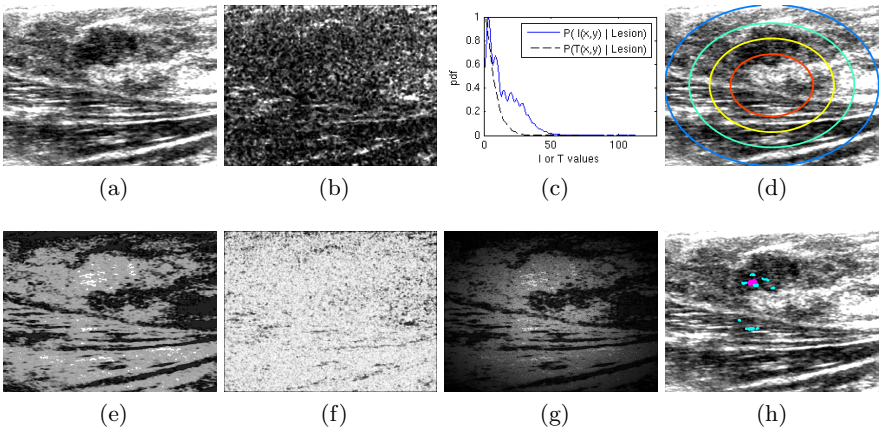

Fig. 2: Seed region selection illustration. (a) pre-processed intensity image (b) texture image (c) intensity and textureProbability Density Functions (d) seed location prior colored as overlay (e) $\Gamma(i)$ (f) $\Gamma(t)$ (g) total joint probability $\tau(x, y)$ (h) candidate regions (in cyan) and the final selected region (in magenta).

For evaluating purposes, a set of 25 sonograms were acquired in the *Hospital Dr. Josep Trueta* of Girona. Each image has seven ground truth delineations provided by different radiology experts. The training and testing of the data is obtained using a leave-one-out methodology.

4.1 Seed region location

When evaluating the seed selection, a key issue is to determine what defines a good seed in terms of the initial seed position. Figure 4a illustrates the ten Areas-of-Interest used in this case of study to test the influence of the lesion center distance and orientation. The Areas-of-Interest have been selected as: out

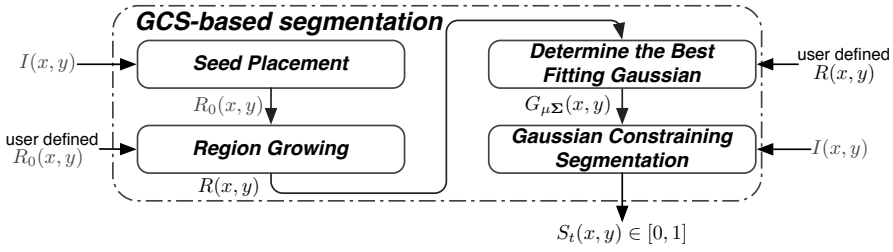

Fig. 3: Methodology block diagram. When user interaction is used (only for semi-automatic segmentation), it overwrites the previous input.

ISBN: 978-87-981270-9-3

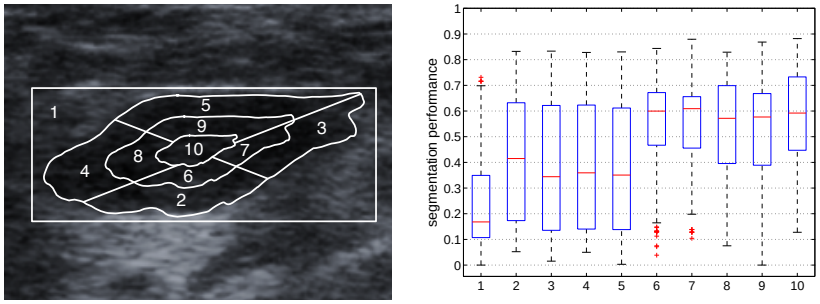

(a) (b)

Fig. 4: First experiment: (a) distribution of the seeds' regions, and (b) segmentation results in terms of μ-coefficient.

of the lesion (1), inside the lesion close to the boundaries (2-5), inside the lesion slightly shifted from the central part (6-9) and, central part of the lesion (10). Figure 4b shows the segmentation results for each Area-of-Interest according to the μ value. Each of the ten Areas-of-Interest has been randomly sampled with 15 seed regions. The boxplots clearly shows that achieving good segmentation results highly depends on locating the seed regions within the lesion (Areas-of-Interest 2 to 10). The figure also shows that the regions can be clustered in three main classes a to c: (a) Areas-of-Interest 6-10 that correspond to the inner lesion area, (b) 2-5 boundary area, and, (c) 1 anything outside the lesion. The results indicates that the better segmentation results are achieved when the seed is placed in (a), but not necessarily in the most inner region.

4.2 Methodology evaluation

As well to determine the role of the seed region location in terms of segmentation results, the proposed seed selection method has been evaluated by comparing to the methods referred in section 2: PR, GB and IBRR. Figure 5 illustrates the obtained results when comparing methodologies. The first plot (fig. 5a) shows the location of the selected seed regions along three areas based on the first experiment. The second plot (fig. 5b) illustrates the mean and variation of the final segmentation results for each methodology and area. Finally, figure 5c illustrates the performance distribution of each methodology regardless of which area the seed regions are placed. Notice that figure 5a is expressed in terms of the seeds distribution within the three groups of Areas-of-Interest while 5b and 5c refers to the μ coefficient to assess the final segmentation results.

Altough the PR and IBRR methods place more seeds in the central area than the proposed ITG method, the latter has the best performance in terms of final segmentation results when the seed is placed in the central area (a). The GB performance is not significant since its ability to place the seed regions within the (a) area is quite low, and most of the seeds fall outside the lesion.

ISBN: 978-87-981270-9-3

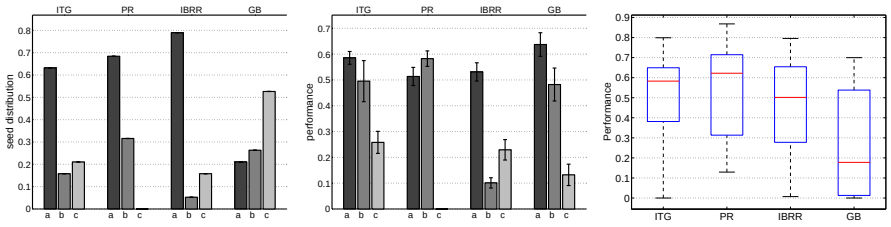

(a) (b) (c)

Fig. 5: Second experiment: comparison between the proposed method (ITG) and the PR, GB and IBRR methods. (a) seed region location (b) μ values depending on the seed location (c) global μ values.

4.3 Noise degradation

This experiment has been devoted to observe the seed placement evolution in challenging noisy scenario by repeating the segmentation on artificially degraded US images. The noise in US images mainly comes from scattering and reflection [9]. The structures present on a sonogram produce an adaptative coherent scatter comonly regarded as a Rician PDF [9], whereas the incoherent or diffuse scattering normally modeled as a Rayleigh PDF [9] leads to speckle artifacts. In order to obtain a fairly realistic US degradation, a percentage of the pixels from the image have been modified by a random walk of aleatory number of steps. For every step within the random walk, an amplitude and phase of the scatter have been simulated. Finally in order to eliminate the impulse nature of the added noise, a spacial correlation has been carried out [8]. From 0% to 100% of the pixels within the images have been alterated following the mentioned scheme by steps of 5%. Accordingly to the doctors, although some images have way more noise than the acceptable for diagnose purposes, the images seem to have been acquired with lower performing US imaging equipment. Figure 6e shows the ratio of seed regions placed within the 75% of the most inner area of the lesion between the ITG method and the PR and IBRR methods. Observe that for the proposed ITG method, values are mainly higher than 0.6 as for the IBRR method. Notice that previous experiments recalled that when the seed is properly placed ITG performs better than IBRR.

5 Conclusions

In this work, the importance of a good seed selection for a region growing like procedure has been stated. Some state-of-the-art seed placement procedures have been implemented, discussed and compared to a novel seed region selection proposal based on assessing the probability of belonging to a lesion for every pixel in the image depending on its intensity, texture and location and selecting the largest area obtained. The location of good seed regions on noisy environments has also been addressed, thus validating the performance and robustness of the methodology when placing seed regions in such noisy environments.

ISBN: 978-87-981270-9-3

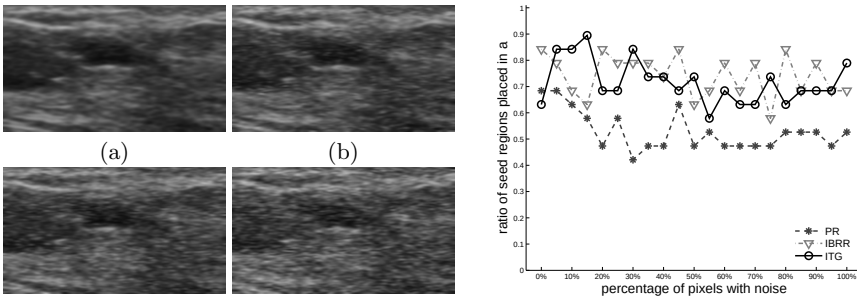

Fig. 6: Third experiment: seed placement performance on noisy enviroment. (a-d) same image with different amount $\{0, 20, 40, 80\}\%$ of added noise (e) ratio of correctly placed seeds at different noise levels.

References

1. Karen Drukker, Maryellen L Giger, Karla Horsch, Matthew A Kupinski, Carl J Vyborny, and Ellen B Mendelson. Computerized lesion detection on breast ultrasound. *Medical Physics*, 29(7):1438–46, Jul 2002.
2. K. Horsch, M.L. Giger, L.A. Venta, and C.J. Vyborny. Automatic segmentation of breast lesions on ultrasound. *Medical Physics*, 28:1652–1659, 2001.
3. M.A. Kupinski and M.L. Giger. Automated seeded lesion segmentation on digital mammograms. *IEEE Trans. Med. Imaging*, 17(4):510–517, 1998.
4. A. Madabhushi and D. Metaxas. Automatic boundary extraction of ultrasonic breast lesions. In *2002 IEEE International Symposium on Biomedical Imaging, 2002. Proceedings*, pages 601–604, 2002.
5. J. Massich, F. Meriaudeau, E. Pérez, R. Martí, A. Oliver, and J. Martí. Lesion segmentation in breast sonography. In *Digital Mammography*, volume 6136 of *LNCS*, pages 39–45, 2010.
6. SK Moore. Better breast cancer detection. *IEEE Spectrum*, 38(5):50–54, 2001.
7. J.A. Noble and D. Boukerroui. Ultrasound image segmentation: A survey. *IEEE Transactions on medical imaging*, 25(8):987–1010, 2006.
8. D Jones R Czerwinski and W. O'Brien. Edge detection in ultrasound speckle noise. *Image Processing*, Jan 1994.
9. J.M. Sandrick H. Lopez R.F. Wagner, S.W. Smith. Statistics of speckle in ultrsound b-scans. volume 30. IEEE Transactions on Sonics and Ultrasonics, 3 1983.
10. Juan Shan, H.D. Cheng, and Yuxuan Wang. A novel automatic seed point selection algorithm for breast ultrasound images. In *Pattern Recognition, 2008. ICPR 2008. 19th International Conference on*, dec 2008.
11. R. Sivaramakrishna, K.A. Powell, M.L. Lieber, W.A. Chilcote, and R. Shekhar. Texture analysis of lesions in breast ultrasound images. *Computerized medical imaging and graphics*, 26(5):303–307, 2002.
12. A.T. Stavros, C.L. Rapp, and S.H. Parker. *Breast ultrasound*. Lippincott Williams & Wilkins, 2004.
13. S.K. Warfield, K.H. Zou, and W.M. Wells. Simultaneous truth and performance level estimation (STAPLE): an algorithm for the validation of image segmentation. *IEEE Transactions on Medical Imaging*, 23(7):903–921, 2004.

ISBN: 978-87-981270-9-3

Segmentation of the Inner Breast Structures in 3D MRI

Yolanda H. Noorda[1], Sven Kabus[2], Lambertus W. Bartels[1], and Josien P.W. Pluim[1]

University Medical Center Utrecht, The Netherlands[1]
Philips Research Hamburg, Germany[2]

Abstract. Segmentation of the glandular and adipose tissue in 3D fat suppressed breast magnetic resonance images (MRI) is performed using a graph-cut scheme. When based on intensity only, the segmentation results are affected by bright shimming artifacts, that occur frequently in these images. To overcome this problem, this approach combines intensity information with spatial information.
The segmentations are performed on clinical data and on volunteer fat-suppressed 3D MRI scans. The clinical results are evaluated by comparing them to manually constructed ground truth segmentations, whereas the volunteer data are compared to fat-selective breast MRI scans.
The automatically generated results agree well with both manual delineations and fat-selective scans, with a mean Dice coefficient of 80% and 88%, respectively. It is clear that graph-cuts are a suitable approach for this segmentation task. By combining intensity information with spatial information, the influence of artifacts on the result is greatly reduced.

Key words: breast MRI, segmentation, graph-cuts, glandular tissue, adipose tissue

1 Introduction

The use of MRI for detecting breast cancer has been a relatively recent development. It has excellent detection sensitivity due to its superior soft tissue contrast. Segmentation of the inner breast structures (glandular and adipose tissue) on MRI images is useful for a variety of purposes, e.g. elastic registration of breast images, HIFU treatment of breast cancer and breast density analysis[1].

Separation of the glandular and adipose tissue has been done by using fuzzy c-mean classification (FCM) [1, 2]. Li *et al.* [3] used localized adaptive thresholding in every slice. In [4], a discriminant analysis method was used for this classification problem. Bakic *et al.* [5] used region growing together with interactive reconstruction by ramification matrices, to segment the glandular tissue. Unfortunately, in [1, 2, 5], user input is required and in [3–5], the segmentation results are not evaluated quantitatively against a ground truth segmentation.

In this paper, inner breast structure segmentation is accomplished by means of graph-cuts. Intensity information as well as spatial information is included,

ISBN: 978-87-981270-9-3

such that the segmentation will not be affected by artifacts. The results are evaluated using manually constructed ground truth segmentations as well as fat-selective MRI scans.

2 Materials and Methods

2.1 Data

Clinical examinations of patients older than 35 years comprised both 1.5T and 3.0T data. The 1.5T data consisted of 3D T1-weighted gradient echo transverse fat-suppressed MRI scans (Philips Achieva, TE/TR 2.2/4.6 ms, flip angle 10°, voxel size: 1 to 2 mm) of 20 patients. For each patient, one breast was selected randomly, some containg tumors. A seven-element SENSE-Breast coil was used.

For another eight patients, 3.0T 3D T1-weighted fast gradient echo transverse fat-suppressed MRI scans were available (Philips Achieva, (TE/TR 1.7/4.5 ms, flip angle 10°, voxel size: 0.65 x 0.65 x 0.80 mm^3), yielding 16 breast images. A four-element SENSE compatible phased-array bilateral breast coil is used.

In addition, for three young volunteers (± 25 years old), a 3D T1-weighted gradient echo transverse anatomical scan (TE/TR 3.4/6.9 ms, flip angle 10°, voxel size: 0.97 x 0.97 x 1.00 mm^3), with spectrally selective attenuated inversion recovery for fat suppression, as well as a 3D T1-weighted gradient echo scan (TE/TR 6.3/33.4 ms, flip angle 30°, voxel size: 0.97 x 0.97 x 1.00 mm^3), with ProSet water suppression were acquired. These fat-selective scans were made for evaluation only, and are not part of a standard clinical breast imaging protocol.

A volume of interest, roughly enclosing the breast, was selected automatically in all scans. For the 1.5T data set, these masks were created using an in-house toolkit, which is a combination of contour extraction and morphological operations. For the other data, masks were created by a combination of gaussian smoothing, histogram analysis and iterative thresholding.

2.2 Preprocessing: Skin and Muscle Removal

To be able to separate the glandular tissue from the adipose tissue, the skin and the breast muscle need to be removed from the image.

To extract the skin, an edge image is generated using a 3D Canny edge detector, on which morphological closing is performed to fill the double skin edge. For the final skin segmentation, a 3D Euclidean distance transform is applied to the breast volume. Each layer of the distance transform of which more than 50% of its voxels belong to the closing of the edge image, is labeled as skin. A constant skin thickness is assumed. To make sure that the skin will not contain holes, a one-layer gap is always filled. The adding of layers stops when two subsequent layers do not fulfil the criterion anymore.

To separate the breast muscle from the breast tissue, a boundary surface is found through the adipose tissue. Because the image is fat-suppressed, the surface is expected to have minimal total intensity value.

ISBN: 978-87-981270-9-3

The surface finding algorithm minimizes an energy term that consists of a distance measure $\mathcal{D}$, based on the voxel intensity values, and a curvature penalizer $\mathcal{S}$, depending on the second derivatives of the surface. Let (x, y, z) span a coordinate system such that z runs in the AP direction. The surface is then defined on the coronal grid (x, y), with $z := f(x, y)$ describing the height of the surface in AP direction. Let I be the 3D image, containing the intensity values. The purpose is to minimize:

$$\mathcal{J}[f] = \mathcal{D} + \rho\mathcal{S} = \frac{1}{2}\iint I(x, y, f(x, y))^2 \,\mathrm{d}x\,\mathrm{d}y + \rho\,\frac{1}{2}\iint \left(\Delta f(x, y)\right)^2 \,\mathrm{d}x\,\mathrm{d}y\ . \quad (1)$$

The parameter ρ governs the smoothing, and it is desired that the surface has minimal curvature. In practice, it was found that a value of $\rho = 10$ yielded the best results.

After skin and muscle removal, a volume of interest is left, containing the inner breast tissue. We will refer to this as the *breast tissue VOI*.

2.3 Separation of Glandular Tissue and Adipose Tissue

Graph-Cuts The image is represented by a graph, connected to a source and a sink, in which the image voxels are associated to the nodes of the graph. The nodes connected to the source/sink belong to the foreground/background, respectively. There are two types of edges in the graph: t-links between a node and the source or sink, and n-links between neighboring nodes. The strength of the t-links reflects the probability of a voxel belonging to the foreground or background, whereas the strength of the n-links is a measure of the similarity between two neighboring voxels. It is possible to set hard constraints if some voxels are known to be foreground or background.

The minimal cut through the graph is found by minimizing the energy function [6]:

$$E(A) = -\lambda R(A) + B(A)\ . \quad (2)$$

Here, A is a binary representation of a specific graph cut, $R(A)$ is a regional term, specified by the t-links that are cut by A, and $B(A)$ is a boundary term, specified by the n-links that are cut by A.

The implementation of Boykov *et al.* [7] is used for calculating the minimal cut.

Segmentation of the Glandular and Adipose Tissue using Intensity and Spatial Information In many breast MR images, shimming artifacts arise from insufficient fat suppression. Fig. 1 shows an example of an artifact occurring in a 1.5T image. These artifacts are very bright and often connected to the glandular tissue, causing glandular tissue to be labeled wrongly as adipose tissue. Therefore, the glandular tissue segmentation scheme consists of two steps. In the first step, the artifacts are segmented. This artifact segmentation is then used as a hard constraint in the second step to segment the glandular tissue.

ISBN: 978-87-981270-9-3

Both steps use an intensity prior P_I and a spatial prior P_S, which indicate the probability of a voxel being foreground or background, based on its intensity and its position, respectively.

The t-links for a voxel p are given by:

$$\begin{aligned} \text{t-link to source:} &= -\alpha \log\left(P_I(I_p|\text{bg})\right) - (1-\alpha)\log\left(P_S(p|\text{bg})\right) \\ \text{t-link to sink:} &= -\alpha \log\left(P_I(I_p|\text{fg})\right) - (1-\alpha)\log\left(P_S(p|\text{fg})\right) \ , \end{aligned} \tag{3}$$

where the parameter α governs the influence of the two priors.

For the intensity prior P_I, intensity histograms are obtained by mixture of Gaussians modeling. The mean intensity and the standard deviation have to be specified for each structure.

The mean value and standard deviation of the glandular tissue and the adipose tissue are estimated by iterative thresholding on the *breast tissue VOI*, where the largest connected component of the foreground is taken as glandular tissue. This is true in general, only in exceptional cases, where there are larger regions of artifacts than glandular tissue, this could give a problem.

The mean value of the artifacts is estimated at 10% above the mean value of the glandular tissue, with the same standard deviation. All probabilities (P_I and P_S) have been normalized.

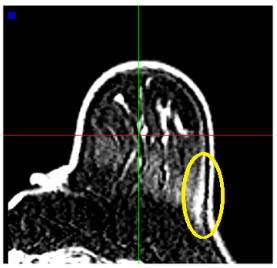

Fig. 1. Artifact in breast MRI image

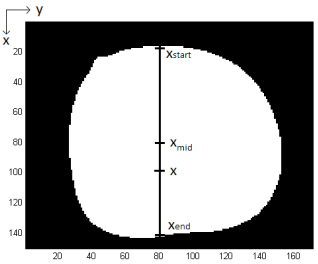

Fig. 2. Defining the spatial prior

In the first step (segmentation of the artifacts), the foreground intensity probability for a voxel p, $P_I\left(I_p|\text{fg}\right)$, is modeled by the Gaussian model of the artifacts. The background intensity component $P_I\left(I_p|\text{bg}\right)$ is modeled by combining the normalized Gaussians $\mathcal{G}\left(p,\mu,\sigma\right)$ of the glandular and adipose tissue, assuming the amount of adipose tissue is twice as large as the amount of glandular tissue. This is not always the case, but works as a rough estimate.

$$\begin{aligned} P_I\left(I_p|\text{fg}\right) &= \mathcal{G}\left(I_p, \mu_{\text{art}}, \sigma_{\text{art}}\right) \\ P_I\left(I_p|\text{bg}\right) &= \mathcal{G}\left(I_p, \mu_{\text{fat}}, \sigma_{\text{fat}}\right) + 0.5\ \mathcal{G}\left(I_p, \mu_{\text{gland}}, \sigma_{\text{gland}}\right) \end{aligned} \tag{4}$$

The artifacts are known to be found in the extreme cranial and caudal slices. The spatial prior P_S is therefore based on the normalized distance of a voxel to

ISBN: 978-87-981270-9-3

the center in CC-direction in each coronal slice (x runs in CC-direction, y runs in LR-direction):

$$P_S\left(p|\text{fg}\right) = \left(\frac{x - x_{\text{mid}}\left(y\right)}{r(y)}\right)^2 \qquad P_S\left(p|\text{bg}\right) = 1 - P_S\left(p|\text{fg}\right) \ , \tag{5}$$

with $x_{\text{mid}} = \frac{1}{2}\left(x_{\text{end}} - x_{\text{start}}\right)$ and $r(y) = x_{\text{end}}(y) - x_{\text{mid}}(y)$ (see Fig. 2). The weights $B_{p,q}$ for the n-links between neighboring voxels p and q are prescribed by:

$$B_{p,q} = \exp\left(-\frac{\left(I_p - I_q\right)^2}{2\sigma^2}\right) \ . \tag{6}$$

The constant λ in (2) is set to 1 and the constant α in (3) is set to 0.7.

In the second step, the result of the artifact segmentation is used for glandular tissue segmentation. This time, the skin is given as a hard constraint, by setting the t-links to 0 and infinity, to stimulate labeling of the artifacts as background. The foreground is modeled by the Gaussian of the glandular tissue, while the background is modeled by a weighted combination (determined experimentally) of the Gaussians of the adipose tissue, skin and artifacts:

$$\begin{aligned} P_I\left(I_p|\text{fg}\right) &= \mathcal{G}\left(I_p, \mu_{\text{gland}}, \sigma_{\text{gland}}\right) \\ P_I\left(I_p|\text{bg}\right) &= \mathcal{G}\left(I_p, \mu_{\text{fat}}, \sigma_{\text{fat}}\right) + 0.2\ \mathcal{G}\left(I_p, \mu_{\text{skin}}, \sigma_{\text{skin}}\right) + 0.15\ \mathcal{G}(I_p, \mu_{\text{art}}, \sigma_{\text{art}}) \ . \end{aligned} \tag{7}$$

A 3D distance transform D is calculated on the artifact segmentation. Its values are made to range from 0 to 0.7, yielding a foreground probability of 0 for voxels belonging to the artifact, and a maximum probability of 0.7 for voxels located far from the artifact. The values need to be limited to this range, to make sure that the adipose tissue can still be labeled as background. The spatial prior is calculated using this distance transform:

$$P_S\left(p|\text{fg}\right) = \left(D\left(p_x, p_y, p_z\right)\right)^\tau \qquad P_S\left(p|\text{bg}\right) = 1 - P_S\left(p|\text{fg}\right) \ . \tag{8}$$

The distance transform is taken to the power of τ, which has to be very small (e.g., 0.05), to yield a steep descent near the boundaries.

The t-links are given by (3), with $\alpha = 0.6$. The n-links are given by (6). The parameter λ in (2) is set to 1.5.

The largest connected component of the foreground is labeled as glandular tissue and the background as adipose tissue (including the artifacts, which are indeed adipose tissue, but not the skin, which had already been labeled).

Glandular Tissue Segmentation Based on Intensity only. For comparison, the glandular tissue is also segmented by taking only intensity information into account (α=1 in (3)). This time, intensity histograms are obtained from the initial estimate directly, since no assumptions need to be made about the artifacts. The skin is used as a hard constraint.

To increase the weight of the hard constraint, the boundary term needs to be of high influence. Therefore, the constant λ in (2) has to be small and is set to 0.8. However, this can lead to an undersegmentation of the glandular tissue.

ISBN: 978-87-981270-9-3

3 Results

For evaluation of the clinical data, 28 ground truth segmentations of the glandular tissue were created semi-automatically prior to method development by the first author. The volunteer fat-selective scans were normalized and thresholded at 0.2 to serve as ground truth segmentations for the volunteer data.

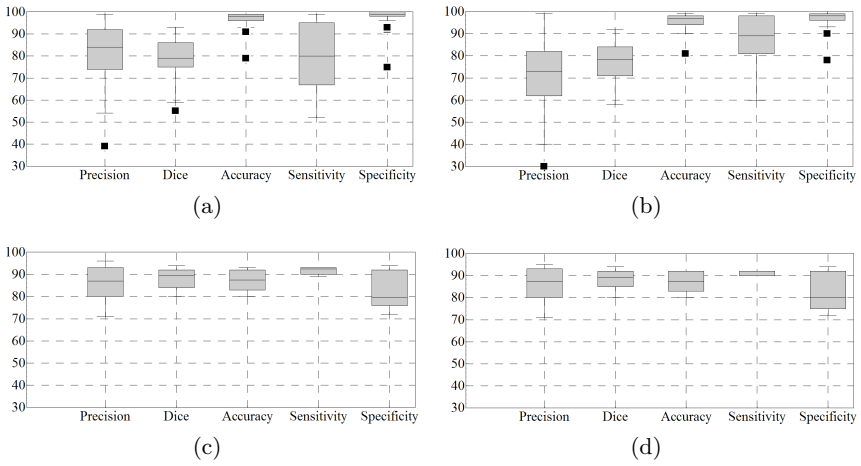

Fig. 3. Evaluation of the clinical glandular tissue segmentation by manually constructed ground truth segmentations (a and b), and evaluation of the volunteer adipose tissue segmentation by fat-selective scans (c and d). Results are based on intensity and spatial information (a and c), and on intensity only (b and d). The length of the whiskers is maximally 3/2 interquartile range.

The evaluation of the glandular tissue segmentations by the manually constructed ground truth segmentations and the evaluation of the adipose tissue segmentation by the fat-selective scans are shown in Fig. 3.

The performance on the clinical data is similar at 1.5T and 3.0T. Accuracy and specificity are high for the clinical data (mean value of 80% and 98%, respectively), mainly due to the relatively large background, consisting of adipose tissue. However, the sensitivity measures are also high (mean value of 81%), indicating that almost all true glandular tissue voxels are segmented correctly. When parts of the artifacts are still included in the segmentation, the number of false positives will be high, explaining the lower value for the precision when only intensity is considered (mean of 72% vs 80%). The Dice coefficient serves as an overlap measure. The glandular tissue contains many thin structures, which are challenging to segment by hand. Therefore, it is likely that the manual segmentation is not completely accurate. Taking this into account, the value of the similarity index (mean of 80%) is good. Including a spatial prior is a benefit for the precision, since it will lower the number of false positives. However, due to undersegmentation, the sensitivity values will decrease (mean of 81% vs 88%).

ISBN: 978-87-981270-9-3

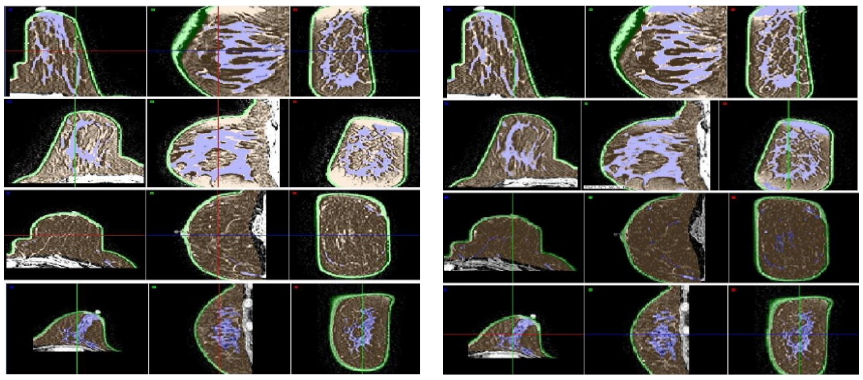

(a) Based on intensity and spatial information.

(b) Based on intensity only.

Fig. 4. Results of total segmentation on four 1.5T images with colored overlays (axial, sagittal and coronal view): skin = green, glandular tissue = blue, adipose tissue = orange, muscle = unlabeled)

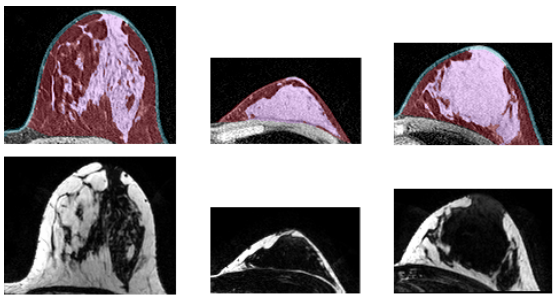

Fig. 5. Segmentation results and fat-selective scans for volunteers (skin = blue, glandular tissue = purple, adipose tissue = red)

The results on the volunteer data generally show a higher sensitivity (mean value of 92%) than accuracy (87%) and specificity (82%), since the foreground (adipose tissue) is large with respect to the background (glandular tissue). The results do not depend on the use of a spatial prior, because the artifacts did not occur in the volunteer data. Performance on the volunteer data is better than on the clinical data, since the acquired scans were of higher quality.

It is shown that the method performs well on all scans. However, evaluation by fat-selective scans is more objective than manual delineation. Therefore, this evaluation method is more reliable.

In Fig. 4, a few typical results of the glandular and adipose tissue separation on the clinical data are shown. In Fig. 5, segmentation results of the volunteer data and the corresponding fat-selective scans are shown.

ISBN: 978-87-981270-9-3

4 Conclusion

Segmentation of the inner breast structures was performed in 3D MRI images. Glandular tissue and adipose tissue have been separated by means of a graph-cuts scheme. The results indicate that this approach is suitable for this particular segmentation task. Even though many parameters have been determined experimentally, the method is robust for different subjects and scans.

The glandular tissue segmentations on clinical scans have been compared against ground truth segmentations yielding succesful results. In addition, the adipose tissue segmentations on volunteer scans have been evaluated by fat-selective MRI scans, yielding even better results. Including a spatial prior helps to avoid artifacts in the adipose tissue from being labeled as glandular tissue.

In the future, further research should be directed to obtaining better input features (better estimation of the intensity distributions, a more accurate spatial prior). In addition, adding more features (e.g., age, patient history, breast volume) might improve the segmentation results, by using them to estimate the parameters of the method.

Acknowledgments This work was financially supported by the project MEDIATE (Patient-Friendly Medical Intervention) in the framework of the EU research programme ITEA (Information Technology for European Advancement).

References

1. Nie, K., Chen, J.H., Chan, S., Chau, M.K., Yu, H.J., Bahri, S., Tseng, T., Nalcioglu, O., Su, M.Y.: Development of a Quantitative Method for Analysis of Breast Density Based on Three-Dimensional Breast MRI. Med. Phys. 35, 5253–5262 (2008)
2. Carballido-Gamio, J., Klifa, C., Majumdar, S., Hylton, N.: Application of a Fuzzy Inference System to the Quantification of 3D Magnetic Resonance Imaging of Breast Tissue. In: Fitzpatrick, J.M., Sonka, M. (eds.) Proc. SPIE Med. Imaging 2004, vol. 5370, pp. 1539–1547 (2004)
3. Li, L., Chu, Y., Salem, A.F., Clark, R.A.: Image Segmentation and 3D Visualization for MRI Mammography. In: Sonka, M., Fitzpatrick, J.M. (eds.) Proc. SPIE Med. Imaging 2002, vol. 4684, pp. 1780–1789 (2002)
4. Li, H., Giger, M.L., Yuan, Y., Jansen, S.A., Lan, L., Bhooshan, N., Newstead, G.M.: Computerized Breast Parenchymal Analysis on DCE-MRI. In: Karssemeijer, N., Giger, M.L. (eds.) Proc. SPIE Med. Imaging 2009, vol. 7260, pp. 72600N–72600N-6 (2009)
5. Bakic, P.R., Rosen, M.A., Maidment, A.D.A.: Comparison of Breast Ductal Branching Pattern Classification Using X-Ray Galactograms and MR Autogalactograms. In: Reinhardt, J.M., Pluim, J.P.W. (eds.) Proc. SPIE Med. Imaging 2006, vol. 6144, pp. 614425-1–614425-10 (2006)
6. Boykov, Y., Funka-Lea, G.: Graph Cuts and Efficient N-D Image Segmentation. Int. J. Comput. Vis. 70, 109–131 (2006)
7. Boykov, Y., Kolmogorov, V.: An Experimental Comparison of Min-Cut/Max-Flow Algorithms for Energy Minimization in Vision. IEEE Trans. Pattern Anal. Mach. Intell. 26, 1124–1137 (2004)

ISBN: 978-87-981270-9-3

Fully automatic fibroglandular tissue segmentation in breast MRI: an atlas-based approach

Albert Gubern-Mérida[1], Michiel Kallenberg[2], Robert Martí[1], and Nico Karssemeijer[2]

[1] University of Girona, Spain
{agubern,marly}@eia.udg.edu
[2] Radboud University Nijmegen Medical Centre, The Netherlands
{m.kallenberg,n.karssemeijer}@rad.umcn.nl

Abstract. Breast density measurement is becoming important due to the relation of dense tissue and risk for developing breast cancer. In this work we develop a fully automatic approach which segments all the structures of the breast to achieve a final delineation of the fibroglandular tissue in Breast Magnetic Resonance Imaging (MRI). The method consists of a first step based on a Bayesian framework using atlas information for the separation of the thoracic area and pectorals from the breast. A second refinement stage by Linear Discriminant Classifier (LDA), which uses intensity for a voxel classification, was applied improving the breast tissues segmentations. The method was evaluated on 27 cases comparing the obtained results to manual segmentations. A Dice Similarity Coefficient (DSC) of 0.75 was obtained for fibroglandular tissue.

Keywords: breast MRI, fibroglandular, segmentation, probabilistic atlas

1 Introduction

Breast Magnetic Resonance Imaging (MRI) is becoming a widely used modality for breast cancer management, providing good tissue contrast between fibroglandular (or dense) and fatty tissues and a three-dimensional characterization of breast composition. Segmentation of the different structures that compose the breast is essential in order to perform an automatic analysis of such images. Related to the presented work, breast tissue density has been identified as an important risk factor for developing breast cancer, being four times larger in women with a breast density higher than 75%, compared to those with little or no density [3]. So far, only a few studies have reported breast density measurement or delineation using MRI [4, 8]. Most of these methods use a two-step approach, first segmenting the breast from the body before performing the dense and fatty tissue segmentation. It appears that segmenting the breast itself is not very easy. Complicating factors are the variation between pectorals of different

ISBN: 978-87-981270-9-3

patients and the similar intensities between the mentioned muscles and the fibroglandular tissue. Other works have focused on such problems delineating the whole breast [5] or finding the boundary between the pectoral muscles and the breast [11].

In this work we present a fully automatic multi-class two-step segmentation algorithm for breast MRI based on a probabilistic atlas to obtain an accurate segmentation of the fibroglandular tissue. Atlas-based segmentation is a powerful technique for automatic delineation of objects in volumetric images and it has been extensively used for MR brain image segmentation [1]. In this study, the atlas is used in a Bayesian framework to segment five classes: pectoral muscles, fatty and fibroglandular breast tissues, heart and lungs. This initial step allows to segment the breast from the rest of the body. In a second step, the segmentation of voxels previously labeled as fatty and dense tissue is refined using a Linear Discriminant Classifier (LDA) taking advantage of the high soft-tissue contrast in MRI.

Next sections describe the material employed (2), the preprocessing applied to the volumes (3.1), the development of the probabilistic atlas (3.2) and its incorporation in a Bayesian voxel classification framework in order to obtain the segmentation (3.3). Qualitative and quantitative results are shown in 4 and finally conclusions are given and discussed in 5.

2 Material

The data set used to construct the atlas and to evaluate the segmentation results consists of 27 pre-contrast T1-weighted MR breast scans obtained from different patients. Breast MRI examinations were performed on a 1.5 T system (Siemens 1.5T, Magnetom Vision), with a dedicated breast coil (CP Breast Array, Siemens, Erlangen). The pixel spacing differed between volumes with values ranging from 0.625 mm to 0.722 mm. The slice thickness was 1.3 mm and the volume size was 512 x 120 x 256 voxels. Patients were scanned in prone position.

In order to obtain ground truth, each MR volume was manually segmented by an experienced observer into 7 classes: background, fatty tissue, glandular tissue, pectoral muscles, lung area and the heart. The seventh class is the "other" class and refers the previous non-labeled voxels of the thorax. Annotations were done every 5-10 slices and linear interpolation was applied to obtain the complete labeling. When needed, and specially for heart, lungs and pectoral muscles, accurate manual delineation was performed. For the manual segmentation of background, fatty and fibroglandular tissue, thresholding was applied over regions of interest provided by the reader. Fig. 1 shows an example of a MRI slice on an axial view and the manual delineation of the mentioned classes. One should note the complexity of performing such ground truth annotations, where each volume takes approximately 45 minutes in a dedicated breast MRI annotation environment.

ISBN: 978-87-981270-9-3

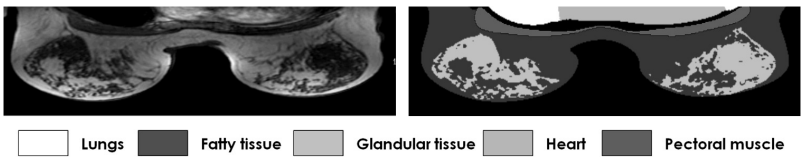

Fig. 1. MR scan on an axial slice of a clinical breast MR T1 weighted volume with the manual annotation of the different structures.

3 Methodology

3.1 Data preprocessing

Because of the inhomogeneity of the breast coil sensitivity, intensity values are corrupted. Signal intensity homogeneity is required because image artifacts can considerably affect registration and segmentation results. For this reason the first step of the methodology consisted of correcting inhomogeneities and variability between images. A bias field correction method using Mean-Shift [7] was applied to each scan. In addition, an image normalization algorithm based on histogram matching was applied to each volume in order to compensate for inter-patient signal intensity variability.

3.2 Construction of the atlas

Since neither previous work in atlas-based segmentation for the delineation of breast structures exists nor public breast MRI probabilistic atlases are available in the literature, a probabilistic atlas was built in this work. The main challenge of this step was to obtain an accurate probability distribution for the pectoral and the thoracic area to discriminate between the pectoral muscles and the fibroglandular tissue, which have similar signal intensity values. Following a leave-one-out evaluation strategy, for each patient segmentation, a full probabilistic atlas was built with the 26 remaining patients. These 26 patients and their segmentations were mapped into the same reference space and the probabilistic atlas was created by computing the frequency with which each location was labeled as a specific organ. A common reference space was used for all the experiments by selecting an extra patient that was not included in the evaluation data set. This extra image became the anatomical image of the atlas. The final smooth probabilistic atlas was obtained using a 3D Gaussian convolution with $\sigma = 7$ mm., which empirically appeared to be the best value to remove the probability distributions irregularities.

The mapping is composed by three different stages: initially the sternum of every patient is automatically localized and is used as a landmark to apply a first translation transform. As it is shown in figure 2.a the sternum is localized between both pectoral muscles. Hence, by accurately localizing the sternum, the pectoral muscles can be aligned. For the sternum landmark detection, we observed that the pectoral muscles border appears as the edge with maximum

ISBN: 978-87-981270-9-3

positive gradient in y direction. Taking advantage of this observation we implemented a first-derivative-based filter to detect the landmark point. Given an MR volume v, the first derivative volumes $v_x = \frac{\delta}{\delta_x} G_{\sigma_1}(v)$, $v_y = \frac{\delta}{\delta_y} G_{\sigma_2}(i)$, $v_z = \frac{\delta}{\delta_z} G_{\sigma_3}(v)$ were computed in each direction at different isotropic Gaussian scales: $\sigma_1 = \sigma_3 = 5$ and $\sigma_2 = 1$ mm. The final output s is given by the subtraction of $v_y - (v_z + v_x)$ in order to obtain higher values for the voxels that are on a strong edge in y direction. Figure 2 shows an example of the output. Finally, a search focused in a 3D region of interest (ROI) centralized on the volume was done computing the average y-coordinates where the output s is maximum.

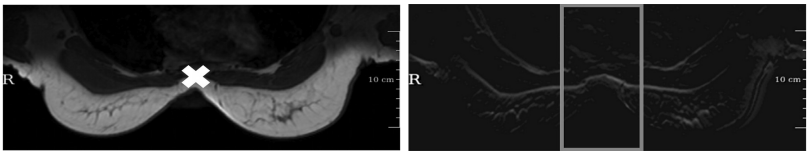

(a) (b)

Fig. 2. (a) MRI axial slice, with the sternum indicated with a cross, and (b) the output obtained applying the filter to detect the sternum point with 3D ROI.

The second mapping step consists of an affine registration focused on a Volume of Interest (VOI) of the upper part of the volume delimited by the sternum landmark to compensate for global differences of position and scale. The breast, which is a structure with high shape variability, is not considered here because it could mess up the thoracic cavity. Finally, a non-rigid registration based on B-Splines [10] was performed to the whole volume to minimize inter-individual variability in the shapes of the anatomical structures. The similarity measure maximized by the framework was Mutual Information (MI) in a multi-resolution scheme, using a stochastic gradient descent optimizer. For non-rigid registration, B-spline grid spacing of 32, 16, 10 and 8 mm was used for each of the 4 resolutions respectively. Elastix [6] was used for the implementation.

3.3 Segmentation

As we mentioned previously, the atlas is used to segment the anatomical structures of the breast MRI image in a first segmentation step based on a Bayesian framework. The approach is based on the work of Park et al. [9]. Figure 3 shows the general schema of the segmentation framework with Bayesian voxel classification algorithm incorporating the use of the probabilistic atlas. Note that, in order to reduce the number of voxels to be segmented, a region growing algorithm was initially applied slice by slice for a first approximation of the background segmentation. A morphological dilation filter with scale 5 x 5 mm was also performed to remove the skin line between the background and the breast.

In the following the true label image (the segmentation or set of labels) is denoted by X and the image (data set of intensity values) is denoted by Y.

ISBN: 978-87-981270-9-3

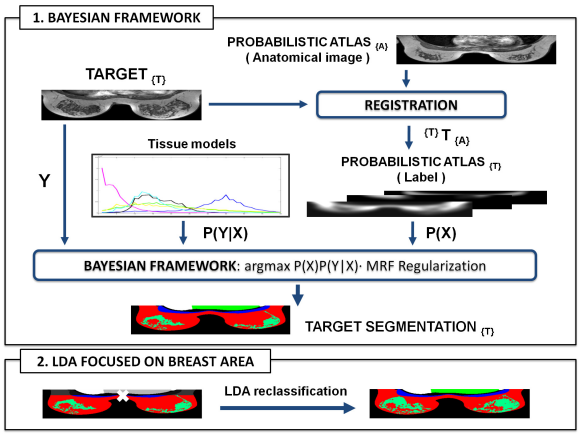

Fig. 3. Voxel classification algorithm overview: from top to bottom, the labels of the probabilistic atlas are mapped onto target image space {T} using the anatomical image of the atlas. The probabilistic atlas, the tissue models and the target are provided to the Bayesian framework as a prior probability $P(X)$, conditional probability $P(Y|X)$ and set of intensity values Y, respectively. The Bayesian framework estimates the segmentation X that maximizes $P(X)P(Y|X)$. Finally, LDA reclassification is done into the breast area defined by the sternum landmark.

Elements of X and Y are arranged by a spatial position denoted by $i \in I$, where I is the simple index (x, y, z) in a 3D rectangular grid. Sample space of X is denoted Ω_x where $\Omega_x = \{\mathrm{x} : x_i \in \{1, 2, ..., 7\}, \forall i \in I\}$. Labels 1-7 are background, fatty tissue, glandular or dense tissue, heart, lungs, pectoral muscles and "other" label respectively.

Segmentation can be formulated as the problem of estimating the label X that best explains the given observation Y according to some cost function. As a decision rule, MAP (maximum a posteriori) was chosen. Using Bayes theorem, the posterior probability to be maximized can be written as $P(Y|X)P(X)$. The probability distribution $P(Y|X)$ of the image Y, given a particular segmentation X, was specified by signal intensity tissue models directly built from the scans and manual segmentations of the data set. For each structure, a histogram of intensity values was computed from the corresponding voxels in the MRI volumes, using the manual segmentations. The probability distribution $P(X)$ is given by the probabilistic atlas once it has been mapped onto the target space using the same registration procedure used in its construction. A Markov Random Field (MRF) regularization is included to smooth the segmentation taking into account neighbourhood information.

In addition, a Linear Discriminant voxel Classification (LDA) based on intensity is performed to refine the segmentation of the fibroglandular tissue. The use of the atlas in the Bayesian approach gives reasonable segmentations for the thoracic area (lungs and heart), for the pectorals and for fatty tissue near the

ISBN: 978-87-981270-9-3

axillas, where the bias field is still present. However, since the fibroglandular tissue shows a high inter-patient variability which, in turn, induces larger registration errors in the breast area, the use of the probabilistic atlas framework for fibroglandular tissue leads to poor results compared to other classes such as pectoral segmentation. Hence, the segmentation refinement using a LDA classifier is performed focusing on the voxels located anterior to the sternum landmark and is based on reclassifying the voxels that were labeled as fatty or fibroglandular tissue in the first Bayesian step.

4 Results

In a leave-one-out experiment we evaluated the obtained segmentations with and without using the second breast refinement step (LDA classifier). The quality of the segmentation was measured by determining the similarity of the segmentation with the ground truth. For all the cases manual annotations were done in order to discard in the evaluation initial and last slices which do not contain relevant information or are clearly affected by noise. As a performance measure the Dice Similarity Coefficient (DSC) was chosen. Figure 4.a shows a box plot with DSC values for the patient segmentations of each organ. Segmentation results for heart (H), lungs (L) and pectorals (P) (DSC medians of 0.76, 0.83 and 0.74) do not change in the second step and they are not shown. DSCs values for segmentations of fatty and fibroglandular tissues (0.91 and 0.75 respectively) show that adding the second step based on breast LDA reclassification to the Bayesian framework (2) outperforms the first Bayesian step (p-values < 0.05, two-sided paired t-test). Overall, final segmentation results can be considered satisfactory for dense tissue and also for the other structures (normally a DSC > 0.7 is considered to be an acceptable segmentation [2]), which is illustrated by Fig. 4.b, where intermediate slices and their segmentations from 3 different patients are shown.

Focusing on the breast tissue, the main goal of this work, another evaluation criteria was used in order to analyze in detail where the misclassification errors are. Confusion matrices are shown for each of the experiments (see Tables 1.a and 1.b). Each cell (j, k), where j and k are the structures analyzed, shows the percentage of j voxels of the ground truth labeled as k in the segmentation. Background (B) and "Other" (O) classes are also shown.

There are two important aspects related to the the fibroglandular tissue segmentation: misclassification errors between dense and fatty tissue and errors between the dense tissue and pectoral muscles. Referring to the former, an improvement is observed. In the first framework, 44% of the voxels labeled in the ground truth as fibroglandular tissue are labeled as fatty. The LDA refinement decreases this percentage until a more acceptable 17%. For the differentiation between pectorals and dense tissue, both tables show that 7% of the voxels that are dense (groundtruth), are classified as pectoral by our method. However, only 1% of pectoral voxels are classified as dense.

ISBN: 978-87-981270-9-3

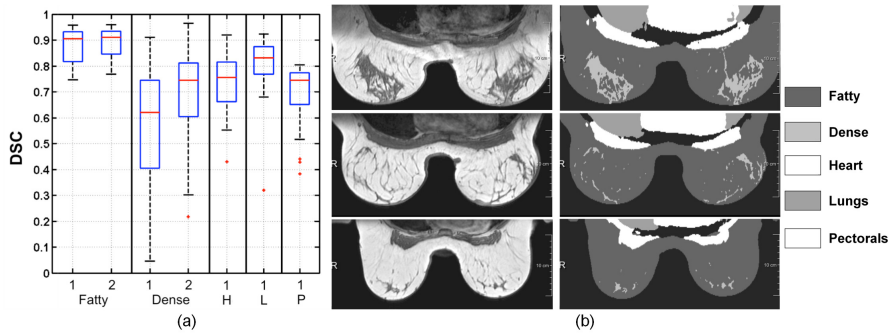

Fig. 4. Segmentation results: (a) Box plot with segmentation DSC values for each tissue after Bayesian approach step (1) and after the second LDA refinement step (2), and (b) intermediate slices from 3 different patients and their segmentation using Bayesian approach + LDA refinement.

Table 1. (a) Confusion matrices for Bayesian Classification approach using atlas and (b) for Bayesian classification approach using atlas + LDA for Fatty (F), Dense (D), Heart (H), Lungs (L), Pectoral (P), Background (B) and "Other" (O) classes.

SEGM.	GROUND TRUTH				
	F	**D**	**H**	**L**	**P**
F	**0.89**	0.44	0.00	0.00	0.04
D	0.01	**0.48**	0.00	0.00	0.01
H	0.00	0.00	**0.67**	0.02	0.00
L	0.00	0.00	0.02	**0.81**	0.00
P	0.02	0.07	0.01	0.02	**0.82**
B	0.06	0.00	0.01	0.03	0.01
O	0.02	0.01	0.29	0.12	0.12

(a)

SEGM.	GROUND TRUTH				
	F	**D**	**H**	**L**	**P**
F	**0.88**	0.17	0.00	0.00	0.04
D	0.02	**0.75**	0.00	0.00	0.01
H	0.00	0.00	**0.67**	0.02	0.00
L	0.00	0.00	0.02	**0.81**	0.00
P	0.02	0.07	0.01	0.02	**0.82**
B	0.06	0.00	0.01	0.03	0.01
O	0.02	0.01	0.29	0.12	0.12

(b)

5 Discussion and Conclusions

In this work we have presented a framework for fully automatic segmentation of fibroglandular tissue, using atlas information for the separation of the breast and the body. Firstly we constructed a probabilistic atlas by registering 26 patient data sets onto a single patient. Thereupon, we integrated it into a Bayesian framework with MRF regularization for segmentation of breast MRI structures, including a second step to refine the dense tissue segmentation by LDA.

Reasonable DSC medians of 0.76, 0.83 and 0.74 for heart, lungs and pectoral muscles were obtained respectively. For pectoral muscle segmentation, inter-observer variability was assessed by computing DSC values for 3 viewers using 8 manual segmentations from different patients. Median of 0.77 was obtained, close to the value given by our method. However, since the high variability of the dense tissue between patients, almost half of this tissue was segmented as fatty because the atlas-based method is not suitable to segment the fibroglandular

ISBN: 978-87-981270-9-3

tissue, due to its highly variable spatial distribution. The second step refinement on the breast area by LDA has been shown as important outperforming the fatty and fibroglandular tissues segmentation given by the Bayesian classification approach.

Further research will be focused on solving the problems we found that affect the pectorals and fibroglandular tissue segmentation results. We observed that incorrect pectoral muscles segmentation are given by the probabilistic atlas which does not overlap correctly with the pectoral area in cases which are really different compared with the reference selected space. Other registration algorithms and reference space selection methods will be studied. Concerning the breast delineation, skin folds which contain air are also segmented as dense tissue. This causes lower DSC values in fatty breasts since the number of false positives are much higher than the true positives. Future approaches will also take into account the segmentation of these areas separately.

References

1. Aljabar, P., Heckemann, R., Hammers, A., Hajnal, J., Rueckert, D.: Multi-atlas based segmentation of brain images: Atlas selection and its effect on accuracy. NeuroImage 46(3), 726 – 738 (2009)
2. Bartko, J.: Measurement and reliability: statistical thinking considerations. Schizophr. Bull. 17(3), 483 – 489 (1991)
3. Boyd, N., Guo, H., Martin, L., Sun, L., Stone, J., Fishell, E., Jong, A., Hislop, G., Chiarelli, A., Minkin, S., Yaffe, M.: Mammographic density and the risk and detection of breast cancer. N.Engl. J. Med. 356, 227–236 (2007)
4. C.Klifa, Carballido-Gamio, J., L.Wilmes, Laprie, A., Shepherd, J., Gibbs, J., Fan, B., Noworolski, S., Hylton, N.: Magnetic resonance imaging for secondary assessment of breast density in a high-risk cohort. Magnetic Resonance Imaging 28(1), 8–15 (2009)
5. Gallego, C., A.L.Martel: Automatic model-based 3d segmentation of the breast in mri. Proc. of SPIE 2011 7962 (2011)
6. Klein, S., Staring, M., Murphy, K., Viergever, M., Pluim, J.: Elastix: a toolbox for intensity based medical image registration. IEEE Transactions on Medical Imaging, 29(1), 196–205 (2010)
7. Makarau, A., Huisman, H., Mus, R., Zijp, M., Karssemeijer, N.: Breast mri intensity non-uniformity correction using mean-shift. In: Proc. of the SPIE 2010. vol. 7624 (2010)
8. Nie, K., Chang, D., Chen, J., Shih, T., Hsu, C., Nalcioglu, O., Su, M.: Impact of skin removal on quantitative measurement of breast density using mri. Med Phys 37(1), 227–233 (2010)
9. Park, H., Bland, P.H., Meyer, C.R.: Construction of an abdominal probabilistic atlas and its application in segmentation. IEEE Trans Med Imaging 22(4), 483–492 (2003)
10. Rueckert, D., Hayes, C., Studholme, C., Summers, P., Leach, M., Hawkes, D.J.: Non-rigid registration of breast mr images using mutual information. Proc. of MICCAI 1998 pp. 1144–1152 (1998)
11. Wang, L., Filippatos, K., Friman, O., Hahn, H.K.: Fully automated segmentation of the pectoralis muscle boundary in breast mr images. Proc. of SPIE 2011 7963 (2011)

ISBN: 978-87-981270-9-3

Pre-Treatment Prediction of Neoadjuvant Chemotherapy Response in Breast Cancer Patients Using DCE-MRI Kinetic Statistics

Ahmed B. Ashraf, Bilwaj Gaonkar, Angela DeMichele, Carolyn Mies, Christos Davatzikos, Mark Rosen, and Despina Kontos

The University of Pennsylvania, Philadelphia, PA 19104, USA,
Ahmed.Ashraf@uphs.upenn.edu

Abstract. The ability to predict response to neoadjuvant chemotherapy for women diagnosed with breast cancer, either before or early on in treatment, is critical to judicious patient selection and tailoring the treatment regimen. In this paper we investigate the role of kinetic features derived from breast DCE-MRI images for predicting treatment response. We present a set of kinetic statistics that differ significantly ($p < 0.05$) between complete responders and non-responders as assessed from imaging exams done prior to the treatment. Based on these features we learn a leave-one-out SVM classifier that performs with AUC=0.91 under the ROC curve. These findings suggest that DCE-MRI kinetic statistics can be used to improve candidate patient selection even before the start of the neoadjuvant treatment.

Keywords: Breast DCE-MRI, kinetic features, classification, neoadjuvant chemotherapy, therapy response prediction

1 Introduction

Use of neoadjuvant chemotherapy in women diagnosed with primary breast cancer is gaining considerable acceptance. It has been reported that neoadjuvant chemotherapy gives high clinical response of up to 70-98%, and can result in a pathologically complete response in 3-34% of patients, [1-4]. On the other hand, it has also been reported that 2-30% of patients may not benefit clinically or pathologically [5]. As a result, the ability to distinguish between highly responsive and non-responsive patients is of critical importance for making treatment choices. Particularly, non-responsive patients, if detected early on, can avoid unnecessary side-effects and can be routed to alternative therapies that may be more effective [5]. Traditionally, therapy response is evaluated by morphological, clinical, and histopathological assessment. Imaging modalities such as computed tomography (CT) and magnetic resonance imaging (MRI) are used to assess tumor response primarily on the basis of tumor size reduction. A notable criterion for therapy response assessment is the Response Evaluation Criterion in Solid Tumors (RECIST) [6]. However, volumetric changes in the tumor due to therapy tend to appear quite late in the course of the treatment. A response as assessed by a reduction in tumor size can cause considerable delay in giving the appropriate treatment to non-responsive patients. As a result devising methods for predicting early therapy response has been an active area of research in recent years.

ISBN: 978-87-981270-9-3

Among the work on early prediction of therapy response, Ah-See et al. [7] have reported correlations between changes in DCE-MRI kinetic parameters (primarily the rate coefficient, K^{trans}) and the final neoadjuvant chemotherapy response. However, the changes in kinetic parameters in the study presented in [7] had a predictive value after two cycles of neoadjuvant treatment. Moreover, the estimation of K^{trans}, that measures the degree of endothelial permeability, involves a series of assumptions and models derived from the pharmacokinetics of the contrast agent distribution [8]. This leads to different estimates of the parameter due to different underlying assumptions [9], making its estimate less robust. More recently Loo et al. [10] have explored the kinetics and morphology of contrast uptake for predicting a patient's response to neoadjuvant chemotherapy. However, like [7] the approach in [10] also becomes predictive at least after two cycles of chemotherapy treatment which, is also the case for other recent research reports [11]. In this paper, to further investigate the role of imaging as a biomarker for early response in treatment, we address the following two important questions:

(a) Whether imaging biomarkers can help predict therapy response *before* the commencement of the first cycle of neoadjuvant chemotherapy;
(b) Whether DCE-MRI kinetic features derived without modeling assumptions have enough predictive power to predict *a priori* response.

In order to answer the above we explore the kinetic inhomogeneities of the tumor. Specifically we suggest partitioning the tumor pixels into sets based on the similarity of their kinetic behavior (Section 3). We show that within these pixel partitions, the statistics of basic kinetic features (peak enhancement, wash-in-slope, wash-out-slope) differ significantly ($p < 0.05$) between the categories of complete responders and non-responders (Section 5). This analysis is based on breast DCE-MRI images captured *prior* to the treatment. We demonstrate that a support vector machine (SVM) classifier based on these kinetic statistics and using leave-one-out cross validation can predict complete versus non-complete responders with an AUC of 0.91 under the ROC curve (Section 5). These findings suggest that non-model based DCE-MRI kinetic statistics could serve as potential imaging biomarkers for predicting response to neoadjuvant chemotherapy even before the initiation of treatment.

We begin with a brief review of non-model based DCE-MRI kinetic features:

2 DCE-MRI kinetic features

Typically, DCE-MRI acquisition includes a pre-contrast image (captured prior to the injection of a contrast agent) and a number of post contrast images, captured at different time points after the injection of the agent. A usual way to quantify the enhancement pattern is to compute percentage enhancements relative to the pre-contrast image, [12]. By computing the relative enhancement on a pixel by pixel basis we can achieve pixel-wise maps of the contrast enhancement. For a particular pixel, the enhancement plotted as a function of time provides the kinetic curve. As reported in the literature (e.g., [13]), a number of basic features can be computed from this kinetic curve, inlcuding peak enhancement (PE), time to peak (TTP), wash-in-slope (WIS), wash-out-slope (WOS). Figure

ISBN: 978-87-981270-9-3

1(a) illustrates these features for a single pixel. From these, we can derive a rich kinetic feature set by computing the pixel-wise map for each feature as depicted in Figure 1(b).

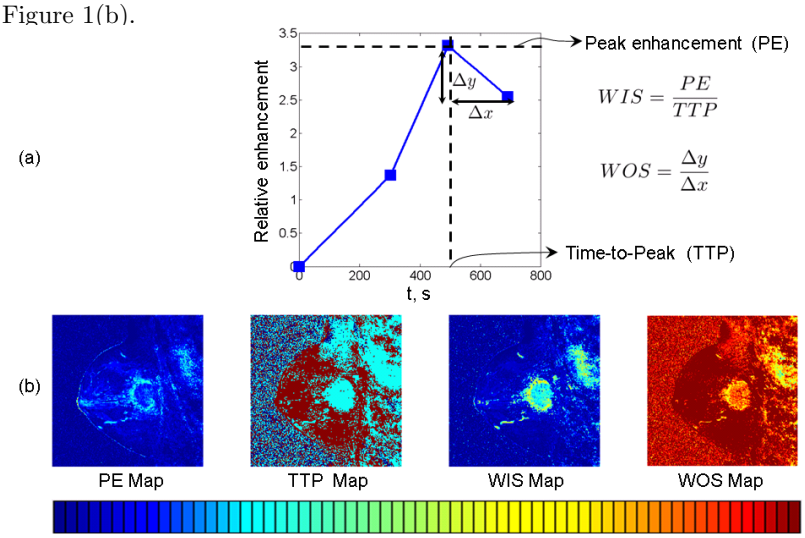

Fig. 1. (a) Illustration of basic kinetic features for a single pixel. (b) Pixel wise maps

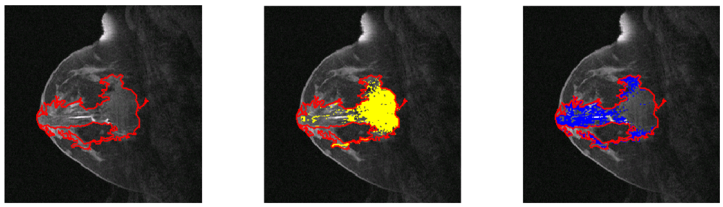

Fig. 2. Illustration of kinetic pixel partitioning for two post contrast time points. (a) Segmented lesion, (b) Set 1 pixels highlighted in yellow, (c) Set 2 pixels highlighted in blue

3 Kinetic partitioning of feature maps

The feature maps shown in Figure 1(b) can be partitioned into different sets based on their kinetic behavior. One way to better interpret the kinetic inhomogeneity is to divide the feature maps into clusters of homogeneity. Here we suggest partitioning the pixels based on their time-to-peak (TTP) value. This step partitions the pixels into as many sets as the number of post-contrast time points. As a result, set i consists of the pixels that achieve their peak enhancement at the i-th post contrast time point. In Figure 2, we illustrate these partitions for two post contrast time points.

3.1 Partition-wise kinetic statistics

Let $\mathcal{M}$ be the pixel partitioning such that $\mathcal{M}_k$ represents the membership mapping of pixel k to its respective set. Based on this partition we may derive the following set-wise statistics:

ISBN: 978-87-981270-9-3

• Posterior probability of observing Set i given the partition $\mathcal{M}$:

$$\mathcal{P}(\mathcal{S}et = i|\mathcal{M}) = \frac{1}{N}\sum_{k=1}^{N}\delta(\mathcal{M}_k = i)\ . \tag{1}$$

where $\delta(\mathcal{M}_k = i)$ is an indicator function that equals 1 when $\mathcal{M}_k = i$, and zero otherwise. N is the total number of pixels. These N pixels may come from an arbitrarily shaped segmentation mask specifying the lesion.

• Mean value of feature map j for Set i:

$$\mu(i,j) = \frac{\sum_{k=1}^{N} f_j(k).\delta(\mathcal{M}_k = i)}{\sum_{k=1}^{N}\delta(\mathcal{M}_k = i)}\ . \tag{2}$$

where $f_j(k)$ is the value of the j-th feature map for k-th pixel, and the feature map can be any of those shown in Figure 1(b).

• Variance of feature map j for Set i:

$$\sigma^2(i,j) = \frac{\sum_{k=1}^{N}(f_j(k) - \mu(i,j))^2.\delta(\mathcal{M}_k = i)}{\sum_{k=1}^{N}\delta(\mathcal{M}_k = i)}\ . \tag{3}$$

Based on the above definitions, m pixel partitions and n feature maps would result into a total of $m(2n+1)$ features. We aim to investigate the utility of these partition-wise kinetic statistics for the task of predicting response to neoadjuvant therapy.

4 Dataset

The study population consisted of a subset of patients enrolled in a multi-site trial of imaging biomarkers in neoadjuvant breast cancer therapy. The subset population consisted of 15 patients: 8 complete responders and 7 non-responders. All patients presented with biopsy-proven T2-3 stage tumors. The patients underwent standard neoadjuvant chemotherapy, which at the time of the study consisted of four cycles of adriamycin/cytoxan, followed by four cycles of taxotere. Local IRB approval was obtained prior to the study, and signed informed consent was obtained in all patients prior to enrollment. Core biopsy and serum samples were collected at comparable times to the MRI scans and obtained pre-treatment, (between 24 and 96 hours after the start of treatment), between treatment regimens (optional) and pre-surgery. Only pre-treatment imaging was used in the analysis presented in this paper. The treatment response and 3 year disease free survival data were collected.

MRI was performed on a 1.5T scanner (Siemens, Sonata©, Erlangen, Germany). Imaging included sagittal T1-weighted 3D volumetric imaging before and after administration of gadodiamide injection (Omniscan©, GEHealthcare). Imaging parameters were as follows: FOV 18-20 cm, matrix 512 × 256 (interpolated to 512 × 512), slice thickness 2mm, TR 27.0, TE 4.76, flip angle 45°. Pre-gadodiamide imaging was performed followed by immediate post-gadolinium images (at 2 minutes) and delayed post-gadodiamide images (at 7 minutes).

For each patient we selected the DCE-MRI exam done prior to the commencement of the treatment. Lesions were segmented in a semi-automated way

ISBN: 978-87-981270-9-3

by seeding an active contour snake [14]. For feature extraction the most representative slice in an image sequence was chosen as a slice for which the lesion area was maximized. Given a representative slice we computed the kinetic statistics defined in Section 3. For this dataset we had two post-contrast time points and based on the TTP values the pixels were partitioned into two sets ($m = 2$). Within these partitions we computed statistics for three feature maps ($n = 3$) i.e., PE, WIS, and WOS. This resulted in $m(2n + 1) = 14$ kinetic statistics. We also computed the following morphological features: tumor ellipticity [15], tumor circularity [16] (both being measures of shape irregularity), tumor area, and tumor perimeter. In all we had 14 kinetic features and 4 morphological features.

5 Classification experiments

Univariate feature analysis: To analyze the features described above we first performed a t-test analysis using leave-one-out cross validation. For each cross validation fold, we selected the features that differed significantly ($p < 0.05$) between the categories of complete responders and non-responders. In total, 12 out of the 14 kinetic features were selected, which persisted through all leave-one-out cycles. None of the morphological features was selected in any cross-validation fold. Box-plots for the 12 significant kinetic features are given in Figure 3. The ROCs for individual feature classifiers with respective AUCs are given in Figure 4 (AUCs range from 0.78 to 0.86). The univariate classification was based on simple thresholding on individual feature values. This analysis suggests that partition based kinetic statistics potentially possess univariate discriminatory power to distinguish between responders and non-responders from their pre-treatment images.

Multivariate classification: Based on the 12 significant kinetic features selected as a result of the univariate analysis we trained a leave-one-out linear SVM classifier. The SVM classifier was able to distinguish between responders and non-responders with an AUC=0.91 under the ROC curve (Figure 5), improving on the best univariate classifier reported above (AUC: 0.86).

6 Discussion

In this paper we have demonstrated that the statistics derived from the kinetic partitioning of DCE-MRI feature maps (peak enhancement, wash-in-slope, and wash-out-slope) are significant predictors of response to neoadjuvant chemotherapy. We have shown that these statistics have predictive power even when derived from a DCE-MRI exam done prior to the commencement of the treatment. This ability can help in selecting the patients that are expected to benefit the most from the treatment, while routing the anticipated non-responders to alternative therapies without the unnecessary exposure to neoadjuvant treatment. Moreover the kinetic statistics presented here are computed without any modeling assumptions.

Compared to the kinetic features, morphological descriptors demonstrated poor performance. In this paper we have focused on images captured before the treatment begins. As such our results suggest that those morphological features

ISBN: 978-87-981270-9-3

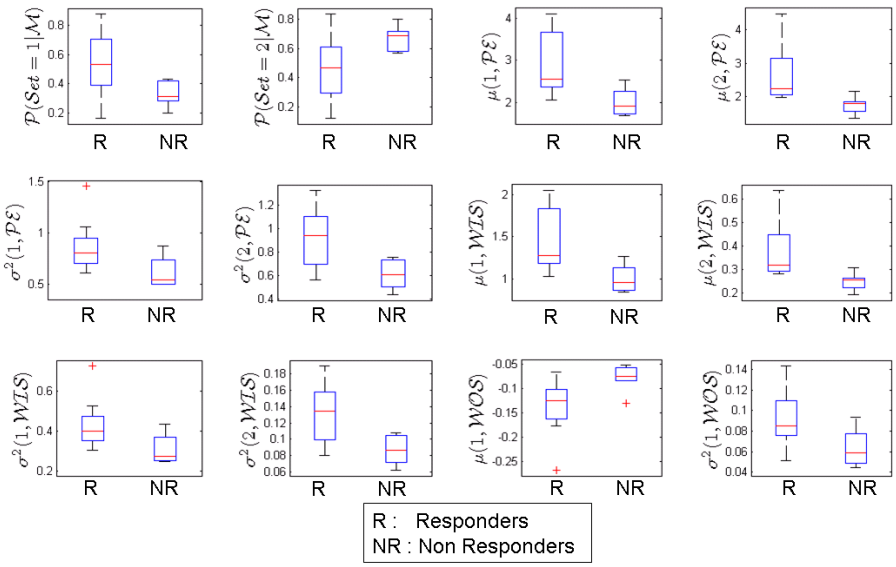

Fig. 3. Box plots for kinetic features that differed significantly (t-test, $p < 0.05$) between the categories. The y-axis shows the respective feature following the notation of Equations 1–3. e.g. $\mu(1, PE)$ represents the mean feature map value of peak-enhancement for Set 1 pixels.

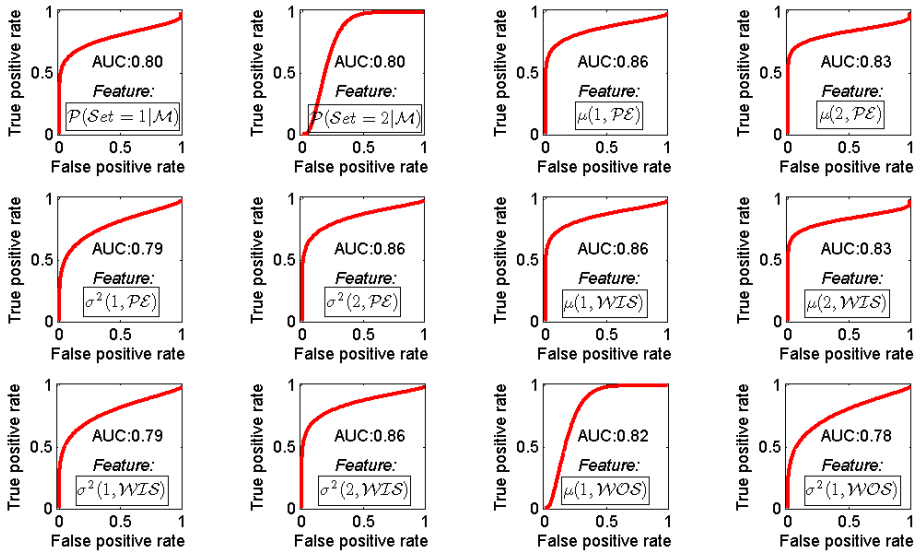

Fig. 4. ROC curves for univariate classifiers.

ISBN: 978-87-981270-9-3

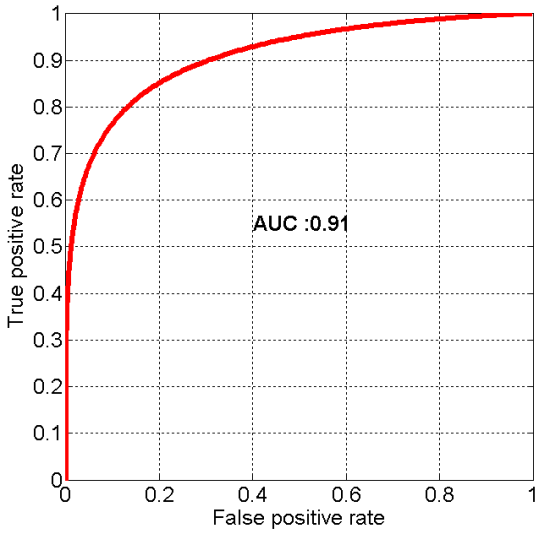

Fig. 5. ROC curves for the multivariate classifier.

fail when presented with the task of predicting therapy response based on a single snapshot of pre-treatment imaging. As the treatment progresses, changes in the morphology during the actual treatment process, rather than the *a priori* imaging on which we focus on this paper, can represent a measure of response as has been explored in other studies.

Two limitations of the current work must be noted. First, although promising, our analysis has been done on a relatively small dataset (15 patients) and therefore larger studies are warranted to confirm generalizability of our findings. Second, the features are currently extracted from a representative 2D slice of the primary lesion. Kinetic partitioning of the entire 3D volume of the lesion could potentially lead to richer statistics that may further improve the prediction of therapy response in the future.

References

[1] Rastogi P., Anderson S.J., Bear H.D., Geyer, C.E., Kahlenberg,M., Robidoux,A., Margolese, R., Hoehn, J., Vogel, V., Dakhil, S., Tamkus, D., King, K., Pajon, E., Wright, M., Robert, J., Paik, S., Mamounas, E., Wolmark, N.: Preoperative chemotherapy updates of National Surgical Adjuvant Breast and Bowel Project Protocols B-18 and B -27, JClin Oncol 26:778-785 (2008)

[2] Bonadonna G.,Valagussa P., Brambilla C., Ferrari, L., Moliterni, A., Terenziani, M., Zambetti, M.: Primary chemotherapy in operable breast cancer: eight-year experience at the Milan Cancer Institute. JClin Oncol, 16:93-100 (1998)

[3] Bear H.D., Anderson S., Brown A., Smith R., Mamounas E., Fisher B., Margolese R., Theoret H., Soran A., Wickerham D., Wolmark N.: The effect on tumor response of adding sequential preoperative docetaxel to preoperative doxorubicin and

cyclophosphamide: preliminary results from National SurgicalAdjuvant Breast and Bowel Project Protocol B-27. JClin Oncol 21:4165-4174 (2003)
[4] Makris A., Powles T.J., Ashley S.E., Chang J., Hickish T., Tidy V.A., Nash A.G., Ford H.T.: A reduction in the requirements for mastectomy in a randomized trial of neoadjuvant chemoendocrine therapy in primary breast cancer. Ann Oncol 9:1179-1184, 1998
[5] Smith I.C., Heys S.D., Hutcheon A.W., Miller I., Payne S., Gilbert F., Ah-See A., Eremin O., Walker L., Sarkar T., Eggleton S., Ogston K.: Neoadjuvant chemotherapy in breast cancer: significantly enhanced response with docetaxel. J Clin Oncol 20:1456-1466, 2002
[6] Hilton, N.: MR imaging for assessment of breast cancer response to neoadjuvant chemotherapy. Magn Reson Imaging Clin N Am.,14(3):383-389 (2006)
[7] Ah-See, M.L.W., Makris,A., Taylor,N.J., Harrison M., Richman P., Burcombe R., Stirling J., dArcy J.A., Collins D.J., Pittam M., Ravichandran D., Padhani A.R.:, Early changes in functional dynamic magnetic resonance imaging predict for pathologic response to neoadjuvant chemotherapy inprimary breast cancer, Clinical Cancer Research, 14(20):65806589, 2008
[8] Cha S., Yang L., Johnson G. Lai A., Chen, M.-H., Tihan T., Wendland M., Dillon W.: Comparison of microvascular permeability measurements,K_{trans}, determined with conventional steady-state T1-weighted and first-pass T2*-weighted MR imaging methods in gliomas and meningiomas. AJNR Am J Neuroradiol. 27:409417, 2006
[9] Tofts P.S., Brix G., Buckly D.L., Evelhoch J.L., Henderson E., Knopp M.V., Larsson H.B., Lee T.Y., Mayr N.A., Parker G.J., Port R., Taylor J., Weisskoff R.M.:. Estimating kinetic parameters from dynamic contrast-enhanced T1-weightedMRIof diffusable tracer: standardized quantities and symbols. J Magn Reson Imaging, 10:223232 (1999)
[10] Loo C.E., Teertstra H.J., Rodenhuis S., van de Viver M.J., Hannemann J., Muller S.H., Peteters M.J., Gilhuijs K.G.: Dynamic contrast-enhanced MRI for prediction of breast cancer response to neoadjuvant chemotherapy: initial results. AJR Am J Roentgenol. 191:13311338 (2008)
[11] Partridge S.C., Vanantwerp R.K., Doot R.K., Chai X., Kurland B.F., Eby P.R., Specht J.M., Dunnwald L.K., Schubert E.K., Lehman C.D., Mankoff D.A.:. Association between serial dynamic contrast-enhanced MRI and dynamic 18F-FDG PET measures in patients undergoing neoadjuvant chemotherapy for locally advanced breast cancer. J Magn Reson Imaging, 32(5):1124-1131 (2010)
[12] Arasu, V. A., Chen, R. C., Newitt, D. N,; Belinda Chang, C., Tso, H., Hylton, N. M., Joe, B. N.: Can Signal Enhancement Ratio (SER) Reduce the Number of Recommended Biopsies without Affecting Cancer Yield in Occult MRI-detected Lesions? Acad Radiol 18:716-721, (2011).
[13] Lee,S.H.,Kim,J.H.,Cho,N.,Park,J.S.,Yang,Z.,Jung,Y.S.,Moon,W.K.,:Multilevel analysis of spatiotemporal association features for differentiation of tumor enhancement patterns in breast DCE-MRI, Med.Phys. 37,3940 (2010)
[14] Kass,M.,Witking,A., Terzopoulos,D.: Snakes: Active Contour Models, IJCV(1988)
[15] Stojmenovic, M., Nayak, A.: Direct Ellipse Fitting and Measuring Based on Shape Boundaries. In: Mery, D., Rueda, L. (eds.) PSIVT 2007. LNCS, 4872:221235 (2007)
[16] Bhooshan,N.,Giger,M.L.,Jansen,S.A.,Li,H.,Newstead,G.M.,: Cancerous breast lesions on DCE MR Images: Computerized characterization for Image based prognostic markers, Radiology, 254(3):680-690 (2010)

Computerized Characterization of Breast Lesions using Dual-Temporal Resolution Dynamic Contrast-Enhanced MR Images

Bram Platel[1], Henkjan Huisman[2], Hendrik Laue[1], Roel Mus[1], Ritse Mann[1], Horst Hahn[1], and Nico Karssemeijer[2]

[1] Fraunhofer MEVIS, Bremen, Germany
[2] Radboud University Nijmegen Medical Centre, the Netherlands

Abstract. To determine the benefits of a dual-temporal resolution dynamic contrast-enhanced MR protocol for the differentiation of mass-like breast lesions we studied the added value of features derived from this protocol in a computer aided diagnosis system. We developed a CADx system based on an SVM classifier to differentiate benign and malignant breast lesions. A cohort of 93 patients with 133 masses was included in the study. We obtained two different dynamic contrast-enhanced MR image series per study; one with high spatial and one with high temporal resolution. Six morphological descriptors were determined from an automatic segmentation of the lesion. Eight kinetic curve features were derived from the high spatial resolution data and six pharmacokinetic parameters were determined from the high temporal resolution data. Our CADx system demonstrated a performance, measured by the area under the ROC curve, of $A_z = 0.85$ for the commonly used combination of kinetic curve features and morphology. A significant improvement in performance is shown by adding the pharmacokinetic parameters; $A_z = 0.88, p = 0.03$.

1 Introduction

Dynamic contrast-enhanced magnetic resonance imaging (DCE-MRI) of the breast has become an invaluable tool in the clinical work-up of patients suspected of having breast carcinoma. The overall sensitivity of DCE-MRI is high, 0.90 (95% CI: 0.88–0.92), however the specificity of DCE-MRI is variable 0.72 (95% CI: 0.67–0.77) [13]. Therefore continued efforts are focused on identifying distinguishing characteristics of malignant and benign lesions. These descriptors include morphological features, kinetic features, and texture features [1, 5, 12, 17]. They form the basis of the development of computer-aided diagnosis (CADx) systems that may improve diagnostic accuracy as well as reduce intra- and inter-observer variability [4, 12, 2].

Current recommendations for the dynamic evaluation of breast lesions [10] state that high spatial resolution T1 weighted MRI images should be obtained at no less than three time points. The first volume is to be acquired before the administration of the contrast agent. A second volume approximately two minutes

ISBN: 978-87-981270-9-3

later to capture the maximum enhancement, and a last volume to observe the late behavior of contrast agent uptake, i.e. increasing enhancement, a plateau, or wash-out.

Accurate pharmacokinetic parameters have been shown to be very beneficial for the classification of lesions [7, 14]. However, the sampling time needed to obtain accurate pharmacokinetic parameters is much shorter than the currently recommended sampling time [6]. The use of high temporal resolution sequences, however, considerably reduces image resolution and SNR, deteriorating morphological and texture features, which in turn may lead to a reduction of CADx performance [9].

For our study we used a scanning protocol that acquired both high temporal resolution, and high spatial resolution time sequence DCE-MRI images. The high temporal resolution data is suitable for the derivation of pharmacokinetic parameters, whereas the high spatial resolution data is needed for morphological as well as texture descriptors [15].

In this article we present a CADx system based on an SVM classifier to differentiate benign and malignant breast lesions. We computed a set of features to describe the properties of each mass. Morphological descriptors are determined from an automatic segmentation of the lesion. Kinetic curve features are derived from the high spatial resolution volume and pharmacokinetic parameters are determined from the high temporal resolution volume.

2 Image Acquisition

All patients included in this study were scanned using a Sonata or Symphony 1.5 Tesla Siemens MRI scanner in combination with a double breast coil. Before the administration of the contrast agent, a T1-weighted FLASH 3D acquisition at a high spatial resolution and a relatively low temporal resolution (TR 7.8 ms, TE 4 ms, FA 20 °, rectangular FOV 340 mm, slice thickness 1.3 mm, orientation coronal) was acquired. After obtaining this image the contrast agent followed by a saline flush, was administered . At the moment of administration, a series of 22 T1-weighted turboFLASH 3D acquisitions (TR 72 ms, TE 1.54 ms, FA 20 °, FOV 340 mm, slice thickness 4.5 mm, orientation transversal) at a high temporal resolution (4.5 s) was started, followed by a high spatial resolution scan. Additional scans were made at later time points to observe the late behavior of the contrast agent uptake. The acquisition protocol is illustrated in Fig. 1.

Obtained from these measurements were a set of high spatial resolution images with signal intensity values S_t at $T = 5$ time points, $(S_0, S_1, ..., S_4)$, and a set of high temporal resolution images with signal intensity values F_t at $T = 31$ time points, $(F_0, F_1, ..., F_{30})$.

Included in this study were a total of 93 patients (mean age 50.4 years, $\sigma = 11.2$, range 28–76 years), with 133 mass lesions (66 benign and 67 malignant as revealed by biopsy). This database has retrospectively been collected from a consecutive set of breast MR studies acquired by the radiology department of the Radboud University Nijmegen Medical Centre, the Netherlands, from Feb.

ISBN: 978-87-981270-9-3

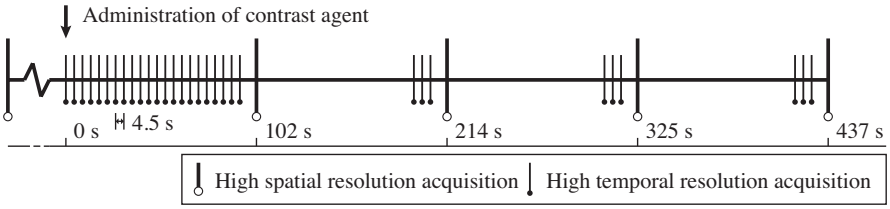

Fig. 1. Illustration of the timeline of the used MRI protocol

2008–Feb. 2010. The pathological classification of the lesions is presented in Tab. 1. All lesions were annotated by an experienced reader. Each annotation consists of a set of spheres, placed such that they cover the full lesion extent.

Pathology	**Occurrence**	**Class**
Invasive Ductal Carcinoma	49	
Invasive Lobular Carcinoma	12	Malignant
Adenocarcinoma	6	
Fibroadenoma	53	
Fibrosis	5	Benign
Adenosis	8	

Table 1. Our study set of 133 lesions, from which 67 are malignant and 66 benign.

2.1 Automatic Lesion Segmentation

To obtain an accurate lesion delineation an adapted version of the *smart opening* algorithm was used. Smart opening was originally developed for nodule and lesion segmentation in CT images [11]. For this study a modified version, which accounts for the difference in lesion appearance between CT and DCE-MRI was used (Fig. 2). The strength of smart opening is its ability to segment lesions that are in contact with vessels and other structures of similar intensities as the lesion itself. To obtain an accurate delineation of the lesion, the high spatial resolution images were used for the segmentation. The enhancement at the first time point ($E_{S_1} = S_1 - S_0$, where S_t is the DCE-MR image at time point t) is used as input for the smart opening algorithm.

The main difference with the algorithm described in [11] is that instead of using predefined Hounsfield units as an initial threshold for region growing, we used statistics to automatically derive this threshold. In an early stage of the algorithm, an estimate of the lesion extent is made by observing the gradient along a set of rays (annotated as area A in Fig. 2a). We used the 5% quantile of the enhancement values E_{S_1} found inside this estimated lesion extent, as the threshold value for the region growing step of the algorithm.

ISBN: 978-87-981270-9-3

For further details about the smart opening algorithm the reader is referred to [11]. The seed point required for the ray casting was taken as the center of the most suspicious region (defined in Sec. 3.2) within the expert's coarse annotation of the lesion.

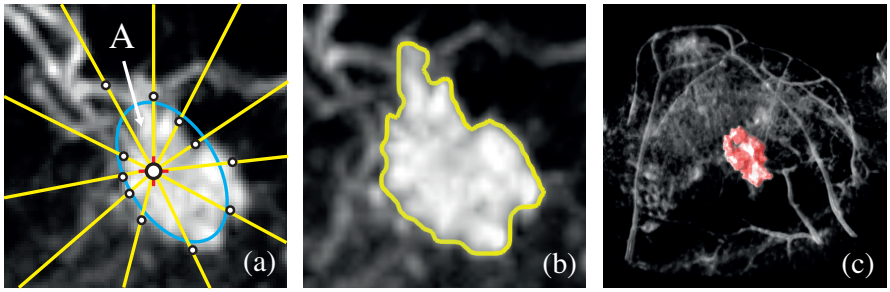

Fig. 2. a) The ray casting used to fit an initial ellipsoid, b) the segmentation resulting from smart opening, c) 3D rendering of the lesion segmentation.

3 Feature Extraction

For this study we used a combination of morphological features derived from the high spatial resolution data and kinetic features, obtained from both high spatial and high temporal resolution data.

3.1 Morphological Features

We used a set of morphological features to describe the shape information of each lesion [5]. These morphological features were calculated on the basis of the lesion segmentation described in Sec. 2.1.
Circularity of Shape is defined as the percentage of the lesion's volume covering the volume of a sphere with the same volume.
Irregularity is defined as

$$\mathrm{IR} = 1 - \frac{\pi d_{eff}^2}{A}, \quad \text{where} \quad d_{eff} = 2\sqrt[3]{\frac{3V}{4\pi}}, \tag{1}$$

where A is the surface of the lesion and V the volume of the lesion.
Convexity was computed as the percentage of the lesion covering the convex hull of the lesion.
The sharpness of the lesion boundary indicates how well the lesion is delimited. We computed two features that describe this sharpness. For both features we considered a set of voxels inside a margin M of three voxels thick at the boundary

ISBN: 978-87-981270-9-3

of the segmented lesion. Let $S_t(x)$ represent the intensity of a voxel x, at time point t, where t runs from time point 0 (before the injection of the contrast) until time point $T-1$ (with T being the amount of time points recorded).
Margin sharpness is defined as

$$\mathrm{MS} = \max_{t=0,\ldots,T-1} \left\{ \frac{\mathrm{mean}_{x\in M} ||\nabla \left[S_t(x) - S_0(x)\right]||}{\mathrm{mean}_{x\in M} S_t(x)} \right\}, \tag{2}$$

where $\nabla \left[S_t(x) - S_0(x)\right]$ denotes the gradient at location x, of the difference image of time frame t and pre-contrast frame 0. The margin gradient feature is recorded for time point t at which the response is maximal, and is normalized with the mean gray-value of margin voxels at that time point.
Margin Gradient Variance is defined as

$$\mathrm{MV} = \frac{\mathrm{variance}_{x\in M} ||\nabla \left[S_t(x) - S_0(x)\right]||}{\left[\mathrm{mean}_{x\in M} S_t(x)\right]^2}. \tag{3}$$

This feature is calculated for time point t with maximum response in (2).
Radial Gradient Analysis measures how well the gradients of the lesion margin are pointing toward the lesion center. For a detailed description of this feature the reader is referred to [5].

3.2 Kinetic Curve Features

Four kinetic features were extracted from the high spatial resolution volume [1] (Tab. 2). These kinetic features were calculated from the signal intensity values at T time points, $(S_0, S_1, ..., S_{T-1})$. S^* is defined as the maximum of the T signal intensity values and p_s as the time point of S^*.

Maximum enhancement	$\mathrm{ME} = (S^* - S_0)/S_0$
Time to peak	$\mathrm{TTP} = p_s$
Uptake rate	$\mathrm{UR} = \mathrm{ME}/\mathrm{TTP}$
Washout rate	$\mathrm{WR} = \begin{cases} \frac{S^* - S_{T-1}}{S_0 \cdot (T-1-S)} & \text{if } p_s \neq T-1 \\ 0 & \text{if } p_s = T-1. \end{cases}$

Table 2. Kinetic curve features

These descriptors were averaged over the entire lesion, as well as over a small region that is most suspicious. We calculated suspicion as $\mathrm{SU} = \mathrm{UR} + w \cdot \mathrm{WR}$, where w weights the contribution of the washout rate with respect to the uptake rate (we have heuristically set $w = 5$). The most suspicious region (MSR) was chosen as a $3 \times 3 \times 3$ voxel region within the lesion, positioned at the location of the maximum of SU_{av}, where SU_{av} is the result of a $3 \times 3 \times 3$ averaging filter on SU.

ISBN: 978-87-981270-9-3

3.3 Pharmacokinetic Features

Pharmacokinetic parameters for each voxel within the lesion were derived from the high temporal resolution data. The method described in [16] was used to estimate these parameters. For each voxel inside the lesion, an exponential signal enhancement model was fitted to the MR signal of the enhancement time curve. This reduced the curve to a five parameter model: baseline (F_0); start of signal enhancement (t_0); time to peak (τ), maximum enhancement (F_p, where $p = t_0 + \tau$), and the washout rate. The resulting curve was converted to a reduced tracer concentration [mmol/ml] time curve, effectively converting F_p to $C_{GD,p}$ (the peak concentration of contrast agent). The concentration of contrast agent in blood plasma is required to derive the pharmacokinetic parameters. We used the reference tissue method [8] to determine the plasma profile. An automatic method was used to select healthy breast parenchyma as reference tissue.

From the pharmacokinetic model three dynamic parameters were determined:

$$\mathbf{v_e} = \frac{C_{GD,p_{tissue}}}{C_{GD,p_{plasma}}}, \quad \mathbf{k_{ep}} = \frac{1}{\tau_{tissue} - \tau_{plasma}}, \text{and} \quad \mathbf{K^{trans}} = v_e \cdot k_{ep}, \qquad (4)$$

where v_e is an estimate of the extracellular volume [%], K^{trans} the volume transfer constant [l/min], and k_{ep} the rate constant [l/min] between extracellular extravascular and plasma space. The subscript "tissue" denotes a measurement in the voxel under investigation and subscript "plasma" the reference tissue plasma estimates based on literature values [3]. These three features were calculated as an average over the entire lesion, as well as an average over the MSR.

3.4 Results

A total of 20 features (6 morphological features, 8 kinetic curve features, 6 pharmacokinetic model parameters) was used to train and test the classifier. Receiver operating characteristic (ROC) analysis was applied to evaluate the performance of each classification task. We used the area under the ROC curve, A_z, as the index of performance. A support vector machine (SVM) classifier with a radial basis function kernel, was applied. A scheme with 10 fold cross validation was executed 10 times resulting in 100 A_z values per classification experiment. For each fold the SVM parameters (cost and gamma) were optimized using a grid search.

Six classification experiments with different combinations of the feature sets were conducted. The classification performance results are shown in Tab. 3.

4 Discussion and Conclusion

Our results demonstrate the benefits of using dual-temporal resolution dynamic contrast-enhanced MR images for the task of computerized differentiation between benign and malignant breast masses.

ISBN: 978-87-981270-9-3

Morphological Feat.	**Kinetic Curve Feat.**	**Pharmacokinetic Par.**
Circularity of shape	Maximum enhancement, WHL	v_e, WHL
Irregularity	Time to peak, WHL	k_{ep}, WHL
Convexity	Uptake rate, WHL	K^{trans}, WHL
Margin sharpness	Washout rate, WHL	v_e, MSR
Margin variance	Maximum enhancement, MSR	k_{ep}, MSR
Radial gradient analysis	Time to peak, MSR	K^{trans}, MSR
	Uptake rate, MSR	
	Washout rate, MSR	

A_Z= 0.74 (95% CI = 0.71–0.77)	A_Z= 0.77 (95% CI = 0.74–0.80)	A_Z=0.71 (95% CI = 0.68–0.74)
A_Z= 0.85 (95% CI = 0.83–0.87)		
	A_Z= 0.81 (95% CI = 0.78–0.84)	
A_Z=0.88 (95% CI = 0.86–0.90)		

Table 3. The feature sets used for the classification. The area under the ROC curve, A_z, and the 95% confidence intervals are given for the different classification results. The kinetic features are averaged over the whole lesion (WHL) and for the most suspicious region (MSR).

The results presented in Tab. 3 show a significant improvement in diagnostic performance of our CADx system ($A_z = 0.85$ to $A_z = 0.88, p = 0.03$), when morphological and kinetic curve features derived from high spatial resolution data, were combined with pharmacokinetic parameters computed from high temporal resolution data.

In line with findings presented in [7], the classification performance increased when the kinetic curve features derived from high spatial resolution data, and pharmacokinetic parameters from high temporal resolution images were combined. The results show that the area under the ROC curve (A_z) increases significantly in this case ($A_z = 0.77$ to $A_z = 0.81$, $p = 0.02$). This implies that pharmacokinetic parameters derived from high temporal resolution data contain additional information over kinetic features obtained from high spatial resolution data, and vice versa.

Additional features, such as texture features, have not been included in this study. These features might further improve the diagnostic performance of the CADx system, but would most likely not reduce the added value of the pharmacokinetic parameters derived from the high temporal resolution data.

References

1. W. Chen, M. Giger, U. Bick, et al. Automatic identification and classification of characteristic kinetic curves of breast lesions on dce-mri. *Med Phys*, 33(8):2878–2887, Aug 2006.
2. W. Chen, M. Giger, G. Newstead, U. Bick, et al. Computerized assessment of breast lesion malignancy using dce-mri robustness study on two independent clinical datasets from two manufacturers. *Acad Radiol*, 17(7):822–829, Jul 2010.

ISBN: 978-87-981270-9-3

3. K. Donahue, R. Weisskoff, D. Parmelee, et al. Dynamic gd-dtpa enhanced mri measurement of tissue cell volume fraction. *Magn Reson Med*, 34(3):423–432, Sep 1995.
4. K. Gilhuijs, E. Deurloo, S. Muller, et al. Breast mr imaging in women at increased lifetime risk of breast cancer: clinical system for computerized assessment of breast lesions initial results. *Radiology*, 225(3):907–916, Dec 2002.
5. K. Gilhuijs, M. Giger, and U. Bick. Computerized analysis of breast lesions in three dimensions using dynamic magnetic-resonance imaging. *Medical Physics*, 25(9):1647–1654, Sep 1998.
6. M. Heisen, X. Fan, J. Buurman, et al. The influence of temporal resolution in determining pharmacokinetic parameters from dce-mri data. *Magn Reson Med*, 63(3):811–816, Mar 2010.
7. H. Huisman, J. Veltman, M. Zijp, et al. Dual-time resolution characterization of masses on breast DCEMR. In *Annual Meeting of the Radiological Society of North America*, 2010.
8. D. Kovar, M. Lewis, and G. Karczmar. A new method for imaging perfusion and contrast extraction fraction: input functions derived from reference tissues. *J Magn Reson Imaging*, 8(5):1126–1134, 1998.
9. C. Kuhl, H. Schild, and N. Morakkabati. Dynamic bilateral contrast-enhanced mr imaging of the breast: trade-off between spatial and temporal resolution. *Radiology*, 236(3):789–800, Sep 2005.
10. R. Mann, C. Kuhl, K. Kinkel, and C. Boetes. Breast mri: guidelines from the european society of breast imaging. *Eur Radiol*, 18(7):1307–1318, Jul 2008.
11. J. Moltz, L. Bornemann, J.-M. Kuhnigk, et al. Advanced segmentation techniques for lung nodules, liver metastases, and enlarged lymph nodes in CT scans. *IEEE Journal of Selected Topics in Signal Processing*, 3(1):122–134, 2009.
12. D. Newell, K. Nie, J. Chen, et al. Selection of diagnostic features on breast mri to differentiate between malignant and benign lesions using computer-aided diagnosis: differences in lesions presenting as mass and non-mass-like enhancement. *European Radiology*, 20(4):771–781, Apr 2010.
13. N. Peters, I. Borel Rinkes, N. Zuithoff, et al. Meta-analysis of mr imaging in the diagnosis of breast lesions. *Radiology*, 246(1):116–124, Jan 2008.
14. M. Schabel, G. Morrell, K. Oh, et al. Pharmacokinetic mapping for lesion classification in dynamic breast mri. *J Magn Reson Imaging*, 31(6):1371–1378, Jun 2010.
15. J. Veltman, M. Stoutjesdijk, R. Mann, et al. Contrast-enhanced magnetic resonance imaging of the breast: the value of pharmacokinetic parameters derived from fast dynamic imaging during initial enhancement in classifying lesions. *European Radiology*, 18(6):1123–1133, Jun 2008.
16. P. Vos, T. Hambrock, C. Hulsbergen van de Kaa, et al. Computerized analysis of prostate lesions in the peripheral zone using dynamic contrast enhanced MRI. *Medical Physics*, 35(3):888–899, Mar 2008.
17. T. Williams, W. DeMartini, S. Partridge, et al. newblock Breast mr imaging: computer-aided evaluation program for discriminating benign from malignant lesions. *Radiology*, 244(1):94–103, Jul 2007.

ISBN: 978-87-981270-9-3

Initial Experience with the Development of Quantitative Image Analysis Methods for Dedicated Positron Emission Mammography: Lesion Segmentation

Karen Drukker[1], Maryellen Giger[1], Kirti Kulkarni[1], Adam Starkey[1], Claire Salling[1], Ken Yamaguchi[1], and Gillian Newstead[1]

University of Chicago, Department of Radiology, Chicago, USA
kdrukker@uchicago.edu

Abstract. The purpose of this research was to determine whether computerized methods originally developed for other breast imaging modalities could be successfully adapted for positron emission mammography (PEM). Here, the focus was on lesion segmentation since that is the first - and a very important - step in automated lesion characterization and determination of response to therapy.
The database contained PEM exams of 17 breast cancer patients obtained in a clinical trial at our institution. Five of these patients underwent one or two follow-up scans over a time period of months. In order to obtain the segmentation 'truth', the lesions were outlined on a per-slice basis by an experienced radiologist who was allowed to consult other imaging data (such as magnetic resonance imaging) and clinical patient reports. This resulted in 552 lesion outlines. We investigated two automated seeded lesion segmentation methods on a per-slice basis: radial gradient index (RGI) segmentation and watershed segmentation.
The RGI segmentation method, originally developed for - and successfully applied to - X-ray mammography, obtained extremely poor results when applied un-altered to the PEM images. After modification of the lesion area criteria used in the search for lesion candidates, the segmentation performance improved and satisfactory agreement with the radiologist outlines was obtained for 63% of the outlines. The watershed segmentation obtained similar performance with 62% of the segmentations being satisfactory or better. When the RGI method was further modified to allow limited user-interaction in the determination of the lesion contour (one click extra), the performance improved significantly ($p \propto 10^{-11}$) and 80% of the segmentations were satisfactory or better.
After modification, the RGI method obtained lesion contours that were of high enough quality to be used in further quantitative image analysis of PEM images, e.g., in the assessment of response to therapy.

1 Introduction

Dedicated breast positron emission tomography (PET) is an emerging technology. The Naviscan PEM Flex Solo II® positron emission mammography (PEM)

ISBN: 978-87-981270-9-3

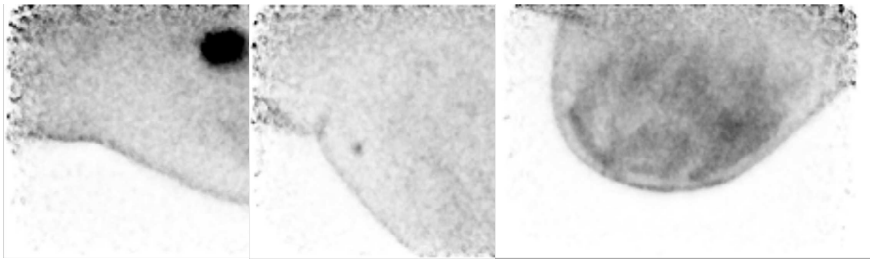

Fig. 1. Examples of PEM slices: An 'easy' case, (left), an 'intermediate' case (middle), and a 'difficult' case (right). Slices were displayed for the radiologist in the manner conventional for PET imaging (uptake is dark) with their colormaps/contrast aimed at achieving optimal viewing conditions.

system[4] is currently being used in a clinical trial at our institution for the determination of disease extent and response to therapy in breast cancer patients. PEM is a 3-dimensional imaging modality in which patients are injected with 18-Fluorodeoxyglucose (a glucose analog and positron emitter) which concentrates in glucose metabolizing cells including malignancies.

The long-term aim of this study was to develop quantitative image analysis (QIA) methods for this modality to ultimately help radiologists in their clinical decision making. Here we discuss our initial experience.

2 Methods

The database consisted of PEM exams of 17 breast cancer patients. Three of these patients underwent 3 exams about a month apart. Two patients underwent two exams, while the remainder of the patients underwent a single exam. In this initial study, all exams were considered separately. Each exam generally consisted of 3 'views' of each breast (CC, MLO, and ML) and a single 'view' of each axilla (as well as a control 'view' of the foot in which the radioactive material was injected and an image of an arm). Only image data pertaining to the breast or axilla were used in this study and breast lesions as well as lymph nodes were analyzed. Each 'view' consisted of 12 slices of image data where the in-slice pixel size was 1.2 mm by 1.2 mm and the resolution in the orthogonal direction ranged from 2.9 to 7.8 mm. Note that not only the overall spatial resolution was very low but also highly anisotropic.

An expert radiologist provided lesion outlines (a total of 552) in all slices where a lesion or lymph node was visible. The radiologist had access to all patient reports and additional imaging data when available. For 7 of the patients, breast magnetic resonance imaging (MRI) data was consulted prior to the outlining because of ambiguity of the PEM data. For 3 of these patients, the PEM data

ISBN: 978-87-981270-9-3

alone was so difficult to interpret that consultation of MRI was necessary to determine the lesion location as well as its shape. Figure 1 depicts example PEM slices with a subjective degree of difficulty.

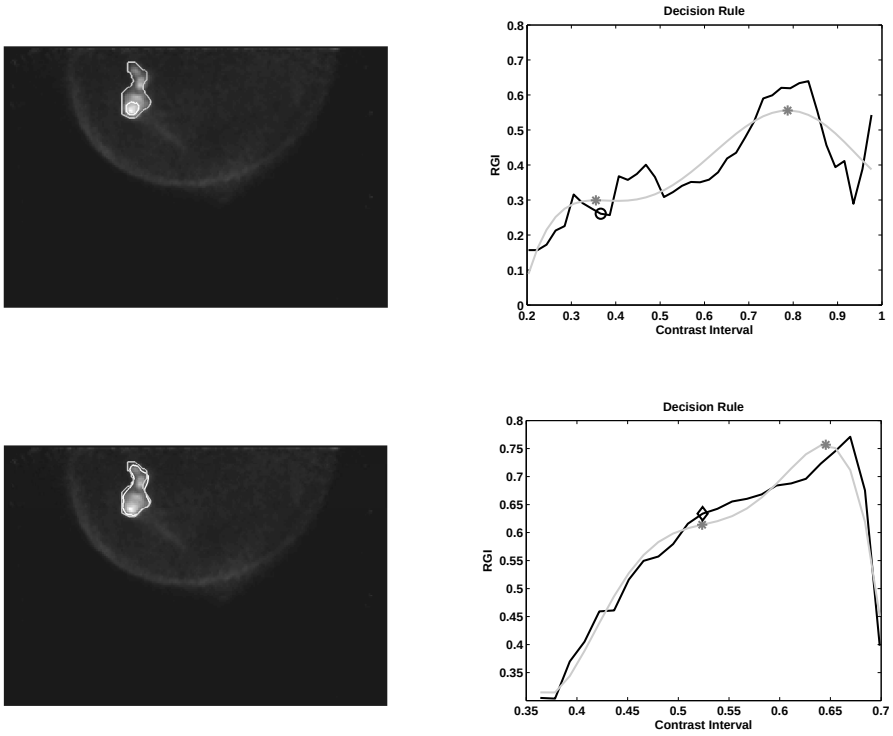

Fig. 2. Comparison of the segmentations of the original RGI method (top) and the modified method (bottom) for an example PEM slice. Here, the PEM images are shown in original form without any processing. The expert outline (light gray solid line) and the computer outline (white solid line) are displayed. On the RGI 'decision profiles', the raw RGI profile (black solid line) is depicted along with a 5th-degree polynomial fit (gray solid line). The roots of the polynomial are indicated with asterisks and the automatically selected points determining the final segmentation contour are indicated with a circle (original method) and an diamond (modified method).

We investigated two segmentation methods on a per-slice basis: the radial gradient index (RGI) segmentation method[2] and watershed segmentation[3]. For the former, we investigated 3 different implementations.

For original implementations of both segmentation methods, the user only needed to indicate a seed-point within the lesion. The RGI method[2] was initially developed for lesion segmentation on mammograms. This method relies

ISBN: 978-87-981270-9-3

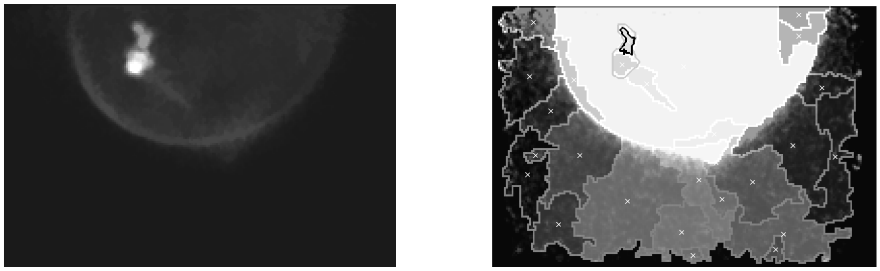

Fig. 3. Preprocessed image for watershed segmentation (left) and watershed segmentation (right) of the same slice as in Figure 2. The candidate watershed regions are indicated by different shades of gray with their centers marked by an 'x'. The radiologist center (black 'x') determined which candidate region yielded the lesion segmentation (black solid line).

on gray level thresholding after image multiplication with a Gaussian constraint function. Here, we used an isotropic 2D Gaussian with a width of 15 mm as the constraining function. For all candidate lesion contours the RGI value is calculated and used as a criterion to determine the best contour candidate for each imaged lesion. RGI as a feature describes lesion shape as well as its margin and it is by definition normalized between -1 and $+1$. Assuming that lesions appear brighter than the background, RGI values close to $+1$ describe circular well-circumscribed lesions. The RGI method employs gray value thresholding based on increasing contrast intervals (of the lesion candidate with respect to the background). For each gray value threshold, a candidate contour is obtained, and the RGI is calculated and plotted as a function of the corresponding contrast interval (Figure 2). Each point on this RGI 'decision profile' corresponds to a unique candidate contour, with contour size generally increasing with increasing contrast interval. Local maxima in the RGI 'decision profile' indicate locally optimal lesion contours. Note that the RGI-value is on the y-axis (Figure 2) in these 'decision profiles' and that hence there may not be a single 'best' contour candidate, i.e., multiple contour candidates may have the same RGI-value. In the original RGI method[2], the first local maximum in RGI as a function of the contrast interval provided the best estimate for the lesion contour. To diminish the effect of noise, a fifth degree polynomial was first fitted though the RGI 'decision profile'. The first root of this polynomial subsequently determined the final lesion contour.

Our first implementation of the RGI method was the original method[2]. Our second implementation of the RGI method involved a modification in the search for lesion contour candidates. The original implementation implicitly assumed 'well-behaved' lesions, i.e., that there are no disconnected regions in a candidate segmentation and that the candidate segmentations always contain the user-indicated seed-point. The low signal-to-noise ratio and low spatial resolution of PEM images, however, proved challenging. Hence, our modification

ISBN: 978-87-981270-9-3

explicitly included only areas containing the user-indicated seed-points in the search for lesion contour candidates. This second implementation will also be referred to as the 'automated modified' RGI method. Note that here we use the term 'automated' as pertaining to the methodology after the initial indication of a seed-point.

In the third implementation of the RGI method, we allowed further user-interaction in that the user was able to select the decision rule on the RGI 'decision profile'. This involved at a minimum a single extra mouse click by the user (so two clicks total including indicating the initial seed-point), but allowed multiple additional clicks until the user was satisfied that the resulting contour was the best obtainable one with RGI. All mouse clicks were mapped on the RGI 'decision profile' by the x-position of the click, i.e., mouse clicks determined the contrast interval for the determination of the lesion contour candidate. This third implementation will also be referred to as the 'semi-automated' RGI method. Note that the latter in principle allows the user to click multiple times in any location along the x-axis (contrast interval) and doing so naively would be very time consuming and would in principle be equivalent to iterative gray-value thresholding and would not benefit from the RGI information. But obviously the RGI values provide a guide for the user which value(s) for the contrast interval to try, e.g., in instances where there are multiple RGI maxima of comparable value in the 'decision profile'.

The watershed method[3] has been extensively used in many applications. We preprocessed the images using standard image processing techniques - such as image erosion, dilation, opening and closing - and determined foreground and background markers. Our approach was based on the general example in the matlab® (MathWorks) documentation with some minor fine-tuning and adaptation of the structuring elements for PEM. Subsequently we applied the watershed method to the slices in their entirety. The watershed region containing the radiologist-indicated seed-point determined the final lesion contour.

We used the overlap ratio of the computer segmentations and the radiologist segmentations as a performance criterion. The overlap ratio is given by the intersection of two areas divided by the union of those areas and as such is bound between 0 and 1. The threshold (lower-bound) for the overlap ratio indicating acceptable computer performance was set at a value of 0.4. The statistical significance of differences in performance was assessed with t-tests[1].

3 Results

Our first implementation of the RGI method obtained disappointingly poor results (Figure 5). In our second implementation of the RGI method, the explicit constraint in the modified RGI method (to include only areas containing the seed-point) changed the RGI 'decision profile' in many instances (Figure 2). The overall performance improved considerably after implementation of this constraint (Figure 5). The improvement in segmentation performance was statistically significant with respect to our first implementation (p-value $\propto 10^{-22}$)

ISBN: 978-87-981270-9-3

and the modified method obtained successful segmentation for 63% of the lesion outlines.

The watershed method (Figure 3) obtained performance similar to that of our second implementation of the RGI method (p-value > 0.5) (Figure 5).

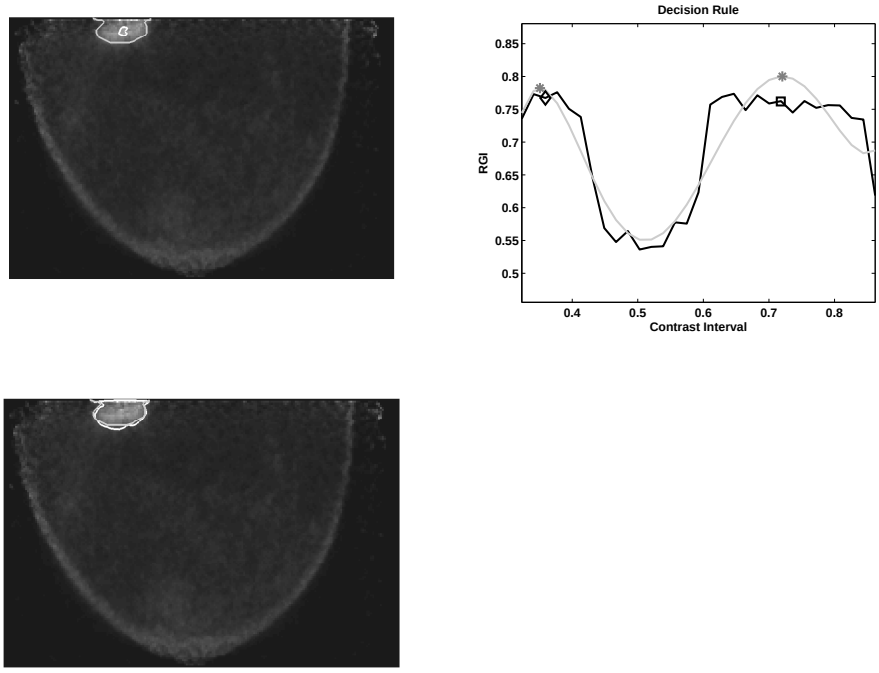

Fig. 4. Example in which the automated modified RGI method yielded a contour in poor agreement with the radiologist outline, and semi-automated adjustment by clicking on the RGI 'decision profile' increased the agreement between computer segmentation and manual outline to an overlap ratio of 0.9. The contrast intervals determining the lesion contours are marked for the modified automated method (diamond) and the semi-automated method (square).

In our third implementation of the RGI method, the additional (but still limited) user-interaction (Figure 4) considerably improved performance. The performance of the more interactive method was significantly better than that of the automated modified RGI method ($p \propto 10^{-11}$). This third implementation of the RGI method obtained adequate or better performance for 80% of the 552 lesion contours. Contours of this semi-automated method differed from those obtained by the automated modified RGI method in slightly less than half of the contours. In other words, the user only needed to modify the decision threshold

ISBN: 978-87-981270-9-3

for the contrast interval in about half of the cases. In the majority of those instances, the user-selected contrast interval corresponded to the second (rather than first as in the original method) local maximum in the RGI 'decision profile'. Although we did not explicitly record this, the additional time spent using the more interactive method - by a user who did not provide (and was unaware of) the 'truth' for segmentation - was modest and comparable to the indication of seed-points to initiate segmentation.

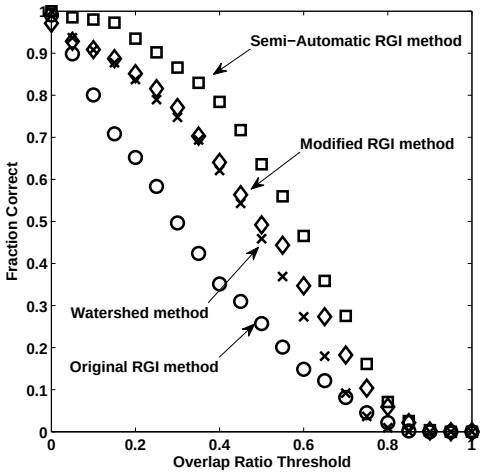

Fig. 5. Overview of the segmentation performance of the methods investigated. Computer segmentations with an overlap ratio larger than 0.4 were considered to be acceptable.

4 Discussion

We obtained encouraging results in this preliminary study on lesion segmentation for dedicated breast positron emission mammography (PEM) images. The quality of the computer segmentations is expected to affect further image analysis such as the determination of tumor response to therapy. The computer segmentation performed best for the semi-automated RGI method. Whether the segmentations of two of the other investigated methods - the modified RGI method and the watershed method - were of high enough quality to allow for accurate further analysis remains to be seen. The semi-automated method required a little extra time, which could be seen as a drawback, but since it resulted in a significant increase in segmentation performance it may be worth the price.

ISBN: 978-87-981270-9-3

One could argue that a limitation of the presented methodology is the per-slice 2D nature. The poor spatial resolution, however, especially in between slices, makes it a difficult problem to tackle with fully 3D methods. Future plans include the investigation of 3D segmentation methods, and the calculation of volumetrics as well as metabolic information to ultimately aid in the determination of tumor response to therapy. The current study contained too few patients with multiple exams over time to conduct a meaningful computational study of response to therapy. Judging from the patient clinical reports and PEM images, however, PEM seems to be well-suited for this task (as expected from the widespread clinical use of 'regular' PET).

One of the limitations of this study was the small dataset size in terms of patients. Since the conclusion of the study reported here, a few more patients underwent PEM exams as part of our clinical trial. But since it is not expected that PEM will become 'main-stream' any time soon, small dataset sizes will likely continue to be an issue. Nevertheless, we expect to learn useful information from PEM about breast cancer and its response to different therapies since its spatial resolution (although admittedly poor compared to many other breast imaging modalities) is considerably better than that of 'regular' whole-body PET. We hope that quantitative image analysis for PEM will find its niche and in the future prove useful for breast cancer patients and their physicians.

References

1. Glantz, S.A.: Primer of biostatistics. McGraw-Hill, New York, USA, 5 edn. (2002)
2. Kupinski, M.A., Giger, M.L.: Automated seeded lesion segmentation on digital mammomgrams. IEEE Trans Med Im 17, 510–517 (1998)
3. Meyer, F.: Topographic distance and watershed lines. Signal Processing 38, 113–125 (1994)
4. Springer, A., Mawlawi, O.R.: Evaluation of the quantitative accuracy of a commercially available positron emission mammography scanner. Med. Phys. 38, 2132–2139 (2011), "DOI: 10.1118/1.3560881"

ISBN: 978-87-981270-9-3

Computer Aided Interpretation of Lesions in Automated 3D Breast Ultrasound

Tao Tan[1], Bram Platel[2], Thorsten.Twellmann[3], Guido van Schie[1], Roel Mus[1], Andre Grivegnee[4], Laszlo Tabar[5], and Nico Karssemeijer[1]

[1] Department of Radiology, Radboud University Nijmegen Medical Centre, the Netherlands
[2] Fraunhofer MEVIS, Bremen, Germany
[3] MeVis Medical Solutions AG, Bremen, Germany
[4] Jules Bordet Institute, Cancer Prevention and Screening Clinic, Brussels, Belgium
[5] Department of Mammography, Falun Central Hospital, Sweden

Abstract. As a new and promising imaging modality for breast cancer diagnosis and screening, automated 3D breast ultrasound is finding its way into clinical applications. In this study we compared the performance of a computer-aided diagnosis (CAD) system and reader performance in characterizing lesions from these images and investigated if the reader performance improves with a CAD system. Our CAD system computes a lesion malignancy score for each lesion. Features representing spiculation, lesion shape, margin contrast, posterior enhancement, texture, and echogenicity were calculated and combined using linear discriminant analysis (LDA). 88 patients were included for an observer study. For each patient one ultrasound view with a lesion was selected. 47 lesions were malignant and 41 were benign. Seven readers (5 radiologists and 2 residents) read the series of cases with and without CAD. To compare performance, ROC analysis was used (DBM MRMC 2.3). With an area under the curve (AUC) of 0.917 CAD performed as well as the best reader (AUC = 0.918). Without CAD the average AUC of the readers was 0.859 (0.876 for the radiologists, 0.818 for the residents). With CAD the performance of the readers increased to 0.880 (0.884 for the radiologists, 0.869 for the residents) non-significantly (p=0.19).

Keywords: Computer aided interpretation, automated 3D breast ultrasound

1 Introduction

Breast cancer is the leading cause of cancer death among women aged 20 to 59 in the United States[1]. Mammography is currently the primary modality for breast diagnosis and screening. However sensitivity of mammography is poor in dense breasts. As a innovative modality, automated 3D breast ultrasound (ABUS) not only inherits the merits of 2D ultrasound in detecting lesions in dense breasts, but also provides a 3D view of a breast and makes the imaging less dependent on the operator. Moreover, in ABUS, spiculation patterns associated with invasive breast cancers are often observed on the coronal planes [2,3] which can not be observed well or are completely absent in 2D ultrasound.

ISBN: 978-87-981270-9-3

To be able to provide fast and accurate diagnosis of breast lesions and help radiologists interpret lesions as a second opinion, computer-aided diagnosis (CAD) systems have been developed extensively for mammography[4,5,6] and 2D US[7]. Initial experience with ABUS indicates that CAD may be very useful in this modality, considering that reading 3D volumetric images is time consuming for readers.

Sahiner et al. [8] already showed that the use of CAD improved the radiologists' accuracy of distinguishing malignant from benign breast masses on 3D US volumetric images from an experimental system which is not automated. For automated 3D breast ultrasound, our preliminary work[9] introduced a CAD system for breast lesions.

The purpose of this work is to compare the performance of CAD stand-alone and observers in classifying breast lesions into malignant and benign in ABUS and to investigate how CAD will affect the performance of observers after using CAD.

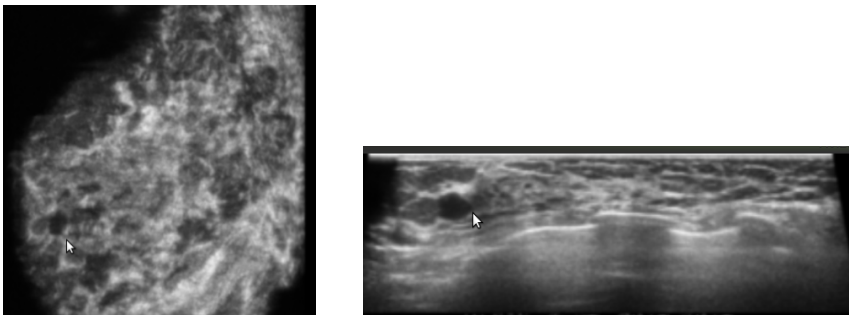

(a) (b)

Fig. 1. A benign lesion in ABUS (indicated by the arrow). Two slices through the lesion are shown, a coronal slice (a) and a transversal slice (b). The latter is similar to the traditional 2D ultrasound view

2 Materials and Methods

2.1 Dataset

All breast ultrasound images used in this study were obtained from Radboud University Nijmegen Medical Centre (Nijmegen, The Netherlands), Falun Central Hospital (Falun, Sweden), and The Jules Bordet Institute (Brussels, Belgium). All the centers used the automated 3D breast ultrasound system developed by U-systems, Inc. (SomoVu, Sunnyvale, CA, USA). For all images a 8MHz transducer with an width of 14.5 cm was used. During imaging, patients were in supine position and the breast was compressed by a dedicated membrane.

ISBN: 978-87-981270-9-3

The scanning device automatically translated the transducer in the cross-plane direction during acquisition. Each 3D volumetric view was generated with an in-plane resolution 0.285 mm by 0.285 mm or 0.134 mm and a slice thickness of 0.6 mm. We resampled the images to obtain 0.6 mm cubic voxels to develop our CAD system. Fig. 1 shows a coronal view and a transversal view of a breast with a benign lesion.

A dataset of 201 lesions (table 1) from 158 patients who underwent ABUS Imaging between 2006 and 2010 was used. All malignant lesions were confirmed by biopsies and benign lesions were either confirmed by biopsy, image interpretation alone or by combining information from different imaging modalities.

Table 1. Number of lesions of different histology types in the complete dataset and observer study dataset

Histology information	The complete dataset	Observer study dataset
Malignant lesions		
Infiltrative ductal carcinoma	60	38
Ductal carcinoma in situ	3	1
Infiltrative lobular carcinoma	7	6
Other	15	2
Total	85	47
Benign		
Cyst	47	9
Fibroadenoma	24	14
Fibrocystic change	24	11
Other	21	7
Total	116	41

2.2 Computer-Aided Diagnosis

Lesion segmentation is a prerequisite step that needs to be executed before extracting lesions features for classification. Segmentation of breast lesions in ABUS is challenging because of inherent image speckles and unclear lesion boundaries, posterior acoustic behavior, and inhomogeneous lesions. We have extended the dynamic programming approach based on a spiral scanning technique introduced by Wang et al.[10] for pulmonary nodule segmentation in CT. The segmentation involves a cost function that deals with edge detection locally [11] and meanwhile prevents leakage of the segmentation by including a smoothness term in the cost function.

Given the segmentation of a lesion V_l, features can be computed to represent its shape, margin, intensities and texture. In our previous work [9], we computed spiculation feature, volumetric height-to-width ratio, margin contrast, posterior acoustic behavior feature, entropy of the lesion region, DICE coefficient between a segmented lesion and a registered smooth object and echogenicity. Among

ISBN: 978-87-981270-9-3

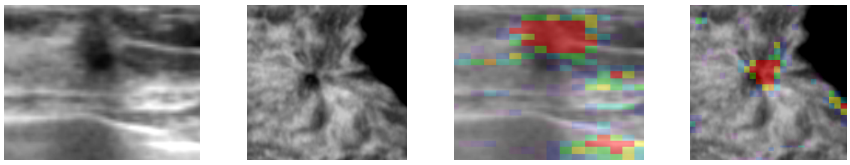

(a) (b) (c) (d)

Fig. 2. Figures (a) and (b) show a malignant lesion in transversal and coronal views, respectively. Spiculation can be observed well in the coronal view. Figures (c) and (d) show the lesion with the spiculation feature map in color overlay. The spiculation value of the overlay increase with the color changing from blue to red.

these features, margin contrast and spiculation feature appeared to be the best features for the classification.

In this study, we replaced the spiculation feature in [9] with five features. The spiculation values [12] present the amount of voxels pointing to the region center and are normalized with respect to a random orientation pattern (Figure 2). We included the average spiculation value of the segmented lesion as a feature. When spiculation patterns are visible in malignant lesions, the lesion centers of 2D coronal slices usually have higher spiculation values than the periphery. To extract spiculation features near the center region we created a cylinder CR with a radius of $3mm$ and with an axis through the center (in 3D) of the lesion along the depth direction. The length of the cylinder was determined by the depth of the lesion. The cylinder was divided evenly into three small segments along the depth direction (see Fig. 3). To extract spiculation features at different depths, we computed the average spciculation values of the three segments. We also computed the maximum average spciulation among coronal slices of the complete cylinder CR as another feature.

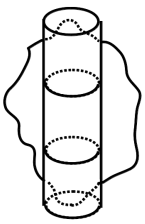

Fig. 3. In transversal view, a cylinder was created through the center of the lesion along the depth direction and it is evenly divided into small segments.

To measure the irregularity of a lesion, we registered a sphere with the same volume as the segmented lesion V_l to the segmented lesion with an affine trans-

ISBN: 978-87-981270-9-3

formation. Besides the Dice coefficient of the segmentation V_l and the registered result V_r, we calculated volume difference (DF) between V_l and V_r:

$$DF = |V_r| + |V_l| - 2|V_l \cap V_r| \quad (1)$$

We also computed variance of intensities inside a lesion, variance of intensities of its inner border (voxels within 1.2 mm of the boundary) and the volume of a lesion as additional features. In total, combining the new features with those in [9], 15 features were computed.

Linear discriminant analysis (LDA) was used to combine 15 extracted features. To get an independent score indicating the malignancy of each lesion between 0 (benign) and 1 (malignant), we performed 10-fold cross-validation on the complete dataset of 201 lesions (table 1)

2.3 Observer Study Design

Seven readers, of which five were certified radiologists and two were residents were invited for an observer study in which we aimed to compare the diagnostic performance of our CAD system and observers and to investigate the effect of CAD on observer performance. Two radiologists and one resident had extensive experience with ABUS image interpretation. The remaining three radiologists and one resident had no experience with ABUS but had extensive experience with interpreting 2D ultrasound images.

For this observer study, a subset of the dataset including 88 patient was included. For each patient one ABUS view with a lesion was selected. 47 were malignant lesions and 41 were benign lesions (table 1). Another subset of 26 patients with 23 benign and 14 malignant lesions from the dataset were used to train the readers before the experiment.

Images with original resolutions were displayed in a dedicated workstation (HAMAM prototype, MeVis Medical Solutions, Bremen) on a color monitor with a display resolution 2560 by 1200. The workstation allowed to scroll through slices with synchronized viewing of coronal, transversal, and sagittal slices. The synchronization could be disabled or enabled by the push of a button. The window level could be automatically or manually adjusted. The lesion to be assessed was identified by a yellow rectangle marker with a fixed size located at the lesion center. The marker could easily be switched on and off to avoid obscuring the lesion while reading. The workstation could be configured such that it would or would not show the associated CAD score next to the marker.

The experiment consisted of two separate reading sessions. Before the experiment, each reader started with a training program. Readers were presented a series of 26 training cases with 23 benign and 14 malignant lesions. The training cases served to acquaint the observers with the system, including synchronized orthogonal views, interpreting CAD scores and the controls for adjusting window level of the displayed images. During the training program, CAD scores were shown and the ground truth of all the marked lesions was supplied in a printed document. After the training program, the first session continued with the actual experiment. Readers were asked to first read a set of 45 cases (set

ISBN: 978-87-981270-9-3

A) with CAD scores shown and subsequently a second set of other 43 cases (set B) without CAD scores. For each patient, a single lesion was shown and readers were asked to rate this lesion on a scale between 0 (benign) and 100 (malignant). After a break (few hours to several days), the experiment continued with the second session. In this session readers were asked to rate the same lesions, but in the second session they read set A without CAD and set B with CAD. Readers were asked to rate these lesions again. Readers were reminded of the importance of using the same scale to rate the lesions during the whole experiment and they were informed that approximately half of all the lesions that were shown in this experiment were malignant and the other half were benign. The order of the cases within each subset was randomized in the two sessions to minimize reading order effects. There was no limit on the reading time.

2.4 Data Analysis

Receiver operating characteristic (ROC) was used to analyze the diagnostic performance without and with using CAD for individual readers, as well as for the average reader and the CAD standalone. The area under the ROC curve (AUC) was used to evaluate the performance. The AUC was obtained using the proper binormal model[13] using DBM MRMC 2.3 developed by researchers from the University of Iowa and the University of Chicago[14,15]. Using the same software, the significance of differences in reader performance between reading with and without using CAD was analyzed with the Dorfman-Berbaum-Metz method[14,15], which performs an analysis of variance allowing to treat both readers and cases as random samples.

3 Result

The AUC value of the performance of standalone CAD was 0.917 (Fig. 4) which was not significant different than that of all readers (p=0.085), radiologists (p=0.194), or residents (p=0.283) without using CAD. As shown in Table 2, the AUC values of performances of readers without CAD ranges from 0.767 to 0.918 and with CAD the AUC values range from 0.821 to 0.927. By using CAD, the average AUC value increased from 0.876 to 0.884 for radiologists, from 0.818 to 0.917 for residents, and from 0.859 to 0.880 for all readers. The difference was not significant for radiologists (p=0.256) and for all readers (p=0.188), but the difference was significant for residents (p=0.003). Fig. 4 shows the ROC curves of the performance of the readers with and without CAD and CAD standalone.

4 Discussion and conclusion

Sahiner et al. [8] showed that the use of CAD improved radiologists' accuracy in distinguishing malignant from benign breast masses on 3D US volumetric images. In our study, the accuracy of the performance of readers with CAD also

ISBN: 978-87-981270-9-3

Table 2. AUC Values of Performances of Readers without and with CAD

Reader:	Without CAD	With CAD
Radiologist 1.	0.906	0.896
Radiologist 2.	0.918	0.927
Radiologist 3.	0.827	0.864
Radiologist 4.	0.871	0.860
Radiologist 5.	0.855	0.876
Mean of Radiologists	0.876	0.884
Resident 1.	0.869	0.917
Resident 2.	0.767	0.821
Mean of Residents	0.818	0.869
Mean of all readers	0.859	0.880

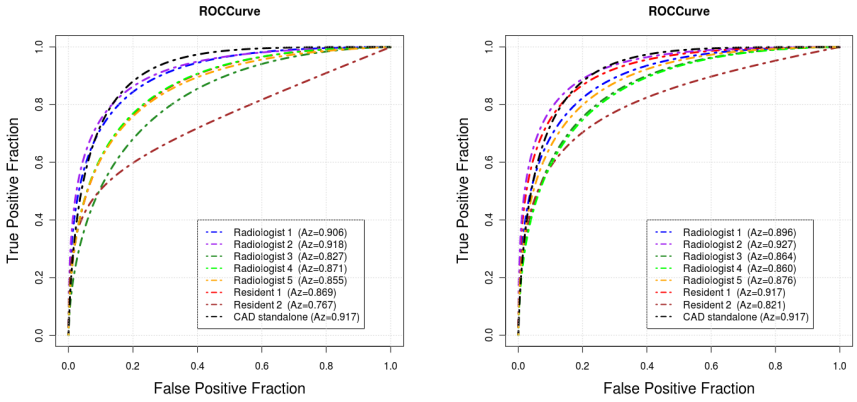

(a) (b)

Fig. 4. (a) ROC curves of observers without CAD and CAD standalone. (b) ROC curves of observers with CAD and CAD standalone.

increased in terms of AUC values, but the increase with CAD was not statistically significant. This may be because the power of our study was lower and the readers had limited experience with interpretation of lesions when using CAD in ABUS. Average AUC value of residents increased more than average AUC value of radiologists. For residents, the performance was significantly improved using CAD ($p = 0.003$). This indicates that the CAD system is more helpful for unexperienced readers (residents) when interpreting ABUS images.

In conclusion, a CAD system was developed for classifying lesions into malignant and benign lesions in ABUS. There are no significant difference between performance of the CAD system and readers. Reader performance did not increase significantly when working with CAD, which may be due to inexperience with ABUS and CAD.

ISBN: 978-87-981270-9-3

References

1. A. Jemal, R. Siegel, J. Xu, and E. Ward. Cancer statistics, 2010. *CA Cancer J Clin*, 60:277–300, 2010.
2. D. Rotten, J. M. Levaillant, and L. Zerat. Analysis of normal breast tissue and of solid breast masses using three-dimensional ultrasound mammography. *Ultrasound Obstet Gynecol*, 14(2):114–124, Aug 1999.
3. D. O. Watermann, M. Fldi, A. Hanjalic-Beck, A. Hasenburg, A. Lghausen, H. Prmpeler, G. Gitsch, and E. Stickeler. Three-dimensional ultrasound for the assessment of breast lesions. *Ultrasound Obstet Gynecol*, 25(6):592–598, Jun 2005.
4. H. P. Chan, B. Sahiner, M. A. Helvie, N. Petrick, M. A. Roubidoux, T. E. Wilson, D. D. Adler, C. Paramagul, J. S. Newman, and S. Sanjay-Gopal. Improvement of radiologists' characterization of mammographic masses by using computer-aided diagnosis: an ROC study. *Radiology*, 212(3):817–827, Sep 1999.
5. Lubomir Hadjiiski, Heang-Ping Chan, Berkman Sahiner, Mark A Helvie, Marilyn A Roubidoux, Caroline Blane, Chintana Paramagul, Nicholas Petrick, Janet Bailey, Katherine Klein, Michelle Foster, Stephanie Patterson, Dorit Adler, Alexis Nees, and Joseph Shen. Improvement in radiologists' characterization of malignant and benign breast masses on serial mammograms with computer-aided diagnosis: an roc study. *Radiology*, 233(1):255–265, Oct 2004.
6. Sheila Timp, Celia Varela, and Nico Karssemeijer. Computer-aided diagnosis with temporal analysis to improve radiologists' interpretation of mammographic mass lesions. *IEEE Trans Inf Technol Biomed*, 14(3):803–808, May 2010.
7. Karla Horsch, Maryellen L Giger, Carl J Vyborny, and Luz A Venta. Performance of computer-aided diagnosis in the interpretation of lesions on breast sonography. *Acad Radiol*, 11(3):272–280, Mar 2004.
8. Berkman Sahiner, Heang-Ping Chan, Marilyn A Roubidoux, Lubomir M Hadjiiski, Mark A Helvie, Chintana Paramagul, Janet Bailey, Alexis V Nees, and Caroline Blane. Malignant and benign breast masses on 3D US volumetric images: effect of computer-aided diagnosis on radiologist accuracy. *Radiology*, 242(3):716–724, Mar 2007.
9. T. Tan, H.J. Huisman, B. Platel, A. Grivignee, R. Mus, and N. Karssemeijer. Classification of breast lesions in automated 3D breast ultrasound. In *Medical Imaging*, volume 7963 of *Proceedings of the SPIE*, page 79630X, 2011.
10. Jiahui Wang, Roger Engelmann, and Qiang Li. Segmentation of pulmonary nodules in three-dimensional CT images by use of a spiral-scanning technique. *Med Phys*, 34(12):4678–4689, 2007.
11. S. Timp and N. Karssemeijer. A new 2D segmentation method based on dynamic programming applied to computer aided detection in mammography. *Med Phys*, 31(5):958–971, 2004.
12. N. Karssemeijer and G. M. te Brake. Detection of stellate distortions in mammograms. *IEEE Trans Med Imaging*, 15(5):611–619, 1996.
13. Metz and Pan. "proper" binormal ROC curves: Theory and maximum-likelihood estimation. *J Math Psychol*, 43(1):1–33, Mar 1999.
14. D. D. Dorfman, K. S. Berbaum, and C. E. Metz. Receiver operating characteristic rating analysis: Generalization to the population of readers and patients with the jackknife method. *Invest Radiol*, 27:723–731, 1992.
15. Stephen L Hillis, Kevin S Berbaum, and Charles E Metz. Recent developments in the dorfman-berbaum-metz procedure for multireader ROC study analysis. *Acad Radiol*, 15(5):647–661, May 2008.

ISBN: 978-87-981270-9-3

Fully-automatic breast density assessment from full field digital mammograms

Harald Heese, Klaus Erhard, and André Gooßen

Philips Research Europe – Hamburg,
Roentgenstr. 24 – 26, 22335 Hamburg, Germany
{harald.heese,klaus.erhard,andre.goossen}@philips.com

Abstract. Mammographic breast density is associated with an increased risk of developing breast cancer. However, the estimation of radiographic breast density suffers from a high inter-observer variability. A fully automated solution for objective and consistent assessment of breast density from full field digital mammography (FFDM) data is presented. For the automatic computation of mammographic density, a region of interest (ROI) is automatically extracted from the mammograms. Segmentation into adipose and glandular tissue is performed within this ROI using a Gaussian mixture model in combination with a histogram threshold adjustment from calibration data. Breast density is finally computed as fraction of glandular tissue area to overall area of the ROI. The fully automated approach provides breast density estimates that show good to excellent correlation with the reference standard ($r \in [0.72, 0.86]$), with deviations ranging between -37% (q=0.025) and +22% (q=0.975).

Keywords: mammographic breast density, breast cancer risk assessment, mammography, FFDM

1 Introduction

Mammographic breast density is associated with an increased risk of developing breast cancer [1, 11, 15]. Moreover, detecting early stages of breast cancer in women with dense breasts is more difficult than in women with mainly adipose breast tissue. In [10], for example, it has been shown that breast density is a major risk factor for interval breast cancer, i.e. women with dense breast tissue have an increased risk that a developing breast cancer is missed during routine screening. Recently, regulation authorities have acted by requiring the enlisting of breast density in the mammographic report with a recommendation for subsequent ultra-sound or MRI examinations for women with dense breasts [14].

The importance of breast density is increasing in its role as a personalized risk indicator, whereas the definition of breast density and its measurement in clinical practice requires some more attention. The two most common definitions of breast density are the *mammographic percent density* relating to the area fraction of the amount of glandular tissue in a mammographic projection image of the breast and the *volumetric breast density* measuring the volume fraction of

ISBN: 978-87-981270-9-3

glandular tissue within the physical breast volume. The first definition reflects current clinical practice, whereas the latter provides radiologists with a new physical quantity that may lead to new insights.

For measuring mammographic percent density a semi-automatic software, Cumulus [2], is widely used in evaluation and comparison studies [7, 8]. Recently, an automatic breast density segmentation tool has been proposed in [7], which incorporates different approaches using feature extraction and analysis.

The assessment of volumetric breast density is based on a physical model of the mammographic image formation process. Several methods for estimating volumetric breast density have been proposed that either require the simultaneous acquisition of the breast with a calibration phantom [3] or try to estimate the attenuation of an adipose pixel value directly from the image [5, 13].

In the following, we present a method for the fully-automatic assessment of mammographic percent density that is based on a Gaussian mixture model for tissue separation. A 3D breast model and calibration-based models for height and voltage dependent effective linear attenuation coefficients of adipose and glandular tissue are used to stabilize tissue separation with respect to imperfections such as visible skin folds or uncompressed peripheral breast tissue.

The proposed method has been validated against manual ground truth scorings from 5 different readers on clinical data from 82 patients, revealing performance almost comparable to inter-reader deviations. Thus, the presented approach is a major step towards routine use of fully-automated estimation of mammography percent density in clinical practice.

2 Methods and Materials

The suggested approach has been developed using raw data ($0.085 \times 0.085\,\mathrm{mm}^2$ resolution, 2084×2800 pixel matrix) from Philips MammoDiagnost DR 1.0 X-ray mammography systems (Philips Medical Systems DMC GmbH, Hamburg, Germany) as input data.

2.1 Image and ground truth data

Image data of 100 patients (age: 29 - 84 years, median age: 50 years) has been collected from 4 different diagnostic institutions between July 2007 and August 2009. For each patient, 4 standard views (i.e. cranio-caudal (CC) and medio-lateral oblique (MLO), left and right) were acquired. Only patients that had unsuspicious findings and no implants were included in the collection. Distribution of clinical density classification was chosen to adequately represent all categories (ACR 1: 24; ACR 2: 26; ACR 3: 38; ACR 4: 12).

After a first analysis of the data, 14 patients were excluded due to wrong acquisition parameter settings (X-ray tube used with wrong power settings). Additionally, for this study the results from 4 patients had to be excluded due to incomplete visual readings.

ISBN: 978-87-981270-9-3

Ground truth data was established as follows: Five experts, skilled in reading digital mammograms, blindly graded mammographic percent density on the set of collected image data (displayed using the vendor's standard post-processing) using an eleven-point-scale (0, 10, ..., 100 %) on a per patient basis, i.e. all four mammographic views were shown together.

2.2 System Calibration

Incorporation of physical quantities from the mammographic image formation process requires system calibration, which has been performed on a lab system, whereas the performance has been evaluated on clinical data. The linear attenuation coefficient μ and the measured intensity $\mathcal{I}$ are related via Beer's law

$$\mathcal{I} = \mathcal{I}_0 \cdot e^{-\mu h} \quad , \tag{1}$$

where $\mathcal{I}_0$ denotes the initial or non-attenuated intensity, h denotes the thickness of the radiated object, and where the assumption has been made that μ is constant along the beam path. As for larger breasts with high thickness the intensity has to be higher, non-attenuated areas result in saturated detector pixels, hampering an extraction of the initial intensity $\mathcal{I}_0$ directly from the image.

We performed calibration measurements of $\mathcal{I}_0$ against the exposure settings, i.e. tube voltage U, tube current I, and exposure time t, observing a direct proportional dependency between $\mathcal{I}_0$ and the exposure It, and moreover, a linear dependency between detector sensitivity g and tube voltage, allowing to model

$$\mathcal{I}_0 = g\,It = (g_0 + g_1 U)\,It \quad . \tag{2}$$

For calibration of attenuation coefficients of the mammography system a set of dedicated step wedge phantoms composed of two materials with attenuations equivalent to adipose and glandular breast tissue was used (CIRS Inc., Norfolk, Virginia), respectively (cf. Fig. 1 (a)). By help of these phantoms effective linear attenuation coefficients μ_{fat} and μ_{gland} have been derived for all combinations of specified tube voltages $U \in 23, 24, \ldots, 35\,\text{kV}$ and tissue heights $h \in 10, 20, \ldots, 120\,\text{mm}$. Using biquadratic regression allows to represent $\mu_{\text{fat}}\,(U, h)$ and $\mu_{\text{gland}}\,(U, h)$ as polynomials,

$$\mu(U, h) = a_0 + a_1 U + a_2 U^2 + a_3 h + a_4 h^2 \quad . \tag{3}$$

With an average deviation of 2.5 % from the measured attenuation, a precise and compact model for the attenuation of breast tissue within the specified system boundaries has been derived. Fig. 1 (b) depicts the models for μ_{fat} and μ_{gland} in a combined plot.

2.3 Preprocessing

Typical mammograms contain four different major regions (background, uncompressed breast tissue, compressed breast tissue, pectoral muscle – cf. Fig. 2 (a)) that need to be identified in preprocessing steps in order to extract a region of interest (ROI) for mammographic percent density estimation.

ISBN: 978-87-981270-9-3

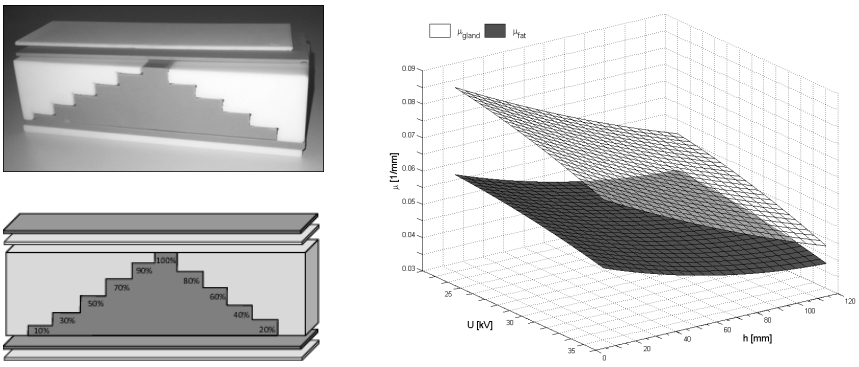

(a) Calibration phantom (b) Regression polynomials

Fig. 1. System calibration. (a) A calibration phantom consisting of adipose and glandular tissue equivalent material, assembled in a step wedge. With a constant height, the phantom contains steps with 0, 10, ..., 100 % of either tissue type. In order to cover the full range of possible tissue heights the step wedges exist in different sizes, and additional thin plates can be used to measure intermediate heights. (b) Results of a biquadratic regression through the measured effective linear attenuation coefficients for adipose and glandular tissue equivalent material plotted against tube voltage U and tissue height h. The polynomials serve as model for fatty and glandular breast tissue attenuation at a given voltage and tissue height.

Background detection: In the suggested approach, a Gauss-Deriche filter (kernel size $\sigma = 0.75\,\mathrm{mm}$) is applied for downsampling the input image data to a resolution of $0.68 \times 0.68\,\mathrm{mm}^2$. Using a connected component analysis with an 8-point neighbourhood on the filter result thresholded with respect to edge strength, the skinline of the breast is identified as the strongest component with respect to accumulated edge strength. The detected skinline divides the image into two regions, and the background region is identified as the one with higher average grey value.

Pectoral muscle segmentation: According to the BI-RADS atlas for mammography [4], the pectoral muscle should not be included in the evaluation of mammographic percent density. The proposed approach therefore segments the pectoral muscle in MLO views and excludes the resulting region from the ROI for mammographic percent density estimation. In a first step, feature points for the pectoral muscle outline are extracted from downsampled and directional gradient filtered image data [16] by row-wise selecting the first local minimum within the tissue region. Orientation of the pectoral muscle outline is then determined from the feature points via a Hough Transform for a range of plausible orientations ($110° - 175°$). The pectoral muscle is determined as the region between the upper right corner of the image and the contour given by tracing the local minima between adjacent validated feature points (deviating less than 1 mm from the result of the Hough Transform).

ISBN: 978-87-981270-9-3

Breast height modelling: The detected skinline also serves as initialization for breast height modelling. Similar to [12], the breast is modelled as a block of compressed tissue with constant height in the interior, and by semi-circles of matching diameter perpendicular to the skinline in the periphery. In order to establish a corresponding height map for the breast, first a distance map to the skinline is generated via a fast marching algorithm. The tissue height is computed via

$$h(x,y) = \begin{cases} 2\sqrt{d_s(x,y)(h_0 - d_s(x,y))}, & d_s(x,y) < 0.5h_0 \\ h_0, & d_s(x,y) \geq 0.5h_0 \end{cases}, \tag{4}$$

where h_0 is the compression height (i.e. distance between compression paddle and detector cover) in millimetres, and d_s is the distance to the extracted skinline.

Region of interest extraction: For the suggested approach, the ROI for mammographic percent density estimation is defined as the region of breast tissue with $h > 0.85h_0$ according to the breast height model, i.e. where at least 85 % of the space between compression paddle and detector cover are filled by tissue. An example result of the pre-processing is shown in Fig. 2 (b).

2.4 Mammographic percent density estimation

For mammographic percent density estimation, the measured raw image data is transformed by inverting Beer's law (1), where the non-attenuated intensity is derived using (2). Normalization of the uncompressed breast tissue region within the ROI for breast density estimation is carried out by computing the effective linear attenuation coefficient for adipose tissue using (3), and by subsequently padding the uncompressed breast tissue region artificially with adipose tissue up to the compression height h_0 by means of adding

$$(h_0 - h(x,y))\mu_{\text{fat}}(U,h) \tag{5}$$

within the ROI analogously to [12].

Subsequently, a 3-class Gaussian Mixture Model (GMM) is fitted to the thus normalized data, where the central class is merged to one of the remaining classes, such that the in-class variance is minimized. The interface between the two resulting classes serves as histogram threshold for separation into adipose and glandular tissue regions.

As tissue separation into two classes may fail in extreme cases of completely fatty or dense breasts, the histogram threshold selection from the GMM fit is checked for plausibility against calibration data for $\mu_{\text{fat}}(U,h)$ and $\mu_{\text{gland}}(U,h)$, and clamped to

$$h_0\left[\mu_{\text{fat}}(U,h) + 0.2\left(\mu_{\text{gland}}(U,h) - \mu_{\text{fat}}(U,h)\right)\right] \tag{6}$$

as the lowest acceptable histogram threshold. Finally, mammographic density D_{mam} is computed as the area fraction of segmented glandular tissue within the ROI. Thus, the presented method can also be seen as an extension to [6], in the sense that the volumetric threshold is not fixed but data-driven from the GMM fit.

ISBN: 978-87-981270-9-3

Table 1. Observer Variability. Correlation of the presented approach to each reader's gradings is given in top row. First and second order statistics over deviation of reader's gradings and automated results versus all reader gradings is shown in bottom rows.

	reader I	reader II	reader III	reader IV	reader V	D_{mam}
corr. to D_{mam}	0.86	0.86	0.83	0.72	0.85	n/a
mean dev.	11.94	-0.83	-8.76	-1.36	-0.98	-9.21
stddev. of dev.	13.12	13.33	12.79	18.09	13.51	15.35

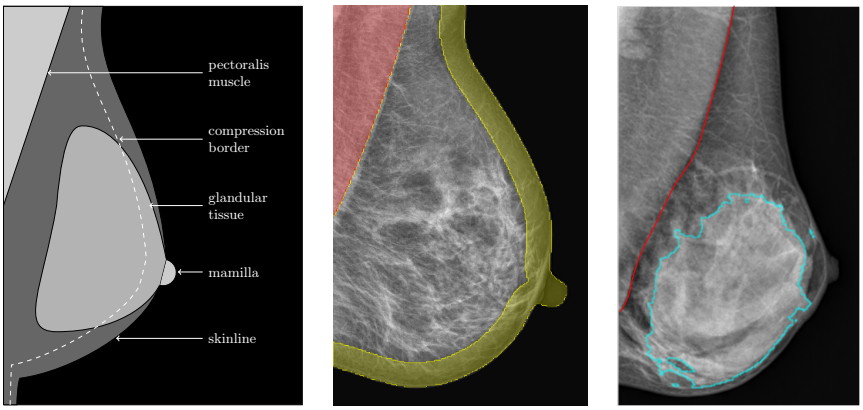

(a) MLO atlas (b) Pre-processing result (c) Segmentation result

Fig. 2. MLO atlas and example results. (a) Schematic drawing of mammogram characteristics for an MLO view. (b) Example of preprocessing result. Pectoral muscle segmentation in red, peripheral margin in yellow, ROI for percent density estimation without color overlay. (c) Example segmentation of a breast with D_{mam}=59 %.

3 Results

Analysis of inter-observer variation revealed inter-reader correlations ranging from $r = 0.96$ (Reader III vs. Reader V) to $r = 0.76$ (Reader IV vs. Reader V) with deviations to the respective reference ranging from $[-20, +30]$ (Reader V) up to $[-40, +40]$ (Reader I) for the 95 % confidence interval and min/max deviations of $[-60, +60]$. Mean deviations ranged from -8.8 (Reader III) to $+11.9$ (Reader I) with standard deviations ranging from $\sigma = 12.8$ (Reader III) to $\sigma = 18.1$ (Reader IV). The automated approach shows good to excellent correlation to the respective readers (Reader IV: $r = 0.72$; Reader I: $r = 0.86$) with a deviation range of $[-37, +22]$ for the 95 % confidence interval and $[-57, +47]$ for min/max deviations. Its average deviation is -9.2 with standard deviation $\sigma = 15.3$ (cf. Fig. 3 and Table 1).

Consistency of the method was evaluated by correlating CC and MLO views on a per breast basis resulting in excellent correlation (r=0.88). Runtime performance is 1.5 s per image on a standard PC. An example result of the method is shown in Fig. 2 (c).

ISBN: 978-87-981270-9-3

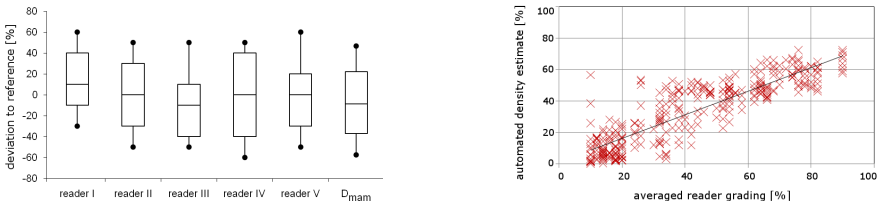

(a) Box-and-whisker plot (b) Scatter plot

Fig. 3. Observer Variations and Algorithm Performance. (a) Box-and-whisker plot of reader and algorithm deviations. Each box reflects the median and 95 % confidence interval, whiskers indicate minimum and maximum. (b) Scatter plot of algorithm results vs. averaged reader gradings.

4 Discussion

The proposed method shows performance similar to the approach recently published by Kallenberg et al. [7], although the studies differ in various aspects. While Kallenberg resorts to film screen image data focussing on MLO views of the left breast, we developed our method for both CC and MLO views of state-of-the-art FFDM data. Moreover, the patient population followed different design aspects (screening vs. diagnostic, all diagnoses vs. unsuspicious findings only, different distributions of clinical ACR classification).

Most notable is the validation scheme chosen in this study. The presented approach displays the power of estimating mammographic percent density about as well as a skilled human reader (cf. Table 1). Although Readers I, II, III and V perform slightly better, one has to keep in mind that human reading was done on a per patient basis reflecting clinical practice, whereas the presented algorithm works on a per image basis. Additionally, readers were using a discrete 11-scale categorial assessment (workflow issues did not allow to use Cumulus [2] as reference standard) as a compromise between routine ACR classifications and the continuous scale, on which automated results are given. Both factors contribute towards agreement being more easily achievable between two human readers than between the automated approach and a human reader.

Fig. 3 (b) reveals that the automated breast density estimates do not exceed 80 % and consistently follow a less steep slope. This behaviour confirms the general observation that humans tend to underestimate the size of peripheral regions, and thus overestimate percent density especially in dense breasts [9].

Although the BI-RADS standard for mammography [4] requires the pectoral muscle also to be visible on CC views, the requirement is not satisfied in the majority of image data. As, moreover, the influence on breast density estimates is reduced on CC views due to the visible portion being small compared to the entire depicted tissue region, the current approach does not include pectoral muscle segmentation on CC views.

ISBN: 978-87-981270-9-3

Currently, a clinical acceptance study with experienced radiologists is ongoing, demonstrating that our approach for fully-automated breast density assessment seamlessly integrates into clinical routine for breast cancer screening.

References

1. Boyd, N.F., Martin, L.J., Rommens, J.M., et al.: Mammographic density: a heritable risk factor for breast cancer. Methods Mol Biol 472, 343–60 (2009)
2. Byng, J.W., Boyd, N.F., Fishell, E., et al.: The quantitative analysis of mammographic densities. Phys Med Biol 39(10), 1629–38 (1994)
3. Diffey, J., Hufton, A., Astley, S., et al.: Estimating individual cancer risks in the UK national breast screening programme: A feasibility study. In: IWDM'08. LNCS, vol. 5116, pp. 469–76. Springer (2008)
4. D'Orsi, C.J., Bassett, L.W., Berg, W.A., et al.: BI-RADS: Mammography, 4th edition. In: D'Orsi, C.J., Mendelson, E.B., Ikeda, D.M., et al. (eds.) Breast Imaging Reporting and Data System: ACR BI-RADS - Breast Imaging Atlas. American College of Radiology, Reston, VA (2003)
5. van Engeland, S., Snoeren, P.R., Huisman, H., et al.: Volumetric breast density estimation from full-field digital mammograms. IEEE Trans Med Imaging 25(3), 273–82 (2006)
6. Jeffries-Chung, C., Diffey, J., Berks, M., et al.: Automated assessment of area of dense tissue in the breast: A comparison with human estimation. In: Marti, J., et al. (eds.) IWDM'10. LNCS, vol. 6136, pp. 168–74. Springer (2010)
7. Kallenberg, M.G.J., Lokate, M., van Gils, C.H., Karssemeijer, N.: Automatic breast density segmentation: an integration of different approaches. Phys Med Biol 56(9), 2715–29 (2011)
8. Kontos, D., Bakic, P., Acciavatti, R., et al.: A comparative study of volumetric and area-based breast density estimation in digital mammography: Results from a screening population. In: Mart, J., Oliver, A., Freixenet, J., Mart, R. (eds.) Digital Mammography, LNCS, vol. 6136, pp. 378–85. Springer (2010)
9. Makaronidis, J., Berks, M., Sergeant, J., et al.: Assessment of breast density: reader performance using synthetic mammographic images. In: Proc SPIE Med Imaging 2011. vol. 7966, p. 796603. SPIE (2011)
10. Mandelson, M.T., Oestreicher, N., Porter, P.L., et al.: Breast density as a predictor of mammographic detection: comparison of interval- and screen-detected cancers. J Natl Cancer Inst 92(13), 1081–7 (2000)
11. Saftlas, A.F., Hoover, R.N., Brinton, L.A., et al.: Mammographic densities and risk of breast cancer. Cancer 67(11), 2833–8 (1991)
12. Snoeren, P.R., Karssemeijer, N.: Thickness correction of mammographic images by means of a global parameter model of the compressed breast. IEEE Trans Med Imaging 23(7), 799–806 (2004)
13. Tromans, C., Brady, M.: An alternative approach to measuring volumetric mammographic breast density. In: Astley, S.M., Brady, M., Rose, C., Zwiggelaar, R. (eds.) IWDM'06. LNCS, vol. 4046, pp. 26–33. Springer (2006)
14. U.S. Connecticut Senate (ed.): Bill No. 458. Public Act No. 09-41 (2009)
15. Wolfe, J.N.: Breast patterns as an index of risk for developing breast cancer. AJR Am J Roentgenol 126(6), 1130–7 (1976)
16. Zhou, C.A., Wei, J., Chan, H.P., et al.: Computerized image analysis: Texture-field orientation method for pectoral muscle identification on MLO-view mammograms. Med Phys 37(5), 2289–99 (2010)

ISBN: 978-87-981270-9-3

An Automated Workflow for Patient-Specific Biomechanics-based Breast Image Analysis

Vijay Rajagopal[1⋆], Richard G. Boyes[1], Mihailo Azhar[1], Thiranja Prasad Babarenda Gamage[1], Poul M.F. Nielsen[1], and Martyn P. Nash[1]

Auckland Bioengineering Institute, University of Auckland, Level 6, 70 Symonds Street, Auckland, New Zealand
v.rajagopal@auckland.ac.nz

Abstract. We present a completely automated process of creating finite element models of the breast for individual-specific biomechanical simulations of patient re-positioning from the prone to other gravity-loading orientations. Breast MRIs of 22 patients were automatically segmented for the skin and rib surfaces. A training set of finite element models was created from these datasets and principal component analysis was conducted to quantify dimensions of shape variation. A novel method of using the results from principal component analysis to automatically create a finite element mesh for an unseen dataset is presented. The final models captured unseen breast shapes with mean ± SD root mean squared projection error (from surface data to model surface)of $1.52mm \pm 0.33mm$ compared to manually guided fitting procedures which create models with average errors of $1.26mm \pm 0.29mm$. We also demonstrate the usability of these models in performing completely automatic, unsupervised biomechanics simulations of the prone to supine reorientation typically required for breast biopsies or second-look ultrasound.

Keywords: breast biomechanics, principal component analysis, breast image analysis, geometric fitting

1 Introduction

Finite element modelling of breast biomechanics has the potential to assist clinicians with the reliable diagnosis of breast cancer by using physics based mechanics simulations to fuse medical images of the breast across different imaging modalities such as x-ray mammograms, magnetic resonanace images (MRI) and ultrasound (US) [3, 10, 5]. A significant challenge that researchers face is the translation of research-based software and expertise into reliable and user-friendly applications that form part of routine analysis of breast cancer images in the clinic.

Challenges facing adoption of finite element models into routine clinical practice include the laborious task of creating models, streamlined methods for identifying parameters necessary for modeling the breast of a specific individual and

⋆ The authors thank Dr. Nico Karssemeijer for providing the breast MRI datasets used in this study. We thank Mr. Ju Zhang and Ms. Nancy Yan for valuable discussions.

speed of computations. Statistical shape models [10] have recently been used as a work around to these problems by establishing a database of patient breast models from which a large set of simulated shapes can be pre-computed. The pre-computed solutions of a specific model which is similar to an "unseen" patient's breast shape is then chosen from the database to provide a prediction of tissue movement for this specific individual.

Although such databases can provide fast predictions of breast deformation for an individual, the accuracy of these model predictions is somewhat compromised because the predictions are not based on a model specific to the individual. Depending on the clinical application and accuracy requirements, patient-specific modelling can further benefit clinical practice of breast cancer diagnosis. For example, tumour tracking between different orientations such as prone and supine must be of sufficient accuracy to ensure that biopsy procedures do not miss cancerous lesions.

We present new methods for a completely automated process of model creation from prone MR images, to model simulation and image warping to create a synthetic prediction of the supine MR image. Such methods remove the need for any manual intervention or expert supervision, thus making it possible to integrate biomechanical modelling into routine clinical practice. The following sections describe the methods that have been developed and demonstrate the automatic process with a database of 22 clinical MR images.

2 Methods

2.1 Data and Image Segmentation

T1-weighted prone MR images were acquired on a 1.5T Siemens Magnetom Vision (TR=8.1, TE=4.0, Matrix 256 X 256 1.25 X 1.25 mm, 108 1.5 mm slices) of 22 subjects from the NHL hospital, UMCN St Radboud, the Netherlands. We corrected all images for non-uniformity using N3 [8].

We use a completely automated process for segmenting breast tissues from MRI based on multi-atlas methods previously used in brain segmentation [1]. The multi-atlas method allows for automatic segmentation for any new MR scan by using a database of manually labelled segmentations as a training set from which a small subset of labelled data sets are selected by the algorithm based on their similarity to the new MR scan (based on mutual information). To create the manual segmentations, we used a thresholding approach combined with manual tracing to outline the skin and chest wall. Once a subset of training scans are selected, they are then automatically registered with the new MR scan to find the optimum alignment and the results are combined using shape space averaging [7] to produce a final segmentation of left and right breast in the new MR scan. The resulting mask from the segmentation process were decimated into a cloud of data points that cover the skin and rib surfaces. This technique was tested on the 22 patient datasets by creating a database from these patient datasets, and automatically segmenting each image stack via a leave one out approach.

ISBN: 978-87-981270-9-3

2.2 Mesh Generation and Principal Component Analysis

Once a segmentation of breast images is acquired, there exist third-party software that automatically create tetrahedral meshes as outlined by [9, 3]. However, our aim is to develop a method for automatic mesh generation using principal component analysis (PCA) for two main purposes: (i) To establish a framework for automatic incorporation of new patient data and meshes into the PCA framework for iterative improvement in our quantification of breast shape variation and (ii) by performing PCA, we can establish node-to-node correspondence between all the patient models and breast anatomy. As will be shown in Section 3.3 this enables automation of defining kinematic constraints in mechanics simulations because of the association of anatomical regions with specific nodes (such as the nipple or ribs).

We model breast deformations using a cubic-Hermite interpolation based hexahedral finite element representation of breast geometry [4]. Unlike traditional finite element description schemes such as linear interpolation, cubic-Hermites are favoured due to their superior solution convergence properties in mechanics simulations [11]. However, critical to the successful use of these techniques is a good initial mesh geometry. This is conventionally acquired by manual positioning of nodes of a generic mesh to capture the gross contours of the breast. This is a tedious task that is compounded by the significant variation in breast shape across the population. We propose a novel method of combining the knowledge about breast shape variation with the least-squares fitting procedure to develop a completely automated method for mesh generation.

The basis of this new method is a training set or database of breast shapes that are used to quantify the variation in shape across the population via PCA [2]. Let us define $\mathbf{x}_i$ as the shape vector representing i^{th} dataset in the population: $\mathbf{x}_i = \{x_{i\mu} : \mu = 1..d \times n_P\}$ where d is the number of dimensions and n_P is the number of landmarks (be it anatomical, mathematical or pseudo landmarks) used to describe the shape of the object. With the goal of performing PCA on a significantly large training dataset, our aim was to identify landmarks that are straightforward to distinguish from MR images. However, apart from the nipple, there are typically few other readily identifiable anatomical landmarks. Therefore, we manually created a finite element mesh for each training dataset using the techniques in [4] together with a single template mesh in order to establish an approximate point-to-point correspondence of the nodes. The node representing the nipple on the template mesh was manually positioned and fixed to match the position of the nipple in each of the 22 patient MR scans. Nodes of the template mesh were manually adjusted to represent the interface between the arm and the chest in each of the data sets that the model was fitted to. Most other nodes in the template mesh were evenly distributed (manually) across the breast surface for each scan, thus making them additional pseudo landmarks. These nodes of each fitted mesh were then concatenated into a shape vector.

The shape vectors of each patient dataset were collated into a $d \times n_P \times n_s$ matrix, $\mathbf{M}$, where n_s is the size of the sample of breast shapes used to quantify the shape variation. Principal component analysis using singular value decom-

ISBN: 978-87-981270-9-3

position on $\mathbf{M}$ provided the mean shape vector, $\overline{\mathbf{x}}$, and $n_s - 1$ singular values and associated vectors (equivalent to eigenvectors and eigenvalues when performing eigen analysis on the co-variance matrix of $\mathbf{M}$) that quantify the orthonormal directions and magnitudes of the principal modes of variation. An unseen shape can thus be approximated by the mean and a weighted (w_j) sum of the principal components as $\mathbf{x}_{new} = \overline{\mathbf{x}} + w_j \mathbf{N}_j \quad j = 1..n_s - 1$ where $\mathbf{N}_j$ is the j^{th} principal vector. Hence, given a data set for a new patient, an optimal set of weights that best approximate the new shape can be computed. The objective function of this optimisation problem was set to be the minimum root-mean-squared error of closest-approach projections from each data point onto the mesh surface.

The efficacy of this algorithm in automatically providing a good initial mesh was determined by performing the complete series of leave-one-out tests. PCA was conducted on 21 out of the 22 models repeatedly until every patient dataset had been left out of the analysis once. The PCA results were then used in the PCA-based fitting algorithm to fit the "unseen" dataset that was left out of the principal component analysis. Each of these fits was first done using all 21 modes of variation. The errors from these different fits were assessed for the closeness of the initial model to the unseen dataset. The models were then further fitted to completely match the unseen data using the nonlinear least squares technique mentioned earlier. A select few models were also fitted using 14 modes (explaining 95% of the variation), 7 modes of variation (explaining 82% of variation) and 4 modes of variation (explaining 72% of the variation in the population) to investigate the possibility of reducing the number of weights that need to be identified.

2.3 Biomechanics Framework

We model breast deformations under gravity loading using the finite element implementation of large deformation elasticity theory. Model simulations include the calculation of an unloaded state of the breast without the effects of gravity to ensure accuracy as stated by [6]. The breast constitutes fat and fibroglandular tissue enclosed by a layer of skin. While most recent studies [10] discuss the need for anisotropic constitutive relations to describe the mechanical behaviour of the breast, we use the neo-Hookean model, $c_1(I_1 - 3)$, representing isotropic, incompressible behaviour for demonstration of automaticity here. The methods described in this study can readily be applied with other constitutive equations. The stiffness value was set to $0.1kPa$ based on previous literature estimates [6]. We set a tissue density of $0.001g/mm^3$ based on the assumption that biological tissues are predominantly composed of water. With regards to boundary conditions for these illustrative simulations, we assumed that the breast tissue was firmly fixed to the rib surface and let the displacements of all other degrees of freedom be determined by solving the mechanics equations. Additionally, nodes that formed part of the interface between the arm and chest as the person lies prone on the bed for imaging were also fixed to represent the arms being held straight and close to the body. Since a template mesh was used to fit each MR

ISBN: 978-87-981270-9-3

data scan and a few pseudo landmarks were positioned to represent the arm-chest interface (as described in section 2.2), the node numbers for this region were known a-priori and automatically selected in order to enforce displacement boundary conditions in that region.

3 Results and Discussion

3.1 Principal Components of Breast Shape

A table of the proportion of variance captured by each principal component is shown in Table 1. Table 2 shows the first three modes of shape variation. Principal component one accounts for overall size of the breast (i.e. scaling), principal component two explains variations in chest width and principal component three explains variations in breast cup size.

Table 1. Proportion of total variance described by each principal component

Mode	1	2	3	4	5	6	7	8	9	10	11-21
% of variation	48%	11%	7%	5%	4%	3.5%	3.1%	2.7%	2.3%	2.1%	11.3%

Table 2. First 3 principal components of breast shape.

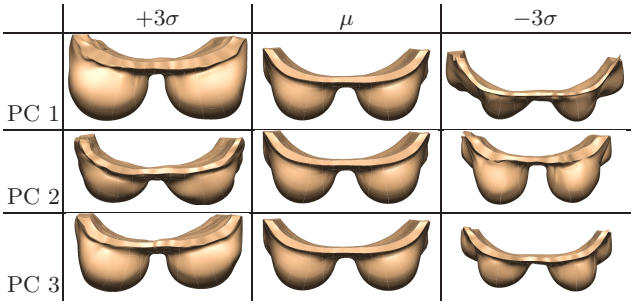

3.2 PCA for Mesh Generation

Table 3 shows the performance of the PCA-based fitting method in creating a suitable initial mesh in the leave-one-out tests when using all 21 principal modes of variation. The first column presents the errors from a manual fit of the generic model to each patient breast shape for comparison ($\mu = 1.26mm$, $\sigma = 0.29mm$).

ISBN: 978-87-981270-9-3

The second column shows the errors from only optimising for the weights on the principal components for each unseen dataset ($\mu = 3.36mm$, $\sigma = 0.33mm$). The final column shows the final errors after the PCA-based models were further fitted to match the patient breast shape using a standard non-linear least squares technique ($\mu = 1.52mm$, $\sigma = 0.41mm$). These fits were conducted completely automatically, without any manual intervention.

These results show that PCA-based fitting provides a good initial mesh for further refinement. The higher average error at the end of a PCA-based fit is primarily due to the availability of only 21 degrees of freedom (the 21 PC weights) as opposed to the 2160 degrees of freedom (all the nodal degrees of freedom in the mesh) during a standard non-linear least-squares fit. It is likely that this error would also reduce when using a larger database of patient datasets. The large error for patient 5 is due to the significant compression imposed on the breast by the compression pads in the breast MR coil which makes this shape significantly different from the rest of the shapes in the database. Nevertheless, PCA-based fitting completely removes the need for manual guidance of model creation. The last row of Table 3 shows that when a t-test is performed between column 3 (PCA-based refined fit) and column 1 (individual mesh fits), the p-value of 0.58 indicates there being no evidence of differences in error between the two methods. The reported error magnitudes for our proposed method do not preclude the method from being used in a clinical environment.

PCA-based fits were also conducted using only 14 modes, 7 modes and 4 modes for the first 4 patient datasets. These were conducted to determine if fewer number of weights would suffice for the generation of an initial mesh and it was indeed possible to even use as low as 4 principal components to generate a suitable initial mesh.

3.3 Unsupervised Simulation of the Supine Breast

Once a finite element model has been automatically fitted to a specific patient's breast shape, it is then possible to establish a consistent set of loading and boundary constraints to initiate a biomechanics simulation from the prone to the supine configuration. We have the capability to embed medical images into these models to then simulate clinical images in other orientations of interest. Here we show (Fig. 1) the process of transforming the prone MRI of patient 19 into synthetic MRIs depicting the breast shape and tissue configuration in the supine orientation. Since the boundary and loading conditions on the breast under gravity are the same across the entire population (only mechanical properties and breast shape vary) this simulation can be conducted completely unsupervised. We envision that with this power, simulations and generation of supine images could be conducted on a dedicated server for a clinician to later download and visualise during their diagnosis or surgical procedure.

ISBN: 978-87-981270-9-3

Table 3. Performance of PCA-based mesh fitting. RMS projection errors (in mm) are presented.

Patient	Individual-Fit	21 PC-Based-Fit	Final Fit Error
1	1.73	3.0	1.33
2	1.8	3.3	1.26
3	1.87	2.94	1.67
4	1.5	3.29	1.02
5	1.45	3.52	2.77
6	1.4	3.9	1.73
7	1.74	3.4	2.00
8	1.68	2.62	1.35
9	1.66	3.12	1.27
10	1.69	3.18	1.98
11	1.31	2.94	1.14
12	0.84	3.36	1.57
13	1.56	3.1	1.28
14	0.83	3.19	1.82
15	1.53	3.49	1.03
16	1.48	3.61	1.67
17	1.66	3.69	1.32
18	1.56	3.65	1.15
19	1.32	3.84	1.93
20	1.21	3.47	1.41
21	1.2	3.9	1.42
22	0.99	3.3	1.26
mean±SD	1.26±0.29	3.36±0.33	1.52±0.41
t-test	col1 vs col2	col2 vs col3	col3 vs col1
P-value	3.4869E-14	2.12457E-14	0.58

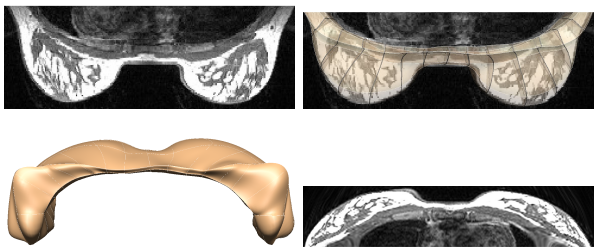

Fig. 1. Automatic creation and solution of a finite element model of the breast from prone MR images to simulate the supine configuration. Top left: Prone MRI slice, top right: MRI embedded in 3D model, bottom left: model predicted supine shape, bottom right: synthetic supine MRI slice.

ISBN: 978-87-981270-9-3

4 Conclusions

We have presented a completely automated method for creating biomechanical models of the breast from patient MR images and for simulating the supine breast MRI. Model creation involves the use of principal component analysis on a database of breast shapes. Any unseen patient breast shape can be expressed as a weighted sum of the principal components. As such, a template model was fitted to an unseen dataset by finding an optimal set of weights of the principal components that minimise the error in capturing the patient's breast skin and rib surfaces. The complete procedure can produce meshes with $\mu = 1.52mm$, $\sigma = 0.41mm$ root mean squared errors. We have also demonstrated the capability to use these models to simulate the supine breast shape and produce synthetic supine MRI. These methods demonstrate for the first time, the possibility of using patient-specific biomechanical modelling in an unsupervised manner to enable ready integration into routine clinical workflows.

References

1. Aljabar, P., Heckemann, R., Hammers, A., Hajnal, J., Rueckert, D.: Multi-atlas based segmentation of brain images: Atlas selection and its effect on accuracy. NeuroImage 46, 726–738 (2009)
2. Davies, R., Twining, C., Taylor, C.: Statistical Models of Shape: Optimisation and Evaluation. Springer (2008)
3. Del Palomar, A., Calvo, B., Herrero, J., Lopez, J., Doblare, M.: A finite element model to accurately predict real deformations of the breast. Medical Engineering and Physics 30, 1089–1097 (2008)
4. Fernandez, J., Mithraratne, P., Thrupp, S., Tawhai, M., Hunter, P.: Anatomically based geometric modelling of the musculo-skeletal system and other organs. Biomechanics and Modeling in Mechanobiology 2, 139–155 (2004)
5. Lee, A., Schnabel, J., Rajagopal, V., Nielsen, P., Nash, M.: Breast image registration by combining finite elements and free-form deformations. Lecture Notes in Computer Science 6136/2010, 736–743 (2010)
6. Rajagopal, V., Lee, A., Chung, J., Warren, R., Highnam, R., Nash, M., Nielsen, P.: Creating individual-specific biomechanical models of the breast for medical image analysis. Academic Radiology 15(11), 1425–1436 (2008)
7. Rohlfing, T., Maurer, C.: Shape based averaging. IEEE Transactions on Medical Imaging 16, 153–161 (2007)
8. Sled, J., Zijdenbos, A., Evans, A.: A non-parametric method for automatic correction of intensity nonuniformity in mri data. IEEE Transactions in Medical Imaging 17, 87–97 (1998)
9. Tanner, C., Hipwell, J., Hawkes, D.: Statistical deformation models of breast compressions from biomechanical simulations. Lecture Notes in Computer Science 5116, 426–432 (2008)
10. Tanner, C., White, M., Hawkes, D., Guarino, S., Douek, M., Craggs, M.: Large breast compressions: Observations and evaluation of simulations. Medical Physics 38(682) (2011)
11. Zienkiewicz, O., Taylor, R.: The Finite Element Method: The Basis, vol. 1. Butterworth-Heinemann, 5 edn. (2000)

ISBN: 978-87-981270-9-3

Breast X-ray and MR Image Fusion using Finite Element Modelling

Angela W. C. Lee[1], Vijay Rajagopal[1], Hayley M. Reynolds, Anthony Doyle[2], Poul M. F. Nielsen[1,3] and Martyn P. Nash[1,3]

[1]Auckland Bioengineering Institute, The University of Auckland, New Zealand
(angela.lee@auckland.ac.nz)
[2]Auckland City Hospital, Auckland, New Zealand
[3]Department of Engineering Science, The University of Auckland, New Zealand

Abstract. We present a novel multi-modality image registration technique based on individual-specific biomechanical finite element (FE) models of the breasts. Information from 3D magnetic resonance (MR) images was aligned with X-ray mammographic images using non-linear FE models to simulate the large compressive deformations between the two modalities. A perspective ray-casting algorithm was used to generate 2D projections of the FE-warped 3D MR images. The clinical applicability of the method was demonstrated using X-ray and MR images of a breast cancer patient. This novel framework integrates modelling and image processing techniques, which allows us to iteratively improve the predictions of the biomechanical models by modifying modelling assumptions regarding the boundary conditions and mechanical properties of the breasts.

1 Introduction

X-ray mammography and magnetic resonance imaging (MRI) are two commonly used modalities to image the breast in the diagnosis and management of breast cancer. X-ray mammograms are useful for locating tumours and micro-calcifications, whereas contrast-enhanced MR images can indicate regions of angiogenesis, which may be associated with breast cancer. It would therefore be of clinical benefit to be able to collocate information from the 2D X-ray mammograms of the compressed breast with information from 3D MRI of the pendulous breast.

In previous studies, the difference in the shape of the breast was accounted for during image registration using simple transformations of the breast MR images such as affine deformations [1], using geometric approaches [2], or thin plate splines to align projections of the MR image with mammograms [3]. Although these methods allow for simplified and fast calculations, they do not reliably reproduce the deformation of the breast tissues from the prone to compressed states and this may give rise to substantial registration errors. Further studies have shown that affine transformations were insufficient to recover the non-linear deformations between sequential prone MRI acquisitions [4]. Thus, for the much larger deformations of the

ISBN: 978-87-981270-9-3

breast tissues during mammographic compressions, it is unlikely that such image transformations would be suitable for multi-modality data fusion.

Small-strain finite element (FE) models derived from prone MRI have been proposed to simulate mammographic compressions [3]. However, no validation of these linear FE models for mammographic breast compressions was performed, and since the small-strain theory is not valid for large deformations (>1%), the mechanics predictions are likely to be questionable. Finite strain formulations have thus been used to model compressive deformations of the breasts [5, 6].

In this paper, we describe a novel method for the multi-modal 3D-2D non-rigid registration of prone MRI to X-ray mammography using non-linear FE models. This method was systematically validated using images from compression experiments on a breast phantom, and then applied to clinical images from a breast cancer patient. The integration of individual-specific finite element models of the breast using finite deformation elasticity coupled with contact mechanics and a perspective ray-casting algorithm to generate realistic mammograms has not been previously investigated. The resulting pseudo-mammograms were compared with the clinical X-ray mammograms, and the results were used to assess the modelling assumptions and update the parameters of the FE models. This iterative approach of comparing clinical mammograms and FE model predictions as feedback to the modelling framework has not been previously explored.

2 Methods

2.1 Multi-modality imaging

A CIRS triple modality breast shaped phantom was imaged before and during 46% and 49% compressions in its anterior-posterior (AP) and cranial-caudal (CC) axes, respectively, using a 1.5T Siemens MRI scanner and a GE Senograph DS mammography system. A T_1 weighted FL3D pulse sequence was used for MR acquisition and the imaging parameters were: dimensions 512 x 512 pixels; field of view 350mm x 350mm; 176 slices; slice thickness 0.75mm. The breast phantom contained 12 distinct inclusions that were visible under MR and X-ray imaging. The same systems were used to acquire images from a breast cancer patient with two small tumours in order to illustrate the clinical utility of the proposed methods.

2.2 FEM compression and MR image warping

The MRI data for the uncompressed phantom and the prone breasts were segmented and used to create customised FE models [6]. Compression was modelled using finite deformation elasticity coupled with contact constraints based on the penalty method [7]. The biomechanics reference state was estimated by removing gravity from the uncompressed models [9]. The FE compression models were used to non-rigidly warp the MR images of the uncompressed bodies [Figure 1]. The breast phantom was modelled using the isotropic and incompressible neo-Hookean constitutive relation: $W=C_1(I_1-3)$, where I_1 is the first principal invariant of the

ISBN: 978-87-981270-9-3

deformation tensor and C_1 is the stiffness parameter, which was previously estimated as C_1=1.07kPa [10]. The frictional coefficient between the breast phantom and our perspex compression device was determined experimentally to be 0.95. The penalty values for the normal (frictionless) and tangential (frictional) components of the contact between the breast phantom and the compression device were set to 50MPa/m and 60kPa/m, respectively.

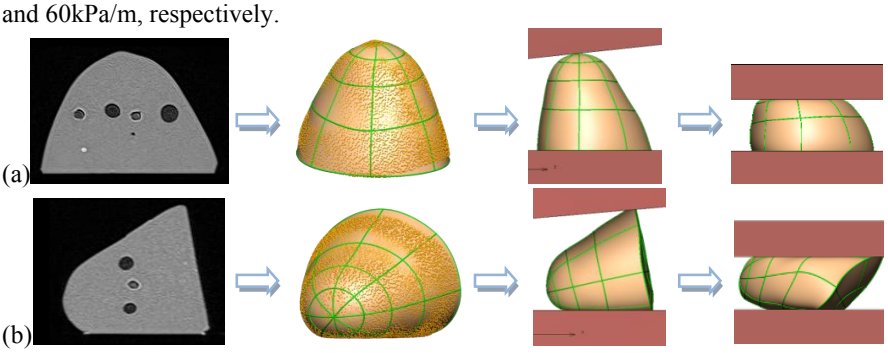

Figure 1: MR images of the uncompressed breast phantom were segmented to create FE models for simulating the AP (a) and CC (b) modes of compression.

The breast tissues were modelled as isotropic, homogeneous, and incompressible solids. The biomechanical reference state for compression was determined by using the model to reverse the effect of gravity on the prone configuration. The initial stiffness value for the breast tissues was previously estimated to be 400Pa [6].

The breast tissues were allowed to slide over the surface of the ribs to mimic the loose attachment via Cooper's ligaments. In several previous studies using biomechanical FE models of the breasts [3, 5], displacements of nodes on the skin surface were explicitly prescribed, however this gives rise to physically implausible reaction forces on the free (skin) surface of the breast. In contrast, the contact constraints between the plates and the chest wall [6, 11] used in this study more closely matches the physical situation. The final distances between the compression plates were recorded as 64mm, corresponding to 52% compression for the patient.

2.3 Generating a pseudo-mammogram from FE-warped MRI

X-rays in a mammography system emanate from a point source. To simulate this process, a perspective ray-casting algorithm was used to project the 3D images into 2D [3, 7]. A pseudo mammogram image was then calculated using the Beer-Lambert law:$I = I_0 e^{-\sum_i \mu_i x_i}$, where the transmitted, I and incident, I_0 X-rays are related using the path length, x_i through material i, and its effective attenuation coefficient, μ_i.

Effective attenuation coefficients can be calculated from the energy spectrum that is emitted by the mammography machine and the attenuation coefficient spectrum using: $\mu_i = -\frac{1}{x}\ln\left[\sum_{j=1}^{N}\frac{I_j}{I_0}\mathrm{e}^{-\mu_j x}\right]$, where I_j is the number of photons at the energy value j, I_0 is the incident energy beam (approximated as a sum of the photons at each energy level j), μ_j is the mass attenuation coefficient at energy j, and x is an arbitrary thickness of tissue through which the beam passes [12]. The physical density and

ISBN: 978-87-981270-9-3

attenuation characteristics of the bulk of the breast phantom simulates that of an average 50% glandular breast [13]. The cystic and solid masses were represented as water and ductal infiltrating carcinoma, respectively [14]. Based on the polyenergetic X-ray spectrum for a rhodium anode and rhodium filtering at 31kVp [13], the effective attenuation parameters for the bulk, solid and cystic masses were estimated to be $0.79cm^{-1}$, $1.04cm^{-1}$ and $0.99cm^{-1}$, respectively. For the patient case, the peak voltage was 29kVp, so the monoenergetic equivalent attenuation coefficients for adipose, glandular, skeletal muscle, and infiltrating ductal carcinoma were calculated as: $0.73cm^{-1}$, $0.92cm^{-1}$, $1.10cm^{-1}$ and $1.09cm^{-1}$, respectively.

The above methods provide an approximation of an initial "for processing" (raw) mammogram. However, the acquisition provided "for presentation" images, which involve certain image processing enhancements to allow the clinicians to better interpret the information. For the GE Senographe system, this involves unsharp masking, thickness equalisation and a negative logarithmic transform. Unsharp masking is used to sharpen an image (from y to y') and can be expressed as $y' = y + c * \big(y - s(\sigma)\big)$, where s is the smoothed image and c is a constant determining the level of enhancement [15]. The blurring was performed using Gaussian smoothing.

Thickness equalisation compensates for the lower image intensities at the edge of the compressed breast by the addition of an image representing the tissue thickness. A 2D image was generated by projecting through a 3D mask of the FE warped image. This image was then normalised and inverted, then multiplied with a correction factor representing the image intensity of the fatty tissue or bulk material (obtained from the X-ray image) to generate the thickness image.

3 Results

3.1 Validation using a breast-shaped phantom

(a) (b) (c) (d)

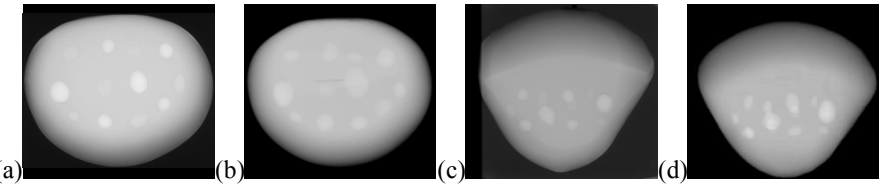

Figure 2: Experimental compressed (a) AP and (c) CC X-rays are compared against (b) AP and (d) CC pseudo X-rays generated from FE-warped 3D images.

The FE model of the breast phantom was compressed and used to deform the segmented images of the phantom. A 2D projection image was then generated from the 3D FE-warped image via the Beer-Lambert law and compared with the experimental X-ray image [Figure 2]. Landmark based measures such as the area overlap (*Dice* coefficient); symmetric mean absolute surface distance (*SMAD*), and the centroid location were evaluated for each of the inclusions. The mean (±SE) errors between the experimental X-rays and the projected FE-warped pseudo X-rays were: *Dice*: 78.6% ± 0.9%; *SMAD*: 1.10mm ± 0.04mm; centroid error: 1.35mm ± 0.06mm.

ISBN: 978-87-981270-9-3

$$Dice = \frac{2|A_j \cap B_j|}{|A_j|+|B_j|} * 100,\ j = 1..12 \qquad \boldsymbol{SMAD} = \frac{\mathbf{1}}{\boldsymbol{n_a + n_b}}\left(\sum_{\boldsymbol{n_a}} \left|\boldsymbol{d_k^{ab}}\right| + \sum_{\boldsymbol{n_b}} \left|\boldsymbol{d_k^{ba}}\right|\right)$$

where A is the target image, B is the simulated image, d_k^{ab} is the minimum distance between the k^{th} surface voxel on A and the surface voxels on B, and n_a, n_b are the number of surface voxels in A and B, respectively.

3.2 Application to clinical images from breast cancer patients

Having now developed and validated a modelling framework for 3D-2D multimodality image registration, the approach was demonstrated using clinical images from a breast cancer patient. This framework was then used to further improve biomechanical modelling of mammography.

Two small tumours were identified by an expert radiologist on the X-ray mammograms and in the prone MR images of the right breast [Figure 6]. However, it was noted that the two tumours appeared connected in some MRI slices. Therefore in the 2D pseudo-mammogram, one continuous tumour was indicated. The accuracy of the approach was based on the localisation accuracy of this tumour.

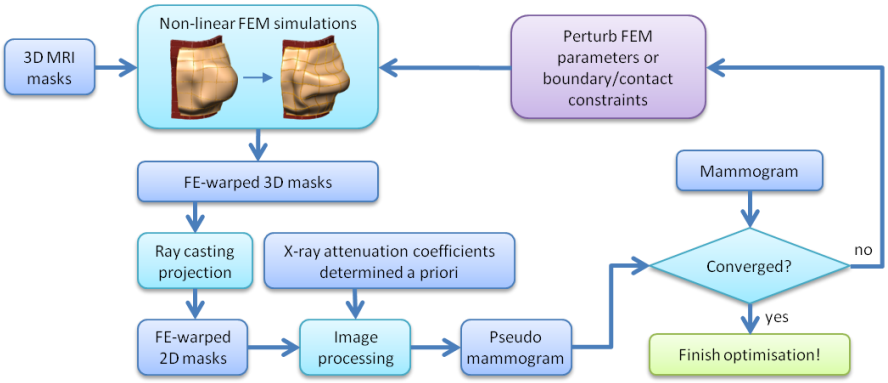

Figure 3: Framework for 3D-2D multimodal image registration to estimate FE-model parameters such as mechanical properties and boundary conditions

The compression constraints have a significant impact on the modelling accuracy. However, the location of the compression plates with respect to the uncompressed breast is unknown. Furthermore, the angle of the compression plates with respect to the patient varies depending on the patient's positions during mammography. For example, a patient can rotate about the vertical (*yaw*) axis, so that more axilla tissue is captured in the image [Figure 4]. In a previous study, this yaw angle was assumed to be 25º towards the axilla edge: this was based on a subjective visual assessment comparing the contours of the breast in the mammogram with the model [6]. Patients can also lean to the side resulting in rotation about longitudinal axis (*roll*). This rotational information is not captured during mammographic imaging, thus the intial roll angle was set to 0º. Novel methods were developed to automate the plate alignment based on the X-ray images, and hence reduce the subjectivity [Figure 3].

ISBN: 978-87-981270-9-3

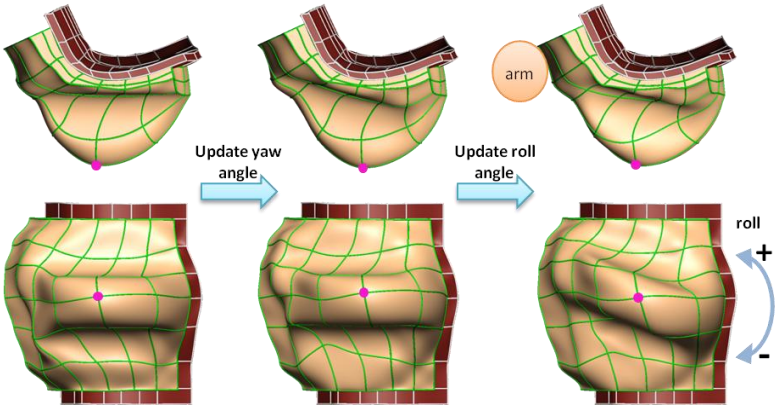

Figure 4: The location of the compression plates was altered by updating the yaw and roll angles based on image similarity.

As one of the few consistent landmarks in the breast, the nipple was used to set the translation of the compression plates. The yaw angle was then set by maximising the normalised cross correlation using a rigid rotation centered about the nipple location. The positioning of the compression plates was then updated and the FE simulation was repeated until the yaw rotation angle and translation parameters were converged [Figure 4]. This calculation of the yaw angle and translation substantially improved the accuracy of the tumour alignment (SMAD reduced from 16.4mm to 8.4mm).

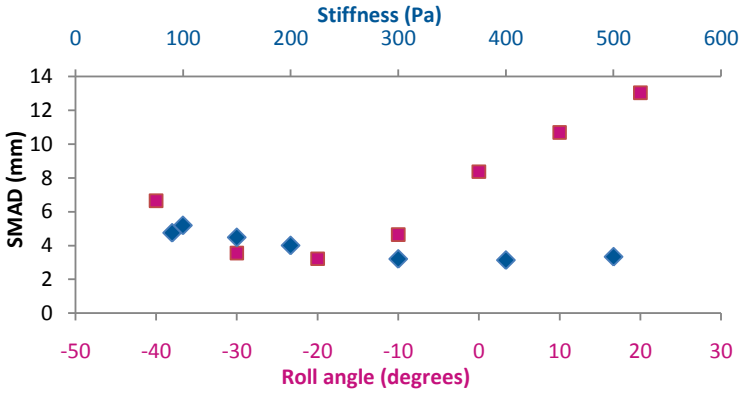

Figure 5: Sensitivity of the FE model deformations with respect to the roll angle of the compression plates and the mechanical stiffness of the breast model.

The effects of breast roll and stiffness were also considered. In a previous study [5], the roll was assumed to deviate by ±30º. Here, the sensitivity to breast roll was assessed at 10º intervals from -40º to 20º using the SMAD of the tumour as an accuracy measure [Figure 5]. Note that the minimum error occurred at a roll angle of -20º, but the error remained relatively stable between roll angles of -30º to -10º. This indicates that breast roll needs to be accounted for in simulating mammographic compressions; however it is sufficient to be accurate to within ± 10º.

ISBN: 978-87-981270-9-3

Figure 6, shows how modifying the location of the compression plates substantially improved the tumour alignment. It should be noted that for the case study considered here, the tumour was located near the sternum and close to the skin. The sensitivity of the localisation accuracy with respect to the roll angle is likely to be greater in this case compared to that with a tumour located more centrally within the breast.

The sensitivity of the material stiffness (with C_1 ranging from 90Pa to 500Pa) was also investigated using the tumour *SMAD* as an accuracy measure. In Figure 5, the SMAD for the tumour was approximately constant for stiffness values between 300-500Pa, with the error ranging from 3.1mm to 3.3mm. Thus, the kinematics of compression may have a greater effect on the accuracy of the FE model deformations compared to the breast tissue stiffness. It is thus possible that customised estimation of the mechanical properties is not required for reliable compression simulations, although this needs to be verified using additional patient data.

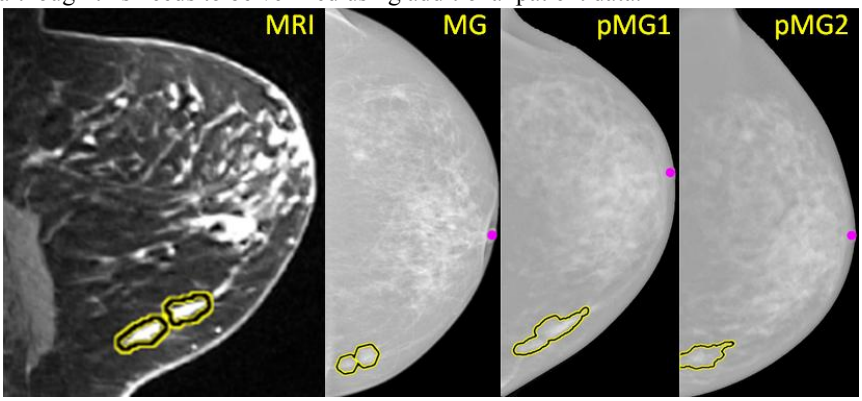

Figure 6: Prone MRI, mammogram (MG) and pseudo-mammograms (pMG) for a breast cancer patient. Tumours are outlined in yellow and the nipple location is highlighted in pink. Initially the plates were positioned by visual alignment (pMG1). Automatically updating the translation, yaw and roll of the compression plates substantially improved the alignment (pMG2).

4 Discussion

We have proposed a new method for non-rigid registration of 3D MR images to 2D X-ray mammograms using non-linear FE modelling of the breast to predict the tissue deformations from the prone gravity-loaded state to a compressed configuration. The method was validated using MR and X-ray images of a breast phantom under various levels of compression and the target registration error (based on the 12 inclusions) was less than the size of 2 MRI voxels (0.68mm x 0.68mm x 0.75mm).

We have demonstrated the applicability of this approach to breast cancer imaging. The sensitivity of the material properties and boundary conditions on mammographic compression simulations was assessed for a breast cancer patient. A novel automated method for defining the location and orientation of the compression plates based on the clinical images of the breasts was proposed and demonstrated. Best localisation

ISBN: 978-87-981270-9-3

results were found with a roll between -10º and -30º, whereas the error was relatively insensitive to mechanical stiffness based on a single case study with one feature used for the error measure. Currently these techniques are being applied to other patient cases. In future work, heterogeneous mechanical properties of the internal structures will need to be incorporated into the mechanics simulations.

The use of a biophysically-based modelling tool that can co-localise features across different breast imaging modalities, including MRI and X-ray mammography, will potentially help clinicians in the diagnosis and management of breast cancer.

5 References

1. Kita, Y., et al., *A CAD system for the 3D location of lesions in mammograms.* Med Image Anal, 2002. **6**(3): p. 267-73.
2. Behrenbruch, C.P., et al., *Fusion of contrast-enhanced breast MR and mammographic imaging data.* Br J Radiol, 2004. **77**: p. S201-S208.
3. Hipwell, J.H., et al., *A new validation method for X-ray mammogram registration algorithms using a projection model of breast X-ray compression.* IEEE Trans. on Med. Imag., 2007. **26**(9): p. 1190-1200.
4. Rueckert, D., et al., *Nonrigid registration using free-form deformations: Application to breast MR images.* IEEE Trans. on Med. Imag., 1999. **18**(8): p. 712-721.
5. Tanner, C., et al., *Breast shapes on real and simulated Mammograms.* LNCS, 2010. **6136**: p. 540-547.
6. Reynolds, H.M., et al. *Mapping breast cancer between clinical X-ray and MR images*. in *Computational Biomechanics for Medicine V (MICCAI2010 Workshop)*. 2010: Springer (in press).
7. Pinto Pereira, S.M., et al., *Automated registration of diagnostic to prediagnostic X-ray mammograms: evaluation and comparison to radiologists' accuracy.* Med Phys, 2010. **37**(9): p. 4530-9.
8. Schnabel, J.A., et al., *Validation of nonrigid image registration using finite-element methods: application to breast MR images.* IEEE Trans. on Med. Imag., 2003. **22**(2): p. 238-47.
9. Rajagopal, V., et al., *Determining the finite elasticity reference state from a loaded configuration.* International Journal for Numerical Methods in Engineering, 2007. **72**(12): p. 1434-1451.
10. Lee, A., et al., *Breast image registration by combining finite elements and free-form deformations.* LNCS, 2010. **6136**: p. 736-743.
11. Chung, J.H., et al., *Modelling mammographic compression of the breast.* LNCS, 2008. **5242**: p. 758-65.
12. Robinson, D.M. and J.W. Scrimger, *Monoenergetic approximately of a polyenergetic beam: a theoretical approach.* Br J Radiol, 1991. **64**(761): p. 452-4.
13. Bushberg, J.T., et al., *The essential physics of medical imaging*. 2nd ed. 2002, Philadelphia, Pa. ; London: Lippincott Williams & Wilkins. 848p.
14. Hubbell, J.H. and S.M. Seltzer, *Tables of X-ray mass attenuation coefficients and mass energy-absorption coefficients*. 2004, National Institute of Standards and Technology,Gaithersburg, MD.
15. Bick, U., F. Diekmann, and SpringerLink (Online service), *Digital Mammography*, in *Medical Radiology,*. 2010, Springer-Verlag Berlin Heidelberg: Berlin, Heidelberg.

ISBN: 978-87-981270-9-3

Towards Navigated Breast Surgery Using Efficient Breast Deformation Simulation

Markus T. Harz*[1], Joachim Georgii[1], Kathy Schilling[2], and Horst K. Hahn[1]

[1] Fraunhofer MEVIS, Bremen, Germany
[2] Boca Raton Regional Hospital, Boca Raton, FL, U.S.A.

Abstract. Localization of target structures in open surgical breast procedures relies on metal wire guides to give orientation hints, together with radiological images. Patient positioning, however, is different for image acquisition and surgery. We propose to simulate the breast deformation between these positions to track and visualize the target position, while acquiring the interventional breast shape to guide the deformation. In the proposed setup, a structured light scanning system allows the scan of the surface, and the display of information onto the patient skin. An interactive update of the simulated deformation requires a fast scanning procedure and a real-time capable, robust deformation simulation. In this paper, besides the general system we propose specific extensions of a highly efficient dynamic corotated finite element method (FEM) to incorporate non-linear material properties while maintaining stability and speed of the original simulation. We assess the prone-supine surface distance after deformation of the prone data on a set of five volunteer images.

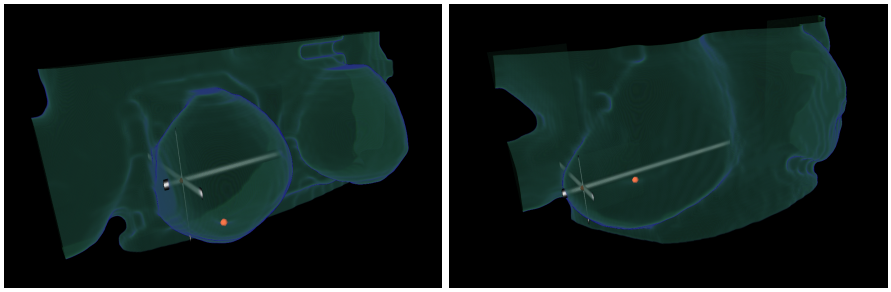

(a) (b)

Fig. 1. The nipple position and a landmark position (cross) visualized in renderings of the prone (a) and supine (b) breast.

* markus.harz@mevis.fraunhofer.de

ISBN: 978-87-981270-9-3

1 Introduction

Motivation and state of the art. Breast conserving breast cancer surgery, i.e. lumpectomy and open biopsies, suffer a high recurrence rate (8% to 14%) and high number of positive margins (17% to 59%, [3]) and often poor cosmetic results, which is due to the way of indicating the target area with metal wire guides most often inserted under mammographic image guidance.

Several attempts have been made to improve surgical outcomes, relying on ultrasound imaging, on mammography, and on MRI. Methods employing robotic approaches for the placement of biopsy needles may eventually become available [10], but solve only a very constrained problem of placing a needle in a fixated breast, while approaches that help the surgeon to navigate more safely are more challenging and less developed. The study of Alderliesten et al. using MRI-based navigation tackles the problem of tracking the breast surface from a supine MRI scan to the surgery position [1], but neither support navigation in open breast surgery nor account for deformations in the prone positioning. Support of open surgery is attempted in the ultrasonography-based approach presented by Sato et al. [15]. Their approach, however, requires a tracking equipment to be positioned in the operating room, and will display the superimposed target area only in a computer monitor.

Previous work tried to match prone and supine breast shapes by employing finite element analysis using non-linear material laws [13].However, the computational complexity of this approach is high and thus difficult to be performed in clinical routine. The fastest available implementations of dynamic non-linear models [7] are based on explicit finite element approaches, which limit the magintude of the largest possible time step in a dynamic simulation. Furthermore, the deformation simulation has to be followed by a non-rigid registration step to achieve the final result. The contribution of Carter et al. addresses intra-interventional visualization of target structures with a technical setup that is not feasible practically [2]. Most closely resembling the setup in our contribution is the work of del Palomar [11], who matched the deformed mesh to a body scan of the women standing upright. These scans require a technical setup not suited to the situation in the operating room.

Contribution. We propose to use the pre-interventional MRI scans which are routinely taken to assess disease extent and inspect the contralateral breast. Based on these scans, we attempt to convey the target area to the breast surgeon during intervention. A prerequisite is to model the deformation of the breast from MRI in the prone position (using breast coils) to the supine position used in surgery to provide the current lesion position, which can then be displayed onto the breast using the scanner hardware that is employed to acquire the breast surface. The central element in this setup is the lesion tracing from the prone MRI scan into the current interventional position (see Figure 1).

Previous methods either lack speed or require extensive manual interaction as well as a sophisticated technical setup. Therefore, we propose an approach that combines automatic segmentation and meshing methods with a fast, real-time

ISBN: 978-87-981270-9-3

capable deformation simulation. Our goal is to integrate an isotropic non-linear material law by adjusting the per-element elastic modulus in every simulation step. While anisotropic hyperelastic material laws further increase the physical accuracy of the results, they increase the computational effort significantly, and they require higher resolved meshes to represent the underlying biomechanical structures. Therefore, for a clinical setting, a compromise has to be made between fast calculations and highly realistic material behavior. We describe methods to systematically adjust the per-element elastic modulus between single steps of the simulation. Interactive speed of the simulation is maintained regardless of this addition, making it feasible for peri-interventional application.

Computationally, our approach has several beneficial properties. It avoids complicated measurements to determine non-linear material parameters, and by being based on Hooke's law, it can be integrated into existing linear elastic code, thereby assuming non-linear or co-rotated strain formulations to enable large deformations. We approximate microscopic material tissue properties on a macroscopic scale by effectively stiffening the material under load to avoid unnatural behavior, e.g. inverted finite elements. The API to call the simulation code does not require to determine stress or strain values and therefore the method is transparent to the strain formulation (co-rotated or Green strain).

2 Material and Methods

Our proposed system starts with MR images taken in the prone position that are automatically segmented into deformable and fixed tissues using the methods proposed by Wang et al. [17]. The segmentation is used to setup the FE model, before the interactive deformation simulation starts in the operating room. A highly efficient FEM-based breast deformation approach is used to simulate the shape change from MRI to the current interventional positioning, even allowing for real-time repositioning at moderate mesh resolutions.

In the operating room, a surface scan of the patient is obtained using structured light scanning [9]. From the acquired point cloud, a mesh is built up, forming the target shape into which the MRI scan-based model is then fitted by optimizing parameters of the simulation. Finally, the display of the lesion position is achieved using the structured light projector.

MRI Data and Model Generation Standard non-fat-suppressed T2-weighted breast MRI data were obtained from five volunteers with voxel sizes in the order of $1 \times 1 \times 5$ mm, once in prone (facing down) and once in supine (facing up) position. All datasets were segmented into rigid and deformable tissue, where the breast parenchyma and the adipose tissue were considered elastic, and the thorax was considered fixed. A volumetric tetrahedral mesh was generated from a downsampled version of this data, resulting in meshes consisting of between 50k and 300k elements.

Breast Deformation Simulation Our approach is based on a multigrid finite element framework developed by Georgii and Westermann [5], which efficiently

ISBN: 978-87-981270-9-3

simulates deformations of the breasts using the so-called co-rotated Cauchy strain formulation from Rankin and Brogan [14]. One novel aspect of our work is to update the per-element elastic modulus based on the shape change that the element experiences in a given simulation step. By this explicit per-element elasticity update, we effectively model a non-linear isotropic material law.

The deformation of a volumetric object is described by a displacement field $u(x)$, $u : \mathbb{R}^3 \to \mathbb{R}^3$; $x \in \mathbb{R}^3$, which maps the reference configuration Ω to the deformed configuration $\{x + u(x) \mid x \in \Omega\}$. Driven by external forces f, a deformed solid is governed by the well-known Lagrangian equation of motion, $M\ddot{u} + C\dot{u} + Ku = f$, where M, C, and K are respectively known as the mass, damping and stiffness matrices, u denotes the composition of the displacement vectors of all vertices, and f consists of the force vectors applied to these vertices. The stiffness matrix K is assembled from the so-called element stiffness matrices K^e. Typically, every element in a finite element discretization has only a very small number of neighbors, and thus the resulting stiffness matrix is very sparse. The element matrices are precomputed with a fixed elastic modulus E_0. Due to the linearity of the underlying material law, the element matrix of a particular element can then be obtained by scaling K^e by the stiffness value of this element relative to $E_0 \in \mathbb{R}$. Therefore, we can update the stiffness values within the assembling process at nearly no additional computational costs and thus achieve a fast update of stiffness values in the FE model analogously to previous approaches [4, 16]. To efficiently update the data structures of the numerical multigrid solver, we make use of a fast approach to compute sparse-sparse matrix products [6].

Non-linear Material Modeling We propose a novel measure of element deformation that is based on the change of element shapes. The shape of the element is considered in undeformed and deformed state, and the two states are compared. Note that the undeformed tetrahedra are dissimilar in shape, hence we calculate for each vertex of one element the largest relative change of distance to the three opposite edges, i.e. the maximum from twelve distances per element. By only considering contracting distances, this yields relative shape change values $s \in [0, 1]$, from which a stiffness update has to be derived. Here, the initial hypothesis was that breast tissue is composed of lumps of stiff material that can move about with little friction, which requires a small elastic modulus on a macroscopic scale. However, under compression one observes a non-linear behavior, since now the stiff tissue parts determine the material behavior, i.e., the stiffness increases when the stress increases in our macroscopic model. The element relative elastic modulus is set to $E_\mathrm{r} = 1 + \alpha \cdot s$ with $\alpha \in \mathbb{R}$ a user-defined scalar factor greater than zero that has been fixed at a value of 2.5 for all data in our experiments, and $s \in \mathbb{R}$ the shape-based change value.

Explicit updates of the per-element elastic modulus in the simulation steps have to be performed carefully to ensure stability of the approach. This is due to the fact that internal forces in the body are mainly proportional to the elastic modulus, and thus updating this value while keeping the deformation increases the stored elastic energy. Therefore, we propose to use a dynamic simulation

ISBN: 978-87-981270-9-3

model exhibiting damping and inertia, and to update the elastic modulus in small steps. This is accomplished by an automatically set stiffness damping coefficient proportional to the global average of element stiffness changes. In all our tests, with a time step of 0.033 s we achieved stable behavior with this damping scheme.

Body Surface Scanning A robust and proven structured light scanning system using binary reflected Gray code patterns was set up to allow for a setup 1 m from the patient. From the point cloud, a mesh is reconstructed and later used as a reference state into which to deform the breast as acquired in the pre-interventional MRI scan. This approach has been chosen over other technologies since it is easily scalable in terms of speed, coverage, and resolution, transportable, and requires minimal setup. To determine the orientation of the scanned surface in the world coordinate system, an inertia measurement unit (IMU) is attached to the structured light scanner setup. After calibrating to the horizontal plane, it tracks the orientation of the scanner and can thus provide the orientation of the camera and hence the direction of the gravity with respect to the observed scene. Point clouds were in this work simulated based on supine MRI.

MRI-to-Surface Matching and Target Area Display The intraoperative matching of the deformed MRI scan to the body surface observed with the structured light scanner is accomplished by adjusting the base elastic modulus and the orientation of the patient, which has been approximated by the IMU sensor data. The four degrees of freedom in this formulation may be optimized using any optimization algorithm. To accelerate the simulation, we apply gravity in the opposite supine direction to achieve a gravity-free state and simultaneously apply gravity in the direction corresponding to the interventional setting. While this process is generally not applicable in case of non-linear material laws, in our setting it gives reasonable results which is due to the heuristic approach to stiffen the material under compression.

In this contribution we assess only the performance of the deformation simulation in terms of the distance between the surface of the deformed prone MRI scan and the surface derived from the supine MRI. We use the method of Quinlan et al. to assess the distances, whereby distances are always measured to the closest point in the other mesh [12].

When the optimized breast deformation has been found, the surface of the deformed tetrahedral mesh is used to calculate the projection of the target position onto this surface. Our intention is to use information of a tracked surgical tool to define the viewing direction, and the intersection of this direction with the scanned surface will be used to visualize the target position on the patient's skin.

3 Results

The shape-based stiffness update has been developed and evaluated on an artificial dataset prior to the application to breast MRI data. In these experiments, the shape based update criterion was able to produce plausible deformations of

ISBN: 978-87-981270-9-3

the model which where in line with the observed real-world behavior. Based on literature values, a Poisson ratio of 0.43 and a base elastic modulus of 10^3 Pa was chosen to characterize the breast tissue material (cf. [7]).

For specific combinations of base elastic modulus and the weight parameter α in the update function, however, oscillations can be observed due to the discrete update that causes jumps in the material modeling. This was addressed with the implementation of a damping method for the stiffness updates. Curves were plotted to track the average update of relative stiffness values from simulation step to simulation step. From these plots it was observed that an update using the shape-based distance metric yielded a more robust behavior than an analogous approach based on the von Mises stress norm [8]. The reason for this difference is the unboundedness of the von Mises stress, while the limit of the shape-based update is determined by the update function, since the values derived from the shape change are always in the interval [0..1].

Simple volume mesh phantoms (cf. [8]) also allowed us to compare the different metrics to elucidate the reasons for the oscillations. For this experiment, the relative stiffness values were visualized for individual tetrahedra to assess the smoothness of the relative stiffness map. The resulting maps exhibit smooth transitions of relative stiffness values between neighboring tetrahedra, which is beneficial since larger jumps are known to affect the stability of FEM solvers.

Four of the five volunteer data sets were evaluated regarding the average distance of the meshes for the region encompassing the deformable part of the breast. In one data set, the supine scan was not segmented by the automatic algorithm. Fig. 2 shows pairs of images in undeformed and deformed state.

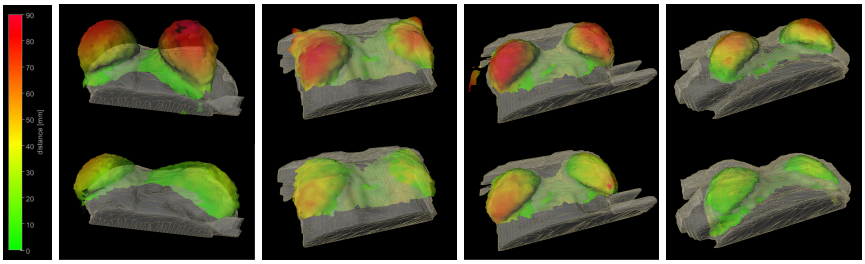

Fig. 2. Distance measurements between original prone and supine surfaces derived from prone/supine MRI scans (top row) and simulated supine (from prone) and original supine surfaces (bottom row) for different data sets (from left to right). A uniformly scaled color map (green to red: 0 to 90 mm distance) was used for all images to visualize the distances.

The performance of the implementation using a damped shape-based update of the elastic modulus is summarized in Table 3. Datasets were sampled to $5 \times 5 \times 5$ mm resolution. Note that by enlarging voxels to $10 \times 10 \times 10$ mm one can increase the speed by a factor of 8, thereby allowing real-time updates. For

ISBN: 978-87-981270-9-3

the practical application, only the simulation of either the left or the right breast is required, approximately doubling the speed in both cases.

Table 1. Timing statistics. 25 simulation time steps (sim.) were performed, and the same number of per-element stiffness update operations (up.). Timings were measured on an Intel Core i7 Quad 3.0GHz CPU.

ID	#ele.	time sim. [ms]	time up. [ms]	total 25 steps [sec]
4	47,895	189	48	5.9
2	99,390	400	98	12.5
0	158,340	644	149	19.8
3	158,340	628	149	19.4
1	313,335	1432	318	43.8

4 Conclusion

Physically convincing breast deformations can be handled with our efficient framework. It is particularly beneficial for practical applicability, since after calibration and initialization no further parameters need to be adjusted. Also, the fast, automatic segmentation of the data and the easy setup and execution of the simulation will help to proceed with further pre-clinical tests of the setup.

There are a number of topics, however, that we wish to address in the future. At the moment, we use a simple approach to determine the gravity-free state, which does not account for non-linearities in the material behavior. We plan to refine the process of generating a gravity-free state similar to previous approaches, where the reference state was iteratively approximated from a loaded configuration [13]. In addition, we will have to consider the unknown compression introduced by the breast coil. Unfortunately, this will also increase the computational costs for the simulation.

Also, the simulation cannot adequately deal with deformations that are observed in volunteers with large or fatty-replaced breasts. Our ongoing work therefore introduces contact surfaces with frictional forces to model the physical situation between soft tissue and the rib cage more accurately; also we are examining a coupled simulation of a deformable body filled with a viscous fluid.

Last, the structured light scanning approach will have to prove its usability in a clinical setting, both regarding field of view and achievable contrast and speed. In case of a successful application, extensions can be made, for example regarding a simultaneous scan-display mode using a real-time capable structured light scanning approach [18].

Acknowledgements

This work has partially been funded by the HAMAM project in the European FP7 program.

References

1. Alderliesten, T., Loo, C., Paape, A., Muller, S., Rutgers, E., Peeters, M.J.V., Gilhuijs, K.: On the feasibility of MRI-guided navigation to demarcate breast cancer for breast-conserving surgery. Medical physics 37(6), 2617–2626 (2010)
2. Carter, T.J., Tanner, C., Crum, W.R., Beechey-Newman, N., Hawkes, D.J.: A framework for image-guided breast surgery. In: MIAR'06. pp. 203–210 (2006)
3. Coopey, S., Smith, B.L., Hanson, S., Buckley, J., Hughes, K.S., Gadd, M., Specht, M.C.: The Safety of Multiple Re-excisions after Lumpectomy for Breast Cancer. Annals of surgical oncology (Jun 2011)
4. Dick, C., Georgii, J., Burgkart, R., Westermann, R.: Computational steering for patient-specific implant planning in orthopedics. In: Proceedings of Visual Computing for Biomedicine 2008. pp. 83–92 (2008)
5. Georgii, J., Westermann, R.: Corotated finite elements made fast and stable. In: Proceedings of the 5th Workshop On Virtual Reality Interaction and Physical Simulation. pp. 11–19 (2008)
6. Georgii, J., Westermann, R.: A streaming approach for sparse matrix products and its application in Galerkin multigrid methods. Electronic Transactions on Numerical Analysis, to appear (2010)
7. Han, L., Hipwell, J., Mertzanidou, T., Carter, T., Modat, M., Ourselin, S., Hawkes, D.: A hybrid FEM-based method for aligning prone and supine images for image guided breast surgery. ISBI 2011 pp. 1239–1242 (2011)
8. Harz, M.T., Georgii, J., Schilling, K., Hahn, H.K.: Real-time breast deformation using non-linear tissue properties. In: Lecture Notes in Informatics (2011)
9. Lanman, D., Taubin, G.: Build your own 3d scanner: 3d photograhy for beginners. In: SIGGRAPH '09: ACM SIGGRAPH 2009 courses. pp. 1–87. ACM, New York, NY, USA (2009)
10. Mallapragada, V., Sarkar, N., Podder, T.K.: Toward a Robot-Assisted Breast Intervention System. Mechatronics, IEEE/ASME Transactions on PP(99), 1–10 (2010)
11. del Palomar, A.P., Calvo, B., Herrero, J., López, J., Doblaré, M.: A finite element model to accurately predict real deformations of the breast. Medical engineering & physics 30(9), 1089–1097 (2008)
12. Quinlan, S.: Efficient distance computation between non-convex objects. In: Robotics and Automation, 1994. Proceedings., 1994 IEEE International Conference on. pp. 3324–3329. IEEE (2002)
13. Rajagopal, V., Chung, J.H., Bullivant, D., Nielsen, P.M.F., Nash, M.P.: Determining the finite elasticity reference state from a loaded configuration. International Journal for Numerical Methods in Engineering 72(12), 1434–1451 (2007)
14. Rankin, C., Brogan, F.: An element-independent co-rotational procedure for the treatment of large rotations. ASME J. Pressure Vessel Tchn. 108, 165–174 (1986)
15. Sato, Y., Nakamoto, M., Tamaki, Y., Sasama, T., Sakita, I., Nakajima, Y., Monden, M., Tamura, S.: Image guidance of breast cancer surgery using 3-D ultrasound images and augmented reality visualization. Medical Imaging, IEEE Transactions on 17(5), 681–693 (1998)
16. Schiwietz, T., Georgii, J., Westermann, R.: Freeform image. In: Proceedings of Pacific Graphics (2007)
17. Wang, L., Filippatos, K., Friman, O., Hahn, H.: Fully automated segmentation of the pectoralis muscle boundary in breast MR images. In: SPIE Medical Imaging, Computer-Aided Diagnosis. vol. 7963 (2011)
18. Zhang, S., Huang, P., et al.: High-resolution, real-time three-dimensional shape measurement. Optical Engineering 45, 123601 (2006)

ISBN: 978-87-981270-9-3

Configurable Framework for Automatic Multimodal 2D/3D Registration of Volume Datasets with X-Ray Mammograms

Torsten Hopp and Nicole V. Ruiter

Karlsruhe Institute of Technology, Germany
torsten.hopp@kit.edu

Abstract. Breast cancer is the most common cancer type among women. Currently, the standard screening method is X-ray mammography. Additionally MRI is used in clinical routine. A new imaging method in development is 3D Ultrasound Computer Tomography (USCT). The correlation of MRI and USCT with X-Ray mammography is challenging due to the different image dimensionality, patient positioning and compression state. Image registration is likely to overcome these difficulties. Since different imaging modalities have different registration requirements, a parameterizable registration framework based on FEM modeling of the mammographic compression was developed. First evaluations of the registration using clinical datasets show promising results with a clinically applicable accuracy throughout all modalities. The effect of parameters on the registration accuracy was successfully evaluated: 2D/3D registration of the breast is feasible and may help to improve multimodal diagnosis in future.

Keywords: Registration, Breast Imaging, Multimodal Diagnosis

1 Introduction

Breast cancer is the most common cancer type among women in Europe and North America [1]. For early diagnosis, medical imaging is essential. Currently, X-ray mammography (XRM) is the established screening method to detect breast cancer. It provides high resolution projection images of the breast, is cheap and broadly available. However, the sensitivity of XRM in dense breasts is limited [2].

Additionally to XRM, Magnetic Resonance Imaging (MRI) is used in clinical routine. It offers three-dimensional volumes with high contrast of soft tissue and high diagnostic accuracy [3]. Yet, the specitivity of contrast enhanced MRI is discussed controversially.

A new approach for breast imaging is Ultrasound Computer Tomography (USCT), which offers three-dimensional volumes of the breast in prone position [4]. It provides three types of images: Reflection images display the morphology of tissue. Attenuation and speed of sound (SoS) images provide a tissue characterization.

ISBN: 978-87-981270-9-3

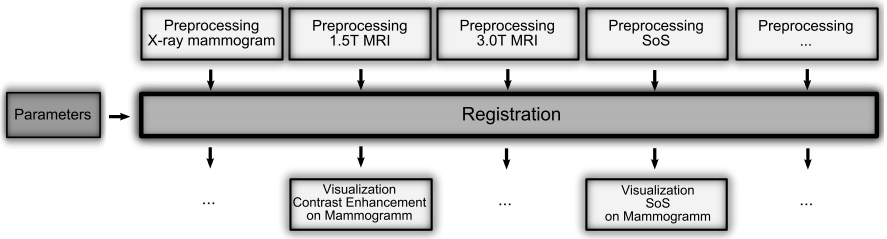

Fig. 1. Simplified architecture of the breast image registration framework.

MRI is usually read in combination with XRM for definite diagnosis. Since USCT is still in development, comparison of images with the standard screening method is of interest for quality measurement. Yet, the correlation of three-dimensional images and XRM is challenging due to their different dimensionality, patient positioning and deformation state of the breast. Image registration may help radiologists in multimodal diagnosis by creating directly comparable images. Since different modalities have different registration requirements, a more general registration framework is required.

In this paper we present a parameterizable model-based framework based on [5] to register volume datasets of different modalities with XRM. The results of studies with clinical 1.5T MRI, 3T MRI and USCT datasets are presented. Furthermore, the effect of various registration parameters on the registration accuracy is evaluated.

2 Methodology

The challenge of the image registration is that XRM shows a two-dimensional projection of a deformed breast, whereas MRI and USCT images render a three-dimensional undeformed breast. The general idea of our registration is mimicking the compression which is applied to the breast during XRM by a Finite Element Method (FEM) simulation. The underlying patient specific biomechanical model is built on the basis of the preprocessed volume image and parameterized using information from the corresponding mammogram. The simulated deformation is applied to the volume image in order to achieve a compressed configuration.

The goal of our registration framework is to provide a parameterizable software, which can handle a wide variety of modalities and is capable of running extensive parameter studies. For example it is of interest to study the behavior of the registration using different material models. The proposed architecture is illustrated in Fig. 1.

2.1 Preprocessing

Because of different physical basis and image acquisition, each modality has its own characteristics. Hence, the preprocessing has to be done specifically for each

ISBN: 978-87-981270-9-3

modality. Our system provides a toolbox for commonly needed preprocessing tasks. Images have to be rotated to fit the internally used coordinate system and scaled to match the resolution of the contrary modality. An interpolation is applied to the volume datasets in order to obtain isotropic voxels. Images are segmented into background and object using thresholding, morphological operations, active contours, de-islanding and three-dimensional smoothing. In an automatic global alignment, the amount of breast tissue imaged in XRM and the volume image is matched by estimating the breast volumes based on the segmented images.

2.2 Registration

To simulate the compression, which is applied to the breast during XRM, a biomechanical model is generated. FEM is used for numerical solution of the deformation process. To describe the geometry of the biomechanical model, the segmented volume image is passed to a surface-oriented meshing algorithm based on Fang et al. [6] resulting in a tetrahedral mesh. Nodes at the back of the model are held in position to model the fixation of the breast at the chest wall. The model is assumed to be in an unloaded configuration, i.e. no mechanical deformation is applied to the breast during the volume image acquisition.

The physical behavior of the model is described by the material model and the boundary conditions of the compression simulation. We assume the breast tissue to be an incompressible material. This is approximated using a Poisson's ratio near 0.5. The stress-strain relationship of the breast tissue is described by a Neo-Hookean model. Material parameters can be chosen, e.g. Wellman's [7] parameters can be used. Isotropic behavior of the material is assumed. Homogeneous as well as heterogeneous models, i.e. fatty and glandular structures, can be applied. Poission's ratio and the applied material model can be changed by the parameter settings.

The mammographic compression is mimicked by a two-step approach. In the first step, compression plates are added to the simulation, which are moved closer until a certain compression thickness is achieved. The thickness of the breast during mammography is readout from the mammogram's metadata. The contact between compression plate and breast surface is modeled by a small-sliding interaction.

Due to uncertainties and simplifications in the biomechanical model, the circumferences of the deformed volume image and XRM usually do not overlay completely after the first simulation step. Therefore, in the second step, a three-dimensional target model of the deformed configuration of the breast during mammography is estimated on basis of the mammogram. This model is compared to the deformed volume image derived from the first simulation step. Displacement vectors between surface nodes of the FEM mesh and the target model are defined by a nearest neighbor measure and used to describe new boundary conditions for the second simulation step. It results in a configuration of the MRI volume which shows congruently overlaying circumferences with the mammogram. All FEM simulations are solved using non linear solvers

ISBN: 978-87-981270-9-3

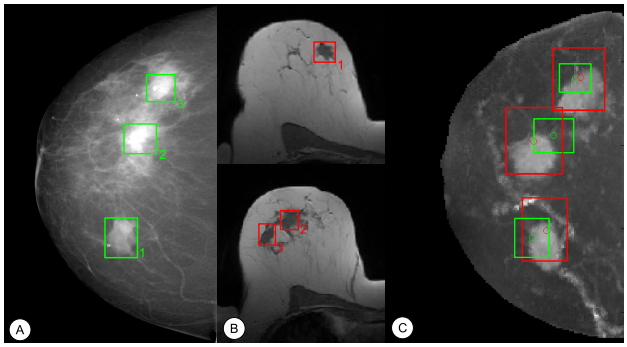

Fig. 2. (A) Three lesions marked in the XRM, (B) three lesions marked in the MRI volume, (C) Registration result: X-ray like projection of the deformed MRI volume.

for large deformations in the FEM software Abaqus. A detailed description of the registration algorithm can be found in [8].

2.3 Visualization

After registering the images, reasonable visualization methods had to be implemented in order to present the combined information to radiologists. Due to overlaying circumferences of the mammogram and the deformed volume image, comparison and combination can be carried out intuitively. For example (semi)-quantitative information obtained from the volume image can be projected on the mammogram, like proposed in [8] or [9].

2.4 Accuracy Evaluation

The quality of the registration can be estimated by the accuracy of the registration of lesions visible in both modalities. Clinical datasets were reviewed by experts and the circumference of the lesion was marked (Fig 2 (A) and (B)). Due to the congruent overlap of the images after the registration, the lesion markings can be compared directly. By measuring the displacement of the centers and the overlap of the lesion marking between XRM and the projection of the deformed volume image, the accuracy of the registration is estimated (Fig 2 (C)). The aim for clinical applicability is a large overlap of the contours and a small deviation between the center position.

3 Results

3.1 Quantitative results with clinical datasets

We evaluated the registration accuracy quantitatively with clinical datasets from different modalities. The parameter set for the registration process was chosen empirically. Exemplary resulting images are shown in Fig. 3.

ISBN: 978-87-981270-9-3

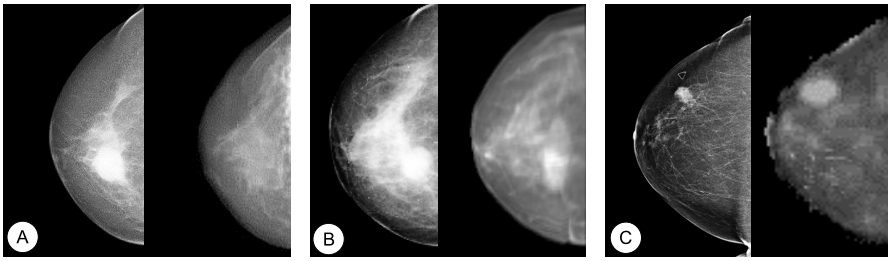

Fig. 3. Registration results with different modalities: XRM (each on the left) and projection image of the registered volume image (each on the right) acquired by (A) 1.5T MRI, (B) 3T MRI, (C) USCT.

In a first study, 11 datasets from a 1.5T MRI provided by University Hospital at Jena (UKJ), Germany, where registered with the corresponding craniocaudal mammograms. Datasets were reviewed in terms of little predeformations to hold the assumption of an unloaded initial configuration. The mean displacement of the lesion markings was 11.8 mm ± 6.4 mm. Three datasets showed a displacement of lesions greater than 15 mm. The mean overlap of lesions was 76% ± 34%.

Seven volume images acquired with a 3T MRI system were provided by UKJ. The images have a higher resolution and different image contrast. Also a different breast coil was used for acquisition, resulting in only little predeformations. The mean displacement of the center of the lesion markings was 8.2 mm ± 6.7 mm, the mean overlap was 79% ± 31%. Only one dataset showed a displacement above 15 mm.

For 15 USCT SoS volumes provided by Karmanos Cancer Institute Detroit, USA, the mean displacement was 12.8 mm ± 12.0 mm without and 7.1 mm ± 5.4 mm with manual corrections of the rotation due to patient positioning during image acquisition of the SoS volume. The mean overlap of lesion markings was 83% ± 27% resp. 91% ± 10%.

3.2 Effect of parameterization

Due to approximations and simplifications during the registration, the accuracy also depends on the parameterization of the process. To quantify the influence of parameterization, we evaluated the effect of several parameters on the registration accuracy.

A MRI dataset from clinical routine provided by UKJ, and the according XRM were chosen. They contain two clearly visible lateral lesions (lesion 1 and 3) and one clearly visible medial lesion (lesion 2, Fig. 2 (A) and (B)). Thus, three landmarks can be used to estimate the spatial variance of the registration accuracy. The aim of the parameter evaluation is to determine the relative effect of parameters on the registration accuracy. Table 1 illustrates the results of seven selected parameters.

ISBN: 978-87-981270-9-3

At first, the coronal slice cut near the chest wall within the MRI was varied, resulting in different amounts of tissue to be registered. The mean standard deviation (SD) of displacements for all three lesions was 5.6 mm. In comparison to our automatic tissue matching, the estimated cut differs only 1 Pixel from the optimal cut for this dataset.

Due to a uncertain mammographic projection angle and differences in patient positioning, datasets might be rotated against each other around the sagittal plane. We evaluated the effect of rotation by rotating the MRI volume between -10° and +10° before registration. The mean SD was 1.4 mm. We found that the registration accuracy can improve in using even greater rotation angles. Hence, the projection angle was varied between -30° and +30°. In this case, the mean SD was 3.1 mm. The medial lesion is affected less by the rotation, since it is positioned closer to the rotation center.

The FEM mesh density was varied from approx. 1,000 Finite Elements (FE) to 100,000 FE in order to find a sufficient refinement regarding preferably low processing time. The registration accuracy did not differ significantly in all registration runs: the mean SD was 1.3 mm. It tends to be preferable to use more than 22,000 FE (mean SD: 0.7 mm against 1.5 mm for less than 22,000 FE).

In the next step, the model was tested with homogeneous against heterogeneous tissue modeling 'fat' and 'gland' differently. The model was built by segmenting fatty and glandular structures within the MRI and applying DelPalomar's material parameters [10]. The percentage of glandular structures was varied from aprrox. 1% to 80% in order to account for under- and over-estimation of the breast density due to segmentation errors. The mean SD within the density variation registrations was 1.3 mm. No major difference against the homogeneous model could be found (mean SD 1.2 mm).

We furthermore evaluated the effect caused by the selection of the stiffness ratio between fatty and glandular tissue (1:0.5 to 1:15) in order to account for the very diverse material models proposed in literature. The results tend to show a slightly better registration accuracy using a higher ratio (e.g. 1:7.5). However, the mean SD is relatively low: 2.4 mm assuming a realistic breast density of approx. 25% for the given case.

Poisson's ratio, which indicates the compressibility of the breast tissue, was varied in a range of 0.3 to 0.495. The overall effect was accounted with a mean SD of 2.2 mm showing slightly better results for a Poisson's ratio near 0.45. The medial lesion tends to be affected more than the lateral lesions, which might be caused by non-linear effects of tissue movement.

At last, the shape of the 3D target model for the second simulation step was varied in order to account for the uncertainties caused by the estimation of the three-dimensional shape from the two-dimensional mammogram. Different curvature estimations of the breast between the compression plates were used for this experiment. The mean SD was 1.8 mm, which shows that the parameterization of our proposed second simulation step does not affect the registration accuracy significantly.

ISBN: 978-87-981270-9-3

Table 1. Standard deviations of the registration accuracy caused by variation of selected parameters.

Parameter	**SD of Displacement**			**Mean of SD**
	Lesion 1	Lesion 2	Lesion 3	
Coronal plane cut	2.5 mm	7.8 mm	6.4 mm	5.6 mm
Sagittal volume rotation	3.8 mm	1.3 mm	4.3 mm	3.1 mm
FEM mesh density	1.3 mm	1.3 mm	1.4 mm	1.3 mm
Breast density threshold	0.8 mm	1.7 mm	1.4 mm	1.3 mm
Fat-gland stiffness ratio	2.7 mm	2.5 mm	2.0 mm	2.4 mm
Poisson's ratio	1.4 mm	3.4 mm	1.8 mm	2.2 mm
3D shape estimation from XRM	2.0 mm	1.7 mm	1.6 mm	1.8 mm

After all parameter variations, the biomechanical model was built with and without chest wall as to evaluate the influence of boundary conditions on the compression simulation. The experiment resulted in a similar registration accuracy. Yet, the displacement of the medial lesion was improved, while the lateral lesions showed a slightly worse registration accuracy by including the chest wall. This might again be due to non-linear effects of tissue movement in the medial position tending to be less shifted anterior when modeling the chest wall. The mean difference in displacement was 3.9 mm.

For the presented dataset, the registration was thereafter carried out with a combination of the optimal values of the described parameters. In comparison to the registration with empirically chosen parameters (lesion 1: 10.3 mm, lesion 2: 25.5 mm, lesion 3: 1.5 mm), the mean registration accuracy was improved by 4.6 mm (lesion 1: 8.6 mm, lesion 2: 11.5 mm, lesion 3: 3.2 mm). This shows the potential in choosing optimal parameters specifically for each dataset.

4 Conclusion

We presented a parameterizable software framework, which allows to register volume images of different modalities with the corresponding XRM patient-specifically. It provides a more general approach to the challenging task of correlating two modalities which differ in dimensionality, patient positioning and deformation state of the breast. Configurability is achieved via a parameterizable registration and modality specific preprocessing of images. The software can easily be expanded for other upcoming 3D imaging modalities like breast CT.

In the present study, our approach has limited applicability for datasets showing major predeformations. Yet, our research focuses on the evaluation and elimination of the effect of predeformations to deal with a larger variety of clinical datasets. Extensive parameter studies will be needed to complete this task, hence our proposed framework provides a good basis for further investigation.

The evaluation of the registration approach with clinical images showed promising result as for all modalities registration accuracy was in a clinically

ISBN: 978-87-981270-9-3

acceptable range in most cases. All registrations were carried out using an empirically chosen set of parameters and completely automated preprocessing and registration. Our investigation of the effect of parameters demonstrates that the registration accuracy can be optimized further. Though only one datasets with three lesions was used due to limitation by computing time, we could show first trends of how the registration accuracy is affected by different parameters. A high variance is caused by the preprocessing. Fewer variations tend to be caused by the composition of the biomechanical model, while some parameters like the density of the FEM mesh seem to have an insignificant influence.

On basis of our presented results we conclude that a 2D/3D registration of breast images is feasible with clinical datasets, however the accuracy might also be highly dependent on the selection of parameters. With an empirically chosen set of parameters, clinically relevant registration accuracies can be achieved.

The comparability of images and implemented visualization techniques are likely to enhance multimodal diganosis in a clinical setting. Radiologists might benefit from the spatial correlation as well as from the combination of two diverse modalities. Our ongoing studies with a higher number of datasets are likely to validate the presented results. In a next step, the automatic patient-specific estimation of optimal parameters, e.g. by using image similarity measures, will be investigated.

References

[1] Fischer, T. et al.: Mammographie-Screening in Deutschland. Vis. J. 15, 62–67 (2007)
[2] Pisano E.D. et al.:Diagnostic Accuracy of Digital versus Film Mammography: Exploratory Analysis of Selected Population Subgroups in DMIST. Radiol. 246(2), 376–383 (2008)
[3] DeMartini, W. et al.: A review of current evidence-based clinical applications for breast magnetic resonance imaging. Top. Magn. Reson. Imaging 19, 143–150 (2008)
[4] Duric, N. et al.: Detection of breast cancer with ultrasound tomography: First results with the computerized ultrasound risk evaluation (C.U.R.E). Med. Phys. 34(2), 773–785 (2007)
[5] Ruiter, N.V. et al.:Model-based registration of X-ray mammogramms and MR images of the female breast IEEE Trans. on Nucl. Sci. 53, 204–211 (2006)
[6] Fang, Q., Boas, D.: Tetrahedral mesh generation from volumetric binary and gray-scale images. Proceedings of IEEE Intern. Symp. Biomed. Imaging, 1142–1145 (2009)
[7] Wellman, P.S. et al.: Breast tissue stiffness in compression is correlated to histological diagnosis. Technical report, Harvard BioRobotics Laboratory (1999)
[8] Hopp, T. et al.: 2D/3D Image Fusion of X-ray Mammograms with Breast MRI: Visualizing Dynamic Contrast Enhancement in Mammograms. Int. J. Comput. Assist. Radiol. Surg. 2011 Jun 5. [Epub ahead of print]
[9] Hopp, T. et al.: 2D/3D Image Fusion of X-ray Mammograms with Speed of Sound Images: Evaluation and Visualization. SPIE Medical Imaging 2011, Orlando, Proc. SPIE 7968, 79680L (2011)
[10] Del Palomar, A.P. et al.: A finite element model to accurately predict real deformations of the breast. Med. Eng. and Phys. 30, 1089–1097 (2008)

ISBN: 978-87-981270-9-3

Biomechanical Modelling of Breast Deformation Under Gravity: An Application for Prone-Supine Image Registration

Lianghao Han[1], John Hipwell[1], Thomy Mertzanidou[1], Chritine Tanner[2], Zeike Taylor[3], Sebastien Ourselin[1], David Hawkes[1]
[1] CMIC, University College London,
Gower Street, London, UK
[2] Computer Vision Laboratory, ETH Zürich, 8092 Zürich, Switzerland
[3] MedTeQ centre, School of Information Technologhy &Electrical Engineering, The University of Queensland, ALD, 4072, Australia
{l.han, j.hipwell, c.tanner, t.mertzanidou, s.ourselin,d.hawkes}@cs.ucl.ac.uk,
z.taylor@itee.uq.edu.au

Abstract. Multimodality breast image registration requires recovering the difference in deformation between two different image modalities, due to the position change of a breast subjected to gravity loading. In this study, we developed a patient-specific biomechanical model to simulate the breast deformation under gravity by using an open-source Graphics Processing Unit (GPU) based high performance nonlinear finite element (FE) solver. An automated procedure has been implemented for generating FE models with a heterogeneous tissue distribution from segmented MR volume images. The developed model was used to simulate the deformation of a breast from prone to supine, with an iteration process to optimize its material property parameters and positions. It was found that either non-rigid intensity-based image registration methods or biomechanical model based methods alone have limited success. However, a hybrid FE-based image registration method, combining biomechanical models and non-rigid intensity-based image registration methods, showed a good performance.

Keywords: Finite Element Method, Graphics Processing Unit (GPU), Non-rigid Image Registration, Biomechanical Modelling, Breast, MRI

1 Introduction

Multimodality imaging, such as X-ray mammography, dynamic contrast enhanced MRI, digital breast tomosynthesis and 3D Ultrasound, has been increasingly employed in the detection, diagnosis, treatment planning/delivery and surgery for breast cancer. Each of these imaging modalities is often acquired with the breast in a different position. For example, preoperative dynamic contrast MRI is performed with the subject prone; while US images and intraoperative MR images are acquired with the subject in the supine position. Due to gravity loading, there exists a large difference in deformation between different image modalities. To align multimodality

ISBN: 978-87-981270-9-3

breast images for assisting cancer diagnosis and therapy, it is critical to recover such a deformation difference. Traditional non-rigid intensity-based image registration methods used to correct the deformation of soft tissues are currently inadequate at correcting these deformations [1-3]. In recent years, biomechanical modelling has increasingly attracted attention because its ability to estimate physically realistic deformations. Biomechanical models implemented with nonlinear finite element methods have been employed to model the large deformation behavior of breasts such as plate compression in X-ray mammography and breast biopsy [4, 5] and under gravity loadings [6]. Previous studies [1-3] have also shown that the use of biomechanical modeling as a prior to non-rigid intensity-based image registration could be used for registering prone and supine MR images. However, in these studies, the material parameters were fixed based on the *in vitro* values from the literature or determined in a simplistic manner. Furthermore, the sliding between the chest wall and breast tissues was either not considered or was modeled on a purely phenomenological basis. Incorrect modelling assumptions can be expected to significantly affect subsequent registration performance [1-3].

In this study, we developed a patient-specific biomechanical model to simulate the breast deformation under gravity by using an open-source GPU-based high performance nonlinear finite element (FE) solver[1]. The breast was considered as a heterogeneous material consisting of glandular tissue, fat and muscle. The large deformation and anisotropic behavior of breast tissues was simulated by using a transversely isotropic hyperelastic model. A contact model was used to simulate the sliding phenomenon between the rib cage and breast tissues. An automated procedure to generate patient-specific FE models from segmented breast MR images was implemented. The developed biomechanical models were combined with non-rigid intensity-based image methods to predict the breast deformation under gravity loadings for registering prone and supine MR breast images.

2 Materials and Methods

2.1 Constitutive Model of Breast Tissues

Like most biological soft tissues, breast tissues exhibit nonlinear, anisotropic, quasi-incompressible and time-dependent response under large deformation. The hyperelastic models are often used to describe the constitutive relations of these materials, which are defined in terms of a strain energy potential. Several forms of strain energy potentials have been proposed, such as the Neo-Hookean form, the Arruda-Boyce form, the Mooney-Rivlin form, the Ogden form, the polynomial form etc. Breast is composed of connective tissues (collagen and elastin) with the strength enhancement by Cooper's ligament and fiber-like structures etc, showing strong anisotropic behavior. Commonly, biological tissues are considered as composite materials where one or more family of (collagen) fibers are embedded in a solid

[1] http://niftysim.sourceforge.net/

ISBN: 978-87-981270-9-3

matrix. For simplicity, here we assume that breast tissues are reinforced by a single family of fibers perfectly dispersed in a preferred direction. That is, a transversely isotropic hyperelastic model was employed and its strain energy potential had the following form [5]:

$$\Psi = \frac{\mu_0}{2}\left(\bar{I}_1 - 3\right) + \frac{k_0}{2}\left(J - 1\right)^2 + \frac{\eta_0}{2}\left(\bar{I}_4 - 1\right)^2 \quad (1)$$

where μ_0 denotes the initial shear modulus; $\bar{I}_1$ represents the first deviatoric strain invariant; k_0 stands for the initial bulk modulus; J is the determinant of the deformation gradient $\mathbf{F}$ and denotes the total volume change; η represents a material parameter with units of Pa; $\bar{I}_4 = \mathbf{a}_0 \cdot \bar{\mathbf{C}} \cdot \mathbf{a}_0$ stands for the pseudo-invariant of $\bar{\mathbf{C}} = J^{-2/3}\mathbf{C}$ with $\mathbf{C} = \mathbf{F}^{\mathrm{T}}\mathbf{F}$ denoting the right Cauchy-Green strain tensor, and $\mathbf{a}_0$ is the preferred direction to present the transversely isotropic response, with $|\mathbf{a}_0| = 1$. The relative compressibility of a material can be expressed in terms of Poisson's ratio, $\nu = \left(3k_0 / \mu_0 - 2\right) / \left(6k_0 / \mu_0 + 2\right)$. Thus, four parameters, μ_0, ν, η_0 and $\mathbf{a}_0$ could determine the model.

2.2 Patient-specific FE Model

To generate a patient-specific finite element model of a breast for biomechanical modelling, four steps were followed: (1) Firstly, MR volume images of a breast were segmented by using an automated method, integrating an intensity model, a spatial regularization scheme and bias field inhomogeneity correction and small amount of manual interaction [7], breast tissues are segmented as fat, glandular and muscle (Fig. 1b) and the rib cage was approximated with a cylinder and a flat-plate (Fig.1a) to facilitate contact modelling; (2) Secondly, the marching cube algorithm was used to construct the surface mesh of the whole breast; (3) Thirdly, TetGen[2] , an open-source mesh generator, was used to generate 3D 4-node tetrahedral elements based on the surface mesh created in Step 2; (4) Fourthly, the tissue type of each element was determined from the segmented MRI image (Fig. 1b) by calculating the volume ratio of each tissue type within the element; (5) Finally, a contact pair between the rib cage and the breast was defined, and material models, their material property parameters and initial boundary conditions were configured.

In this study, tetrahedron elements are chosen to facilitate automatic mesh generation and to yield more accurate shape and anatomical approximation for breasts by using small size elements. Fig. 1b shows that when a fine mesh is used the tissue distribution could be well represented by FE models.

[2] http://tetgen.berlios.de/

ISBN: 978-87-981270-9-3

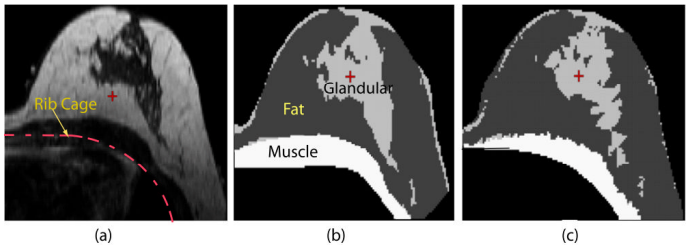

Fig. 1. (a) Original MR prone image (b) Tissue type distribution map after segmentation (c) Tissue type distribution map within an FE model with 191,934 tetrahedron elements.

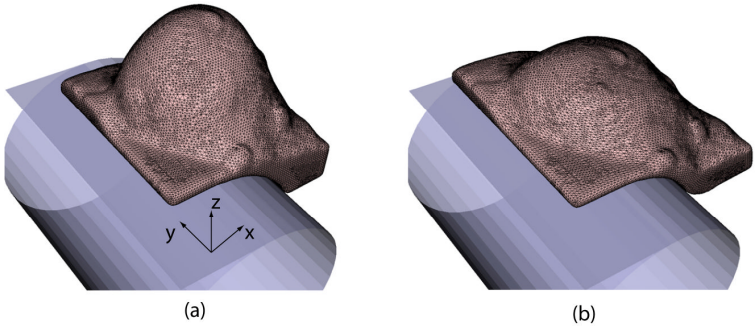

Fig. 2. FE model of a breast (a) undeformed model with 191,934 4-node tetrahedron elements (b) deformed model under gravity;

2.3 Fast GPU-based Explicit Finite Element Solver

An open-source CUDA-based high-performance nonlinear finite element package, Niftysim[3], has been developed at University College London. A key feature is the option of GPU-based execution, which allows the solver to significantly out-perform equivalent commercial packages [5]. The algorithm is based on the finite element method using total Lagrangian formulation and explicit time integration. A full description of the algorithm can be found in [8].

In the solver, both geometrical and material nonlinearity could be handled. Three element types have been included: 8-node linear hexahedron element with reduced integration, 4-node linear tetrahedron element and 4-node linear tetrahedral element with an improved nodal-average pressure formulation for nearly incompressible materials or incompressible materials. Six material constitutive models have been implemented, including neo-Hookean hyperelastic, Arruda-Boyce hyperelastic, polynomial hyperelastic, transversely isotropic hyperelastic, neo-Hookean visco-hyperelastic and transversely isotropic visco-hyperelastic.

A kinetic type contact algorithm [9] between a deformable slave surface and a rigid master surface was also implemented for modeling frictionless contact. In this

ISBN: 978-87-981270-9-3

algorithm, slave nodes found to have penetrated the master surface are relocated to the closest point on the latter, approximating a frictionless interface.

2.4 Deformation Prediction of Breast under Gravity Loading from Prone to Supine

2.4.1 Biomechanical Modelling

Following the procedure described in Section 2.2, we created an FE model (Fig.2a) from a prone DCE MR image (Fig. 1a), acquired by using a breast coil, according to the standard clinical protocol. The breast sliding against the rib cage was simulated as a frictionless contact. A transversely isotropic hyperelastic model described in Section 2.1 was chosen for all three breast tissues. Considering that glandular tissues are connected to the nipple, we assumed that z direction (as shown in Fig.2a) is the preferred direction of tissues. Thus three material parameters for each tissue type, μ_0, v and η_0, are required to define the constitutive model. Since the in vivo mechanical response of the breast varies significantly across individuals, *in vitro* measured results are not reliable for *in vivo* breast deformation simulations. To more accurately predict the deformation of a breast from prone to supine, rather than using fixed *in vitro* material parameters, we adopted an iteration process [5, 10] to obtain optimised material parameters.

The position of the breast is another critical parameter to affect breast deformations. The position change of the breast from the prone position to the supine position was defined by six degrees of freedom, three translation components and three rotation components. However, only three rotation components will affect breast deformation. The optimised deformation prediction from biomechanical modeling was obtained by iteratively updating material parameters of each tissue type and the position of the entire breast in an optimisation procedure. The objective function is to maximise the image similarity within the region of the breast between the FE computed supine MR image and the original supine MR image acquired on a Philips 1.5T MR system. Normalized mutual information [10] was used for image similarity measure. A hybrid simulated annealing algorithm provided in the genetics algorithm and direct search toolbox of Matlab[4] was used to update three material parameters for each tissue type. A stopping condition based on the change in similarity measure at each iteration was used to terminate the registration when there was no further improvement in image similarity or a specified maximum iteration number, 40, is reached.

Typically less than 5 minutes were required in each FE simulation for an FE model with 190k elements and 40k nodes, compared with more than five hours by using commercial FE package, ABAQUS. 50 iterations are normally required for obtaining an optimised deformation approximation from biomechanical modelling. The computational time could be further reduced by using coarse mesh and optimisted time steps.

[4] www.mathworks.com

ISBN: 978-87-981270-9-3

2.4.2 Non-rigid Intensity-based Image Registration Method

The large deformation of soft tissues could also be estimated by using Non-rigid intensity-based image registration methods. The chosen open-source registration algorithm here[5] is a parallel version of B-spline based free form deformation (FFD) image registration methods [12-13], implemented in the GPU. The registration uses normalised mutual information as an image similarity measure.

3 Results

The proposed method is employed for prone-supine image registration The breast deformation from prone to supine only under gravity loading was estimated by using three different methods: Method A: affine registration followed by non-rigid B-spline based FFD registration (Section 2.4.2); Method B: patient-specific biomechanical modelling with both material parameter and position optimization (Section 2.4.1); Method C: A hybrid method by combing Method A with Method B. In Method C, after an approximation of breast deformation in the supine position was estimated through a biomechanical modeling procedure, the non-rigid image registration method in Method A was used to predict the remaining deformation [9]. In this case study, it was observed that the rigid transformation operation had a very little effect on simulations because the rib cage in the supine position was already aligned with that in the prone position well. Figure 3 shows slices of breast MR images along the sagittal, transverse and coronal planes before and after registration using the three different methods. Visually, neither the non-rigid FFD registration method (Fig. 3b) nor biomechanical modelling (Fig. 3c) alone achieves an accurate registration. The hybrid FE-based image registration (Fig. 3d) produces the best alignment.

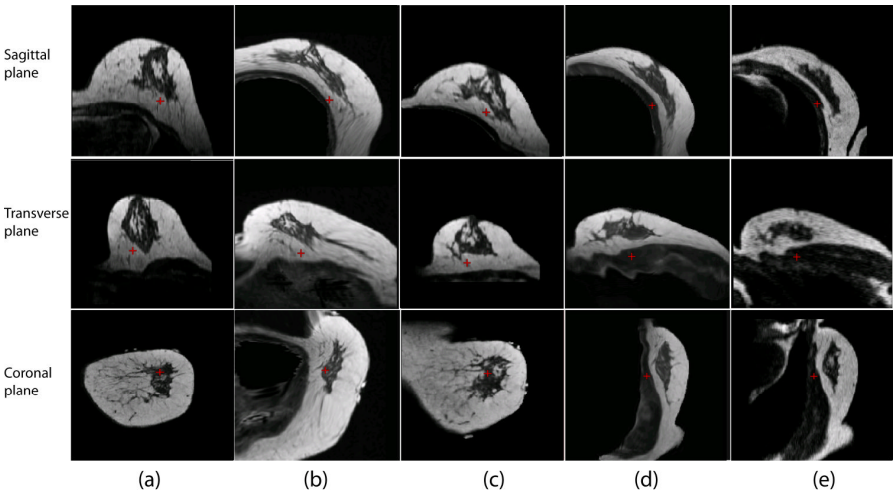

[5] http://sourceforge.net/projects/niftyreg/

Fig. 3. MR image slices before and after registration (a) original prone MR image (b) supine MR image registered using Affine+FFD (method A) (c) FE computed supine MR image (method B) (d) supine MR image registered using hybrid FE-based method (method C) (e) original supine MR image.

To further investigate the registration performance of the proposed method, the nipple position and eight MR-visible fiduciary markers affixed to the breast surface during imaging were selected to calculate a target registration error for the prone-supine registration. In the FE model, the node closest to the centre of each fiduciary marker on the prone MR image was identified as a fiducial node. Since both Method A and Method B visually did not show good alignment, only the registration error from Method C was calculated. With Method C, i.e. the hybrid FE-based image registration method, the root mean square error of the nine selected positions was 5.6 mm and the maximum error was 12.2 mm.

4 Discussions and Conclusions

We have presented in this paper, an automated procedure to generate patient-specific biomechanical models of breasts directly from segmented MR volume images. The developed models were used to estimate the deformation of breasts under gravity loading in prone-supine MR image registration. The deformation was also estimated with non-rigid image registration. It was found neither the non-rigid FFD registration method nor the biomechanical model based registration alone achieves an accurate registration. The hybrid FE-based image registration by combining biomechanical modelling with non-rigid image registration method produces the best alignment. In this method, patient-specific biomechanical modelling, with an optimization of both material parameter and patient positions, captured the major physically realistic deformation and provided a good deformation approximation, while the non-rigid intensity-based image registration was used to find the remaining difference of deformation between the FE prediction and the experimental acquisition. After registration, the surface of the breast in the prone position was well aligned with that in the supine position, which was further confirmed by relatively small registration mean errors of nine selected points on the breast surface (5.6 mm).

In our previous study [10], a similar method was employed to solve the same problem addressed here. It used ABAQUS as an FE solver and took much longer computational time. With a homogeneous material model, we obtained a smaller mean error (2.8mm) for eight surface fiducial markers. It seemed that the registration performance may not be improved by using a heterogeneous material model. However, image similarity was used as an objective function to be maximized in these studies. It is more suitable to track internal markers rather than surface fiducial markers to evaluate how heterogeneous material models will affect the registration performance on internal anatomical structures. Now, we are planning to use clinically implanted fiducials to further validate and evaluate the proposed method. More comparative investigations will be carried out on different patients. The sensitivity of the registration on the accuracy of the segmentation and material parameters will also be further investigated. The presented approach provides a general framework for FE-

ISBN: 978-87-981270-9-3

based image registration and can be applied for other surgery applications (e.g. brain, liver) and multi-modality registrations (e.g. MR-X-Ray, MR-3D ultrasound), where large deformation estimations are required.

Acknowledgments. The work is funded by the European FP7 program, HAMAM.

References

1. Lee, A.W.C., Schnabel, J.A., Rajagopal, V., Nielsen, P.M.F. and Nash, M.P.: Breast Image Registration by Combining Finite Elements and Free-form Deformations, IWDM 2010, LNCS, vol. 6136, pp. 736--743, Springer, Heidelberg (2010)
2. Carter, T., Tanner, C., Beechey-Newman, W., Barratt, D. and Hawkes, D.: MR Navigated Breast Surgery: Method and Initial Clinical Experience, MICCAI 2008, LNCS, vol. 5242, pp. 356—363 (2008)
3. Carter, T., Tanner, C., Crum, W.R., Beechey-Newman, N. and Hawkes, D.J.: A Framework for Image-Guided Breast Surgery. Medical Imaging and Augmented Reality, *MIAR 2006*, LNCS, vol. 4091, pp. 203—210 (2006)
4. Azar, F.S., Metaxas, D.N. and Schnall, M.D.: A Deformable Finite Element Model of the Breast for Predicting Mechanical Deformations under External Perturbations. Acad Radiol. 8, 965--975 (2001)
5. Han, L., Hipwell, J., Taylor, Z., Tanner, C., Ourselin, S. and Hawkes, D.: Fast Deformation Simulation of Breasts Using GPU-Based Dynamic Explicit FEM, IWDM 2010, LNCS vol. 6136, pp. 728—735 (2010)
6. Rajagopal, V.: Modelling Breast Tissue Mechanics Under Gravity Loading. Ph.D. Thesis, The University of Auckland (2007)
7. Mertzanidou, T., Hipwell, J., Cardoso, M., Tanner, C., Ourselin, S. and Hawkes, D.: X-ray Mammography - MRI Registration Using a Volume-Preserving Affine Transformation and an EM-MRF for Breast Tissue Classification. IWDM 2010, LNCS vol. 6136, pp23—30 (2010)
8. Taylor, Z.A., Comas, O., Cheng, M., Passenger, J., Hawkes, D.J., Atkinson, D., Ourselin, S.: On Modelling of Anisotropic Viscoelasticity for Soft Tissue Simulation: Numerical Solution and GPU Execution. Med. Image Anal. 13, 234--244 (2009)
9. Hallquist, J.O.: LS-DYNA Theory Manual. Livermore Software Technology Corporation, Livermore, California (2006)
10. Han, L. Hipwell, J., Mertzanidou, T., Carter, T., Modat, M., Ourselin, S., and Hawkes, D.: A Hybrid FEM-based Method for Aligning Prone and Supine Images for Image Guided Breast Surgery, *IEEE International Symposium on Biomedical Imaging*, pp. 1239--1242 (2011)
11. Studholme, C. D., Hill, D. L. G., and Hawkes, D.J.: An Overlap Invariant Entropy Measure of 3D Medical Image Alignment. Pattern Recognition, 32, pp. 71—86 (1999)
12. Modat, M., Ridgway, G. R., Taylor, Z.A., Lehmann, M., Barnes, J., Hawkes, D.J., Fox, N.C. and Ourselin, S.: Fast Free-form Deformation Using Graphics Processing Units. Comput. Methods Prog. Biomed. 98, pp. 278--284 (2010)
13. Rueckert, D., Sonoda, L., Hayes, C., Hill, D.L.G., Leach, M., and Hawkes, D.J.: Nonrigid Registration Using Free-form Deformations: Application to Breast MR Images, IEEE Transactions on Medical Imaging, 18, pp. 712--721 (1996)

MRI to X-ray mammography registration using an ellipsoidal breast model and biomechanically simulated compressions

Thomy Mertzanidou[1], John Hipwell[1], Lianghao Han[1], Henkjan Huisman[2], Nico Karssemeijer[2], and David Hawkes[1]

[1] Centre for Medical Image Computing, University College London, Gower Street, WC1E 6BT, London, UK
[2] Diagnostic Image Analysis Group, Radboud University Nijmegen Medical Centre, P.O. Box 9102, 6500 HC Nijmegen, The Netherlands
t.mertzanidou@cs.ucl.ac.uk

Abstract. This work presents a novel registration method between MR breast images and X-ray mammograms. We propose the use of an ellipsoidal breast model to approximate the average breast shape and we use biomechanically simulated compressions to learn the deformation during mammogram acquisition. By varying the parameters of the simulations, we simulate a wide range of compressions and then use Principal Component Analysis (PCA) to extract the main modes of variation. During registration, we optimise the coefficients of these modes and the parameters that define the initial position of the breast before compression. The proposed transformation captures the complex mammographic plate compression in only eleven degrees of freedom. The method is automated, does not require manual interaction and is targeted for clinical use. The framework was tested on 10 patients with visible lesions and 8 of these were successfully registered to a mean registration error of 9.8mm.

1 Introduction

Relating findings between an MRI and an X-ray mammogram is a difficult task for radiologists, as one is a volume and the other a projection image. In addition, the appearance of breast tissue structure varies significantly between them. Some breast regions are often obscured in an X-ray, due to its projective nature and the superimposition of normal glandular tissue. Moreover, the breast deformation between the two different image acquisitions is large; women are lying prone in the MR scanner, while they are standing, with their breast compressed between two plates, to obtain an X-ray mammogram. Automatically determining correspondences between the two modalities could assist radiologists in the detection, diagnosis and surgical planning of breast cancer. Furthermore there has been increased interest recently in developing multimodal Computer-Aided Diagnosis algorithms [1], where an automatic registration could aid in associating features representing corresponding locations in the breast.

ISBN: 978-87-981270-9-3

Authors have previously proposed feature-based techniques ([2], [3]) for registration, which can give good results when there are distinctive features available in both modalities, but the feature selection and the 3D-2D matching process are not trivial, can lead to lack of robustness and cannot be used in clinical practice. In our previous work [4] we proposed an intensity-based method with an affine transformation model to deform the 3D volume, which has limitations regarding the range of deformations it can produce to approximate the real breast compression. Ruiter et al. [5] used a patient-specific biomechanical model of the breast. Although biomechanical simulations can produce more realistic deformations, the manual steps involved in building a different model for each patient and the variability in the results depending on the material properties, the meshing and the simulation techniques used, make this framework less suitable for clinical use. Tanner et al. [7] used population-based Statistical Deformation Modeling to overcome this problem. Nevertheless, the large variation between breast shapes can cause significant artifacts when mapping the MR volumes to the same space. Patient-specific biomechanical simulations of large breast compressions were also previously proposed ([8], [9]) but were not tested for MRI/X-ray correspondences.

Validation tests using radiologist's annotations were performed in two of the above techniques. The method of Behrenbruch et al. [2] was successful in 12 out of 14 cases tested, with an error in the range of $4 - 10mm$, depending on the MRI voxel resolution. Ruiter et al. [5] achieved a mean error of $4.3mm$ on 6 cases. However, in a more recent semi-automated version of this approach [6] the authors report a mean error of $8.2 - 8.9mm$ on 7 patients. The benefit and goal of our technique is to provide a computationally tractable, reproducible and generic solution for clinical use, that will not depend on human interaction, while providing accuracy that is clinically useful.

The 3D-2D matching process is a poorly constrained, ill-posed problem and thus the optimisation is prone to terminate in local minima. Keeping the number of degrees of freedom of the transformation to a minimum is therefore essential to provide robustness. We propose learning the space of possible breast deformations by using an ellipsoidal shape of an average size and applying biomechanically simulated compressions. To simulate the mammographic compression, we use a contact model instead of applying displacements on the mesh nodes (as in [5], [7]). This model produces realistic compressed shapes, whilst avoiding artifacts around the breast surface. The main modes of variation are then extracted using PCA. The main advantage of using an ellipsoidal as opposed to a patient-specific deformation model is that a single generic model is created once for all patients, eliminating the need for model creation on a patient by patient basis.

2 Methodology

2.1 Ellipsoidal breast model and compression simulations

To learn the breast deformation between the MR and the X-ray image acquisitions we use an ellipsoidal shape to approximate the average MR breast image

ISBN: 978-87-981270-9-3

and apply biomechanically simulated compressions, similar to the ones applied during mammogram acquisition. As a breast model, we use half an ellipsoid, whose dimensions are calculated from a population of 20 MR breast images. This is given by equation $(x^2/a^2 + y^2/b^2 + z^2/c^2 = 1)$, where the equatorial radii are $a = b = 60mm$ and the polar radius $c = 160mm$.

For the biomechanical simulations, we use a homogeneous transversely isotropic hyperelastic material and we include anisotropy to account for the reinforcement of biomechanical properties from fiber-like connective tissues in preferred directions [10]. Therefore the breast can expand more in the Medial-Lateral (ML) direction, than in the Anterior-Posterior (AP), for a Cranio-Caudal (CC) view compression. This approach can be also justified by the fact that the breast is already extended more in the AP direction due to gravity, as the MRI is acquired in the prone position. For the boundary conditions, we constrain the nodes that are close to the chest wall and allow unconstrained movement of the nodes within that plane. To simulate the compressions, we apply displacements to two contact plates and use a GPU implementation of an explicit Finite Element (FE) solver [11]. To create a range of different deformations, we vary the amount of compression, the ratio of tissue enhancement coefficient and the Poisson's ratio, that controls the amount of breast volume change. For each compression the parameters are chosen randomly from the distributions shown in table 1.

Table 1. Parameters that vary between the different compressions and their distributions taken from the literature ([7], [10]).

Parameter	**Distribution**
Amount of compression	Normal ($\mu = 55\%$, $std = 4\%$)
Poisson's ratio	Uniform [0.45, 0.498]
Ratio of tissue enhancement coefficient	Uniform [1, 512]

2.2 Building a deformation model using PCA

After simulating a range of compressions, the next step is learning the breast deformations using PCA. This method provides the benefit that results are less dependent on the modeling and the FE solver that are used, than the patient-specific modeling. The resulting displacement fields that represent the mean deformation and the deviations from it can then be mapped to the new patient.

The mapping is done using a registration that includes scaling and translation between the space of the ellipsoid model and the patient's MRI. Another advantage of using the ellipsoid model is that this mapping process is only done once, after performing the PCA and extracting the main components. When using a population model, all breast shapes need to be mapped to the same space and given their large variability and the lack of anatomical correspondences, the registrations of the deformation fields can cause significant artifacts. As a result, these artifacts will then appear in the main PCA components, while they should

ISBN: 978-87-981270-9-3

be excluded. Applying all the compressions on one shape instead, provides a solution to this problem.

After simulating n different compressions, each deformation vector $\mathbf{D}_i$ consists of the concatenation of the displacements in the X, Y and Z directions on a regular grid across the volume, that contains m points, so that $\mathbf{D}_i = (\mathbf{d}_1, ..., \mathbf{d}_{3m})$. In a similar way to [12], PCA is used to extract the main modes of variation and approximate any deformation field $\mathbf{D}$ by:

$$\mathbf{D} = \widehat{\mathbf{D}} + \mathbf{P} \cdot \mathbf{b} \tag{1}$$

where $\widehat{\mathbf{D}}$ is the mean deformation field, $\mathbf{P}$ is the matrix of the first t principal components (eigenvectors) and $\mathbf{b}$ is a vector of weights for each one of the t eigenvectors used. The eigenvectors $\mathbf{e}_i$ and their corresponding eigen values λ_i are extracted from the covariance matrix:

$$\mathbf{S} = \frac{1}{n} \Sigma_{i=1}^{n} (\mathbf{D}_i - \widehat{\mathbf{D}})(\mathbf{D}_i - \widehat{\mathbf{D}})^T \tag{2}$$

Figure 1 shows the effect of varying the first 3 principal components of the learnt deformations.

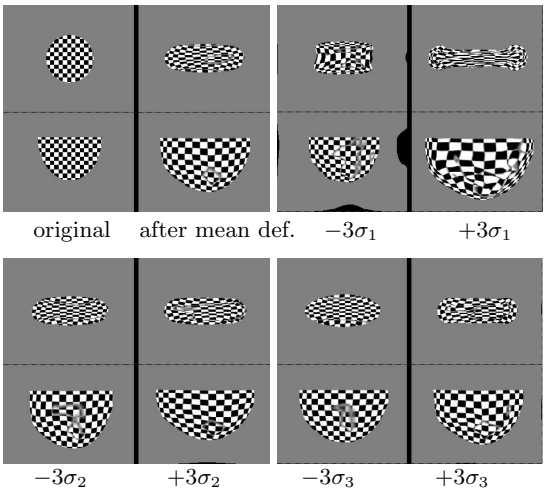

Fig. 1. Coronal (top) and axial (bottom) views of the ellipsoid used, with a superimposed checkerboard pattern. The first component shows the effect of varying the amount of compression, the second the anisotropy ratio (notice change in extension in the axial view) and the third the breast shape under compression (coronal view).

2.3 Registration framework

An overview of the framework is given in table 2. Apart from the main registration process that is updated iteratively, it consists of two more parts that

ISBN: 978-87-981270-9-3

are performed in advance, off-line. The first is the PCA analysis, explained in section 2.2 that needs to be done only once.

Table 2. Overview of the proposed framework.

Once before registration	1. Extract the mean dimensions of an ellipsoid, from a population of breast MRIs 2. Simulate compressions on the ellipsoidal model 3. Extract the mean deformation and the main modes of variation using PCA
Once for each patient	1. Map the PCA components to the new patient 2. Segment the pre-contrast MR to fibro-glandular tissue & fat 3. Simulate a volume corresponding to X-ray attenuation
Iterative registration process	X-ray mammogram: *target*, X-ray attenuation volume: *moving*
	1. Cast rays through the transformed *moving* image 2. Calculate the similarity measure in 2D between the real and the simulated mammogram 3. Update the 3D transformation parameters, according to the derivative of the similarity 4. Go to step (1) until convergence

The second part, also performed before registration, needs to be repeated for each patient. Firstly, we map the PCA components to the new patient space using a translation and scaling registration. Then, we need to transform the MR intensities of the pre-contrast image to X-ray attenuation, so that the perspective projection of the new volume will resemble an X-ray mammogram. For this, we initially segment the volume into fibro-glandular tissue and fat and then acquire the X-ray attenuation volume with the method described in [4]. This is the *moving* image of the registration and the real mammogram is the *target*.

During the registration process, we use ray-casting from the 2D *target* space through the 3D grid of the moving image and integrate the intensities of each transformed intersection of the ray with the 3D grid. This way we avoid an extra 3D interpolation of the transformed 3D volume that would add computational cost. As the transformation is defined from the *compressed* to the *uncompressed* breast space, the transformation of each point is described by equation 3. The total number of degrees of freedom is $n + 5 + 3$, where n is the number of components used. The extra five parameters are three translations along each axis and two rotations; one for the rotation about the AP axis the of the breast (rolling) and one for the rotation about the superior-inferior axis (in-plane). Finally, the last 3 parameters are the scaling factors applied on the displacement fields, when mapped from the ellipsoid to the new patient space. After transforming and projecting the X-ray attenuation volume, we compute the similarity between the real and the simulated mammogram and update the parameters of the transformation $T(x)$ iteratively. For a point x_i the transformation is:

$$T(x_i) = T_3(T_2(T_1(x_i))) \tag{3}$$

ISBN: 978-87-981270-9-3

where:

$$T_1(x_i) = T_{translation}(R_{in-plane}(x_i)) \tag{4}$$

$$T_2(x_i) = x_i + \widehat{D^i} + b_1 \cdot D_1^i + b_2 \cdot D_2^i + ... + b_n \cdot D_n^i \tag{5}$$

$$T_3(x_i) = R_{rolling}(x_i) \tag{6}$$

3 Experiments

For the experiments we used half an ellipsoid of resolution $[1 \times 1 \times 1]mm^3$. The surface mesh was extracted using the vtk marching cubes algorithm and the tetrahedral elements were generated using an opensource software package[3]. The final model consisted of $3,535$ nodes and $12,056$ elements. For the compression simulations we used an opensource GPU implementation of an explicit FE solver[4] to simulate 100 compressions. For the PCA, we have subsampled the deformation fields by a factor of two to reduce the computational cost. In the registration process, we used 3 PCA components (so 11 degrees of freedom); the similarity measure was Normalised Cross Correlation.

For validation we used MRIs and CC view X-ray mammograms of 10 patients, acquired approximately at the same time point. The patient group was different to that used to extract the mean ellipsoid dimensions. The voxel resolution of the MRIs was $[0.9 \times 0.9 \times 1.0]mm^3$ for 3 cases and $[0.6 \times 0.6 \times 1.3]mm^3$ for 7. The resolution of the X-ray mammograms was $[0.1 \times 0.1]mm^2$; they were subsampled to $[1 \times 1]mm^2$ for registration. The patients had a range of different pathologies.

Radiologists' annotations were used as ground truth correspondences. The MR lesions were marked using spheres, while the X-ray images using either a circle, or a free-form shape defining the finding. As it is generally harder to annotate the 3D images accurately, the spheres did not always represent the finding's actual volume, but were centred around it. As a result we have used as error metric the distance between the centres of the annotated regions, rather than an overlap measure. In all the results shown below, the registration error is the 2D Euclidean distance between the centres of the X-ray annotation and the projection of the MR annotation, after being deformed, in the first experiments with our method and in the second with an affine transformation [4].

Table 3. Registration error (in mm) of our Ellipsoid SDM (E-SDM) method and comparison with the affine transformation [4].

	p1	p2	p3	p4	p5	p6	p7	p8	p9	p10
E-SDM	7.8	14.0	9.7	5.7	9.3	13.7	6.2	12.3	24.4	24.3
Affine	1.9	14.2	12.6	12.0	28.3	15.1	28.5	14.6	39.1	28.3

[3] http://tetgen.berlios.de/
[4] http://sourceforge.net/projects/niftysim/

ISBN: 978-87-981270-9-3

A summary of the results is given in table 3. Overall our method outperformed the affine transformation by several mm in all cases, apart from one (p1). Figure 2 illustrates the results on 4 cases. We can see that the projection of the MR finding was close to the X-ray annotation and even in cases where the distance was rather high (eg.$p2 = 14mm$), the projection was still inside the annotated X-ray area, shown in green. Two of the cases that gave very high errors are shown in figure 3 together with the MRI annotations, to illustrate the difficulty in registering these findings. In all the other 8 cases the projected MR annotation mask overlapped with the one of the X-ray and the mean registration error was $9.8mm$, as opposed to $15.9mm$ for the affine.

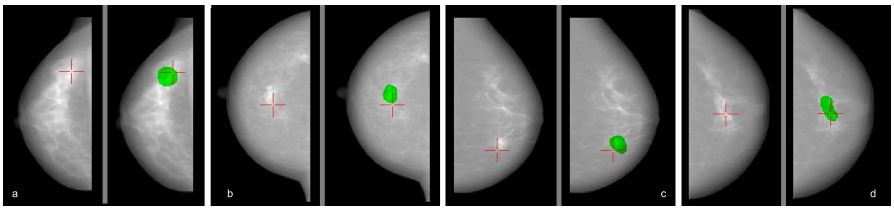

Fig. 2. Registration results on 4 patients. For each case, the left image shows the real mammogram with the centre of mass of the MR annotation after alignment (red cross). The right image in each pair shows again the real mammogram, but in addition to the projected MR annotation, it is this time overlayed by the mask of the X-ray annotation, shown in green.(a) p1 ($7.8mm$), (b) p2 ($14mm$), (c) p3 ($9.7mm$) and (d) p4 ($5.7mm$).

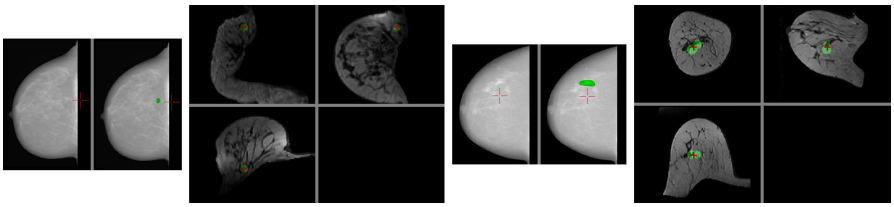

Fig. 3. Cases with high registration error. Patients p9 (left) and p10 (right).

4 Discussion

This study presented a novel framework for registering MRI to X-ray mammograms. The main advantages include the reduced sensitivity to the approximations associated with individual patient-specific modeling and simulations, as well as the improved accuracy compared to an affine transformation. Using a non-rigid transformation learnt from simulated compressions has the benefit of providing physically realistic deformations. Also, the small number of degrees of freedom adds robustness to the 3D-2D matching process. Nevertheless, a potential limitation of the current approach concerns how well an ellipsoid shape can

ISBN: 978-87-981270-9-3

approximate the shape and deformation of a real breast. To answer this question future work includes testing against patient-specific modeling techniques, both learnt before registration and updated inside the iterative registration process. Another factor that can be tested is the removal of the effect of gravity before compression. Finally, further work involves more validation tests on a larger dataset and on the MLO mammographic view.

Acknowledgments. This work was funded by the European 7th Framework Program, HAMAM, ICT-2007.5.3. The authors would like to thank the Radboud University Nijmegen Medical Centre for providing the data with annotations.

References

1. Yuan, Y., Giger, M., Li, H., Bhooshan, N., Sennett, C., Multimodality Computer-Aided Breast Cancer Diagnosis with FFDM and DCE-MRI, Academic Radiology, vol. 17, pp. 1158–1167, 2010.
2. Behrenbruch, C., Marias, K., Armitage, P., Moore, N., English, R., Clarke, J., Brady, M.: Fusion of contrast-enhanced breast MR and mammographic imaging data, Med. Image Anal., vol. 7, pp. 311–340, 2003.
3. Marti, R., Zwiggelaar, R., Rubin, C., Denton, E.: 2D-3D correspondence in mammography, Cybernetics and Systems, vol. 35, pp. 85–105, 2004.
4. Mertzanidou, T., Hipwell, J., Cardoso, M.-J., Tanner, C., Ourselin, S., Hawkes, D.: X-ray mammography - MRI registration using a volume-preserving affine transformation and an EM-MRF for breast tissue classification, Digital Mammography, LNCS, pp. 23–30, 2010.
5. Ruiter, N., Stotzka, R., Muller, T., Gemmeke, H., Reichenbach, J., Kaiser, W.: Model-Based registration of X-ray Mammograms and MR images of the female breast, IEEE Transactions on Nuclear Science, vol. 53, pp. 204–211, 2006.
6. Dietzel, M.,Hopp, T., Ruiter, N., Zoubi, R., Runnebaumd, I., Kaiser, W., Baltzer, P.: Fusion of dynamic contrast-enhanced magnetic resonance mammography at 3.0T with X-raymammograms: Pilot study evaluation using dedicated semi-automatic registration software, European Journal of Radiology, In Press, 2011.
7. Tanner, C., Hipwell, J., Hawkes, D.: Using Statistical Deformation Models for the Registration of Multimodal Breast Images, Proc. SPIE Medical Imaging: Image Processing, vol. 7259, pp. 72590P-72590P-9, 2009.
8. Samani, A., Bishop, J., Yaffe, M., Plewes, D., Biomechanical 3-D Finite Element Modeling of the Human Breast Using MRI Data, IEEE TMI, vol. 20, pp. 271–279, 2001.
9. Chung, J., Rajagopal, V., Nielsen, P., Nash, M.: Modelling Mammographic Compression of the Breast, MICCAI, LNCS, pp. 758–765, 2008.
10. Tanner, C., M. White, M., Guarino, S., Hall-Craggs, M., Douek, M., Hawkes, D., Large breast compressions - Observations and evaluation of simulations, Medical Physics, vol. 38, pp. 682–690, 2011.
11. Taylor, Z., Comas, O., Cheng, M., Passenger, J., Hawkes, D., Atkinson, D., Ourselin, S., On modelling of anisotropic viscoelasticity for soft tissue simulation: Numerical solution and GPU execution, Med. Image Anal., vol. 13, pp. 234–244, 2009.
12. Cootes, T., Edwards, G., Taylor, C., Active Appearance Models, IEEE PAMI, vol. 23, pp.681–685, 2001.

A Multi-Scale Blob Based Representation of Mammographic Parenchymal Patterns for Breast Density Classification

Zhili Chen[1,3], Erika Denton[2], and Reyer Zwiggelaar[1]

[1]Department of Computer Science,
Aberystwyth University, Aberystwyth, SY23 3DB, UK
zzc09@aber.ac.uk, rrz@aber.ac.uk
[2]Department of Radiology,
Norfolk and Norwich University Hospital, Norwich, NR4 7UY, UK
erika.denton@nnuh.nhs.uk
[3]Faculty of Information and Control Engineering,
Shenyang Jianzhu University, Shenyang, 110168, China

Abstract. There is an association between mammographic parenchymal patterns and breast cancer risk. We focus on approximately blob-like dense tissue patterns (e.g. nodular, fibroglandular, and homogeneous tissue) to model breast tissue density. These blob-like tissues are detected based on the Laplacian scale-space representation of mammographic images at a range of scales. The findings are represented as a set of multi-scale blobs. Qualitative relations among these blobs are incorporated in order to capture the breast anatomical structure. The distribution of the multi-scale blobs in scale space can be used as an overall model for breast density classification. The results based on the MIAS database show 79% correct classification according to four BIRADS denstiy classes, and 93% correct classification for two (i.e. low/high) density classes, respectively.

1 Introduction

Parenchymal patterns play an important role in mammographic risk assessment [1]. Parenchymal patterns are formed by the spatial distribution of relatively dense tissues. In this work, we use a set of multi-scale blobs to represent local salient tissue patterns. Effectively, we propose to model noludar and homogeneous tissue with relatively high density as described by Tabár et al. [2]. Some example breast tissue patterns in Tabár's tissue model are shown in Fig. 1.

Scale-space theory provides a framework for image representation at multiple scales, which has been widely applied in describing objects. Blob-like structures can be detected at the local extrema in the scale-space signature. The size of the blobs can be estimated as the scale at which the extrema are obtained [3]. In mammographic image analysis, a number of scale-space based methods have been developed, however, no previous publications have suggested modelling breast tissue based on blob-like tissue patterns. A related method was described in [4], which aimed to detect clustered microcalcifications.

ISBN: 978-87-981270-9-3

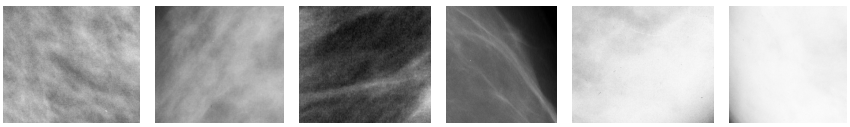

(a) (b) (c) (d) (e) (f)

Fig. 1. Example breast tissue patterns: (a), (b) nodular tissue; (c), (d) linear tissue; (e), (f) homogeneous tissue.

Numerous methods for characterising mammographic parenchymal patterns have been developed. Karssemeijer [5] calculated features based on greylevel histograms. Oliver et al. [6] extracted a set of morphological and texture features from fatty and dense tissue regions. Petroudi et al. [7] proposed a statistical method for modelling parenchymal patterns. Subashini et al. [8] extracted statistical features from the suspicious region of the entire breast, eliminating the artifacts, background and the pectoral muscle. Raundahl et al. [9] used the texture information at each pixel in the segmented breast to score heterogeneity of mammographic patterns. He et al. [10] presented a novel texture signature based mammographic image segmentation method.

It should be noted that there are two differences between our modelling of mammographic parenchymal patterns and exsiting approaches [5–10]. We do not apply an implicit intensity normalisation of the mammographic images to overcome brightness and contrast variations in the acquisition process. In addition, we do not assume that mammograms in the same mammographic risk class have the same texture appearance. In our developed representation of breast parenchymal patterns, multi-scale blobs are local salient features which can accommodate large greylevel variations, and the distribution of these blobs and their qualitative relations can describe the anatomical structures of breast tissues, which have a strong correlation with mammographic risk. The modelling can be considered as the simulation of the mammogram perception process by radiologists, who are sensitive to salient tissue patterns and interpret mammograms according to the distribution and topology of these salient aspects.

In addtion, the developed approach is supported by mammogram synthesis methods. In [13], synthetic mammograms were generated by simulating breast tissues with large and medium scale tissue structures comprising different sized tissue elements (i.e. shells and blobs). The formation of breast parenchymal patterns was modelled by the projection of these compartments. We aim to reverse this generation process, and decompose breast tissues into a set of blobs at different scales (inclusion of shell-like structures is seen as future work).

2 Multi-Scale Blob Representation

The approach used to detect blobs is based on the Laplacian operator. Blob detection is performed by finding the extrema of the normalised Laplacian $\bigtriangledown^2_{norm}L$

ISBN: 978-87-981270-9-3

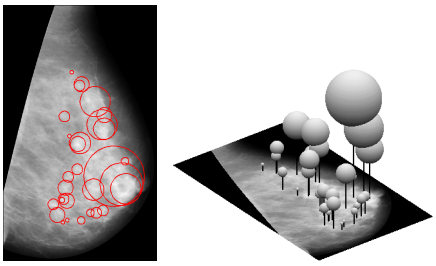

(a) (b)

Fig. 2. Blob detection: (a) detected blobs shown as circles in a mammographic image; (b) three-dimensional view. (The original mammographic image is shown in the horizontal plane, and the vertical dimension corresponds to scale.)

with respect to both space and scale:

$$\nabla^2_{norm} L = t(L_{xx} + L_{yy}) \tag{1}$$

where L is the scale-space representation of image $I(x, y)$, defined by convolution with Gaussian kernels of various width t ($t = \sigma^2$). See [3] for more details. The scale range covers ten scales, where the first scale $\sigma_1 = 8$, and the scale factor $k = \sqrt{2}$. In order to detect the scale-space extrema, each sample point in the breast area is compared with its neighbours within a local region in the current scale-space image and the corresponding "neighbours" in other scale-space images. Only spatial global extrema (either minima or maxima) over all scales are retained [3]. We use 5×5 local regions at each scale (similar size region indicated robustness of results), so the blobs are detected at the global extrema of $5 \times 5 \times 10$ blocks in the scale-space image representation. For efficiency reasons, at each scale instead of increasing the local kernel by the factor k, we downsample the image by the factor $1/k$. We then upsample each result in the hierarchical construction to the full size in order to find the extrema. We indicate these blobs with circles, whose radii are the corresponding scales. To exclude the effects caused by the image margins and the breast boundary, smaller blobs of which the covering regions appear outside the breast area are ignored. The tissue patterns of interest here are high-density regions, which are detected in the form of bright blobs, so the positive extrema (i.e. dark blobs) are discarded. In addition, the extrema with low contrast are also rejected (this step can be regarded as contrast based thresholding taking spatial information into account). The remaining extrema are the blob candidates.

In order to capture the true blob-like dense tissues, it is not sufficient to reject the extrema with weak responses. At larger scales, some false blobs (non-dense tissue) tend to appear along the breast boundary, due to the influence of the natural breast profile. The reduction of the false positives can be easily performed by means of putting a threshold on the mean greylevel within the blob area. To calculate the threshold, the fuzzy c-means based clustering algorithm is used to

ISBN: 978-87-981270-9-3

partition pixels within the breast area into nine clusters [12]. The difference between the mean intensity and the standard deviation of clusters from six to nine (corresponding to dense tissue) is chosen as the threshold. Alternative number of clusters and those selected to represent dense tissue provide similar results. The candidates with the mean intensity below the threshold are removed. A mammographic image with the detected blobs superimposed is shown in Fig. 2(a). The three-dimensional view is shown in Fig. 2(b).

2.1 Merging Multi-Scale Blobs

The multi-scale blobs detected above mainly correspond to the visually blob-like dense tissues. When two blobs are closely located, they will overlap with each other. To generate an overall model of dense tissues, we merge the overlapping blobs based on their qualitative relations. Here, we consider three types of qualitative relations: external, intersection, and internal. The qualitative relation between two blobs depends on their respective radii and the distance between their centre points.

The merging procedure starts from the largest scale and proceeds to smaller scales. The qualitative relations are inspected over all the blobs. To illustrate the qualitative relations among all the blobs, a directed acyclic blob graph is constructed, which can describe the topology of these blobs (see Fig. 3). The hierarchy of the blob graph is from the coarse scale to the fine scale. There is an edge between two blob nodes if they overlap with each other (intersection or internal). The blob at the coarsest scale in a blob cluster is chosen as the root of a subgraph. A virtual top root node (representing the whole breast) is used to form a single rooted graph.

The blob merging is performed based on the following criteria. The external blobs separately located in the image will be retained, while the internal blobs contained by larger ones will be removed. When two blobs A (σ_A, r_A) and B (σ_B, r_B) intersect with each other, if they are extremely closely located ($d \leq r_A - \alpha r_B, r_A \geq r_B, 0.8 < \alpha < 1$), the integration of the Gaussian scale-space signature over the blob area will be calculated by $\int_{blob} g(x, y; \sigma^2) * I(x, y) dxdy$. The blob with the larger value will be retained. A simple example of blob merging is shown in Fig. 3. The structural distribution of the blobs is simplified after merging, moreover, the coarse appearance of dense tissues within the breast is preserved by the remaining blobs. Alternative, scale-space cones based, approaches could be considered for the merging of blobs.

2.2 Encoding Multi-Scale Blobs

The retained blobs after the blob merging can be used to model the breast density. For quantitative analysis, we quantify the breast density by means of encoding the multi-scale blobs. Specifically, the distribution of the blobs is represented by a vector $N = (N_1, N_2, \ldots, N_n)$. The dimensionality n corresponds to the number of scales, where N_i $(i = 1, 2, \ldots, n)$ is the number of blobs at

ISBN: 978-87-981270-9-3

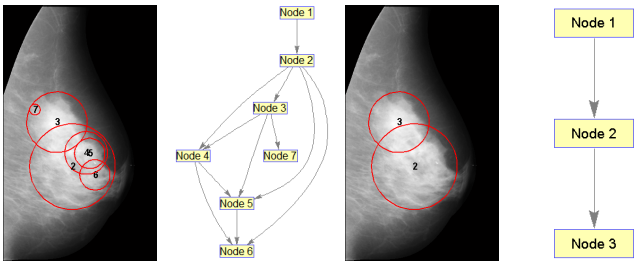

Fig. 3. Blob merging: (a) detected blobs; (b) blob graph; (c) remaining blobs after blob merging; and (d) blob graph after blob merging ($\alpha = 0.84$).

scale i. Subsequently, the vector N is transformed into a unique number by:

$$BLOB = \sum_{i=1}^{n} N_i k^{2(i-1)} \tag{2}$$

where $k = \sqrt{2}$ is the scale factor as described previously. The resultant value "$BLOB$" is defined as the density measurement of the breast, which can be used for breast density classification.

3 Results and Discussion

To evaluate the proposed multi-scale blob based representation of mammographic parenchymal patterns, it has been tested using the Mammographic Image Analysis Society (MIAS) database [11]. Three experts classified 321 mammograms (mdb295ll was excluded for historical reasons) according to the Breast Imaging Reporting and Data System (BIRADS) standard [1]. The consensus result was considered as the classification ground truth.

Three-dimensional views of blobs at ten scales (after merging) detected for example mammograms covering the four BIRADS classes are shown in Fig. 4. For BIRADS I, the breast is almost entirely fatty, only a few small scale blobs are detected; for BIRADS II, some small and medium scale blobs are located at some fibroglandular tissue; for BIRADS III, the breast is heterogeneously dense, the dense area is covered by a few relatively large scale blobs; while for BIRADS IV, the breast is extremely dense, the whole breast is mainly covered by large scale blobs. The distribution of multi-scale blobs is shown as bar charts in Fig. 4. This shows that the number of blobs at larger scales increases with respect to the increasing BIRADS classes. The corresponding value of "$BLOB$" computed by equation (2) is 153, 378, 601, and 1992, respectively.

A leave-one-woman-out evaluation methodology was used for the classification. When classifying one mammogram, the other mammogram from the same

ISBN: 978-87-981270-9-3

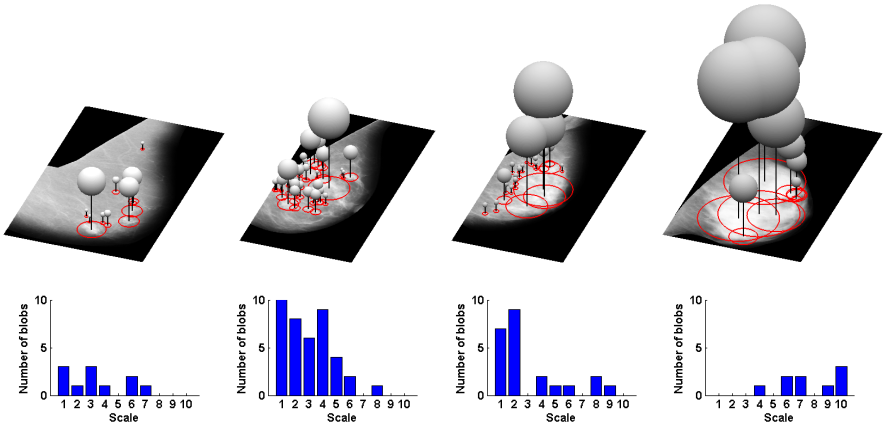

Fig. 4. Three-dimensional views of muiti-scale blobs detected for example mammograms (top row) and the distribution of the blobs in forms of bar charts (bottom row). From left to right, the mammograms are sorted from BIRADS I to BIRADS IV, and the corresponding breast density is from low to high.

woman was excluded from the training samples to avoid bias. We used a K-Nearest Neighbours (KNN) based classifier. A value of K=8 was selected, but small variations in K produced similar results. To avoid bias caused by different sizes of the breast, the density measurement "$BLOB$" was normalised by $BLOB_{norm} = (A_{blob}/A_{breast})BLOB$, where A_{blob} denotes the area of the blob at the finest scale, and A_{breast} represents the area of the whole breast. After normalisation, the density measurement can reflect the relative proportion of dense tissues for the whole breast, which can be linked to the BIRADS criteria. To cope with the multi-class classification (4 classes), initially, a classic KNN was used, but when equal classes were indicated, we used a weighted KNN approach.

Table 1 shows the classification results based on 321 mammograms in the MIAS database [11] according to the four BIRADS classes, where each row corresponds to the consensus truth, and each column corresponds to the automatic classification. The classification accuracy (CA) for the four-class classification is 79%, and increases to 93% when considering the two-class (i.e. low and high density) classification. The relatively poor performance for BIRADS IV might be explained by the lower number of samples for that class. Furthermore, it should be noted that none of mammograms were mis-classified by more than one BIRADS class. We compared the obtained results with some closely related publications for breast density classification. A number of these publications (e.g. [6, 10]) used the same database and the same ground truth, so a direct comparison is possible. Table 2 shows a summary of the comparison.

For blob detection, the Laplacian of Gaussian based blob detector was used, while a range of other blob detectors (e.g. the determinant of Hessian [3], the difference of Gaussian [14], Harris-Laplace [15], Hessian-Laplace [15], or SURF [16])

ISBN: 978-87-981270-9-3

		Automatic				
	BIRADS	I	II	III	IV	CA
Truth	I	72	15	0	0	83%
	II	7	85	11	0	83%
	III	0	11	75	8	80%
	IV	0	0	16	21	57%

Table 1. Confusion matrix of breast density classification, with overall classification accuracy (CA) equal to 79%.

Method	Database	Standard	Classifier	CA
[7]	Oxford	BIRADS	KNN	76%
[6]	MIAS	BIRADS	KNN	77%
[10]	MIAS	BIRADS	KNN	75%
Our	MIAS	BIRADS	KNN	79%

Table 2. Comparison of the proposed method with the closely related work.

could be used. Moreover, we used a greylevel threshold to reduce the false positives. In future work, we will further investigate the aspects of both false positive and false negative reduction. At the blob merging step, some overlapping blobs were removed to simplify the topological structure of multi-scale blobs and fuse them into a general blob representation of parenchymal patterns. The effects of this merging step will be further investigated. In addition, the tissue appearance within the individual blob region will be analysed. The texture signature of different sized blobs will be incorporated into the current blob distribution based representation. We used a leave-one-woman-out methodology in our experiments, where the distribution of training samples in the four classes was unbalanced. BIRADS IV was not well represented in the training set, which might explain the lower performance for this class. The unbalanced training sample problem will be further investigated to optimise the classification. As future work, we will also extend the evaluation into full field digital mammogram databases and alternative (non-BIRADS) classification schemes. In addition, the incorporation of shell-like structures will be investigated.

4 Conclusions

We have proposed a multi-scale blob based representation of mammographic parenchymal patterns, based on the prior knowledge about the breast tissue anatomical structure and the breast tissue elements. We focused on local extrema in scale space, and used multi-scale blobs to represent the approximately blob-like tissue patterns. The qualitative relations and the overall distribution of these blobs were combined to define a density measurement of the breast. For breast density classification, a high agreement has been achieved with the consensus

ISBN: 978-87-981270-9-3

result from three experts. The classification results are comparable with the state of the art. To our knowledge, this work is a first attempt to model the breast density based on the dense tissues with blob-like structures.

References

1. American College of Radiology: Illustrated Breast Imaging Reporting and Data System BIRADS. 3rd ed. Amer. College of Radiol (1998)
2. Tabár, L., Tot, T., Dean, P.B.: Breast Cancer - the Art and Science of Early Detection with Mammography: Perception, Interpretation, Histopathologic Correlation. George Thieme Verlag (2005)
3. Lindeberg, T.: Feature Detection with Automatic Scale Selection. International Journal of Computer Vision 30(2), 79–116 (1998)
4. Netsch, T., Peitgen, H. O.: Scale-space Signatures for the Detection of Clustered Microcalcifications in Digital Mammograms. IEEE Transactions on Medical Imaging 18(9), 774–786 (1999)
5. Karssemeijer, N.: Automated Classification of Parenchymal Patterns in Mammograms. Physics in Medicine and Biology 43, 365–378 (1998)
6. Oliver, A., Freixenet, J., Martí, R., Pont, J., Pérez, E., Denton, E.R.E., Zwiggelaar, R.: A Novel Breast Tissue Density Classification Methodology. IEEE Transactions on Information Technology in Biomedicine 12(1), 55–65 (2008)
7. Petroudi, S., Kadir, T., Brady, M.: Automatic Classification of Mammographic Parenchymal Patterns: A Statistical Approach. In: 25th Annual International Conference of the IEEE Engineering in Medicine and Biology Society, pp. 798–801 (2003)
8. Subashini, T. S., Ramalingam, V., Palanivel, S.: Automated Assessment of Breast Tissue Density in Digital Mammograms. Computer Vision and Image Understanding 114(1), 33–43 (2010)
9. Raundahl, J., Loog, M., Pettersen, P., Tanko, L. B.: Automated Effect-specific Mammographic Pattern Measures. IEEE Transactions on Medical Imaging 27(8), 1054–1060 (2008)
10. He, W., Denton, E.R.E., Zwiggelaar, R.: Mammographic Image Segmentation and Risk Classification Using a Novel Texture Signature Based Methodology. LNCS, vol. 6136, pp. 526–533 (2010)
11. Suckling, J., Parker, J., Dance, D. R., Astley, S., Hutt, I., Boggis, C., Ricketts, I., Stamatakis, E., Cerneaz, N., Kok, S. L., Taylor, P., Betal, D., Savage, J.: The Mammographic Image Analysis Society Digital Mammogram Database. Excerpta Medica. International Congress Series 1069, 375–378 (1994)
12. Chen, Z., Zwiggelaar, R.: A Modified Fuzzy C-Means Algorithm for Breast Tissue Density Segmentation in Mammograms. In: 10th IEEE International Conference on Information Technology and Applications in Biomedicine (2010)
13. Bakic, P.R., Albert, M.: Mammogram Synthesis Using a 3D Simulation. I. Breast Tissue Model and Image Acquisition Simulation. Medical Physics 29(9), 2131–2139 (2002)
14. Lowe, D.G.: Distinctive Image Features from Scale-Invariant Keypoints. International Journal of Computer Vision 60(2), 91–110 (2004)
15. Mikolajczyk, K., Schmid, C.: Scale and Affine Invariant Interest Point Detectors. International Journal of Computer Vision 60(1), 63-86 (2004)
16. Bay, H., Ess, A., Tuytelaars, T., Gool, L.V.: Speeded-Up Robust Features (SURF). Computer Vision and Image Understanding 110(3), 346–359 (2008)

ISBN: 978-87-981270-9-3

Workshop on Breast Image Analysis
In conjunction with MICCAI 2011

Multiscale Breast Mass Analysis Using the Curvelet Transform

Fabián Narváez[1], Gloria Díaz[1], Francisco Gómez[1,2], and Eduardo Romero[1]

[1] Bioingenium Research Group, Departament of Medicine, National University of Colombia, Bogotá, Colombia
[2] Coma Science Group, Cyclotron Research Centre, University of Liège, Liège, Belgium
{frnarvaeze,fagomez,gmdiazc,edromero}@unal.edu.co
http://www.bioingenium.unal.edu.co

Abstract. An objective and detailed description of a particular Region of Interest (RoI) is at the base of the diagnosis process in mammography. A successful automatic analysis starts by choosing discriminant descriptors, capable of capturing the essential tissue properties. This paper presents a new multiscale feature representation for analyzing mammographic masses using the curvelet transform. The marginal curvelet subband distribution and the interscale-orientation statistical dependences are approximated with a generalized Gaussian density (GGD) and the Kullback−Leibler divergence between the GGD statistical parameters is used to measure the distance between images. The effectiveness of the proposed descriptor was twofold evaluated: classifying masses using a simple nearest neighbor classifier, resulting in an sensitivity rate of 96.4%, and retrieving similar images from a reference database, which reports an average precision of 86% and recall of 75%.

Keywords: Breast Cancer, BI-RADS, Content-based Image Retrieval, Curvelet transform

1 Introduction

Breast cancer is the most frequent cancer in women and is considered as a public health problem in the female population. Early detection definitely improves the disease prognosis, reason by which breast cancer screening programs have been worldwide introduced as a diagnostic tool to detect subtle signs in asymptomatic women [1]. Mammography, as part of these screening programs, is considered the most cost-effective method [1]. One of the main signs associated with breast cancer is the presence of masses, coarsely classified as benign or malign. Although the final diagnosis can be only achieved through a biopsied specimen, some specific visual features such as the particular shape and margin are used by the radiologists to set a diagnosis. Mammography interpretation, and particularly mass description, is really a difficult task that requires a lot of experience. Recently, this radiologist's work has been facilitated by the use of new computing tools, known as Computer-Aided-Diagnosis systems (CAD).

ISBN: 978-87-981270-9-3

CAD systems have so far reported a high performance for micro-calcification cluster detection [8]. However, these computational tools have shown relatively low performance for mass detection. Recently, systems based on comparisons with a reference diagnosed database have been proposed as a strategy for improving the radiologist confidence in CAD systems, particularly to improve the analysis performed on an user selected mass [13,9]. In this case, diagnoses obtained from the CAD system should be consistent with the information stored in a database since they must exploit the similarity between the image to analyze and a set of annotated images. Main challenges in such strategies are the extraction of the most discriminative features and the selection of an adequate similarity metrics. Different types of characteristics have been introduced to capture discriminant tissues, for instance by using the Fourier transform, attempting to separate frequential information that contains specific characteristics. Nevertheless, these features are mostly variable and scale-dependent. In contrast, multiresolution analysis allows to preserve image features. Liu et al. [11] demonstrated that the use of a multiresolution wavelet analysis of mammograms, improves the effectiveness of a CAD system. Murtagh and Stark [6] used second, third and fourth order moments of multiresolution transforms (wavelet and curvelet) coefficients as a feature descriptor for classifying mammograms using a K-nearest neighbors as the supervised classifier. Eltoukhy et al.[4] presented a study of mammogram classification, based on the curvelet transform, in which a subset of the largest coefficients from each decomposition level was used as the feature vector. They proved in this case that multiresolution analysis achieved promising results.

In this paper, a new feature extraction approach, based on a multiscale decomposition using the curvelet transform, is assessed for analyzing breast masses. Selected regions containing a mass are firstly preprocessed to enhance the differences between patterns associated to mass and parenchyma tissue. A multiscale curvelet decomposition allows to approach the image statistical properties and a GGD approximates the subband data distribution, whereby any subband is described by means of the GGD parameters, e.g., mean and variance. Finally, the Kullback-Leibler divergence is used to estimate differences between several orientation and scale subbands of the selected region and the images of a reference database. This strategy was compared to a base line constructed with a curvelet-based decomposition and a simple Euclidean distance, resulting our proposal in a best performance for both classification and retrieval tasks.

2 Methodology

2.1 RoI Pre-processing

Mammography analysis is very likely one of the most difficult radiological examinations since these images capture a very complicated anatomical object with a limited spatial resolution. Every image was herein stretched to the maximum and minimum gray level values ($[0, 255]$), adaptively equalizing the histogram so

ISBN: 978-87-981270-9-3

that structural details were preserved. Resultant images were smoothed out by a median filter to remove the remaining noise.

2.2 The curvelet transform

The curvelet transform is a multiscale transform [2], developed to naturally represent bidimensional objects, improving the wavelet 2D limitations. Curvelets constitute an over complete basis which optimally represent 2D curves. While the wavelet provides information about scale and location, the curvelet also yields accurate information about orientation, restricted by the parabolic anisotropic scaling law $width \approx length^2$, or in other words curves at different scale levels preserve their geometrical relationships [2].

In the frequential curvelet plane, radial displacements correspond to different scales, predominant orientation is given by the particular angle and the frequency information is contained in each of the resulting sub-bands. This representation is constructed as the product of two windows: the angular and the radial dyadic frequential coronas. The angular window corresponds to a directional analysis, i.e., a Radon transform, and the radial dyadic window is a bandpass filter, whose cut frequencies which follow the parabolic anisotropic scaling law [2]. Curvelet bases were designed to fully cover the frequency domain, in contrast to other directional multiscale representations such a the Gabor transform [2], from which some information is always lost. Thanks to the anisotropic scale, curvelets adapt much better to scaled curves than Gabor transform, improving the representation at different scales and noise robustness [12,5].

2.3 Statistical characterization

Mammogram masses may be seen as a complex mixture of multiple curves, that depending on the degree of malignity, may exhibit different texture patterns, from very loosen appearances to a dense object with very blurred boundaries [10]. Recent evidence has demonstrated that the curvelet subband marginal distributions have a good characterization power for texture discrimination tasks [12,5]. Our fundamental hypothesis is that the curvelet distribution information may also provide enough characterization power to discriminate texture patterns of benign or malign lesions. In particular, we are supposing that for the same degree of malignity, corresponding curvelet subbands exhibit the same local curve distribution.

As observed in figure 1, the curvelet subband coefficient distributions, obtained from actual breast masses, are characterized by sharper peaks at zero and heavy tails. In this case, usual Gaussian distribution assumptions proposed in the literature [12] are not satisfied. In contrast, a Generalized Gaussian Density (GGD) distribution fully characterizes the subband curvelet distribution [5]. As observed in figure 1, GGD (red) provides a better adjustment to the marginal density than the Gaussian distribution (green). This observation was quantitatively confirmed by comparing the Kullback-Leibler divergence (KLD) between the empirical distribution (ED) and the fitted GGD, and the ED and the fitted

ISBN: 978-87-981270-9-3

Gaussian distribution. For the example, in figure 1 the KLD value for ED-GGD comparison was 0.11 and 0.53 for ED-Gaussian. We extended this analysis to the complete set of 66 subband curvelets for a randomly selected image, resulting in a KLD value of 0.08 ± 0.6 (mean $\pm$ std) for the ED-GGD and 0.44 ± 0.15 for the ED-Gaussian case. This analysis shows that GGD provides a better adjustment to the curvelet subband distribution than the usual Gaussian characterization.

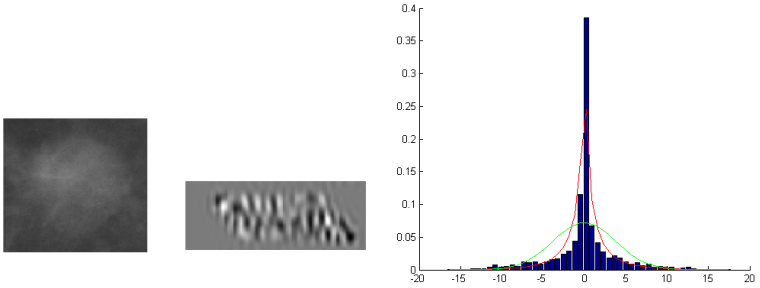

Fig. 1. Curvelet histogram example from a randomly selected subband. (a) RoI containing a breast mass, (b) Curvelet subband corresponding to scale 4 and orientation 59, (c) coefficient distribution with Gaussian (green) and GGD (red) adjustments.

The GGD is defined as

$$p(x;\alpha,\beta) = \frac{\beta}{2\alpha\Gamma(1/\beta)} e^{-(|x|/\alpha)^{\beta}} \tag{1}$$

where $\Gamma(z) = \int_0^{\infty} e^{-t} t^{z-1} dt$, $z > 0$ is the Gamma function, α is the variance and β is related to the decreasing rate of the GGD. The parameters α and β are estimated from the subbband data through Maximum Likelihood [3]. According to [5] the GGD parameters (α,β) may be used as descriptor of the probability density function of the energy levels inside each curvelet subband.

2.4 Similarity measure

The similarity between subband curvelets is measured using the Kullback-Leibler divergence (KLD) of the corresponding GGDs:

$$D(p(.;\alpha_1,\beta_1)||p(.;\alpha_2;\beta_2)) = \log\left(\frac{\beta_1\alpha_2\Gamma(1/\beta_2)}{\beta_2\alpha_1\Gamma(1/\beta_1)}\right) + \left(\frac{\alpha_1}{\alpha_2}\right)^{\beta_2} \frac{\Gamma((\beta_2+1)/\beta_1)}{\Gamma((1/\beta_1)} - \frac{1}{\beta_1}$$

where (α_1,β_1) and (α_2,β_2) are the GGD parameters estimated for each subband. This metric does not require additional normalization and has shown good performance in other multiscale domains [3]. Finally, under the reasonable assumption that curvelet coefficients in different subbands are independent, the

ISBN: 978-87-981270-9-3

similarity between two images I_1 and I_2 is measured as the sum of the distances between corresponding subbands

$$D(I_1, I_2) = \sum_{\forall s} \sum_{\forall \theta} D(p(.; \alpha_1^{s,\theta}; \beta_1^{s,\theta}) || p(.; \alpha_2^{s,\theta}; \beta_2^{s,\theta})) \quad (2)$$

where $(\alpha_1^{s,\theta}, \beta_1^{s,\theta})$ and $(\alpha_2^{s,\theta}, \beta_2^{s,\theta})$, are the GGD parameters estimated for corresponding subbands, i.e., subbands in the same scale s and orientation θ.

2.5 Experimental results

The proposed descriptor was twofold evaluated: first, a K nearest neighbor (KNN) classification strategy was used to label masses as benign or malign, and secondly, a content based image retrieval (CBIR) strategy [7] was used to find similar masses in an annotated database, according to the BIRADS description. In both, cases the proposed descriptor characterized regions containing breast masses and the Kullback-Leibler divergence was the similarity measure. Results were compared with other curvelet representation methods, namely: energy of the curvelet subband plus Euclidian metric ($EUCL\_1$)[12], mean and variance plus Euclidian metric ($EUCL\_2$) [12] and the proposed method GGD plus KLD metric.

Regions of interest (RoIs) containing mass lesions, extracted from the *Digital Database for Screening Mammography (DDSM)* were used for evaluation. A RoI is herein a small image exclusively containing the mass so that the scenario is a specialist selecting a suspicious mass in the mammogram and sending it to the system. These images were previously annotated by a group of breast radiologists following the BI-RADS specification, as shown in Table 1, in terms of mass characterization. Each mass description includes shape, margin and pathology .

Table 1. Distribution of the reference data set used for evaluating the proposed approach

$Shape$	$Margin$	$Benign$	$Malignant$
$Lobulated$	$Obscured$	25	25
$Irregular$	$Spicular$	19	31
$Round$	$Circumscribed$	38	12
$Irregular$	$Ill-defined$	14	36
	$Total$	96	104

2.6 Breast mass classification evaluation

The classification task was evaluated on a set of 240 RoIs, 200 used as the reference image set annotated as shown the table 1, and the remaining40 (20 benign and 20 malign) as the test set. Images were curvelet transformed, scale and orientation parameters were set to 4 and 32 respectively, resulting in a descriptor

ISBN: 978-87-981270-9-3

with 66 subbands for each RoI. The discriminant power of the curvelet descriptor was assessed using a very simple classifier, a k nearest neighbor. The best k parameter was found from a 5-fold cross validation performed on the reference set, thereby obtaining an accuracy of $89,9\%$ for $k = 5$. Results were compared with other curvelet description methods, namely: energy of the curvelet subband plus Euclidian metric [12], and mean and variance plus Euclidian metric [12]. Table 2 shows the sensitivity measure for the classification task. The proposed approach outperforms the baseline curvelet representation methods in about a 20% for both benign and malign masses . The sensitivity rate for benign and malign masses are $96,4\%$, and 85.4%, showing a high discriminant power provided by the proposed curvelet representation with a very simple classifier.

Table 2. Classification performance of benign and malign classes

	KLD	$EUCL\_1$	$EUCL\_2$
$Benign$	**85.4**	63.2	71.4
$Malignant$	**96.4**	68.2	76.8

2.7 Content-based image retrieval evaluation

The retrieval performance was assessed by computing the relevance of the recovered images, according to the ground truth DDSM mammogram databases. In contrast with previous works, shape and margin were herein taken into consideration. We defined three levels to describe the degree of relevance , namely $Score = 1$ when two correct labels were found, $Score = 0,5$ for one, $Score = 0$ for null. The Precision-Recall graph was used for evaluating the performance of the CBIR scheme. The precision (P) was defined as the number of relevant images that the system was able to find among all retrieved images, while recall (R) was the number of relevant images that the system was able to find among all the relevant images stored in the database (notice that recall amounts to the sensitivity).

$$P = \frac{\sum_{i=1}^{k} S_i}{K}, \qquad R = \frac{\sum_{i=1}^{k} S_i}{\sum_{i=1}^{n} S_i} \tag{3}$$

where S_i is the score assigned to the i^{th} RoI, K is the number of retrieved images and n is the total number of images in the reference database. Evaluation of the CBIR strategy consisted in calculating the precision and recall of 50 different random queries as follows: from the original dataset of 200 RoIs, a set of 50 randomly selected RoIs was firstly chosen and each was used as a query to retrieve the most 50 similar RoIs. The obtained averaged precision and recall were 89% and 62%, respectively. Figure 2 shows the Precision-Recall curve obtained with incremental steps of 5. Note that in this task the proposed approach (blue line) also outperforms the other curvelet representations.

ISBN: 978-87-981270-9-3

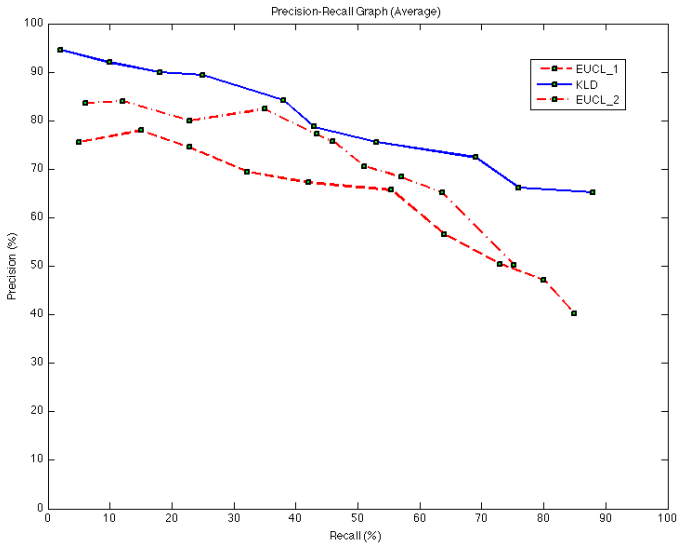

Fig. 2. Precision-Recall curve of content based information retrieval scheme for 50 image queries.

Table 3 shows the mean retrieval performance obtained by the proposed approach for four mass descriptions. The Irregular-ill defined and Irregular-Spicular classes are specially associated to malign masses, whilst the Round-Circumscribed and Lobulated-Obscured classes are associated to benign masses. Average performance was larger than 75%, a figure very acceptable for actual clinical applications.

Table 3. Image retrieval performance of four BI-RADS descriptions

	Precision	Recall
$Irregular - illdefined$	0.91	0.64
$Irregular - Spicular$	0.89	0.76
$Round - Circumscribed$	0.83	0.93
$Lobulated - Obscured$	0.86	0.68
$Average$	0.86	0.75

3 Conclusion and future works

We have introduced a new descriptor for breast masses, based on the curvelet transform and a statistical model of the curvelet coefficients. By applying the

ISBN: 978-87-981270-9-3

curvelet transform and approaching the subband energy with a generalized Gaussian model, we obtained a robust representation which captures the edge distribution at different orientation and scales. Experimental results indicate that the new feature improves the classification and retrieval performance for an relevant mammogram findings, namely mass shape, margin and malign or benign pathology, when compared to other features, also based on curvelets. Future works include improving the feature with invariance to rotation and scale and extensive experimentation in larger mammogram databases.

References

1. Buseman, S., Mouchawar, J., Calonge, N., Byers., T.: Mammography screening matters for young women with breast carcinoma. Cancer 97, 352–358 (2003)
2. Candes, E., Demanet, L., Donoho, D., Ying, L.: Fast discrete curvelet transforms. Multiscale Modeling and Simulation 5(3), 861–899 (2006)
3. Do, M., Vetterli, M.: Wavelet-based texture retrieval using generalized gaussian density and kullback-leibler distance. IEEE Transactions on Image Processing 11(2), 146–158 (2002)
4. Eltoukhy, M., Faye, I., Belhaouari, S.: Breast cancer diagnosis in digital mammogram using multiscale curvelet transform. Computerized Medical Imaging and Graphics 34, 269–276 (2010)
5. Gómez, F., Romero, E.: Texture characterization using a curvelet based descriptor. In: Progress in Pattern Recognition, Image Analysis, Computer Vision, and Applications. vol. 5856/2009, pp. 113–120 (2009)
6. Murtagh, F., Starck, J.: Wavelet and curvelet moments for image classification: Application to aggregate mixture grading. Pattern Recognition Letters 29, 1557 –1564 (2008)
7. Narvaez, F., Diaz, G., Romero, E.: Automatic bi-rads description of mammographic masses. Digital Mammography, 10th international workshop on digital Mammography Volume 6136, 673–681 (2010)
8. Nishikawa, R.M.: Current status and future directions of computer-aided diagnosis in mammography. Computerized Medical Imaging and Graphics 31, 224–235 (2007)
9. Rosa, N.A., Felipe, J.C., Traina, A.J., Rangayyan, R.M., Azevedo-Marques, P.M.: Using relevance feedback to reduce the semantic gap in content-based image retrieval of mammographic masses. Conf Proc IEEE Med Biol Soc pp. 406–409 (2008)
10. Sahiner, B., Chan, H.P., Petrick, N., Helvie, M.A., Goodsitt, M.M.: Computerized characterization of masses on mammograms: The rubber band straightening transform and texture analysis. Medical Physics 25 (1998)
11. Sheng, L., Babbs, C.F., Delp, E.J.: Multiresolution detection of spiculated lesions in digital mammograms. IEEE Transactions on Image Processing 10(6), 874–884 (2001)
12. Sumana, I., Islam, M., Zhang, D., Lu, G.: Content based image retrieval using curvelet transform. In: Proc. of IEEE International Workshop on Multimedia Signal ProcessingMMSP. pp. 11–16 (2008)
13. Zheng, B., Mello-Thoms, C., Wang, X.H., Abrams, G.S., Sumkin, J.H., Chough, D.M., Marie, Ganott, A., Lu, A., Gur, D.: Interactive computer aided diagnosis of breast masses: Computerized selection of visually similar image sets from a reference library. Academical Radiology 14, 917–927 (2007)

ISBN: 978-87-981270-9-3